

**Helicopter Flight in the Airwake of Non-Aviation Ships.**

By Nigel Hugh Wakefield.  
School of Engineering Sciences,  
University of Southampton.

May 2000

This thesis is submitted for examination for the degree  
Doctor of Philosophy.

UNIVERSITY OF SOUTHAMPTON

ABSTRACT

FACULTY OF ENGINEERING AND APPLIED SCIENCE,  
SCHOOL OF ENGINEERING SCIENCES.

Doctor of Philosophy

HELICOPTER FLIGHT IN THE AIRWAKE OF NON-AVIATION SHIPS.

by Nigel Hugh Wakefield.

There are problems specific to the helicopter/ship dynamic interface, which limit helicopter operations. Amongst these is the difficulty associated with landing on a moving platform. The ship airwake, which includes large velocity gradients and areas of turbulence, is considered a crucial factor in limiting these operations. For this reason knowledge of the air flow around the ship and through the helicopter's rotors is necessary to understand the problems the helicopter encounters as it lands and takes off.

A CFD model of a hovering helicopter main rotor is developed to examine airflow in the presence of ship structures and side winds. The rotor is modelled by modifying the governing Navier-Stokes equations in the region of the disc. The extra terms added to the governing equations apply a downforce to the fluid; these forces are independent of the flow around the rotor and equal to the helicopter weight. The boundaries of the computational domain are also modified in order to generate a physically correct solution. Flow solutions in both two and three dimensions are achieved using the commercial flow solver CFX. The flow solutions exhibit very good correlation with established momentum and power principles. The rotor model is also flown in steady horizontal flight. The resultant flow solutions agree with theoretical flow fields thus proving the validity of the rotor model.

An extensive sensitivity study of CFD grid and solver parameters is also presented. This ensures that all flow solutions achieved are of the highest fidelity but are reached in a computationally efficient manner. The turbulence models are adjusted to produce solutions which agree with wind tunnel data. CFD flow solutions are presented which correspond to full-scale version of experimental studies on bluff bodies in wind tunnels. The results show that qualitative features of the wind tunnel flow regimes are recognised and resolved by the computational solution. The CFD also agrees with the quantitative data where available.

Finally the helicopter rotor model and the ship model are combined to yield one flow solution, which cannot be achieved by superposition. The resultant flow yields valuable data about the induced velocities at the rotor which ultimately determine the control pitch and power required to maintain the hover in a given location.

Studies such as these are economic to instigate compared to costly full scale sea trials and wind tunnel tests. Whilst they will never replace experimentally derived operational envelopes they will provide understanding of the airflow and the unique problems it introduces.

# Table of Contents

<b>Abstract</b> .....	ii
<b>Table of Contents</b> .....	iii
<b>Acknowledgements</b> .....	vii
<b>Nomenclature</b> .....	viii
<b>1 Introduction</b> .....	<b>1</b>
<b>2 Literature Review</b> .....	<b>3</b>
2.1 Introduction.....	3
2.2 Flight Simulators .....	4
2.3 Safe Operating Limits.....	4
2.4 Blade Strikes.....	7
2.5 Updating Present Ships and Designing Future Ships .....	8
2.6 Helicopter Undercarriage Dynamics.....	10
2.7 Full Scale Air Flow Data .....	12
2.8 Model Scale Tests in Wind Tunnels.....	13
2.9 Computational Fluid Dynamics (CFD).....	16
<b>3 CFD Applied To Bluff Body Aerodynamics</b> .....	<b>22</b>
3.1 Introduction.....	22
3.2 Description of Flow Solver.....	23
3.3 2D Surface Mounted Block Parameters.....	24
3.4 Optimised Solution Process.....	27
3.4.1 Pressure Correction Method .....	27
3.4.2 Relaxation Factors .....	28
3.4.3 Equation Solvers .....	29
3.5 2D Optimum Location of Boundaries. ....	30
3.5.1 Downstream Boundary.....	31
3.5.2 Upstream Boundary .....	31
3.5.3 Upper Boundary .....	32
3.6 Upper Boundary Condition Applied.....	33
3.7 Optimum Grid Density. ....	36
3.8 Block Structure. ....	41
3.9 3D Surface Mounted Block. ....	47

3.10	Comparison of CFD and Experimental Data.....	51
3.10.1	Introduction.....	51
3.10.2	Experimental Model.....	52
3.10.3	CFD Turbulence Models.....	53
3.10.4	Comparison and Discussion.....	56
3.11	Conclusion.....	59
<b>4</b>	<b>Modelling a Helicopter Using CFD.....</b>	<b>61</b>
4.1	Introduction.....	61
4.2	The Helicopter Model.....	62
4.2.1	The Main Rotor.....	62
4.2.2	The Tail Rotor.....	64
4.2.3	The Fuselage.....	65
4.3	Verification of Rotor Model.....	66
4.4	Deficiencies of Existing Boundary Conditions.....	70
4.5	Theory of The New Boundary Condition.....	72
4.6	Verification of Boundary Conditions.....	75
4.6.1	Introduction.....	75
4.6.2	Flow Solver.....	75
4.6.3	General Geometry of Verification Model.....	75
4.6.4	Evaluation of Flow Solution.....	77
4.6.5	Parameters Varied.....	78
4.6.5.1	Effect of Peripheral Block Depth.....	78
4.6.5.2	Effect of Number of Cells in Peripheral Blocks.....	80
4.6.5.3	Effect of Total Thrust Exerted.....	81
4.6.5.4	Effect of Grid Coarseness.....	82
4.6.5.5	Effect of Domain Size.....	83
4.6.5.6	Effect of Domain Shape.....	85
4.6.5.7	Effect of Overall Model Size.....	87
4.6.5.8	Effect of Fluid Viscosity.....	89
4.6.5.9	Effect of Number of Cells in Disc Depth.....	89
4.6.6	Detailed Analysis of Momentum and Power.....	90
4.7	3D Rotor Model.....	94
4.7.1	Introduction.....	94
4.7.2	Grid and Turbulence Parameters.....	95
4.7.3	Constant Thrust Model.....	97

4.7.3.1	Thrust Definition .....	97
4.7.3.2	Constant Thrust Model Flow Analysis.....	97
4.7.4	Blade Element Thrust Model .....	100
4.7.4.1	Thrust Definition .....	100
4.7.4.2	Blade Element Thrust Model Flow Analysis.....	103
4.8	Conclusion .....	107
<b>5</b>	<b>Power Requirements of Helicopter Hovering in Ground Effect .....</b>	<b>109</b>
5.1	Introduction.....	109
5.2	Nomenclature.....	109
5.3	Description of Geometry and Boundary Conditions.....	109
5.4	Description of Actuator Disc .....	110
5.5	Flow Solver.....	111
5.6	Results.....	112
5.6.1	Infinite Height .....	112
5.6.2	Ground Effect.....	115
5.7	Conclusion .....	120
5.8	Comparison.....	120
<b>6</b>	<b>2D Helicopter Flight Over a Frigate Helideck .....</b>	<b>124</b>
6.1	Introduction.....	124
6.2	The Rotor Model.....	124
6.3	Modified Boundary Conditions .....	125
6.4	Rotor In Hover .....	125
6.5	Ship Airwake .....	128
6.6	Ship/Helicopter Interaction.....	129
6.6.1	Zero Wind .....	131
6.6.2	Wind 30 Knots, Port to Starboard.....	134
6.6.3	Wind 60 Knots, Port to Starboard.....	137
6.6.4	Wind 30 Knots, Starboard to Port.....	140
6.7	Conclusions.....	143
<b>7</b>	<b>3D Forward Flight Inflow Models.....</b>	<b>145</b>
7.1	Summary .....	145
7.2	Description of Geometry and Boundary Conditions.....	145
7.3	Constant Thrust Model, Forward Flight .....	146
7.3.1	Induced Velocity Along Rotor Centreline .....	146
7.3.2	Glauert Inflow Factor.....	148

7.3.2.1	Introduction .....	148
7.3.2.2	CFD Prediction and Analysis .....	149
7.4	Blade Element Thrust Model, Forward Flight.....	155
7.4.1	Comparison to Theoretical Inflow .....	155
7.4.2	40 Knots Forward Flight.....	156
7.5	Discussion of Results.....	160
7.6	Scale Dependency Study.....	162
7.9	Conclusion .....	164
<b>8</b>	<b>3D Helicopter Flight Around A Ship's Superstructure. ....</b>	<b>166</b>
8.1	Introduction.....	166
8.2	Ship Model.....	166
8.3	Ship Airwake .....	166
8.3.1	Introduction.....	166
8.3.2	Zero Degrees.....	167
8.3.3	45 Degrees.....	173
8.3.4	90 Degrees.....	178
8.3.5	Conclusion .....	181
8.4	Helicopter Flight.....	182
8.4.1	Introduction.....	182
8.4.2	Helicopter Model.....	183
8.4.3	Helicopter Location and Flow Directions .....	183
8.4.3.1	Zero Degrees.....	184
8.4.3.2	90 Degrees .....	188
8.4.3.3	180 Degrees .....	192
8.4.4	Analysis and Discussion of Flow Solutions.....	196
8.4.5	Conclusion .....	198
<b>9</b>	<b>Conclusions and Future Work .....</b>	<b>200</b>
9.1	Conclusions.....	200
9.2	Future Work.....	202
<b>10</b>	<b>References.....</b>	<b>206</b>

## **Acknowledgements**

Many people have inspired and encouraged me to complete this thesis both intentionally and otherwise. Firstly I would like to thank the delegates I have encountered at conferences, whose interest and enthusiasm about this work provided encouragement often at times of despondency.

I would like to thank my supervisors, Dr. Simon Newman and Mr. Phil Wilson, who have had the task of looking after me over the last few years. I have spent long hours with Simon in his office, making each other perform mental acrobatics as we discuss ideas. Fortunately these sessions were terminated with coffee, biscuits and a friendly conversation about something other than ships and helicopters.

My family and Rachel have provided me with immeasurable support, despite initial scepticism about this venture.

## Nomenclature

$a$	blade lift slope coefficient
$A$	area
$A_R$	area of rotor model/actuator disc
$A_{DW}$	area of rotor downwash
$A_1, B_1$	longitudinal and lateral pitch incidence variations.
$\bar{A}$	area vector
$B_x, B_y, B_z$	body force exerted on fluid in coordinate system ( $N/m^3$ )
$\bar{B}$	vector of body force
$B, C$	Dimensions of computational domain
$c$	rotor blade chord
$C_d$	rotor blade coefficient of drag
$C_T$	rotor coefficient of thrust
$C_{T_{INF}}$	rotor coefficient of thrust, out of ground effect
$D$	blade drag
$D_p$	Thickness of peripheral blocks
$E$	Glauert inflow factor
$EF\%$	percent difference between $T_{APP}$ and $T_{DEF}$
$EP\%$	percent difference between ideal power and measured power
$\bar{F}$	Force exerted on a control volume of fluid
$\bar{F}_p$	Force exerted around the perimeter surface of a control volume of fluid
$\bar{F}_{sw}$	Horizontal swirl force induced by blades' rotational motion
$g$	gravitational acceleration ( $9.81m/s^2$ )
$H$	thickness of actuator disc model
$k$	turbulent kinetic energy
$k_0$	initial turbulent kinetic energy
$L$	blade lift
$m$	mass of helicopter
$N$	number of rotor blades
$N_p, N_x, N_y$	Grid division parameters
$p$	pressure
$\Delta p$	pressure discontinuity across the rotor model/actuator disc
$P$	Power
$P_H$	Power to hover out of ground effect, 2D model (Chapter 6 only)

$\%P_H$	Power to hold station as percent of hover power, 2D model (Chapter 6 only)
$P_{INF}$	Power at an infinite height from the ground
$P_{IDEAL}$	Theoretical ideal power
$p_{INF}$	static pressure, distant from rotor
$p_{DOM}$	static pressure of fluid on entry into computational domain
$Q$	Torque
$r$	radial distance from rotor centre
$R$	rotor radius
$T$	thrust
$\overline{T}_{APP}$	apparent thrust of rotor model, found from momentum considerations
$T_{APP}$	magnitude of $\overline{T}_{APP}$
$\overline{T}_{DEF}$	thrust of rotor model
$T_{DEF}$	magnitude of $\overline{T}_{DEF}$
$U_T$	relative velocity between blade element and surrounding fluid
$u,v,w$	time varying component of velocity components (Chapter 3 only)
$u,v,w$	components of velocity
$\overline{u^2}, \overline{v^2}, \overline{w^2}$	mean square of time varying component of velocity components
$V$	velocity scalar
$\overline{V}$	velocity vector
$v_i$	Induced velocity through rotor
$v_{iG}$	Glauert induced velocity through rotor
$V_\theta$	fluid velocity, horizontal and perpendicular to radius
$V_1$	induced velocity scalar (momentum theory)
$V_2$	velocity scalar downstream of rotor (momentum theory)
$V_{DOM}$	velocity scalar on entry to domain
$V_F$	forward speed of helicopter rotor
$V_T$	blade tip speed, $R\Omega$
$V_{AV}$	average lateral velocity component at rotor. (Chapter 6)
$W_P$	vertical velocity component at 5m port of rotor centreline. (Chapter 6)
$W_S$	vertical velocity component at 5m starboard of rotor centreline. (Chapter 6)
$\Delta W$	$W_P - W_S$ . (Chapter 6)
$x,y,x$	Cartesian coordinate system.

$r, z, \theta$	cylindrical coordinate system (Chapter 5 only)
$Z$	height of rotor above ground (Chapter 5 only)
$\chi$	angle between axis of the wake and normal to tip-path plane
$\varepsilon$	turbulent dissipation
$\varepsilon_0$	initial turbulent dissipation
$\overline{\Phi}$	momentum flux
$\phi$	angle between fluid and blade motions
$\kappa$	linear blade twist along length
$\lambda$	non-dimensional inflow, $V_I/V_T$
$\mu$	advance ratio, $V_F/V_T$
$\mu_{\text{EFF}}$	effective viscosity
$\mu_{\text{LAMINAR}}$	laminar viscosity
$\mu_{\text{TURBULENT}}$	turbulent viscosity
$\Omega$	rotor blade speed of rotation
$\psi$	blade azimuth location
$\rho$	density of air
$\theta$	blade element angle from horizontal.

## **1 Introduction**

The demand for the use of helicopters in marine environments such as ships and oil rigs has risen steadily in recent years. The helicopter provides a fast method of transport whilst requiring less storage space and take-off facilities than fixed wing aircraft. The helicopter has also developed specialised military uses such as submarine detection and air to surface targeting. The flexibility of helicopters is reflected in the increased demand to operate in ever worsening environmental conditions.

At present, the established method for determining safe helicopter operating limits is a very costly series of full-scale trials. This usually involves waiting at sea for appropriate environmental conditions to occur when a test pilot performs the takeoff and landing manoeuvres. The landing is rated according to the workload the pilot experiences and varies from low to dangerous. The whole procedure has to be repeated for every ship/helicopter combination, and each landing spot on the ship.

An experimental SHOL (Safe Helicopter Operating Limit) such as this has the advantage of being realistic but it also requires the provision of vast resources both in finance and time. These studies also provide no systematic information about the areas in which the pilot experienced difficulties. Obtaining such a SHOL, by definition, contains a degree of danger.

The landing manoeuvre is not the only operational aspect which limits helicopter usage. During normal flight conditions the rotor blades are held out horizontally by centripetal forces. Modern helicopters use engine governors to assure the rotor speed is kept at the prescribed level. The centripetal stiffening of the blades is proportional to the square of the rotational speed and therefore during rotor engagement and disengagement the blades experience vastly reduced outward forces. This is rarely a problem on land but at sea the rotor will experience vertical airflow components which create vertical forces that are no longer resisted by large centripetal forces. These large displacements are known as blade sailing. In extreme cases, large tip displacements have caused fatalities to the ground crew. Aircraft have been rendered inoperable by blades striking the fuselage.

The dynamic interface contains many problems. This study attempts to unlock the mysteries associated with airwake and prove it is possible to model the ship airwake, helicopter wake and both individually and in combination. This study does not profess to solve the whole problem and provide a safe and accurate helicopter clearance program. At present such a tool is not available on a computer, as there is always a highly subjective nature to a test pilot's workload rating. A CFD generated airflow solution will indicate whether the airwake is prohibitive to helicopter flight. Even if the airwake is acceptable there are many other factors which may prevent helicopter operation, for example ship motions. A CFD analysis has many advantages. The most evident is the cost and speed at which one can be obtained. Results from such an analysis are repeatable and not subject to experimental errors. The accuracy of CFD solutions are limited by the numerical methods and the modelling assumptions. These solutions, once obtained, give pressure and velocity components at every location throughout the model. The flow data obtained can be used in simulators so that pilots can practice landing on ships safely. A CFD study can also be performed on ship designs whilst in the conceptual stage. Thus the effectiveness of helideck and hangar designs can be tested to reduce turbulence over the flight deck. Naturally the fidelity of the predictions must be of the highest quality.

## 2 Literature Review

### 2.1 Introduction

Whilst there has been much research into the flow around aerodynamic bodies, there has been little into bluff body aerodynamics. A bluff body is defined as a body whose drag consists largely of form drag, caused by large regions of separated airflow. The superstructures of ships are such bluff bodies consisting of large box-like shapes and to the author's knowledge no superstructures have been designed with any aerodynamic considerations. As a result non-aviation ships such as frigates have helidecks which are wholly unsuited to efficient helicopter/ship interfacing. Helicopter operations at sea are highly restricted. Healey [2.1] states that helicopter operations are limited to 10% of the total time at sea for a 400-ft frigate in the North Sea in wintertime.

The work on ship airwake being undertaken presently can be categorised under several objectives and three distinct methods of research. Detailed knowledge of the airwake is necessary for use in flight simulators, determining safe operating envelopes, blade strike prediction, forces on helicopter undercarriage, updating present ships, and future aerodynamically designed ships. The methods of research can be divided into several broad categories, full scale, model scale, computational fluid dynamics (CFD) or a combination of these three. Carico [2.3] compares and contrasts the merits of each of these methods.

From the literature review it has become apparent that only a few nations are currently researching the ship/helicopter dynamic interface. There is a collaboration between USA, Canada, Australia and UK, and is known as the Tripartite Technical Co-operation Program (TTCP). [2.8] states this collaboration has been instigated to progress the simulation of the operation of the maritime helicopter. The only other nations, to the author's knowledge, with any publications are Italy and Holland.

All of the publications discussed below have been broadly categorised into seven sections according to the emphasis. The sections comprise reasons for research, flight simulators, safe operations, blade strikes, updating present ships,

undercarriage dynamics, and methods of gaining data full scale, model scale and CFD results. There is however some interaction between the sections.

## **2.2 Flight Simulators**

J. Val. Healey [2.4] considered data used for the NASA Ames ‘Shipboard Simulator’. Using a wind tunnel with an atmospheric boundary layer model and turbulence induced by placing objects on the wind tunnel floor, he discovered that the existing data used in the simulation was faulty. He took data at 17 points along a typical glide path aft of the ship previous to landing. At each point measurements of velocity components and turbulence components were recorded. He discovered that the new data conflicted with the old data and the turbulence intensity trends were reversed. The measurements yielded spectra of the turbulence. He concluded that an atmospheric boundary layer could be satisfactorily modelled within a wind tunnel. The points near the model had low mean velocity so the measurements with a triple hot-wire probe may not have been completely reliable. He suggests retaking these values with either a pulsed wire or Laser Doppler Anemometer (LDA).

The Defence Research Agency (DRA) has an Advanced Flight Simulator (AFS). Tate [2.6] discusses the present state of this simulator. He quotes a reference (Jewell et al. [2.7]) that highlighted the ‘importance of realism in modelling the ship airwake’. He also describes how work began in 1992 to develop a generic airwake model, although this did not feature within the simulator at that time. At the end of the paper, future work is described that would include the introduction of a new ship airwake model, possibly obtained from full-scale data.

## **2.3 Safe Operating Limits**

Fang [2.9] describes the method the Dutch use to ascertain the safe operating envelope. This starts with preliminary wind tunnel tests to ascertain the relationship between the ship’s anemometer and the wind over deck (WOD). No reference is made to simulating an atmospheric boundary layer. The results are used to make initial assumptions about safe take-off/landing paths. The emphasis

given is that these tests will ensure that the full-scale tests can be performed efficiently.

At full scale, trained test pilots are employed to take off and land using one of the three procedures outlined, namely fore-aft, relative wind and cross deck. These three procedures relate to the helicopter's final approach to the ship prior to landing in relation to the ship and the wind direction.

The final result is a polar plot of relative wind direction and relative wind speeds, on which are marked various regions. Each region indicates the safe apparent wind directions and speeds at which the helicopter can perform the takeoff and landing procedures. For each all up weight of the helicopter, there exists a region on the polar plot.

This paper, whilst interesting, does nothing to address the problem of increasing the limited operational conditions. It also uses a very restricted understanding of the problem and a purely experimental method of determining limits; however it can be argued that this is the most accurate way of determining limits for existing ship/helicopter combinations.

Finlay [2.10] outlines the method the Aeroplane and Armament Experimental Establishment (A&AEE) in the UK uses to determine operating limits. In the introduction the author describes how the method, although having undergone a few refinements since the 1960's, is basically the same as that used 35 years ago. This method requires a few full-scale flight tests over land to establish the following before performing any ship trials:

- The aircraft's low speed envelope, with adequate control and power margins.
- The hover performance at operational mass, for various atmospheric conditions.
- The relationship between pedal position and relative wind speed and direction.
- The adequacy of control margins with varying centre of gravity (CG).

- The effect of changes in aircraft payload and the pedal position/relative wind correlation.

Full-scale tests are then performed by test pilots; these are graded on a scale from one to six. One to four represents acceptable pilot effort and workload, five represents unacceptable and six corresponds to a dangerous situation. Emphasis is placed on landing, which is generally considered to be more dangerous than taking off (it is assumed that if it is possible to land it is possible to take off). During the full-scale trial the helicopter is instrumented, with engine torque, tail-rotor pitch, main-rotor pitch and rotor speed data gathered. The deck motion, helicopter mass and air density are also recorded.

These tests usually take around two to three weeks and culminate in a polar plot of safe operating envelopes. Incorporated into this plot are values of all-up helicopter mass (AHM) - the plots with lower AHM have larger operating envelopes as lighter helicopters have greater control and manoeuvrability.

Trials performed before 1990 by the Italian Navy are recorded in [2.11]. This paper emphasises evaluation of helicopter handling capabilities around ships and evaluating various landing techniques. There is no reference to any theoretical modelling, so one assumes this is another example of trial and error testing.

Wensheng [2.12] uses a simple CFD model to calculate safe operating envelope, which is discussed in Section 2.9.

The four member nations of the TTCP co-authored a review paper [2.8], which describes the state of research within UK, USA, Australia and Canada defence organisations. The paper identifies that safe helicopter operations are limited by available control margins, thus agreeing with Wakefield [2.44]. The UK and Australia are currently incorporating look-up tables into their flight simulators. A test pilot has to land a helicopter using the simulator, and the landing manoeuvre is analysed to determine the workload and if the process was safe enough for repetitive operational purposes. The airwake data used within the simulator is found from CFD codes and does not include any ship-helicopter flow interaction or ship motions.

## 2.4 Blade Strikes

During normal operation, helicopters have a nearly constant rotor speed; this varies between helicopter types but is usually in the range 200-350 rpm. The rotor blades are not fixed rigidly at the hub but are hinged in the directions parallel (lag) and perpendicular (flap) to the rotation plane. In flight, vertical thrust applied by the blade aerodynamics is balanced against the centrifugal load from rotation; for example, the acceleration experienced by the rotor tip of a Westland Sea King is around 463G, the vertical thrust only deflects the blades around 5 degrees [2.15]. Most helicopter blades are attached to the hub using hinges to form what is known as an articulated hub. This system is used to remove the moments that the rotor blades would exert on the hub with a rigid blade attachment.

The phenomenon of blade sailing occurs during the period of rotor engagement or disengagement. The rotor must accelerate from zero to operating speed during engagement and from operating to zero speed during disengagement. At lower rotational speeds the blades no longer experience large centrifugal forces and it is during these times that the blades are susceptible to dangerously large displacements, since a large aerodynamic moment can be generated which is not sufficiently counteracted by the reduced centripetal acceleration.

The loads exerted on the blades to create such large displacements can be attributed to local turbulence or varying flow fields around the rotor azimuth. Blade sailing can occur on land but the separation regions in a ship airwake are especially conducive to blade sailing, where large wind components perpendicular to the rotor plane are common. Healey [2.17] notes that blade strikes can lead to complete loss of a helicopter. Crowley [2.18] performed a study into helicopter fatalities within the US Army between 1972 and 1991, not considering crash fatalities. He found that there had been 24 blade strikes reported during this period involving human injury. Of these 11 were fatal, with 65% of all strikes head injuries, 17% chest, 7% abdomen. Whether the strikes occurred at sea or on land, is not stated.

Newman has published numerous papers on this topic [2.13], [2.14], [2.15] and [2.16]. He describes scale-model tests in a wind tunnel and numerical calculations. The models are based on a Rover Class Royal Fleet Auxiliary (RFA)

yawed at 90 degrees to the wind with a Westland Lynx helicopter placed at various locations around the deck. The numerical simulation used air flow data taken from wind tunnel tests.

Both the numerical and experimental results show that the greatest blade displacements occur immediately after rotor engagement commences and immediately before zero rotor speed during disengagement. Both experiment and computation revealed maximum displacement of around 25 degrees and minimum around -10 degrees, these being the mechanical flapping limits of the rotor model.

The wind-tunnel tests on the Rover Class RFA showed that the flow separated at the windward edge of the flight deck, where the separated region extended upwards at an angle of around thirty degrees to the horizontal flight deck. The greatest motions occurred when the rotor hub centre was placed at the shear-layer interface between the flow adjacent to the flight deck and the smooth external flow. This can be attributed to characteristics of the two different flow regions, one being turbulent with insignificant net flow, the other being relatively uniform but containing a large vertical velocity component. The smallest rotor displacements occurred when the entire span of the rotor was immersed within the recirculation region.

Smith [2.19] reviews the analytical methods of determining blade displacements during engagement and disengagement. This publication discusses the work within 20 references, offering no new data or analysis methods.

## **2.5 Updating Present Ships and Designing Future Ships**

A new generation of ships could represent increased operating envelopes for specific ship/helicopter combinations. Healey [2.17] discusses, at great length, possible innovations to existing ships.

Healey suggests three methods of improving ships presently in service. Firstly the use of deflectors around the hangar and edges of the deck to tailor the flow characteristics. For this he notes that initial studies indicate that the deflectors are successful at controlling separation at the edges of the deck but aggravate the problems around the hangar.

Secondly the introduction of a porous helideck above the existing one, which would bring the flight deck to a level similar to the hangar roof and remove the problems associated with separation around the aft face of the hangar. The helicopter would have to be winched down by some mechanism to access the hangar for storage.

The final suggestion for existing ships is sheltering the helideck. This follows the philosophy that removing kinetic energy from the airflow will reduce velocity and possible flow problems. Two methods of slowing the flow are presented. The first is the introduction of a windbreak, which is the nautical equivalent to trees on land; this would have to take the form of densely clustered masts of various sizes. The second suggestion requires wind turbines to be placed around the deck, thus absorbing the wind's kinetic energy.

Healey [2.17] briefly discusses the results of initial work into the use of deflectors but gives no references. However, Rhoades [2.20] performs wind-tunnel tests on a model with deflectors attached. This paper presents results from wind tunnel tests in three forms, photographs, diagrams of particle traces and qualitative verbal descriptions of the flow.

When considering the next generation of ships, Healey [2.17] makes several suggestions for future ship designs that he considers would reduce cost of interface testing and increase operating envelopes. The first suggestion discusses the general hull shape. The paper states that the helideck should be as close to the water as possible, the benefits being twofold. Wind strength diminishes as you approach the sea surface and also a lower deck creates less blockage and thus less upflow at the windward edge of the deck. The possibility of using a Small Waterplane Area Twin Hull (SWATH) is considered, the advantage being the large storage volume at a low height above the sea. The helicopter could be lowered on a platform into the hangar below the flight deck.

The paper then considers the possibility of airflow improvement given that the ship must have a hangar above deck level. Healey states that the helideck should be well away from the hangar either behind or forward of the superstructure. The hangar should have rounded edges that inhibit airflow separation. Again it is

suggested that the helideck should be raised to the same level as the hangar roof, and lowered after the helicopter lands.

Finally, the paper discusses the need for rounded deck edges that would reduce the size of the separated region and decrease turbulence intensities. As a final comment, Healey suggests that the design of non-aviation ships should take the general leads of the aerodynamics field, in the use of a computational/experimental approach before construction is initiated.

## **2.6 Helicopter Undercarriage Dynamics**

An understanding of the helicopter dynamics is required to estimate loads exerted on the undercarriage during landing, and calculate the ship/helicopter reaction and frictional forces prior to takeoff and after landing.

Work performed by the Aeronautical Research Laboratory in Australia [2.21], [2.22] and [2.23] discusses creating a model to simulate the control required to land a helicopter on a small frigate and the forces exerted on the undercarriage both prior to take off and upon landing. Arney et al. [2.21] identifies key areas that need to be addressed, radome clearance on landing, undercarriage loads, and pilot control margins. The mathematical model that has been constructed has several modules, ship motion, undercarriage, helicopter aerodynamics, engine transmission and pilot control modules. Three applications of the model are shown. Firstly the pilot control is delayed resulting in radome contact with the helideck upon landing. Secondly the lack of ground effect is modelled resulting in reduced control to the pilot. Finally the ship motions are used to find relative helicopter/deck clearances.

Arney, Blackwell, Erm and Gilbert [2.22] describes improvements to the model which included full-scale wind tests and static trials performed on a Seahawk undercarriage. The static trials involved sitting the helicopter on three load cells, one for each wheel and jacking up the helicopter incrementally whilst recording load and displacements. The concept of the dynamic trials was discussed in the paper but these had not been performed. Full-scale ship airwake data was

obtained as described in section 2.7. The improved values found were fed into the simulation code.

Blackwell, Arney, Gilbert and Truong [2.23] describe the continuation of the work performed in [2.22]. The paper describes the current status of the Seahawk/FFG-7 interface model. The model now includes dynamic values for damping coefficients of the oleos and tyres. The airwake used in the model now has turbulent components. It is planned to use this model to assist the Royal Australian Navy in determining safe operating limits for this helicopter/ship combination.

Fu-Shang, Baitis and Meyers [2.25] describe a computer program that will calculate the maximum ship motions below which it is safe to leave an untethered helicopter sitting on the deck. The program in Quick Basic found the ship motions that satisfied two conditions. Firstly, the frictional force between the deck and the wheels was great enough to prevent the helicopter sliding, and secondly all three wheels had a positive reaction force, or put alternatively, they remained in contact with the deck and the helicopter was not in danger of toppling.

In the analysis, various assumptions were made: - the helicopter fuselage is rigid, helicopter/ship motions are small and the angles are linearised, the helicopter landing gear is linearly damped, wind speed and direction remain constant over a time period of one third of a second. The unclear assumption stated is 'All aerodynamic tables are determined as a function of steady wind angle with respect to the longitudinal axis of the helicopter when the ship is at the level position'. The author used various values for a coefficient of friction.

Other parts of the calculations about which the reader is not informed include how the ship accelerations on the helideck were found. There are no details of frequency used in the ship roll motions or the helicopter inertia. The forces that the rotating/non-rotating blades exert on the helicopter are found as if there is a steady wind over the deck ('The aerodynamic forces and moments due to steady wind are determined').

The outcome of the analysis is a series of graphs and tables that show that the helicopter is more likely to slide off the deck than roll over. All results are expressed as extreme roll angles. The authors state that such a program should be available onboard all frigates and the relevant parameters fed into the program prior to helicopter use.

Ferrier, Polvi and Thibodeau [2.2] and Ferrier and Langlois [2.26] consider the problem of helicopters sliding on the flight deck, tipping over and even unintentional takeoffs. The objective of the simulator model was to identify safe envelopes of deck handling. The final result of the simulation was a polar plot of safe envelopes but with wave direction plotted around the azimuthal axis and wave height plotted radially. Again, various deck conditions were considered, dry, wet and oily. This study gives no reference to wind velocities or the resultant loads on the helicopter. The motions of the ship are derived from a simple method of RAOs (response amplitude operators) as described in [2.27] which was written in 1953.

## **2.7 Full Scale Ship Airwake Data**

There are few publications detailing full-scale ship airwake measurements. Carico [2.3] and Reddy [2.24] discuss the merits and limitations of various methods of measuring full-scale wind data.

Arney, Blackwell, Erm and Gilbert [2.21] detail a full scale trial performed by the Aeronautical Research Laboratory for the Royal Australian Navy. Measurements of both ship motion and airwake were recorded whilst the ship was en route between Sydney and New Zealand, from 18th-21st September 1989.

Measurement of airwake data was taken using a mobile mast at 13 locations around the flight deck. The mast had three tri-axial anemometers positioned at various heights up the mast. A 'reference' wind velocity was obtained using two anemometers at the rear of the flight deck. A 'freestream' velocity was obtained using the ship's anemometer.

The ship accelerometer data was used to subtract the components of the wind induced by ship motions. The wind data was sampled at 15Hz allowing spectral

analysis of the turbulence up to a frequency of 7.5Hz. In the paper, the turbulence magnitude was given as a percent of the local average velocity. This compared well with model data from a wind tunnel.

## **2.8 Model Scale Tests in Wind Tunnels**

Many papers have been published containing results of wind tunnel tests. Rhoades and Healey [2.28], Healey [2.17], [2.4], Johns and Healey [2.29], and Rhoades [2.30] describe work originating from the Naval Postgraduate School, Monterey, California. Studies undertaken by the Royal Australian Navy are described by Arney, Blackwell, Erm and Gilbert [2.22]. A comprehensive study funded by the Canadian Institute for Aerospace Research that compares full scale, wind tunnel data and CFD results is described in [2.32] by Zan, Syms and Cheney.

The Australian paper by Arney et al. [2.22] considers the whole landing problem from ship motions and airwake through to helicopter undercarriage dynamics. An FFG-7 class frigate, HMAS Darwin, is considered. They used anemometers at full scale to measure the airwake and wind tunnel data in parallel. The wind tunnel experiment was performed without supplementing the inherent turbulence within the tunnel with any additional turbulence. The authors reason that the flow regime of a model test can be used to predict full scale flow that does not include turbulence; turbulence can then be added to the mean velocity components. The authors have not attempted to recreate a realistic sheared boundary layer as described in [2.42] and successfully implemented by Johns and Healey [2.29]. Some comparisons are made between the full scale and the model velocity components; the two exhibit few similarities.

Healey and Johns [2.29] discuss results from a DD-963 destroyer model. Details are given of the method of inducing turbulence and shear layers within the wind tunnel. Results are presented in diagrammatic form of the flow regime, and several photographs of the model using helium bubbles for flow visualisation. It is concluded that the yaw angle of the ship has a greater effect than pitch or roll on the flow characteristics.

Healey [2.17] measures the velocity components and turbulence intensities at 17 points along a typical glide path prior to landing using a 3-D hot wire anemometer. The glide path is one ship length long and ends 2/3 of the hangar height above the flight deck. The velocity components and turbulence intensities are shown for the zero yaw case. Also shown are turbulence spectra at selected points. Healey concludes that the measurements over the flight deck may not be reliable and suggests that a laser Doppler, pulsed-wire or flying wire anemometer would prove more effective.

The work performed for Healey [2.4] is similar to Healey [2.17]. In Healey [2.4] the flow solution found from a wind direction acting from  $30^{\circ}$  off the starboard bow are presented, showing turbulence intensities and spectra along all three axes at all points along the glide path. A graph of the axial velocity variation with height is shown with an equivalent scaled atmospheric boundary layer; these compare very favourably. Furthermore the turbulence intensity variation is plotted and compared to standard turbulence based on non-dimensional roughness heights of 0.001 and 0.01. Except for the points on the floor and near the ceiling the measured data fits within the two standard curves given. The paper concludes that atmospheric boundary conditions can be adequately modelled within a wind tunnel.

Rhoades and Healey [2.28] consider only the airflow over the flight deck at the location of the rotor blades. The ship model is yawed to six wind directions. This study was performed to develop an understanding into the causes of blade strikes. The authors identified four main flow regions, three were fluctuating and exhibited large areas of recirculation adjacent to the ship, and the fourth region was the external flow further from the ship. The paper shows both photographs of the flow and diagrams of particle traces. The photos use helium bubbles and smoke for visualisation.

Mean velocity and turbulence data were recorded at four points, representing the circumference of the rotor blades. The turbulence data was nondimensionalised by dividing by the ship's mean anemometer reading. The authors concluded that pulsed wire, flying wire or laser Doppler anemometers should be used to measure the flow. The low mean velocities and high turbulence levels make a hot wire

anemometer unreliable. They also conclude that the effects of the helicopter fuselage ship oscillations should be investigated.

Rhoades [2.30] makes a comprehensive study of the airflow over and around the flight deck and hangar. He considers six yaw angles of an AOR model ship in a wind tunnel with a simulated atmospheric boundary condition. He also goes on to study one yaw angle, with the addition of wind deflectors. All the results are in photographic or sketched particle trace form. The results are very comprehensive but qualitative in nature, including no numerical values.

The most comprehensive study of the ship airwake is described by Zan, Syms and Cheney [2.32]. Identical models of a slightly simplified frigate shape are analysed using CFD and a wind tunnel; these results are compared to full scale data.

Within the wind tunnel and CFD study they have identified the requirement to model turbulence effectively and to calibrate the ship's anemometer relative to the free stream velocity. Measurements of all three components of turbulence and mean velocity are made at many points around the ship's flight deck. The paper concludes that the wind tunnel data and full scale data are very similar and either can be used to calibrate the CFD results. The CFD predicts a largely correct flow field with the exception that some of the velocity gradients are over predicted.

Syms and Zan [2.33] attempt to ascertain the forces and moments that the helicopter experiences when flying in the ship airwake. Airwake data is found from wind tunnel experimentation, at the location of the rotor and all three mean velocity and turbulence components are recorded. The rotor is 'flown' in the measured airwake and time histories of the forces and moments experienced are found. The method of converting flow information into forces is not explained or referenced. The numerical results are expressed as the mean and standard deviation of the forces the rotor experiences. Findings from the wind tunnel tests are also expressed qualitatively. Ignoring the flaw in the methodology, which is the initial ship airwake data does not contain the influence of the helicopter downwash, this paper does attempt to quantify the forces the helicopter experiences. These forces include not only a mean value but also a time varying component derived from turbulence. This analysis provides more insight into helicopter flight than any of the previous papers mentioned in this section.

All the publications mentioned within this section cite the helicopter/ship interface as the reason for the research being performed. However, none of the work discusses the interaction between the helicopter downwash and the ship airwake. With the exception of [2.33], there is also no attempt to ascertain the influence of the measured data upon the helicopter's operational capability.

## **2.9 Computational Fluid Dynamics (CFD)**

The majority of studies concerning the application of CFD to ship airwake studies have been published within the last ten years. Before this time all attempts at computational modelling were regarded as ineffective. J.V. Healey wrote a general paper in 1987 [2.1], including over 100 references, discussing the understanding of the ship/helicopter dynamic interface at that time. He discards CFD results, referencing work of Mahaffey [2.48] and stating 'Recent attempts by Mahaffey....resulted in the prediction of flows that bear no resemblance to experiment'.

Advancements in the understanding of CFD as a tool and increased computing power have lead to CFD becoming widely accepted. At the NATO conference for 'Fluid Dynamics Problems of Vehicles Operating Near or In The Air-Sea Interface', in Amsterdam in October 1998, the attitude towards CFD had reversed. Twelve papers were given on fixed and rotor wing operations from various ships. Of these papers all included computational or numerical models. Wind tunnel and experimental data was presented for the purpose of validation of computational results.

Tai [2.31] attempts to model the flow over a DD-963 Class Destroyer using a multizone thin-layer Navier-Stokes method; the results are compared to wind tunnel results from Healey [2.20].

The CFD model has an option for either turbulent or laminar flow. The turbulent flow solutions were presented. The results shown were largely in the form of particle traces over the hull and values of velocity downwind of the helideck. It was concluded that this method predicted large areas of separation and vortices

that were observed in the tunnel. It was also suggested that further work should consider the effect of model detail and the effect of roll and trim of the ship.

Tai [2.34] models a conventional aircraft carrier. This appears to use the same solver method as [2.31]. There is no attempt to quantify the effect of the turbulent regions upon aircraft operations. All results are presented as 'steady state' or time averaged solutions although, during the presentation of the paper, he recognised that in reality the flow is unstable and varies with time.

Murakami and Kato [2.35] performed a critical evaluation of various CFD turbulence models against wind tunnel data. They tested a surface mounted block, as this flow would produce turbulence with large regions of separation. It is also easy to grid this model for CFD studies. The central longitudinal plane, parallel to the direction of flow, was used to compare results.

The large eddy simulation (LES) model correlated best to the wind tunnel results. The  $k$ - $\epsilon$  eddy viscosity model (EVM), which is standard in most flow solvers, did not compare so favourably. Significant inaccuracies in the results of the  $k$ - $\epsilon$  EVM were removed in the Algebraic Stress Model (ASM). The Differential Stress Model (DSM) provided the best results.

The magnitude of the turbulence calculated from these computational models is of very limited use without the spectra of the turbulence. It is the spectra that dictates rotor blade response, the computational models return one value that represents the time averaged components of velocity and thus contains no frequency information. Healey discusses this more fully in [2.17].

Wensheng et al. [2.12] use two superimposed perpendicular 2-D airflows to predict airflow over the flight deck. The longitudinal and lateral flows are added to find the overall flow. The airflow at the location of the helicopter rotor blades is determined. The loads exerted on the tail and main rotors are found using control parameters. The loads on the fuselage are found from wind tunnel tests. Using certain control criteria it is determined whether landing is safe; these criteria are the margins of control available to the pilot. These are that 5% collective pitch

control, 5% lateral cyclic control, 6% longitudinal cyclic control, 10% tail rotor control and 7% total power must be available to the pilot.

The authors give no justification of using two 2D flows, other than simplicity. Viscous flows such as these cannot be added algebraically in this manner, although this may give a result that characterises full scale data. There is no reference to the turbulence model used or the levels of turbulence defined in the boundary conditions. There is also no mention of modelling an atmospheric boundary layer. It is not clear what height of horizontal plane was used but it appears to be somewhere between the deck level and hangar roof. The polar plots of safe operating envelopes show that the greatest ship relative wind speed is 50 knots from a bearing of zero degrees.

Landsberg et al. [2.36] appears to be a better attempt at a computational model. They use the flow solver FAST3D and model the ship in three dimensions. The coarseness of the grid is set at 1m throughout the computational domain. The helicopter fuselage and tail rotor are not modelled but the main rotor is represented by an actuator disc, with a constant velocity through it based on a helicopter weighing 11000 lbs. and having a rotor radius of 27ft. An atmospheric boundary layer is placed at the boundary conditions as defined in [2.37]. The exhaust gases from the ship are also modelled. The computational model run is started with the helicopter 165ft from the landing deck at a glide path of 3 degrees. The helicopter takes 18.2s to reach the hover position, where it remains for a further seven seconds.

As the helicopter moves the cells used to model the rotor downwash change. At any given moment the cells used to create the downwash are defined as any cell within 27ft of the rotor hub in a horizontal plane. The helicopter flight lasts for 25 seconds. It is the results from the analysis of these 25 seconds that have been given. The results presented concentrate on the time varying components of the flow.

A frequency domain analysis of the results show that most of the time varying components of the flow occur in the frequency range 0.1Hz to 1Hz. It is concluded that these are the frequencies that will affect rotor dynamics greatest.

Another aspect considered is the stack (exhaust) gas concentrations in the hangar, due to the helicopter downwash, if the doors are left open. It also concludes that the concentrations of this gas reach over 2% within the hangar, which could be dangerous depending on the contents of the gas.

The downwash velocity through the rotor blades is modelled quite simply, that is there is no axial variation along the rotor blades and no adjustments for ground effects when over the ship. The paper puts emphasis on finding the changes to the ship airwake caused by the helicopter thrust rather than finding the changes to the helicopter control and power margins caused by the ship's presence.

The American Naval Air Warfare Center funded a study into the airflow around a ship including the helicopter interaction. Zhang and various co-authors [2.38], [2.39] and [2.40] use potential flow to derive a model that gives the partial ground effect of a ship. The ship is modelled using panels with sources at the centres. The magnitude of these is set to satisfy the no penetration condition. The rotor blade wake is separated into two parts, near wake and far wake. The near wake consists of trailing and shed vortices, the far wake consisting of trailing tip vortices only. Using blade-element analysis and the ground effect coupled to the simulation code, the blades are retrimmed by adjusting collective and cyclic pitch. The final results are power reduction and upwash plotted against both helicopter height and rotor blade azimuth angle. There were also results given that showed variation of average upwash with rotor advance ratio.

The results ended with a comparison of the new ground effect model with the standard widely used model proposed by Cheeseman [2.41]. This comparison showed the panel method predicts the same general increase in ground effect as height decreased as predicted by Cheeseman's potential theory. There was, however, a large discrepancy in the magnitude of the predicted ground effect. This can be attributed to the models used. The panel method uses a ship and includes blade element theory and vorticity. The potential theory includes no radial variation of thrust and the helicopter is placed over solid land. The paper concluded that the new model could calculate partial ground effects assuming the rotors were trimmed correctly, but suggested that it should be compared with

experimental data. This paper is unique in assigning some quantitative values to the ground effect caused by a ship flight deck.

Long et al. [2.43] determine the unsteady ship airwake around a generic ship shape. The ship shape used is a generic frigate devised by the TTCP organisation to enable the different research teams around the world to compare results. The flow solver was restricted to viscous laminar solutions. The flow results were compared with experimental data from [2.28] and exhibited many favourable characteristics. There is great emphasis within the paper on the large computing facilities required to achieve the results. The fastest method found to advance the solution was a 64 processor IBM SP2 operating at 160MHz, which could perform over 200 million floating point operations every second. The only deficiencies of this paper are the lack of helicopter model or an attempt to quantify the interaction and the lack of turbulence within the model.

Wakefield et al. [2.44] demonstrate that a rotor can be modelled in both two and three dimensions within CFD by applying forces to the fluid at the location of the rotor. The resultant flow solutions correlate well with established momentum principles and actuator disc theory (see for example Newman [2.45]). A 2D model of the TTCP generic frigate is considered, with a 2D rotor hovering over the deck. The flow through the plane of the rotor is analysed to find the power exerted and the apparent wind the helicopter experiences. The results show that the helicopter requires negligible power to hold station but experiences large velocity gradients which, in reality, would require large control margins. The chief shortcoming of this paper is the 2D nature of all the results; however it is the only CFD publication that includes a helicopter model, turbulence and a free stream.

Tattersall et al. [2.46] is another comprehensive attempt to model the entire ship/helicopter fluid interaction. The helicopter rotor is modelled within the CFD by applying a pressure discontinuity at the location of the main rotor. The pressure jump exerted on the fluid varies both radially and azimuthally, although the method of determining these variations is not fully explained or referenced. The fuselage is also included. The ship used is an AOR and the flow is assumed incompressible and inviscid. Results are presented showing the ship airwake both

with and without the helicopter present. The flow through the helicopter rotor is analysed to estimate the required collective pitch, lateral pitch and longitudinal pitch input by the pilot. The paper concludes by stating that an accurate model of the main rotor has been instigated but the solution lacks time dependency and turbulence.

Maslov et al. [2.47] discuss the Russian research into airflow around aircraft carriers using CFD. There is special reference to the vortices caused by the 'ski jump' on the bow experienced in head winds. The results indicate that the magnitude of these vortices is very dependent upon the roll and pitch of the vessel. The paper identifies the existence of these vortices but does not evaluate the effect on helicopter or aircraft operations.

The work performed by Zan, Syms and Cheney [2.32] compares full-scale data, wind tunnel data and a CFD study; this is described in Section 2.8.

At present there is a huge disparity between results achieved by the various nations. Wilkinson et al. [2.8] noted that the reattachment point of the flow over the helideck on the TTCP generic frigate varies by half the length of the deck, according to the member nations of the TTCP. Differences such as these demonstrate the unreliability of CFD which will be overcome as knowledge and understanding of the tool become common.

### **3 CFD Applied To Bluff Body Aerodynamics**

#### **3.1 Introduction**

Computational Fluid Dynamics (CFD) is a relatively young subject, still developing at a rapid pace. Until recently the required computing power was prohibitive for everything except very simple geometries. Much of the research performed so far has been applied to predicting lift and drag of aerodynamic forms such as aerofoil sections and aeroplanes. Often the solutions are in the transonic or supersonic region.

The flow regime of the helicopter/ship interface represents another unique problem, to which CFD is being applied. This flow is unusual for a variety of reasons. The low speeds involved do not simplify the solution process because a fluid which is modelled as incompressible is harder to solve than a compressible flow regime.

The ship airwake is also characterised by large areas of turbulence and recirculation, which do not exist around aerodynamic bodies. Two problems stem from the high turbulence. The solver struggles to converge to a solution using the conventional turbulence models because the magnitude of the turbulence within the areas of recirculation exceeds the turbulence found within a commonly studied boundary layer. The standard turbulence models, such as the  $k-\epsilon$  model, have been developed and calibrated against simpler flows that involve boundary layer growth. These turbulence models accurately predict internal flow through a pipe. This chapter determines the applicability of these models to the ship airwake.

Modelling the presence of the helicopter, as demonstrated in Chapter 2, has only been attempted by a handful of researchers. This is a subject within itself and will be covered in Chapter 4. In order to calibrate the helicopter rotor model a hover case must be considered, which introduces another new problem. The flow solution of a hovering helicopter is also unusual because there is no free stream velocity and the fluid flow throughout the domain is induced by the rotor itself. This deems the standard boundary conditions, which induce a freestream velocity, obsolete. Hence new boundary conditions, which apply different flow conditions, must be generated; these are also described and validated in Chapter 4.

This section considers the flow around a surface mounted block and the parameters which affect the solution. Within a CFD study the user can determine an incorrect solution by defining spurious boundaries, grid parameters and turbulence models. The section initially considers the flow around a 2D block mounted on the ground, using standard boundary conditions. The grid coarseness and location of boundaries are varied in order to find positions which do not adversely influence the solution achieved. Various solver parameters are employed to determine the most efficient route to a solution. The shape of the domain is also varied to find whether the solution process can be accelerated by using less grid cells which are placed more strategically.

The grid coarseness and solver parameters are carried forward to a 3D study of a surface mounted block. The flow solution around the 3D block is qualitatively compared to the 2D solution.

A CFD model of a surface mounted block in a wind tunnel is generated and compared to experimental results from the Southampton University wind tunnel. The CFD turbulence model is varied to assess the influence on the flow solution.

The solution process and grid cell size are optimised in two dimensions. Performing this study in three dimensions would require an unreasonable length of time.

### **3.2 Description of Flow Solver.**

All CFD flow solutions within this thesis are produced by the flow solver CFX-F3D, formerly known as FLOW3D. This solver forms part a suite of programs produced commercially by AEA Technologies. The software provides a means for defining the grid and boundary conditions, achieving a flow solution and analysing the results.

The grid generator creates a structured grid, which consists entirely of an arbitrary number of hexahedral blocks; shared faces join these blocks. The flow is induced within the flow domain by defining flow or pressure values at the extremity of the flow, these are known as boundary conditions. Each block is divided into grid cells which are also hexahedral in shape. The velocity and pressure are solved at each grid cell to satisfy the Navier-Stokes equations. Each grid cell is considered

individually as a finite volume, hence this method is called the finite volume method.

The solver has many attributes which are superfluous to this study, for example heat flow and combustion models. The attributes of the solver drawn upon within studies of the dynamic interface are isothermal, single phase, laminar and turbulent flows. The solver can be used to determine 2D or 3D flow solutions. The user can specify a fluid with any density and viscosity. For many flow solutions a steady solution does not exist, for this reason time varying solutions can be found.

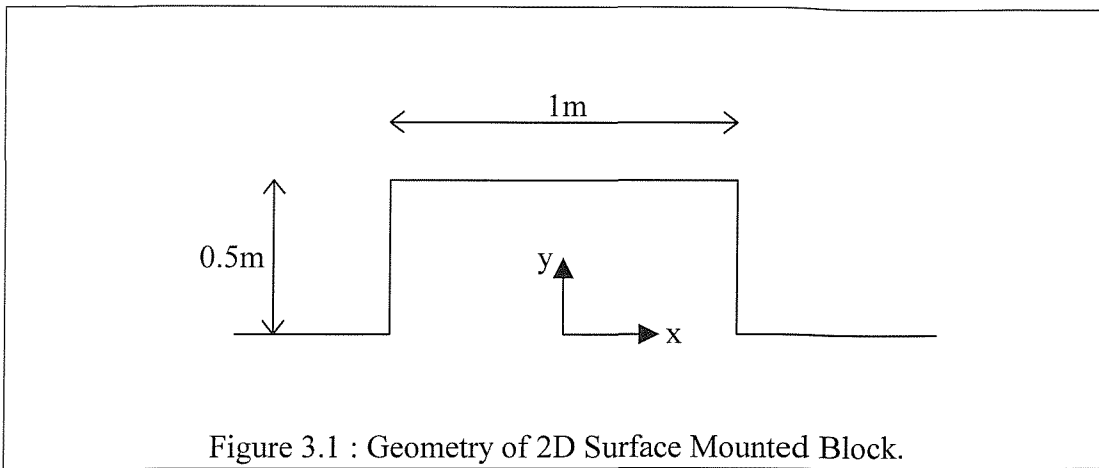
The boundary conditions are defined within the command language. These can be simple uniform free stream velocities at inlets and zero datum pressure at pressure boundaries. More complicated boundary conditions, for example time dependant boundary conditions, are specified using the user FORTRAN subroutines. The turbulence model and turbulence parameters must also be defined.

A large variety of solver methods can be adopted. These not only dictate the speed at which a solution is reached but also the final solution achieved. Care must be taken to ensure that the solver method is compatible with the flow type and grid definition.

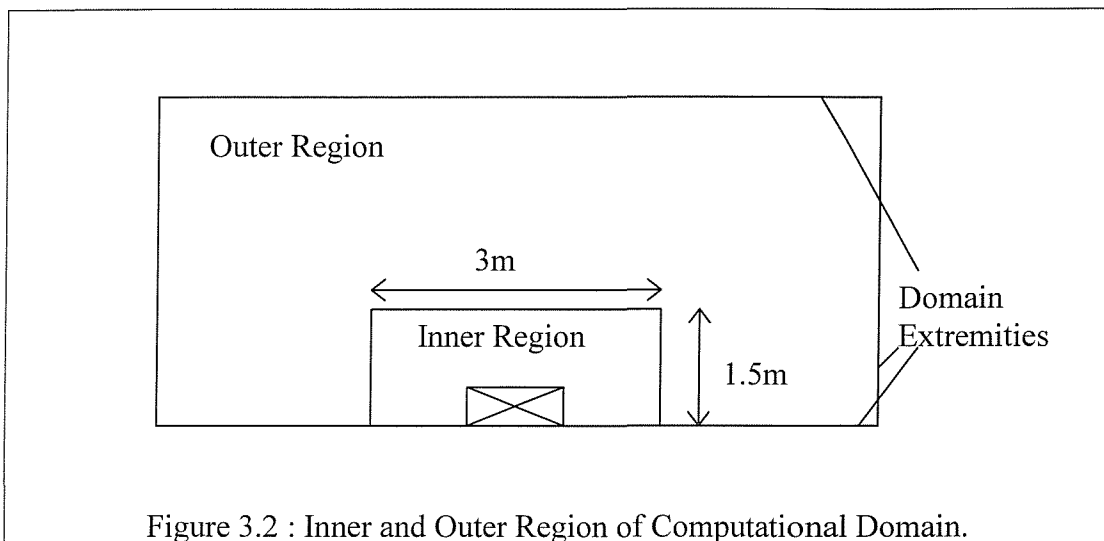
The post-processing module interrogates the flow solution and creates flow diagrams in a variety of formats. The post-processor also creates graphics files which are compatible with other software such as AVS.

### **3.3 2D Surface Mounted Block Parameters.**

The geometry of the block is shown in Figure 3.1. The block has dimensions of 0.5m in height and 1m in width. Only the distance from the block to the boundaries are varied.



The grid was separated into two regions, outer and inner, as shown in Figure 3.2. The inner region is the area immediately surrounding the block; this area covers  $4\text{m}^2$ ; within this area the grid cells are square. The outer region is the rest of the domain, where the grid is coarser. In the example shown in Figure 3.3 it is 0.2m. Only in parts of the outer region are the grid cells square.



This grid is far from ideal, where cells are used with high aspect ratios. However the grid is simple to use. In the cases where the boundaries are moved, the number of cells is also altered proportionally. This ensures that any change of flow solution can be attributed to the boundaries being moved rather than the grid being altered.

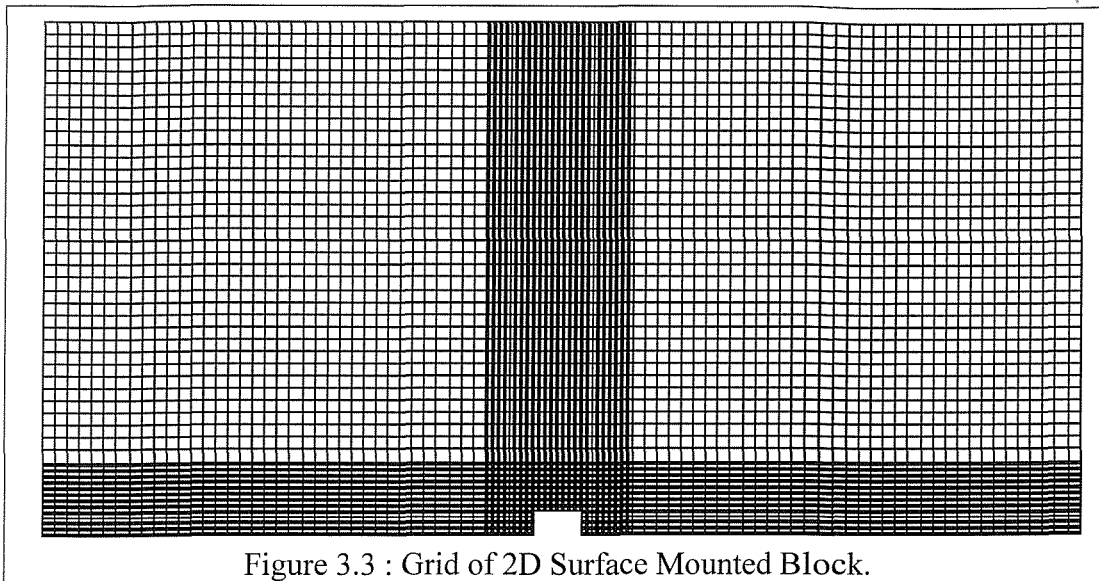


Figure 3.3 : Grid of 2D Surface Mounted Block.

The boundary conditions used for the early part of the study are shown in Figure 3.4 . The surface and the block itself are defined as walls, at these surfaces the no-slip condition is applied. Applying a flow condition at the inlets induces the free stream. In all cases the freestream was 1m/s acting horizontally along the x-axis. The fluid flows out of the domain through the pressure boundary. A zero pressure datum is applied at this boundary; the pressure variations throughout the domain are extrapolated upstream from this plane. Likewise, the velocity variations through the domain are found by extrapolating downstream from the inlets.

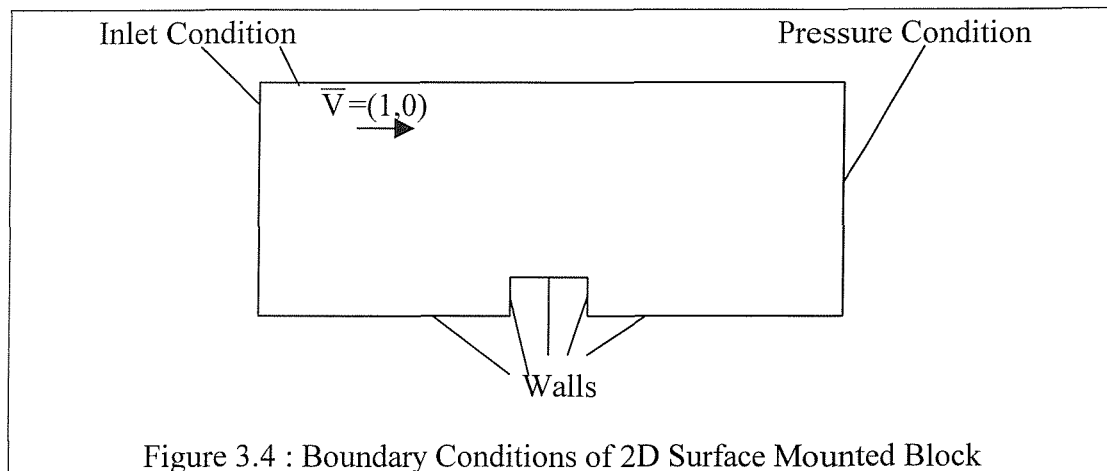


Figure 3.4 : Boundary Conditions of 2D Surface Mounted Block

The fluid was modelled as air, with a density of  $1.2\text{kg/m}^3$  and viscosity of  $1.8 \times 10^{-5}\text{kg/ms}$ . The fluid was considered incompressible, isothermal and turbulent. The k- $\epsilon$  turbulence model was used, with k set as  $0.01\text{ m}^2/\text{s}^2$  and  $\epsilon$  set as  $0.01\text{m}^2\text{s}^{-3}$  at the inlets. Convergence of the flow solutions was defined as a mass source residual of  $10^{-6}\text{ kg/s}$ . The 'Upwind' differencing scheme was adopted to solve the turbulence parameters; this differencing scheme is first order accurate

which prevents the turbulence parameters becoming negative. Negative values of either  $k$  or  $\varepsilon$  are meaningless and cause the solution to diverge. The 'Hybrid' differencing scheme is used to solve velocity and pressure. This scheme is second order accurate. In all studies, the free stream velocity was 1 m/s acting horizontally along the x axis.

### **3.4 Optimised Solution Process**

The flow solver CFX4.1 provides the user with many options within the solution process. All these are assessed with a purely empirical approach, however the theories and merits are discussed in detail in various publications such as [3.3], [3.4] and [3.5]. None of the options within this section influence the final flow solutions but purely dictate the speed and computational efficiency at which they are reached. Flow solutions are found using the geometry described in Section 3.2. The block problem is employed because it is representative of a highly turbulent and recirculating flow. The flow domain extends 10m from the block upstream, downstream and above the block. The freestream velocity is 1m/s. There are 16 grid cells per metre within the region closest to the block and 4 cells per metre in the outer region of the domain.

#### **3.4.1 Pressure Correction Method**

Within CFX the user is given the option of three pressure correction methods, these are SIMPLE, SIMPLEC and PISO, and are described in the references given above. Three solutions were sought using these methods. The relaxation factors were set as 0.5, and the AMG equation solver was used for all variables. The number of iterations and the CPU time for the three solutions were recorded. All three solutions were identical. The results are shown in Table 3.1, which clearly indicates that the PISO pressure correction requires least computing resources. All the correction methods involve a combination of implicit prediction and then explicit correction [3.5]. The PISO method uses two correction steps, which appears to aid efficient flow convergence.

Pressure Correction Method	Iterations	CPU Time (s)
SIMPLE	812	1628
SIMPLEC	1197	2578
PISO	536	1347

Table 3.1 : Solution Times and Number of Iterations, Various Pressure Correction Methods.

### 3.4.2 Relaxation Factors

During the solution process the variables at all positions within the flow domain are iterated. Each variable is assigned a relaxation factor, which determines the amount by which that variable can vary from one iteration to the next. If this value is set to unity, the variable will adopt the predicted value at the end of the iteration. If the relaxation factor is 0.5 the variable will be assigned the mean of the existing value and the predicted value. Relaxation factors of less than unity are used to stabilise the solution process, however they will also slow the rate at which the flow reaches a converged solution.

In addition to under relaxing variables, there is a method known as 'false time steps' [3.3] which helps to stabilise the solution. Without false time steps the solver predicts the values of the variables for a steady state solution reached at an infinite time. False time steps assign a time step to each iteration, these give the transient solutions a more realistic development process. In some cases helping to accelerate the solution process.

Four identical solutions were obtained. A description of the relaxation factors and the resultant processor times are shown in Table 3.2 . The default relaxation is 0.65 for the velocity components, 1.0 for pressure and 0.7 for the turbulence parameters. The SIMPLEC pressure correction method and Algebraic Multi-Grid (AMG) equation solver was used. The results indicate that adopting greater relaxation than the default values slows the solution process. The 'false time steps' appear to make little difference. In both cases slightly less computational time was used.

Relaxation Factors	False Time Step	No. of Iterations	CPU Time (s)
0.5 all variables	None	1197	2578
0.5 all variables	1.0 second	1154	2520
Default	None	686	1506
Default	1.0 second	711	1455

Table 3.2 : Solution Times and Number of Iterations, Various Relaxation Factors.

### 3.4.3 Equation Solvers

Each variable has an equation solver [3.3]. In order to move from one iteration to the next a new value of each variable must be found using one of six equation solvers. Any one of these solvers can be assigned to each of the variables. The solvers do not influence the final solution but merely influence the speed at which the solution is attained.

Seven identical solutions were found using the different solvers. The first six applied the same solver to all variables. A further solution was found using the defaults within CFX. These comprise 'Stone' for the velocity components, 'ICCG' for the pressure and 'Line Solver' for the turbulence parameters. The final solution used the 'Stone' solver for all variables except the pressure which was solved using the 'ICCG' solver. The time taken and number of iterations are shown in Table 3.3.

Equation Solver	Iterations	CPU time (s)
All variables AMG	517	1354
All variables General AMG	517	1809
All variables Stone	458	1057
All variables Block Stone	611	1428
All variables ICCG	523	1285
All variables Line Solver	673	1375
Default: u, v 'Stone', p 'ICCG', k, $\epsilon$ , 'Line Solver'	540	1066
All variables Stone, except Pressure 'ICCG'	523	1037

Table 3.3 : Solution Times and Number of Iterations, Various Equation Solvers.

The results in Table 3.3 show that the various solvers influence the time taken to reach a final solution. The fastest single solver is the Stone solver. The default options took roughly the same amount of time. The final solution found using a combination of ICCG and Stone was marginally the fastest. These three were all significantly faster than the other methods and will be used in future sections.

### 3.5 2D Optimum Location of Boundaries.

The location of the boundaries is essential to ensure the correct solution is achieved efficiently. If they are placed too close to the region of interest, in this case the block, they adversely constrain the solution. When placed an excessive distance from the block, the solution becomes time consuming and uneconomic to reach.

Within a CFD solution a vast quantity of data is generated. A somewhat arbitrary decision must be made to choose a method to judge the fidelity of the result. In this case a vertical line above the mid-span of the block was chosen as the region to be referenced. The pressure and velocity distributions along this axis were obtained for each flow solution and compared with each other.

### 3.5.1 Downstream Boundary

In order to identify an appropriate location for the downstream pressure boundary, four solutions were sought. In all of these the grid around the block remained unchanged, however the boundary was moved away from the block and grid cells added proportionally. The downstream boundary was placed at distances of 4m, 6m, 8m, and 10m from the leeward side of the block. The upper boundary was held at 10m above the block and the inlet was 10m upstream of the block.

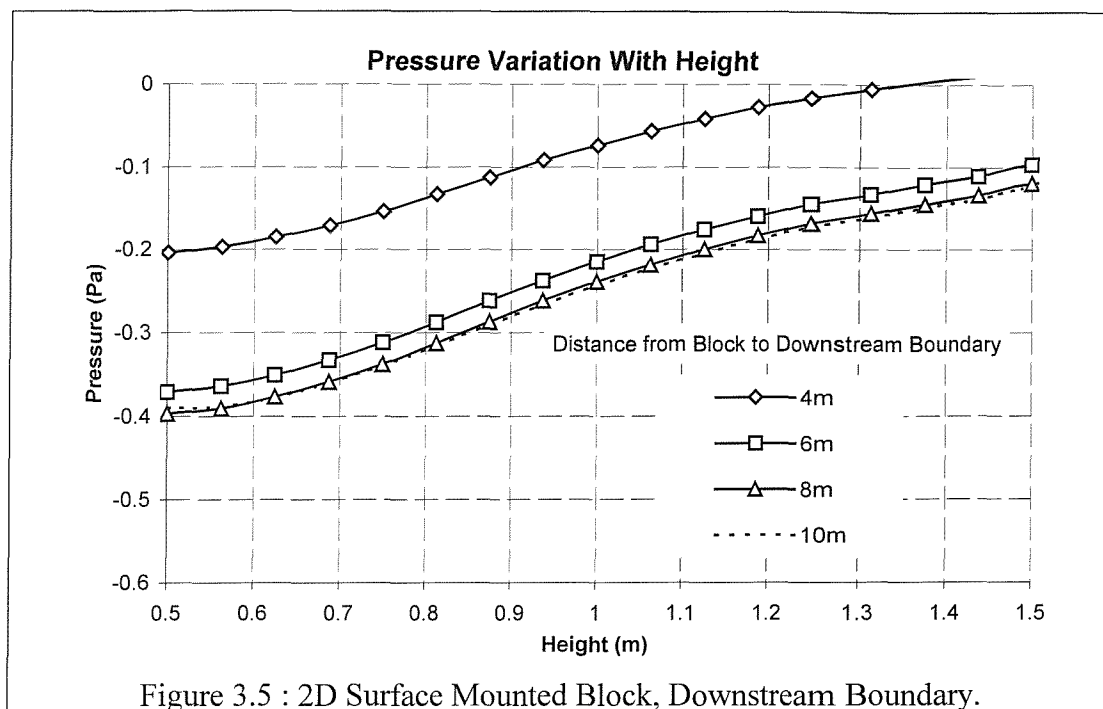


Figure 3.5 : 2D Surface Mounted Block, Downstream Boundary.

The pressure variation above the block is shown in Figure 3.5. The figure shows that whilst virtually identical results were achieved with the boundary 8m and 10m from the block a different result was found using the closer boundaries. Therefore a downstream boundary 8m from the block is sufficiently far from block to not adversely affect or determine the solution. This distance of 8m is carried forward to the next sections.

### 3.5.2 Upstream Boundary

The upstream boundary is defined as a flow velocity equal to the free stream, which is 1m/s in a horizontal direction. This boundary was placed at four distances from the block namely 4m, 6m, 8m and 10m. The results are shown in Figure 3.6. The results show that the solution achieved with the boundary only 4m from the block is significantly different from the results found using the larger

domain. The solutions found using the larger domains of 8m and 10m are similar in value.

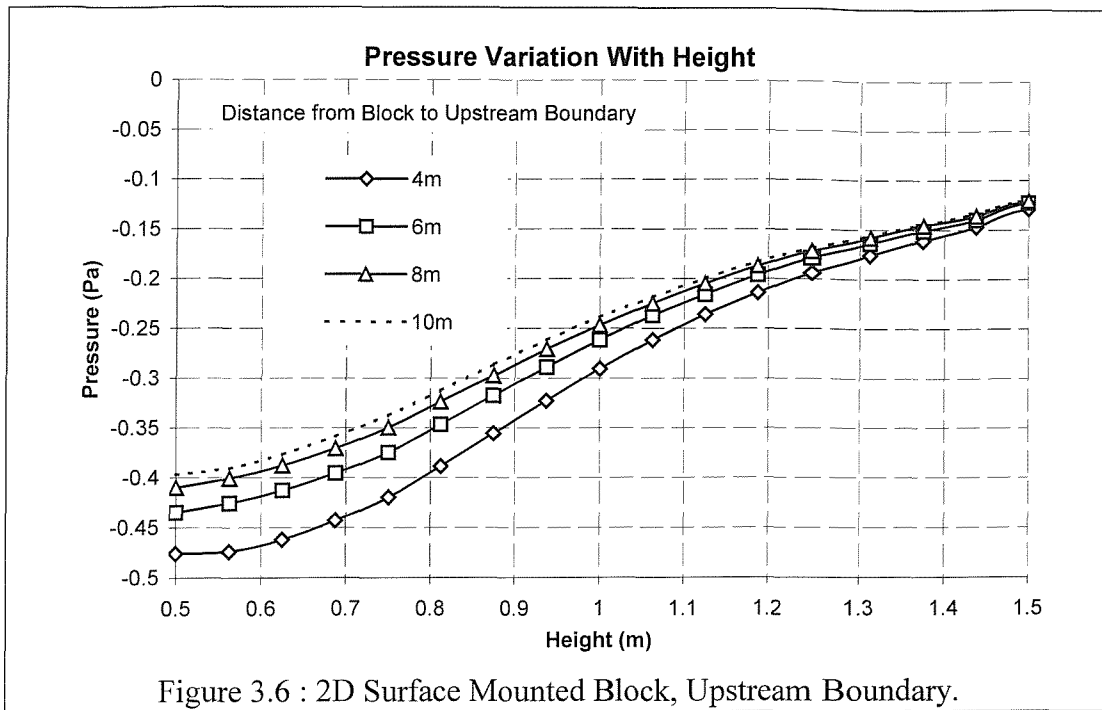
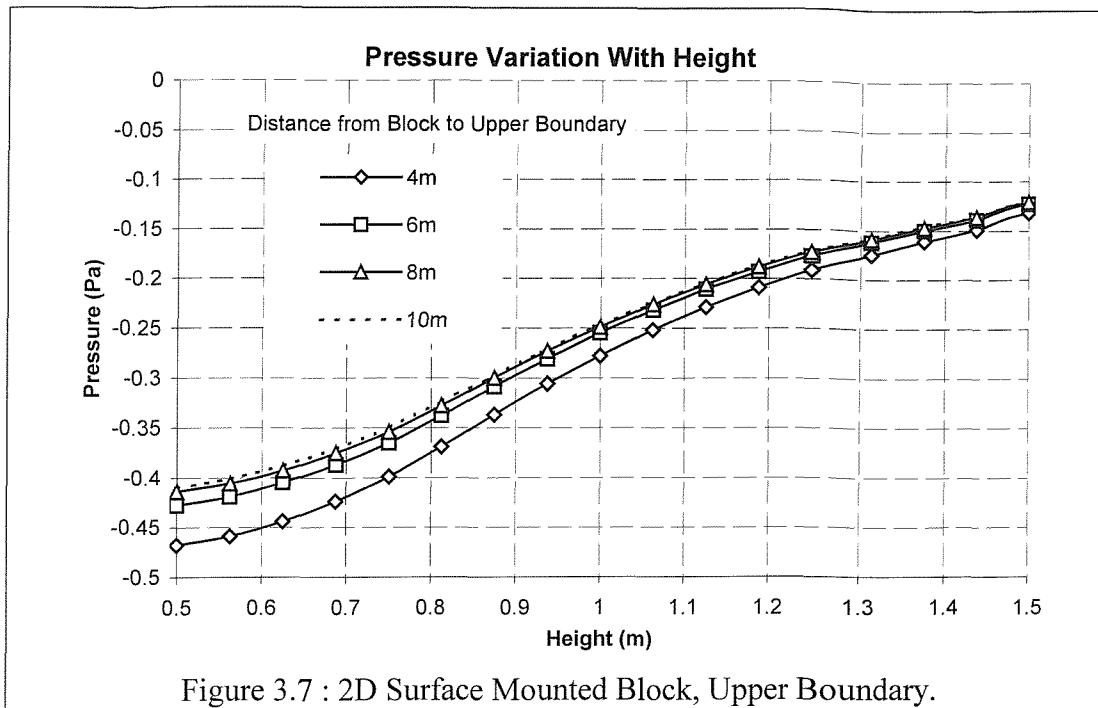


Figure 3.6 : 2D Surface Mounted Block, Upstream Boundary.

For this geometry the upstream boundary must be at least 8m from the block to avoid unfavourably influencing the flow solution achieved.

### 3.5.3 Upper Boundary

Four different distances were chosen between the block's upper edge and the upper boundary, 4m, 6m, 8m and 10m. At the upper boundary the inlet condition is applied, which ensures the free stream velocity, 1m/s, acts at this face.



The pressure distribution above the block for all the flow solutions is shown in Figure 3.7. The figure clearly indicates that the flow varies in all four cases. However, the difference between the flow solution for the 8m and 10m cases are sufficiently similar to assume that any further distance will not significantly alter the flow regime.

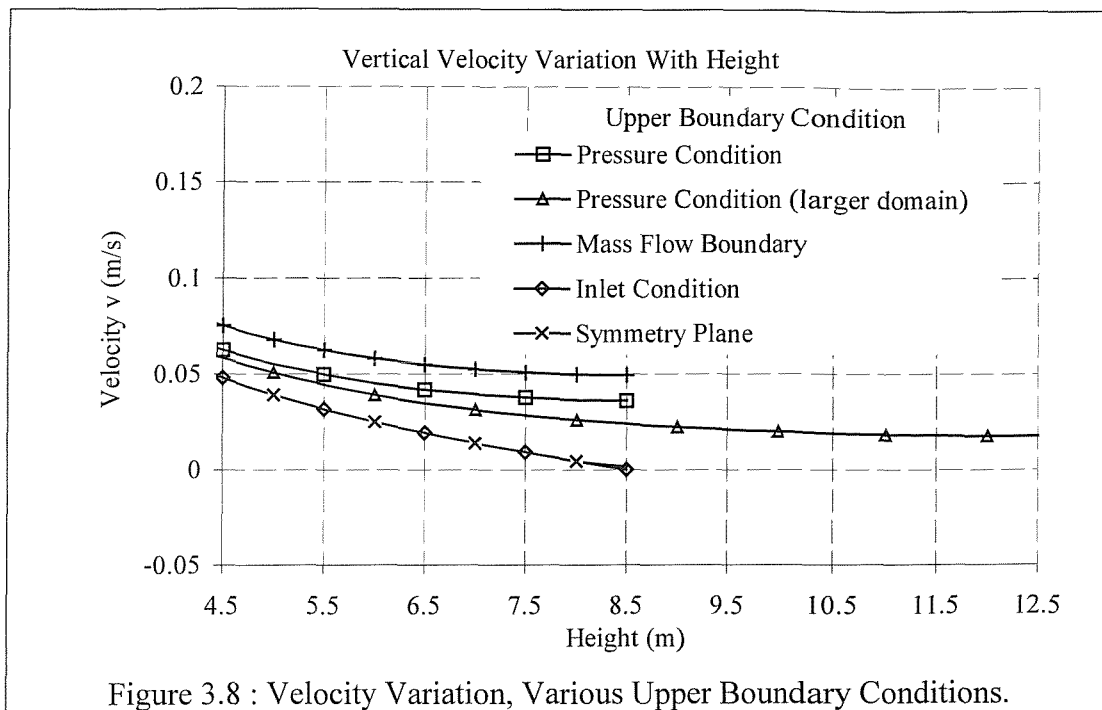
The upper boundary must be 8m from the block to achieve a viable flow regime, which is not influenced detrimentally by the proximity of the boundary.

### 3.6 Upper Boundary Condition Applied

As discussed in the previous section the upper boundary should be placed at a large distance from the perturbation such that it is accurate to approximate the flow to the free stream. Until this point in this chapter, a velocity condition has been applied at the upper boundary. If the upper boundary is placed sufficiently far from the block, the flow along this boundary should be the velocity of the freestream and zero relative pressure.

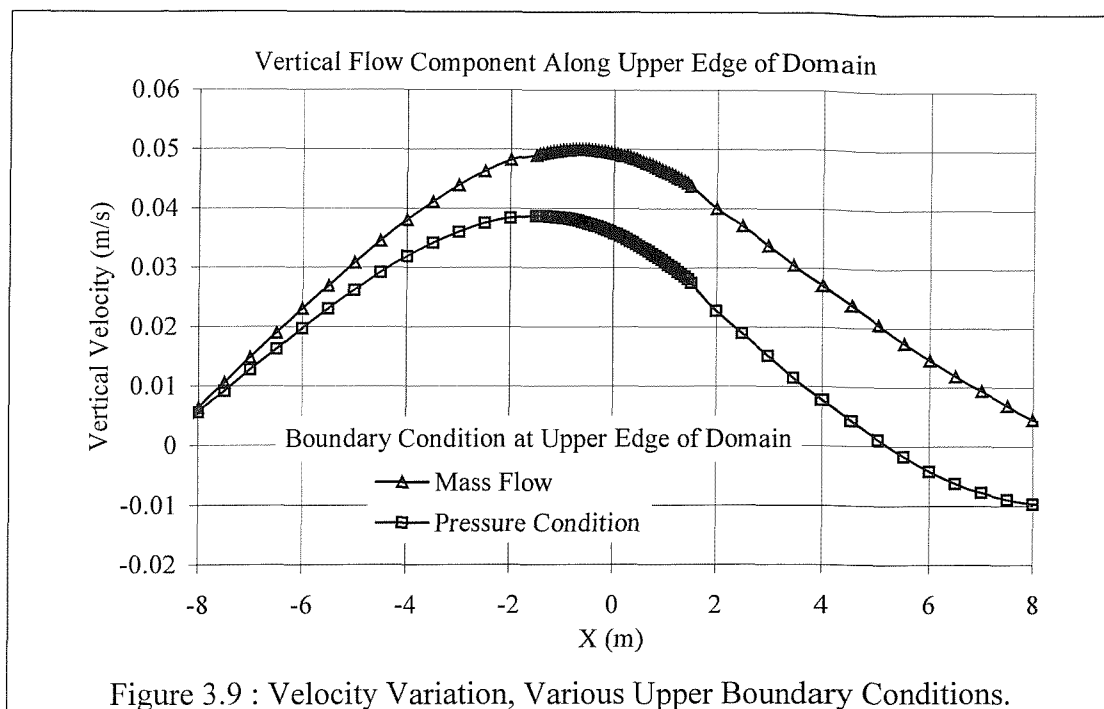
Continuing the logic that the flow at the upper boundary is equal to the freestream, a variety of conditions could theoretically be applied. For example, a pressure boundary, symmetry plane, velocity condition, or mass flow boundary can all satisfy the freestream criteria.

In order to test these boundary conditions and assess their effect on the overall flow solution several flow solutions were obtained. These flow solutions use identical grids around the block and the cells in the outer regions of the domain were of uniform size. The vertical flow component above the block's midspan, in the vicinity of the upper boundary is shown in Figure 3.8. The flow around the block remained virtually unchanged.



A comparison of the flow solutions using a velocity condition and symmetry plane at the upper boundary is shown in Figure 3.8. This figure reveals that the vertical velocity reduces to zero at the upper boundary and these flow solutions are elsewhere very similar. Two solutions were obtained using a pressure condition at the upper boundary. The location of the upper boundary assumed two heights, 8.5m and 12.5m. In both cases there was a small positive vertical velocity component at the upper boundary, however this is less with the larger domain.

A mass flow boundary was also employed; the mass flow boundary also covers the downstream edge of the domain. In this case there is also fluid moving out of the top of the domain.



The vertical velocity along the upper boundary is shown in Figure 3.9. The mass flow boundary condition has produced a flow solution that has fluid flowing out of the top of the domain along the entire boundary. The pressure boundary condition also allows fluid out of the top of the domain along the majority of the length, however fluid is entrained in the last 2m of the boundary.

Table 3.4 shows the horizontal force exerted on the block by the fluid and the iterations required achieving the converged solutions. The solutions requiring least computational iterations used flow conditions at the upper boundary. The pressure and mass flow boundary conditions required greater iterations.

Upper Boundary	Iterations to Converged Solution	Horizontal Force On Block (N)
Inlet Condition	486	0.3488
Symmetry Plane	485	0.3488
Pressure Condition	672	0.3316
Pressure Condition (larger domain)	599	0.3368
Mass Flow Boundary	658	0.3186

Table 3.4 : Various Upper Boundaries, Flow Solutions

Consideration of Figure 3.8 and Table 3.4 reveals a relationship between the force exerted on the block and the flow at the upper edge of the domain. The block experiences greatest horizontal force within the solutions using a symmetry plane and an inlet condition. Within these flow solutions, the flow is bounded at the upper boundary and cannot escape. Most fluid escapes out of the domain through the upper boundary when a mass flow boundary is utilised; consequently the block experiences least drag. It should be noted that the maximum vertical velocity component through the upper boundary is approximately 0.05m/s and hence the fluid is never inclined by an angle of more  $3^\circ$  from the horizontal.

### **3.7 Optimum Grid Density.**

The grid density is another parameter which influences the flow solution achieved. If there are not enough grid cells defined in the flow domain, the solution achieved will be incorrect because the available cells cannot resolve certain flow features. If too many cells are defined, the solution will demand large computational resources to achieve. For example, if the grid cells are half the height of the necessary cell size, a 3D geometry will contain eight times the necessary cells. The solution will require eight times as long to achieve and will require more storage space once found.

An ideal grid would contain cells with an aspect ratio of unity which are not skewed or twisted. In reality this is impossible to achieve around complex shapes. All grids contain a compromise between cell shape and aspect ratio.

The grid density required is also dependent upon the solver schemes adopted. The 'upwind' solver scheme is employed for solving the turbulence parameters  $k$  and  $\epsilon$ . The upwind scheme is accurate to a first order Taylor approximation, which ensures that these variables remain positive throughout the iteration process. When these values drop below zero, which is possible using a second order differencing scheme, the solution diverges rapidly and no flow result is reached. The 'hybrid' scheme is used to solve the pressure and velocity components; this scheme uses a second order approximation [3.4].

For this study the grid has been separated into two regions as described in Section 3.2 and shown in Figure 3.3. The inner region covers the area within 1m of the

block; the outer region covers the area extending out to the domain boundaries. The numbers of subdivisions per unit length within the outer region were varied and the effect assessed. The number of grid cells around the body, within the inner region, was then altered and the solution reassessed. The boundary conditions used were identical to those described in Section 3.3. Using the study in Section 3.5, the upper, upstream and downstream boundaries were located 8m from the body.

Four outer grid cell sizes were chosen: 1.0m, 0.5m, 0.25m and 0.17m. The coarsest grid, using cells 1m in length, failed to achieve a solution. This can be attributed to the high aspect ratios of the grid cells directly upstream and downstream of the block, as shown in Figure 3.3. These cells had an aspect ratio of 20. The solver struggles to solve the transport equations of the turbulence parameters within these cells and the solution becomes unstable, in this case failing to be achieved at all.

The resultant solutions from the three finer grids are shown in Figure 3.10. (Only the pressure variation is shown here however, the velocity components were also very similar between the cases.) There is little variation in the flow, which clearly indicates that relatively few grid cells are required in the region distant from the body, only two per metre. A greater density achieves an identical solution but requiring more computational resources.

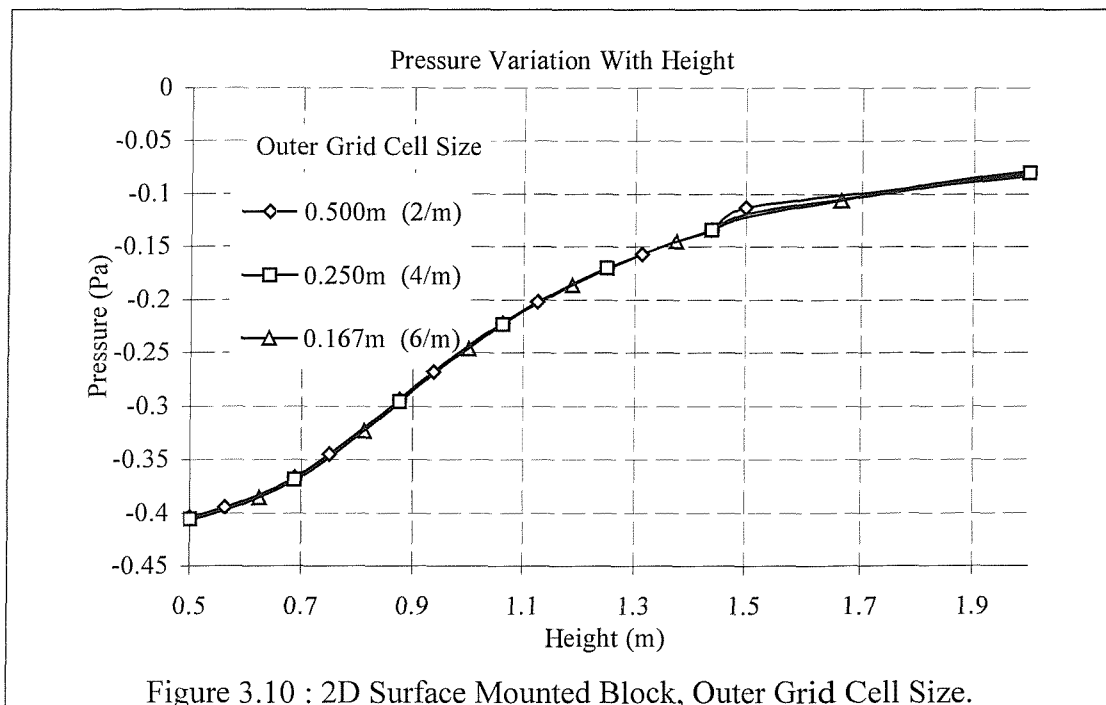


Table 3.5 shows the number of iterations and the time each of the three solutions required to converge. This table demonstrates the detrimental effect of having too many grid cells. The solution requires more iterations but the increase in time taken is far more significant. The refined grid has taken four times as long to achieve essentially the same result.

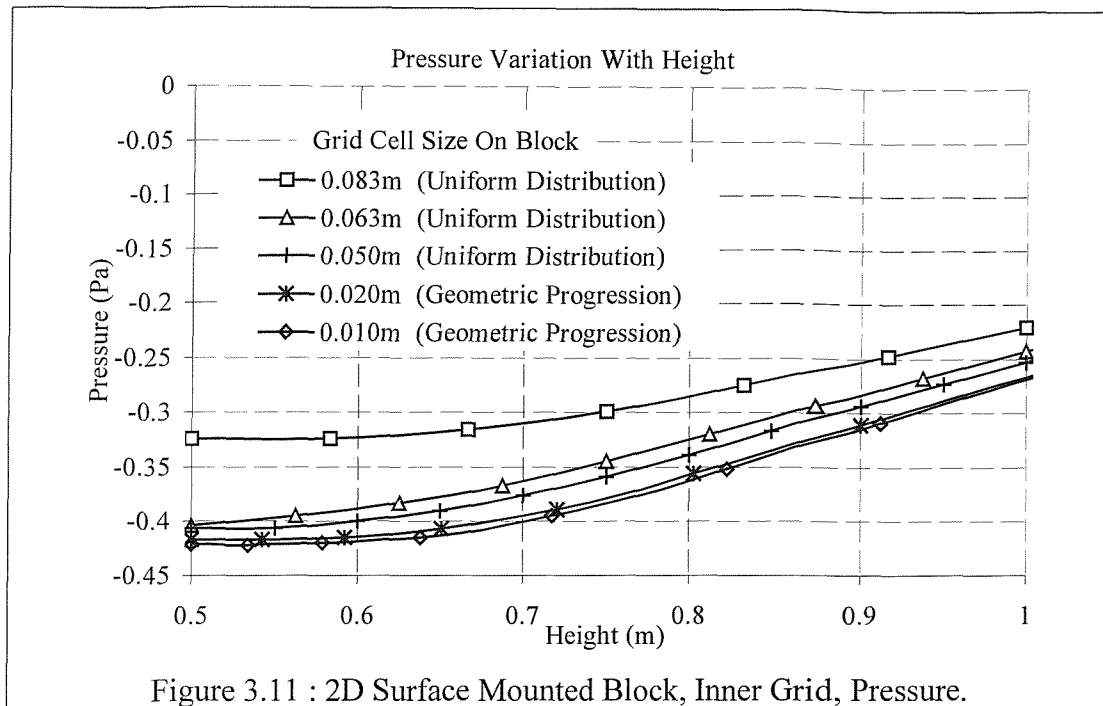
Cells per metre	Number of Iterations	CPU Time (s)
6	542	1730
4	514	902
2	486	411
1	Did not converge	

Table 3.5 : Outer Grid Density, Iterations and Computing Time

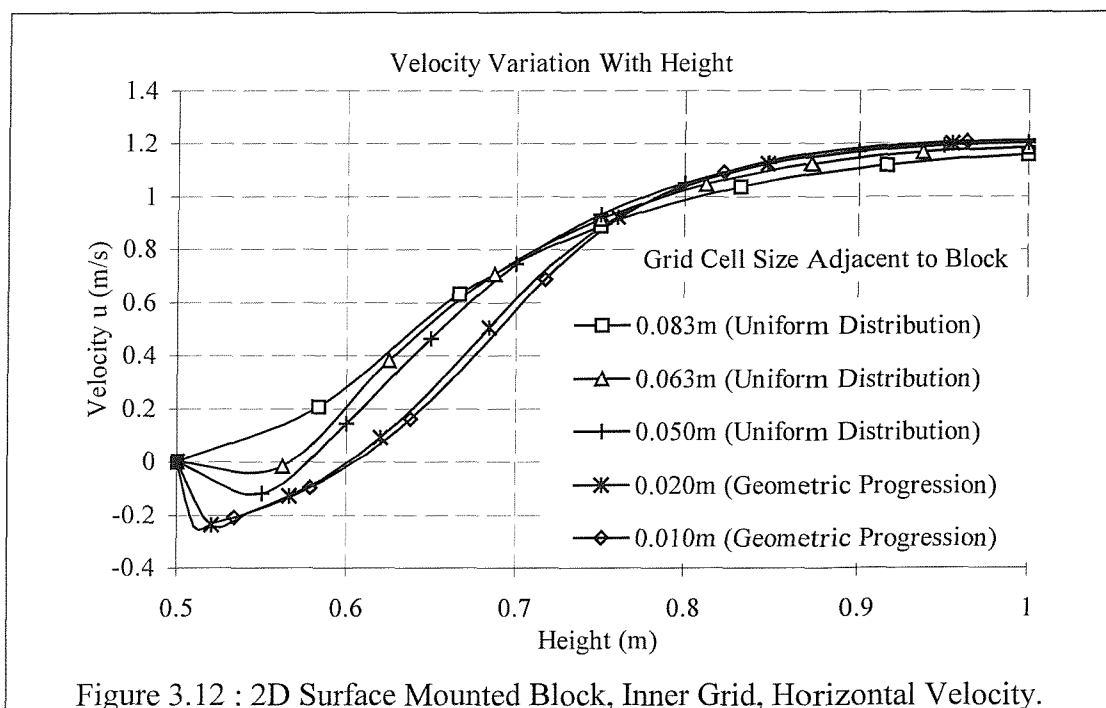
The slight discontinuity in the figure at a height of 1.5m corresponds to the boundary between two blocks of grid cells. The domain was constructed from 14 blocks of cells, not to be confused with the block being modelled itself. The data in Figure 3.10 was obtained from two blocks. This discontinuity only occurs for the coarse grid, and implies that a coarse grid not only fails to resolve all the flow features but also struggles to pass information effectively between the blocks that constitute the fluid domain.

The inner grid, which determines the number of grid cells on the body, used five different grid cell sizes. The first three grid cell sizes correspond to 12 cells/m, 16 cells/m and 20 cells/m. In these cases the grid cells were of uniform size and square in shape.

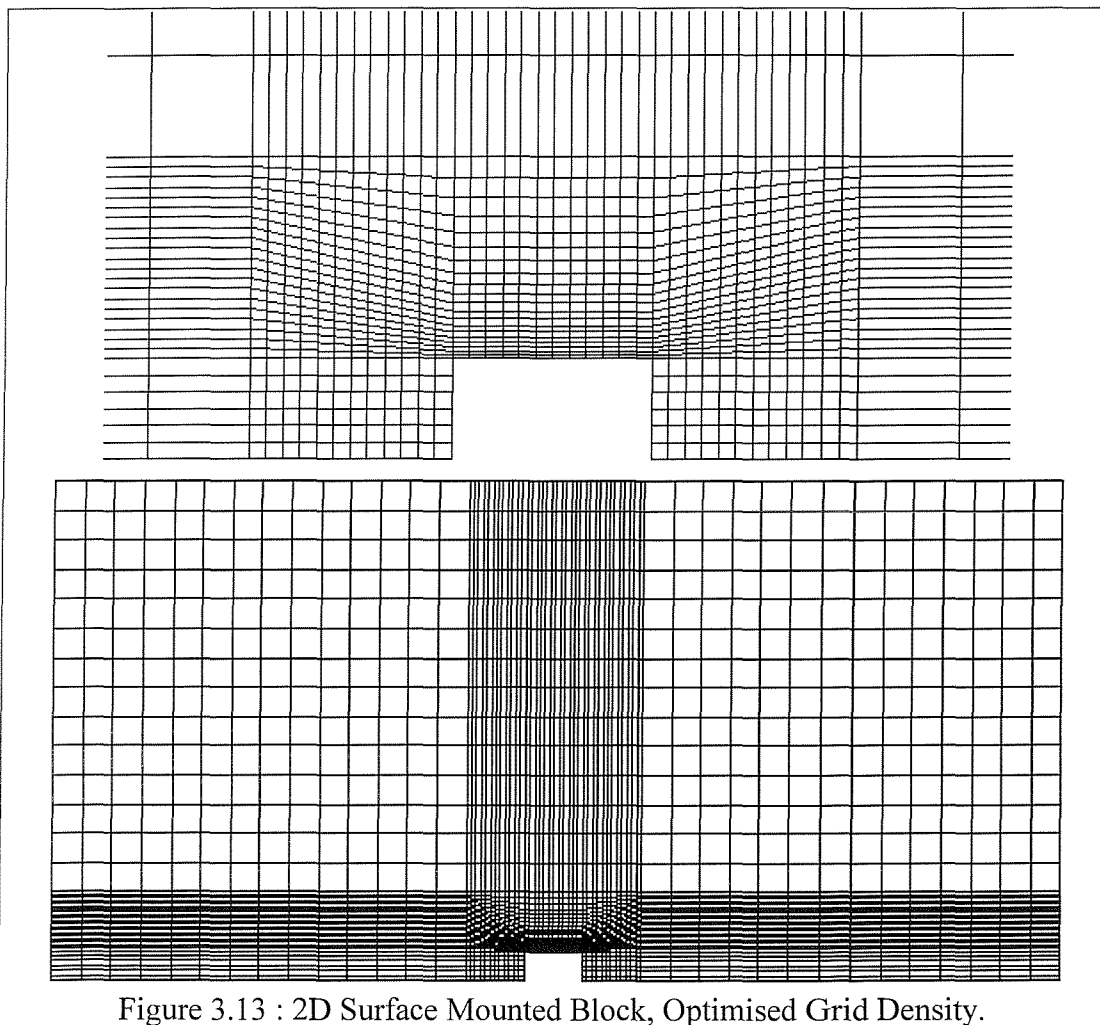
Two further grids were developed which refined the grid directly above the block. The regions adjacent to the sides of the block were subdivided evenly 20 times but the grid cells above the block were clustered near the surface. This attempted to resolve the flow associated with the area recirculation more effectively. Within these grids the cells were 0.02m and 0.01m in height at the upper surface of the block.



The resultant flow solutions are shown in Figure 3.11. The pressure distributions are similar for all except the coarsest grid. The variation of horizontal velocity along a vertical axis is shown in Figure 3.12. Within this figure a negative velocity corresponds to recirculating flow in the opposite direction to the free stream. The coarsest grid shows no negative flow, therefore the grid is not refined enough to resolve this flow feature. The two most refined grids show that the recirculation bubble at the midspan of the block has a height of 0.1m. The other grids predict recirculation but lesser in magnitude.



The results of this study indicate that the outer region of the grid only requires two cells per metre, any less and the solver fails to converge due to the high aspect ratio of the grid in the outer region. The inner part of the grid requires 25 cells per metre, with the cell height directly above the block reduced to 1cm. This grid contains only 4112 grid cells, and is shown in Figure 3.13. As a final check, a further solution was sought using a denser grid, four cells per metre were placed in the outer region and 30 cells per metre in the inner region. The whole grid contained 9425 cells. The solution obtained from the denser grid was only negligibly different to the coarser grid; the result is not shown here. Interestingly the finer grid required 881 iterations whereas the coarser grid needed 1142 iterations to reach a converged solution. However, overall computing times required to reach the solutions were influenced more by the size of the grids, the coarser grid using 1471 seconds whereas the detailed grid 3056 seconds. This indicates a time penalty of a factor of two for 'over specifying' the grid.



In conclusion the number and size of grid cells has a significant effect upon the rate at which a solution is achieved and the quality of the solution. Within areas

of the flow domain where there is little flow variation or velocity gradients, very few cells are required. In the outer region, for example, the factor limiting the cell size was the convergence of the solution; removing small cells and replacement by larger cells made no detrimental effect to the solution achieved.

This study has also demonstrated that using a coarse grid in a region of interest can destroy a flow feature which is captured within a detailed grid. As shown within this section, it can be better to cluster grid cells in the area required rather than simply adding more cells.

The information found within this section will be implemented in further studies. A study such as this should be performed upon all flow solutions before treating the results with any degree of confidence. The flow in the region of the block is shown qualitatively in Figure 3.14. The vectors represent velocity and the contours show pressure variations.

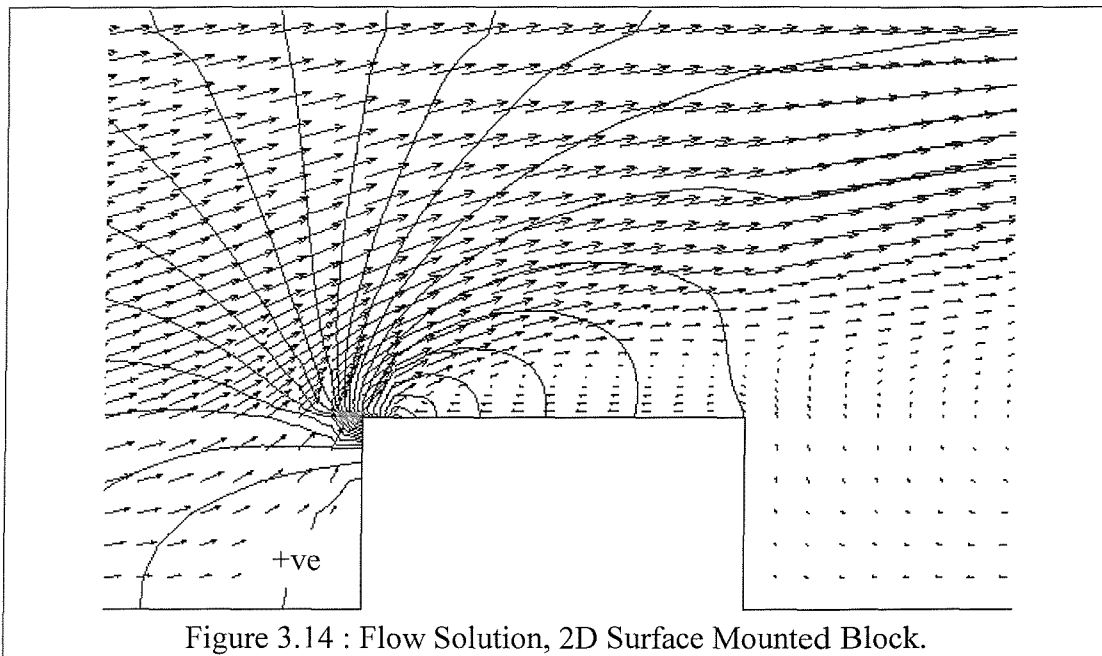


Figure 3.14 : Flow Solution, 2D Surface Mounted Block.

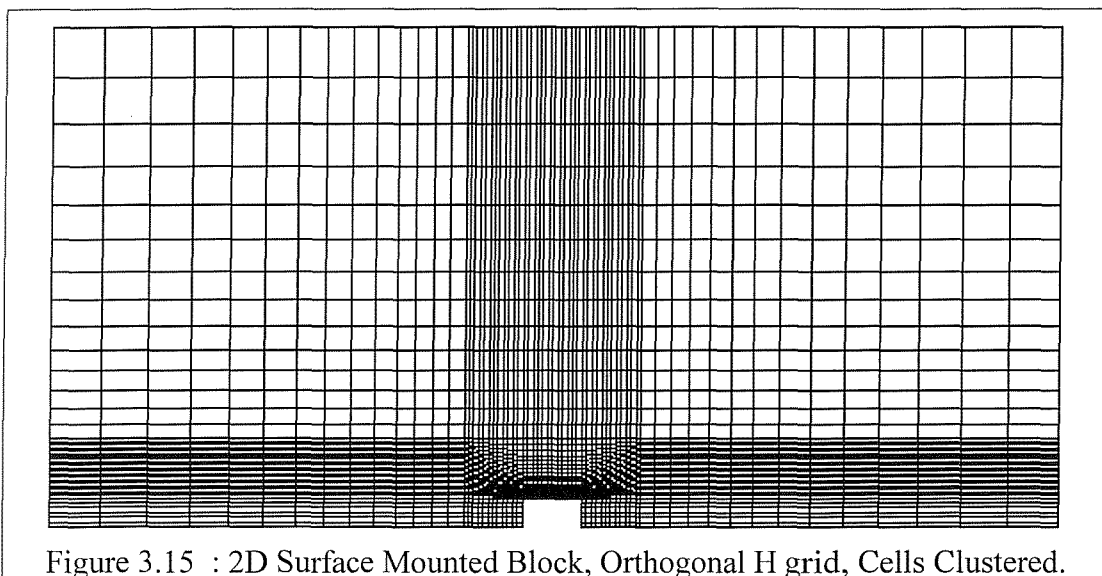
### 3.8 Block Structure.

The topic of grid generation is a research subject within itself. A definitive discussion of the merits and disadvantages of all the possible grid structures around even a simple block is beyond the scope of this study. The optimum grid used is also dependant on the differencing schemes employed. For example, a solver which uses a second order differencing scheme will require less grid cells to resolve the flow than a first order differencing scheme. The pressure correction

Within this section the grid surrounding the block is not changed. The boundary conditions and geometry of the domain are not varied either. Only the location of the blocks which constitute the outer part of the grid and the distribution of the grid cells are varied. Four grids are considered and not only are the solutions considered but the speed at which they are reached is considered. The solutions are compared to determine which grid structure should be carried forward to the 3D surface mounted block.

The first grid considered is the grid found from the studies in Sections 3.5 and 3.7, shown in Figure 3.13 in the previous section. Within this flow domain the grid is a wholly orthogonal H-grid. The cells in the outer region of the domain are uniformly distributed.

The second grid is shown in Figure 3.15. The central part of the grid, around the block, is identical to the previous grid. The only difference being that the cells within the outer region are clustered closer to the centre of the block. This grid is described as an orthogonal H-grid with clustered cells.



Section 3.7 demonstrated that there needs to be very few cells in the outer region. The cell aspect ratios were the factor which determined the minimum number of cells in this region. As the number of grid cells between the block and the domain extremities was reduced, the solution converged quicker with no detrimental effect to the result achieved until a certain threshold value was reached and the solution failed to converge. The third grid, shown in Figure 3.16, attempts to address the instabilities within the solution caused by large aspect ratios. The outer ends of

algorithm and equation solvers do not determine the final solution reached but will influence the rate at which the solution converges towards the final solution.

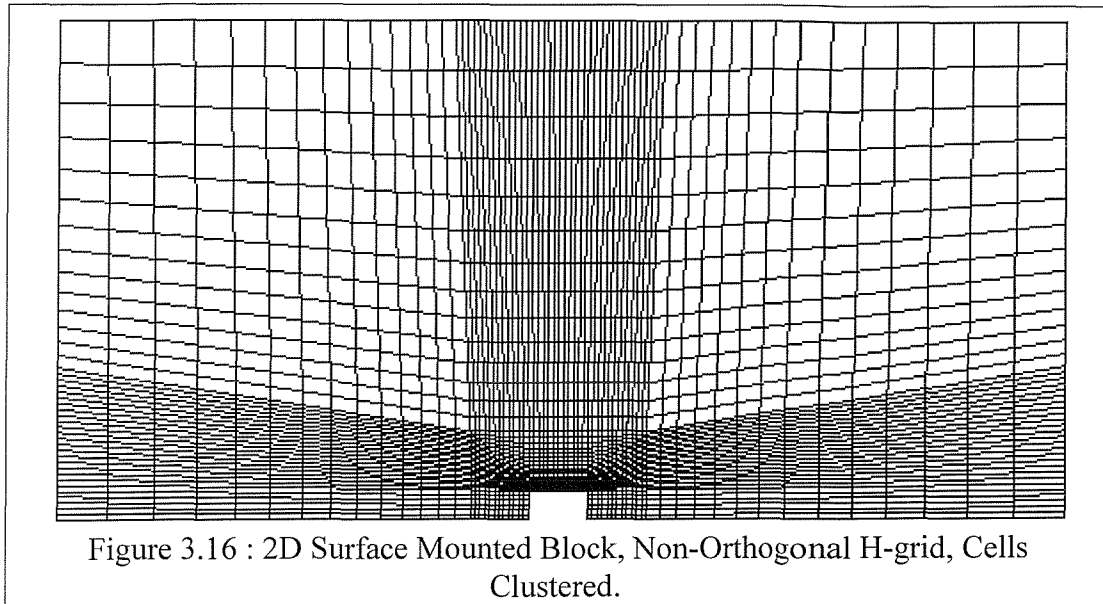
The commercial flow solver CFX4.2 is used to find the results of this study. This solver requires a structured grid which consists completely of hexahedral grid cells. The faces of the cells map exactly onto the faces of the adjacent cells. In 2D the cells are effectively quadrilateral, with each side mapping onto sides of neighbouring cells. This structured nature restricts the distribution of the grid cells.

The alternative to a structured grid is an unstructured grid. This consists of irregularly placed shapes including tetrahedra and hexahedra. Unstructured grids have both advantages and disadvantages. Unstructured grids take longer to generate, since the grid cells are arranged in an irregular pattern. More data must be stored including the information about adjacent cells. The solver takes longer to iterate the solution for each cell because it takes longer to retrieve the flow data of the adjacent cells. However, an unstructured grid can model complicated shapes easily without encountering any of the difficulties discussed in this chapter.

As outlined in earlier sections a 2D grid cell has two key properties which can be used to assess its geometric quality, orthogonality and aspect ratio. Grid cells with approximately equal length sides will resolve the flow most effectively, however aspect ratios of five or less are generally accepted as adequate. The orthogonality of a cell measures the deviation of the cell from a rectangular shape to a parallelogram shape. Internal angles of less than  $45^\circ$  and greater than  $135^\circ$  should be avoided. Additionally, grid cells should be aligned in the direction of the local flow. Despite the apparent importance of grid generation, there is relatively little published information. Ilinica et. al [3.1] derive a method to determine the error contained in a cell. They deduce that the square root of the second moment of area gives a good indication of the cell's quality. Oliger and Zhu [3.2] use, amongst other variables, the sum of the length of edges of the cell as the measure of quality. These studies were considering unstructured meshes containing triangular elements, however they indicate that skewed or stretched cells should be avoided where possible.

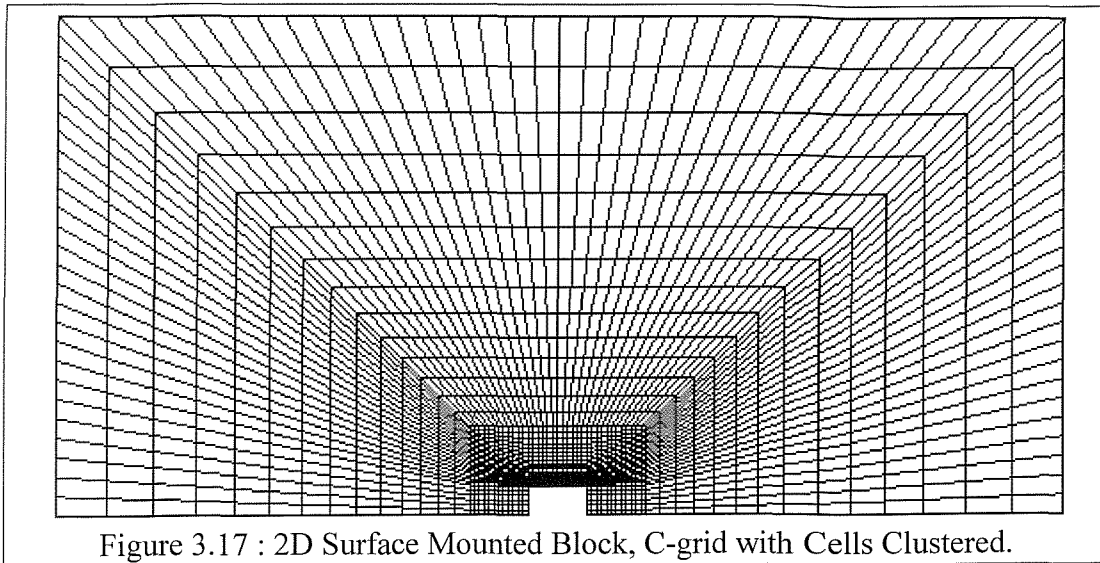
the blocks touching the domain extremities are moved in order to stretch the grid cells in this region.

Within these blocks the distribution of grid cells is clustered identically to the previous grid. This grid therefore contains an identical number of grid cells to both previous grids.



The fourth grid is shown in Figure 3.17. This grid varies fundamentally from the previous three. The two upper and outer blocks of grid cells have been removed. The outer region of the grid can be described as C-grid because this region of the grid is wrapped around the inner region. The cells within the inner region remain unchanged.

The advantages of this grid are that none of the grid cells have excessive aspect ratios, making the solution more stable and quicker to reach. This grid also contains less grid cells, which accelerates the iterative process and reduces the storage difficulties. The disadvantages are that many of the cells are highly skewed and tapered.



The horizontal velocity and pressure distributions above the block are shown in Figure 3.18. The velocity above the block found from all four grids is almost identical. The height of the recirculation at the block's midspan is 0.1m. A comparison of the vertical velocities above the block is not shown here, but the solutions also vary negligibly in this respect.

The pressure variation above the block is also shown in Figure 3.18. There is a marked difference between the pressure field around the block found using the H-grids and the solution from the C-grid. This discrepancy does not affect the flow velocities around the block.

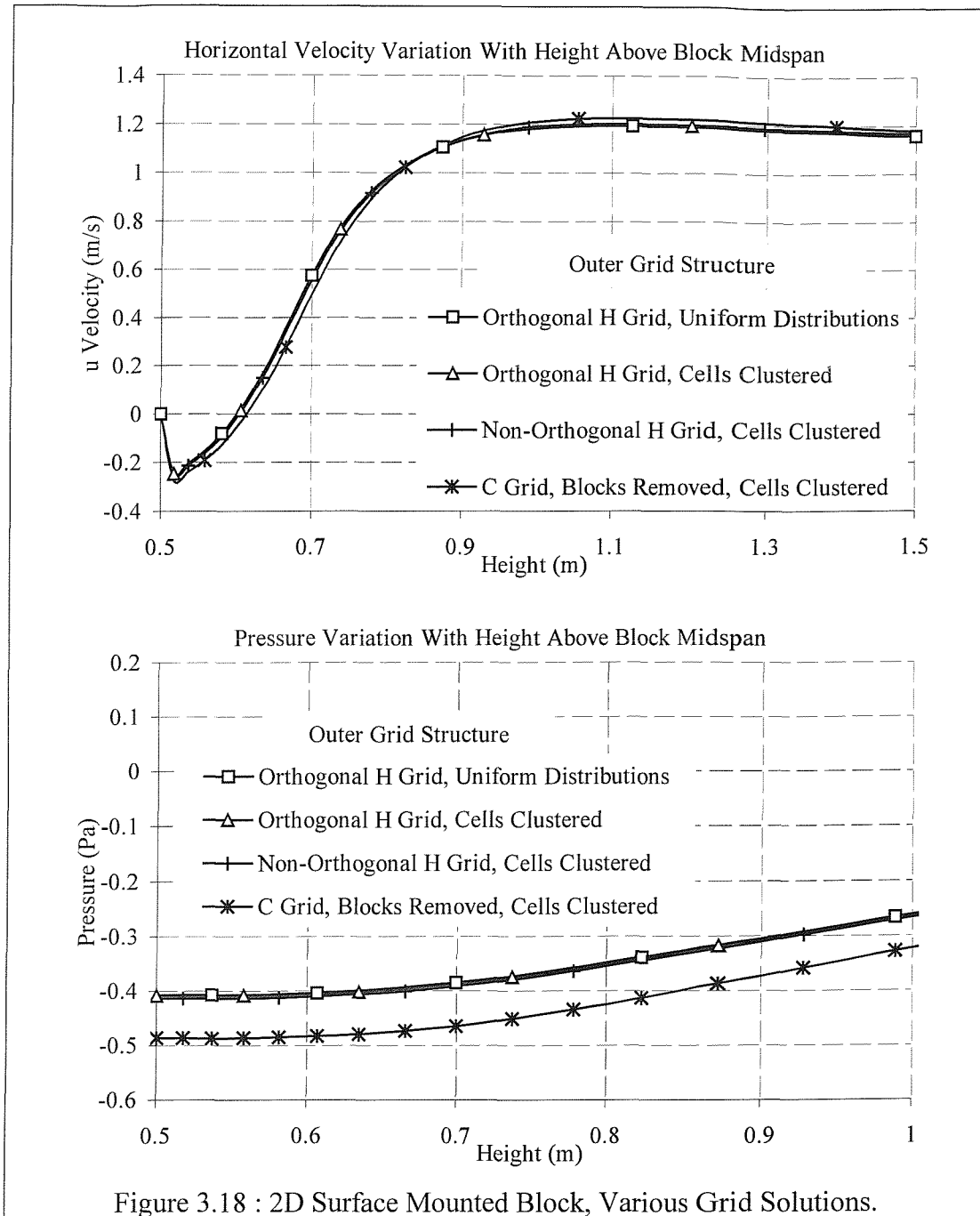


Figure 3.18 : 2D Surface Mounted Block, Various Grid Solutions.

The number of iterations required and time taken for each solution to converge is shown in Table 3.6 . The solution found using the unconventional C-grid was achieved in the least amount of time. This advantage is not only attributable to the reduction of cells within the grid but that less iterations are used.

Grid Description	Figure No.	Number of Cells	Iterations to Solve	Time (s)
Orthogonal H grid, Cells not Clustered.	Figure 3.13	2488	654	505
Orthogonal H-grid, Cells Clustered.	Figure 3.15	2488	617	466
Non-Orthogonal H-grid, Cells Clustered.	Figure 3.16	2488	443	336
C-grid, Cells Clustered.	Figure 3.17	2096	322	196

Table 3.6 : 2D Surface Mounted Block, Various Grids, Solution Statistics.

This study has indicated that cells of large aspect ratio do not adversely affect the solution achieved, but require a disproportionate amount of time to converge.

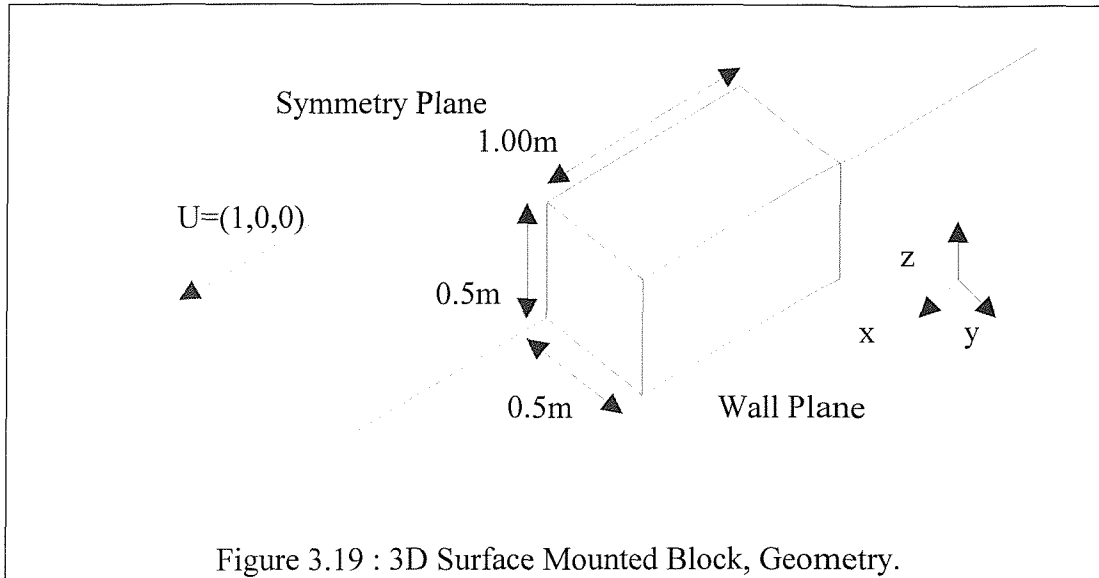
This creates a 'no win' situation when using an H grid. In order to avoid cells of high aspect ratio more cells must be added within the grid. Adding more cells requires greater computational storage space and slows the convergence process. It can be concluded from this section and Section 3.6 that the optimum aspect ratio in the outer region of the grid is the largest within which a flow solution converges.

One method to remove the problems associated with cells of high aspect ratio is to utilise the combination of an H-grid and a C-grid as shown in Figure 3.17. Grids such as these contain skewed cells with reduced orthogonality. These cells introduce errors into the solution but it is reached much quicker. There is an obvious trade-off between speed and accuracy. In this case, the loss in accuracy is small compared with the speed gain achieved using a smaller grid. The C-grid has 15% less cells than the H-grid in this 2D problem. This difference will extend to around 40% within a 3D grid, depending on exact cell distributions, and also providing the associated reduction of iterations used. The C-grid will be used for the 3D study.

### 3.9 3D Surface Mounted Block.

A brief study of the flow around a 3D surface mounted block is presented within this section. The modelled block is 0.5m high, 1m long and 1m wide. The

computational domain is bounded by inlets at the upstream and outer edges of the domain. At the downstream boundary the pressure condition is applied. The no-slip condition is applied to the bottom of the domain and the faces of the block. In order to accelerate the solution process a longitudinal symmetry plane is employed, hence only half of the airflow is modelled. This information is shown in Figure 3.19.

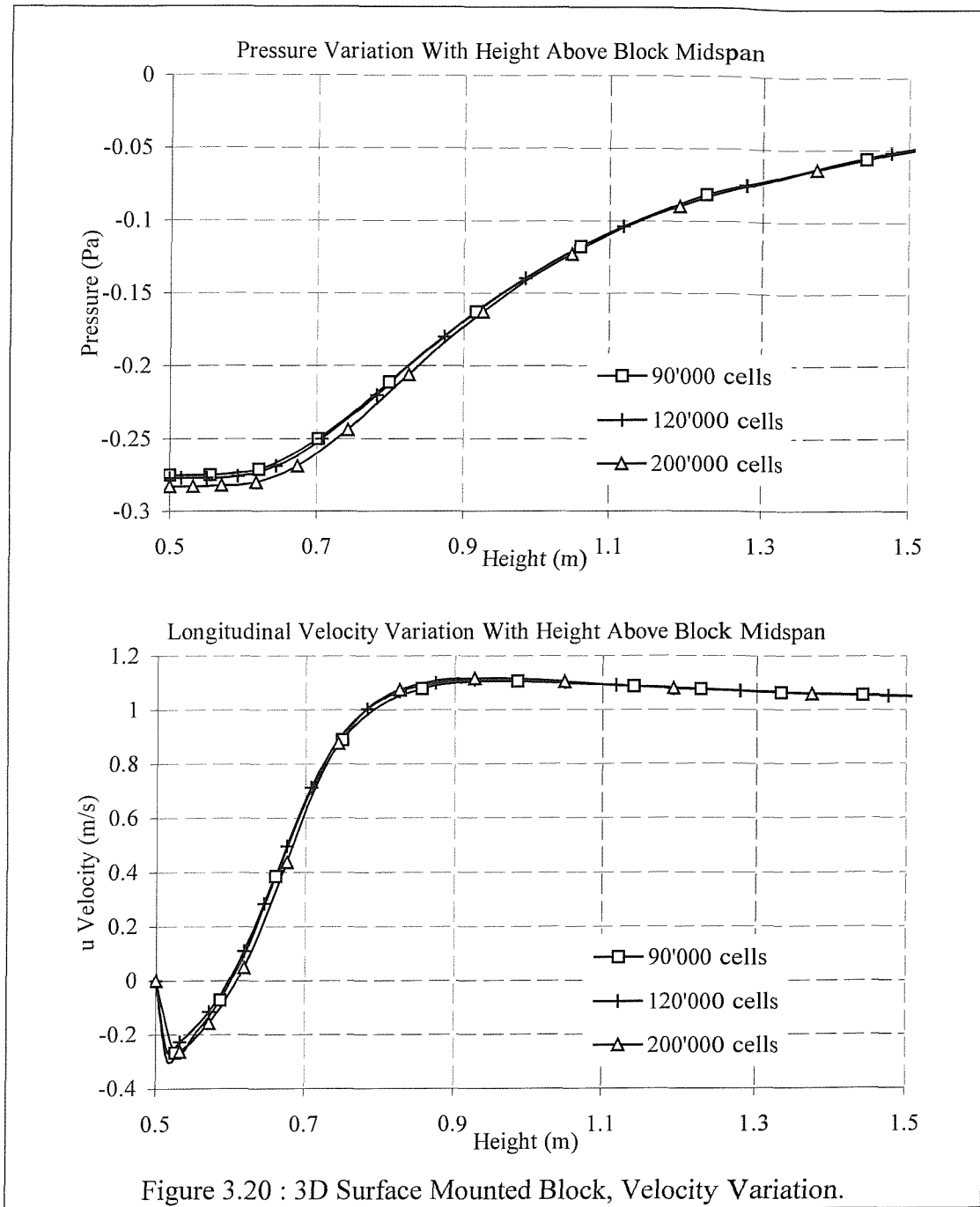


The freestream velocity is 1m/s acting along the x-axis. The domain extremities are 8m from the block in all directions. The grid is a combination of an H-grid around the block and a C-grid in the outer region adjacent to the boundaries, as described in the previous section.

The optimum grid density found from Section 3.7 was used to define the grid. This grid contained 120000 cells. Two further grids were developed. The first included less grid cells on the upper and outer faces of the block; this grid contained 90000 cells. The third grid contained 200,000 cells.

In order to compare the solutions a reference axis was chosen. In this case the axis extends vertically upwards from the centre of the block's top face. The pressure and velocities are measured along this axis. Comparisons of the results are shown in Figure 3.20.

This figure indicates only minor differences between the three solutions obtained. The small differences demonstrate that there are sufficient grid cells in all the solutions to resolve the basic flow features around the block.



The flow features around the 3D block are similar to the 2D block. At the central longitudinal plane, the flow separates at the upper windward edge of the block and remains separated across the whole of the block's length. The flow solution in this plane is shown in Figure 3.21 . The vectors represent flow speed and the contours are pressure spaced at 0.1Pa. This flow coincides with the symmetry plane in the model; therefore all flow is in the longitudinal and vertical directions.

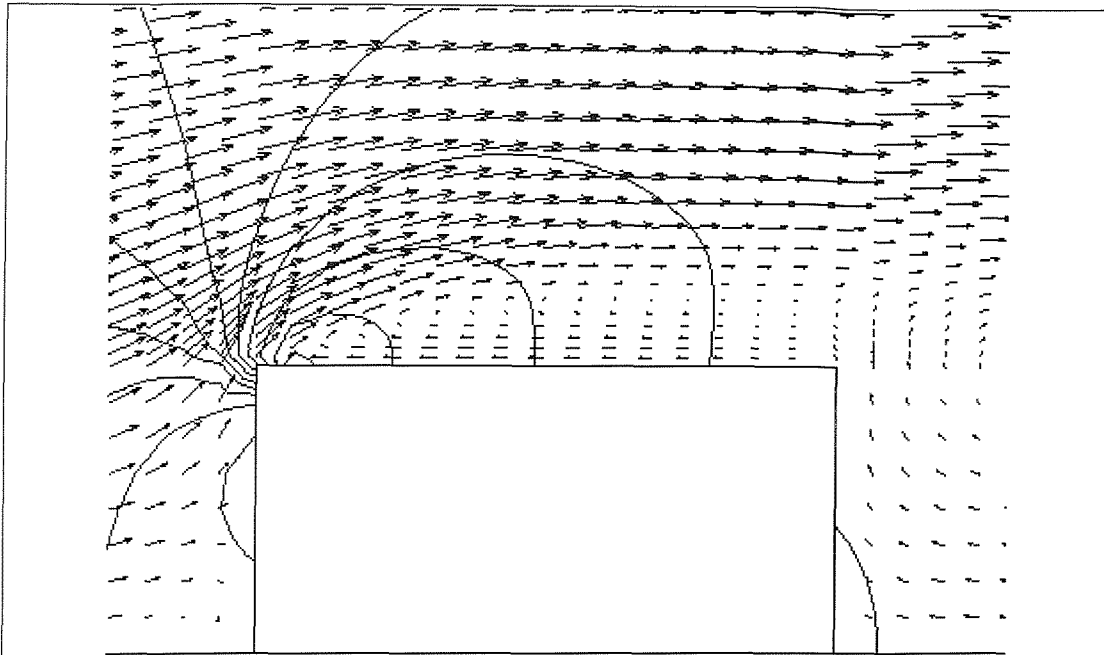


Figure 3.21 : 3D Surface Mounted Block, Flow Across Central Longitudinal Plane.

Figure 3.22 shows the flow in the longitudinal plane, which coincides with the outer edge of the block. This plane is offset by 0.5m from the central or symmetry plane. At this location the flow appears to remain attached along the topside of the block. This figure gives no indication of the lateral flow component. The figure shows a region of high pressure upstream of the block and low pressure just after the separation at the windward edge.

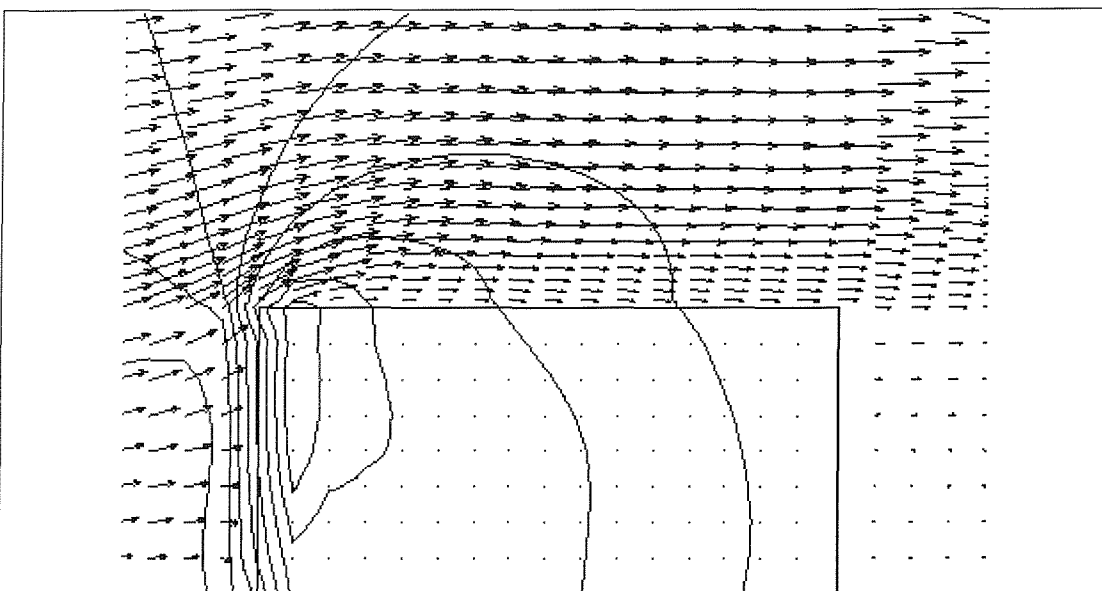
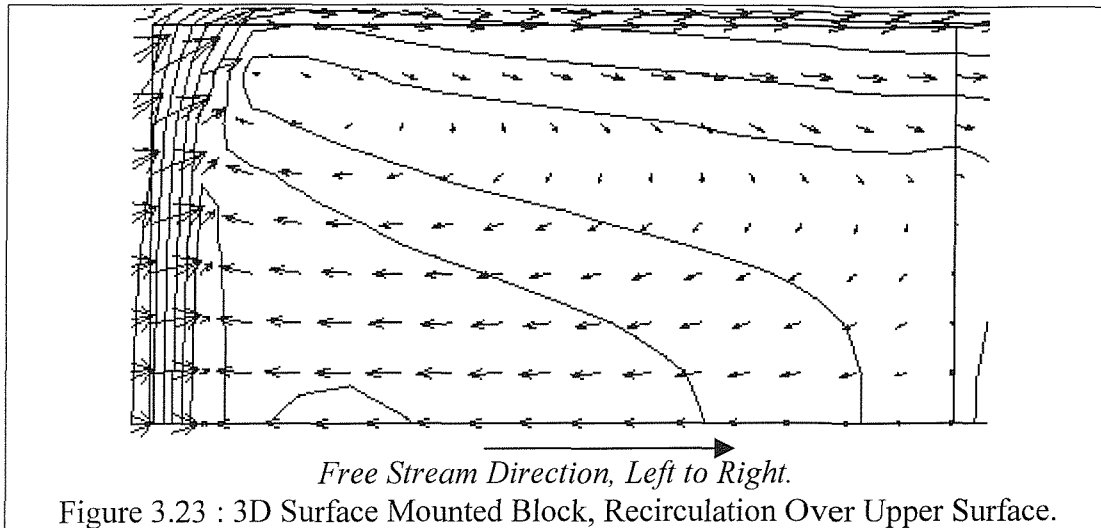


Figure 3.22 : 3D Surface Mounted Block, Flow Across Offset Longitudinal Plane.

The combination of the separated flow at the block's midplane and attached flow at the outer regions gives a very interesting recirculation region. Figure 3.23 shows the flow in a horizontal plane 1.5cms above the block. The flow solution in

Figure 3.23 is viewed as seen from above, with the freestream velocity from left to right. The symmetry plane or block's centreline is at the base of the figure and the outer face of the block is at the top of the figure. This figure shows that the fluid in the recirculation region comes from flow initially at the outer face of the block. It also demonstrates that there are large lateral components to the flow velocity over the top edge of the block.



This section has shown that the flow around a block is truly three dimensional. The geometry used within this study is very simple and general, however the results were not a foregone conclusion. The airflow around a complex geometry, such as a ship, is not only difficult to predict but complicated to model.

### 3.10 Comparison of CFD and Experimental Data

#### 3.10.1 Introduction

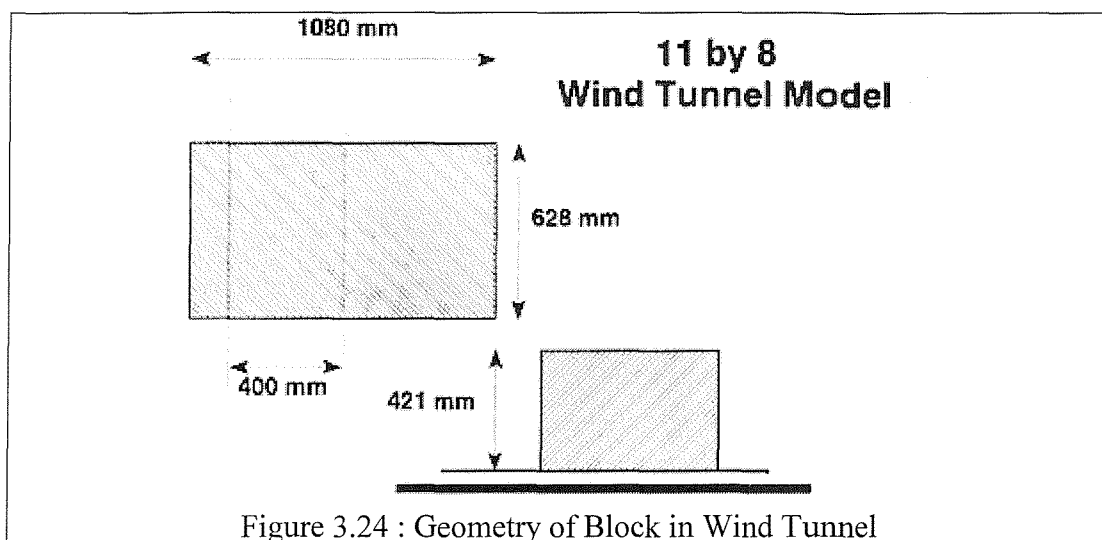
The previous sections within this chapter have provided insight into achieving a flow solution efficiently without introducing any erroneous effects from an inadequate grid. At no point within these sections have the flow solutions been compared with experimental data. This section generates a series of flow solutions which represent the flow around a block in a wind tunnel. The experimental results are taken from the study of the airflow around a block modelling a ship's flight deck in a wind tunnel.

The comparison of experimental and CFD data provides an opportunity to assess the turbulence models available within CFX and the overall accuracy of CFD.

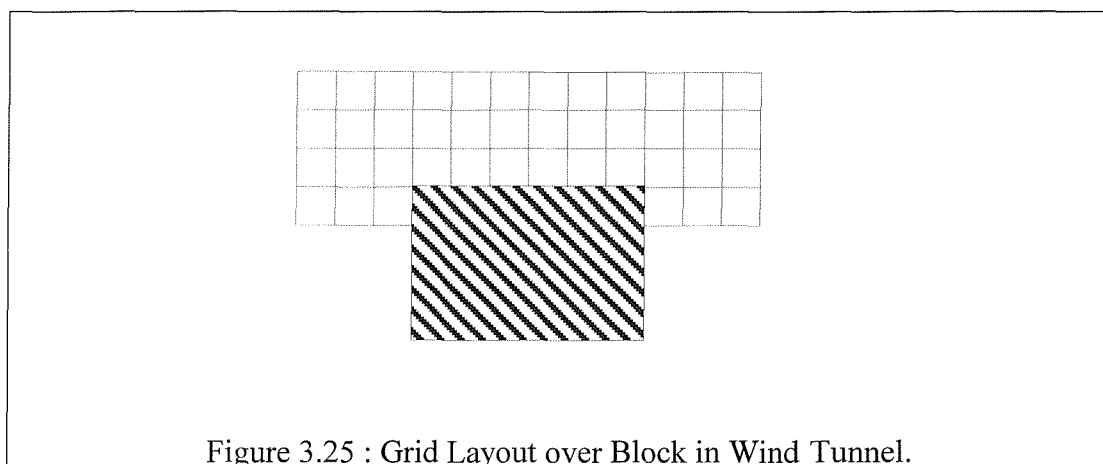
There are seven turbulence models available within CFX; results found using a selection of these are presented below.

### 3.10.2 Experimental Model

The experimental data were found from an investigation into the flow around a ship's flight deck by Newman described in [3.7]. A block was placed in a wind tunnel mounted on a sheet of plywood, as shown in Figure 3.24. The plywood had dimensions 4ft by 8ft and was placed across the centre of the wind tunnel, raised to a height of 0.15m. The block was placed at the centre of the plywood. The wind tunnel was 11ft wide and 8ft tall.



Vertical and longitudinal velocity components around the block were measured. Figure 3.25 shows the grid around the block; mean velocity components were recorded at each grid point using a Laser Doppler Anemometer. The grid lies in the longitudinal plane at the block's centreline and offset laterally by 400mm. Two freestream velocities were used, 5m/s and 2.5m/s.



### 3.10.3 CFD Turbulence Models

The grid around the block was defined according to the grid density parameters found in Section 3.7. The grid contains 120,000 cells. A length of wind tunnel seven metres long was modelled, in order to place the boundaries sufficiently far from the region of interest, not because the wind tunnel was seven metres long.

Turbulence within the k- $\epsilon$  model is defined by two quantities, turbulent kinetic energy,  $k$ , and turbulent dissipation rate, epsilon. The turbulent kinetic energy,  $k$ , is the mean square of the time varying components of the velocity,  $u$ ,  $v$ , and  $w$ , as shown in equation (3.1). The viscosity of the fluid within a turbulent calculation is modelled with two constituent parts, the laminar viscosity and the turbulent component, which is assumed to be proportional to  $k^2$ , as shown in equation (3.2). The additional component is sometimes referred to as the eddy viscosity or turbulent viscosity [3.3].

$$k = \frac{1}{2} (\overline{u^2} + \overline{v^2} + \overline{w^2}) \quad (3.1)$$

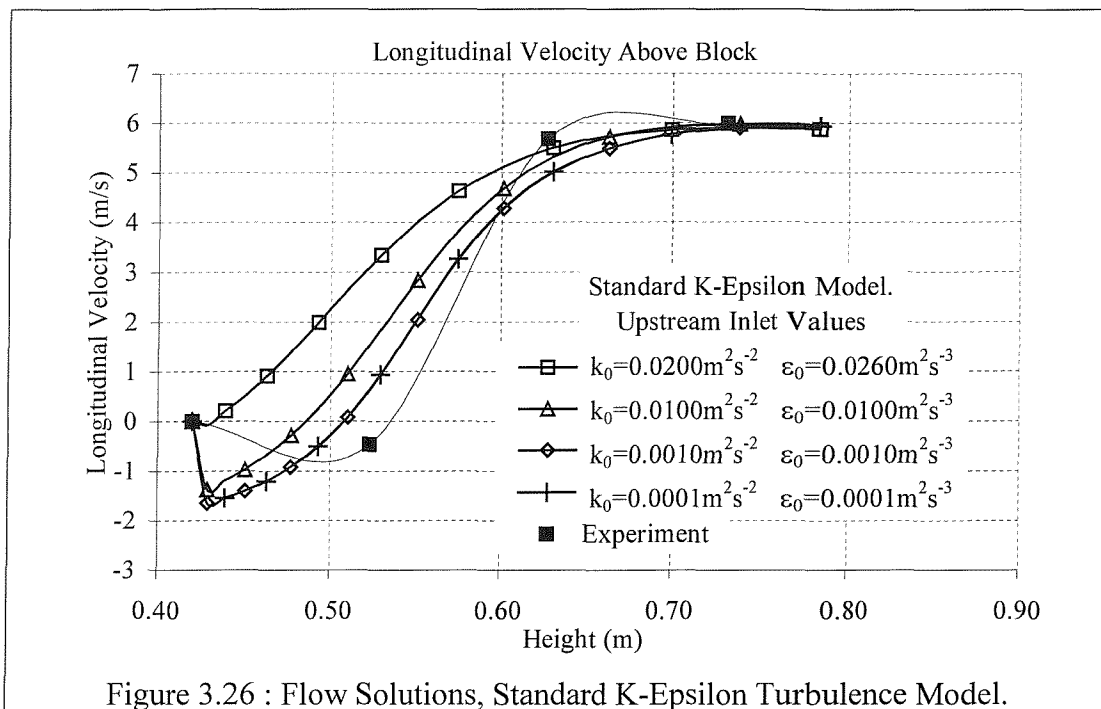
$$\begin{aligned} \mu_{\text{EFF}} &= \mu_{\text{LAMINAR}} + \mu_{\text{TURBULENT}} \\ &= \mu_{\text{LAMINAR}} + C_{\mu} \rho \frac{k^2}{\epsilon} \end{aligned} \quad (3.2)$$

The definition and transport equation of  $\epsilon$  depend upon the exact turbulence model [3.3].

The values of  $k$  and epsilon are solved throughout the flow solution. The only region in which the user must define the turbulent parameters is at the upwind inlet to the domain. The governing transport equations are described in more detail in many standard texts such as the CFX Manual [3.3] and Versteeg and Malalasekera [3.5].

Flow solutions have been found using four established turbulence models, the standard k-epsilon, the RNG k-epsilon, the Algebraic Stress Model and the Differential Stress Model.

CFX Manual [3.3] is an empirical estimate for the turbulence quantities at the inlet to an internal flow problem. This algorithm predicted initial turbulent kinetic energy,  $k_0$ , as  $0.2\text{m}^2/\text{s}^2$  and epsilon,  $\epsilon_0$ , as  $0.026\text{m}^2/\text{s}^3$ ; a solution was found using these values. Three further solutions were found using inlet values of  $k$   $0.01\text{m}^2/\text{s}^2$ ,  $0.001\text{m}^2/\text{s}^2$  and  $0.0001\text{m}^2/\text{s}^2$  and inlet values of epsilon  $0.01\text{m}^2/\text{s}^3$ ,  $0.001\text{m}^2/\text{s}^3$  and  $0.0001\text{m}^2/\text{s}^3$ . The resultant longitudinal velocity above the centre of the block is shown in Figure 3.26, along with experimental data. This figure demonstrates that the empirical estimate of inlet turbulence quantities gives a highly spurious result. In this case there is no recirculation over the block. The reduced inlet values of  $k$  and epsilon provide results more consistent with the experimental data. This figure also shows that using turbulence intensity of  $0.001\text{m}^2/\text{s}^2$  or less at the inlet does not influence the flow solution.



The majority of the grid points within the CFD model were clustered around the block. It is difficult to determine whether the boundary layers along the walls of the wind tunnel are being sufficiently treated. In order to find whether this is a problem and whether it makes any difference, a solution was found within which the walls of the wind tunnel were frictionless and thus did not generate a boundary layer. Comparison of results indicated that identical flow solutions are achieved modelling the walls with the 'no slip' condition and defining the walls as frictionless.

Further solutions were sought using a variation of the standard k-e model, the RNG k-epsilon model. The RNG model is suited to higher Reynolds numbers. Several solutions were obtained using various turbulence inlet values; the longitudinal flow values were recorded and compared with experimental results as shown in Figure 3.27. These results compare more favourably with the experimental data.

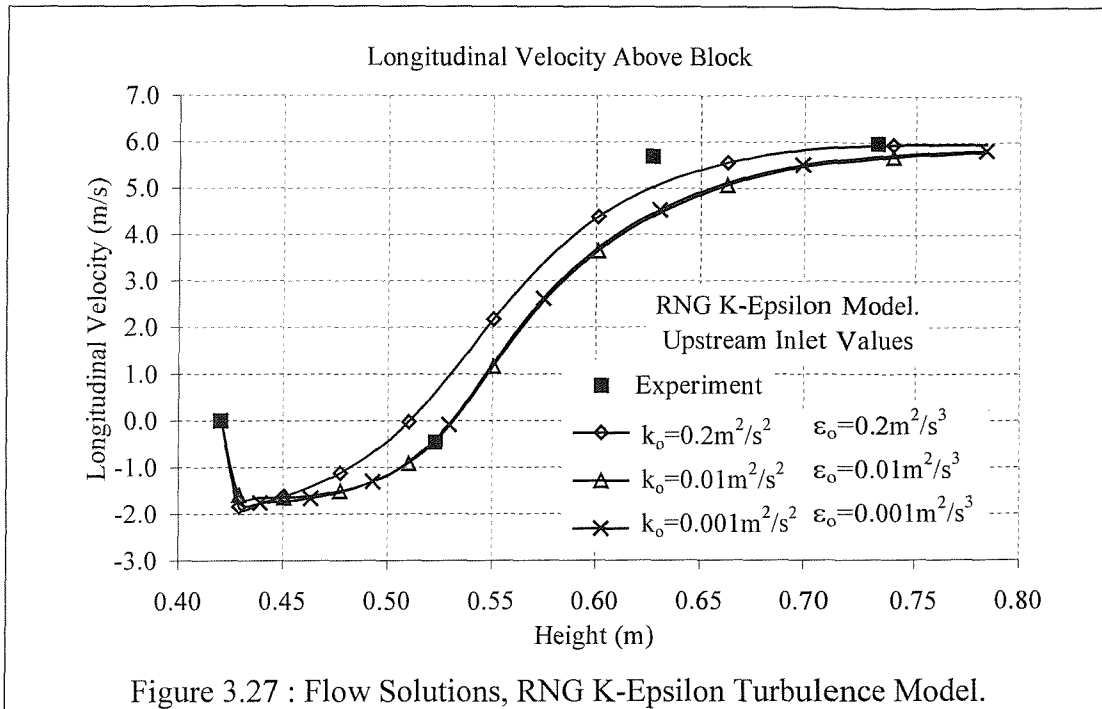
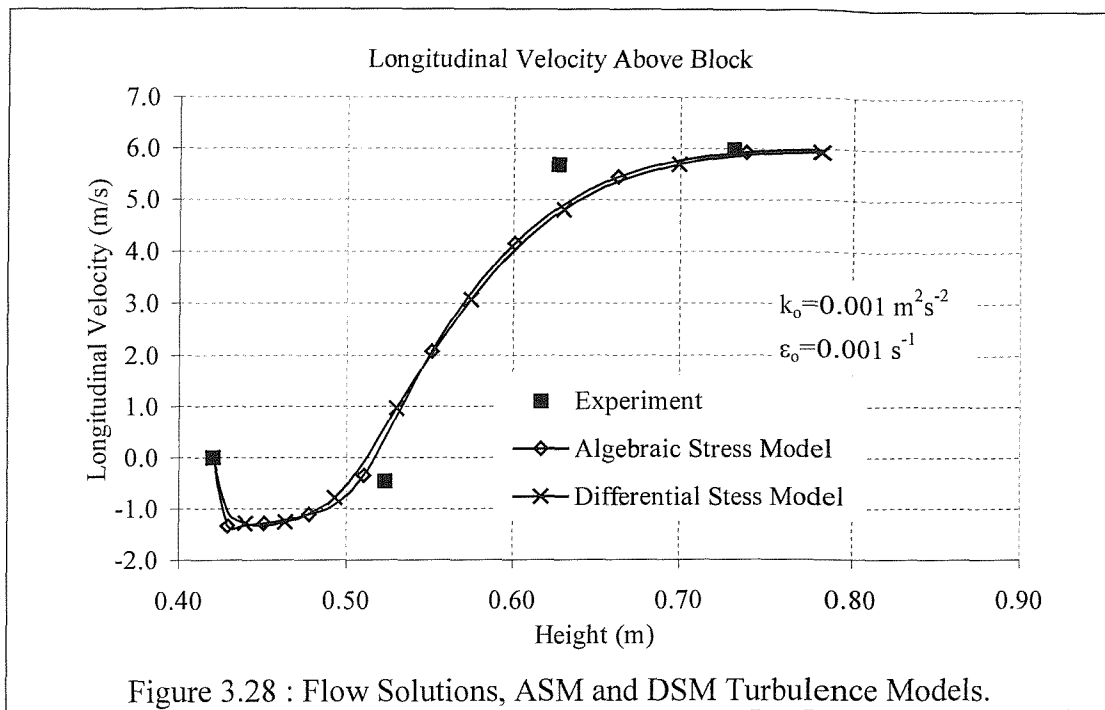


Figure 3.27 : Flow Solutions, RNG K-Epsilon Turbulence Model.

There are two Reynold's Stress models, the Algebraic Stress Model (ASM) and the Differential Stress Model (DSM) [3.3]. Two solutions were found using these turbulence models, in both cases the turbulent kinetic energy and dissipation were set as  $0.001\text{m}^2/\text{s}^2$  and  $0.001\text{m}^2/\text{s}^3$  respectively at the inlet. The longitudinal velocities over the block's centre are compared to experimental results in Figure 3.28. The turbulence models produce similar flow solutions, with the ASM solution slightly more in agreement with the experimental data.



### 3.10.4 Comparison and Discussion

The flow solutions outlined in Section 3.10.3 used various turbulence models and considered the effect of the turbulence parameters at the upstream boundary. The model that appears to correspond most closely with the experimental results used the RNG k-epsilon turbulence model with inlet turbulence values of  $0.001\text{m}^2\text{s}^{-2}$  and inlet dissipation  $0.001\text{m}^2\text{s}^{-3}$ . Within this section this flow solution is compared in more detail with the experimental results.

The CFD flow solution is shown in Figure 3.29 and the experimental results are shown in Figure 3.30. The recirculation regions above the blocks are very similar to each other.

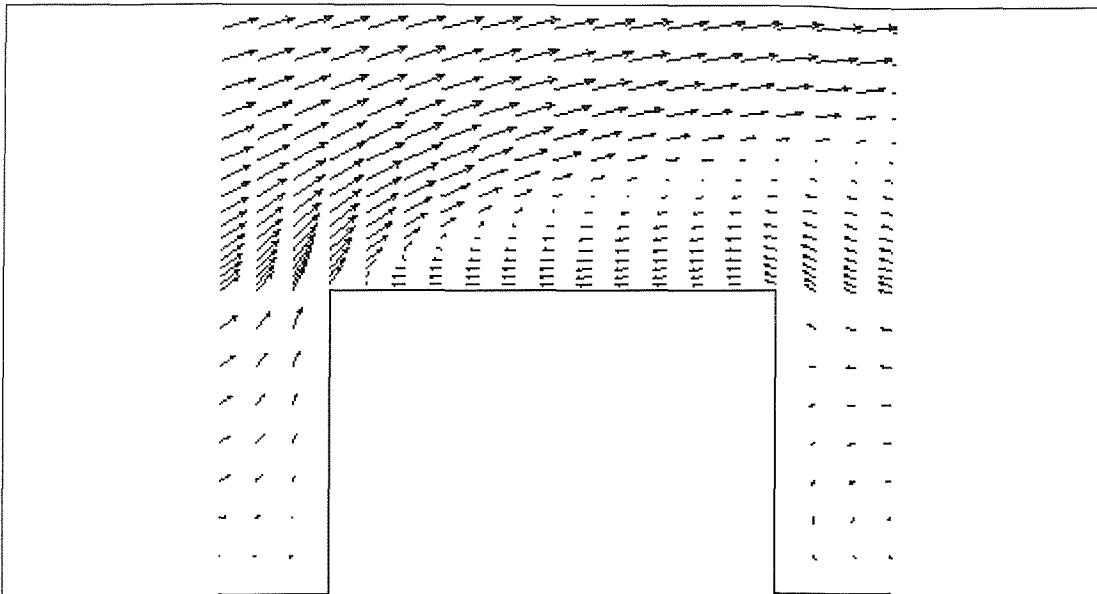


Figure 3.29 : CFD Flow Solution.

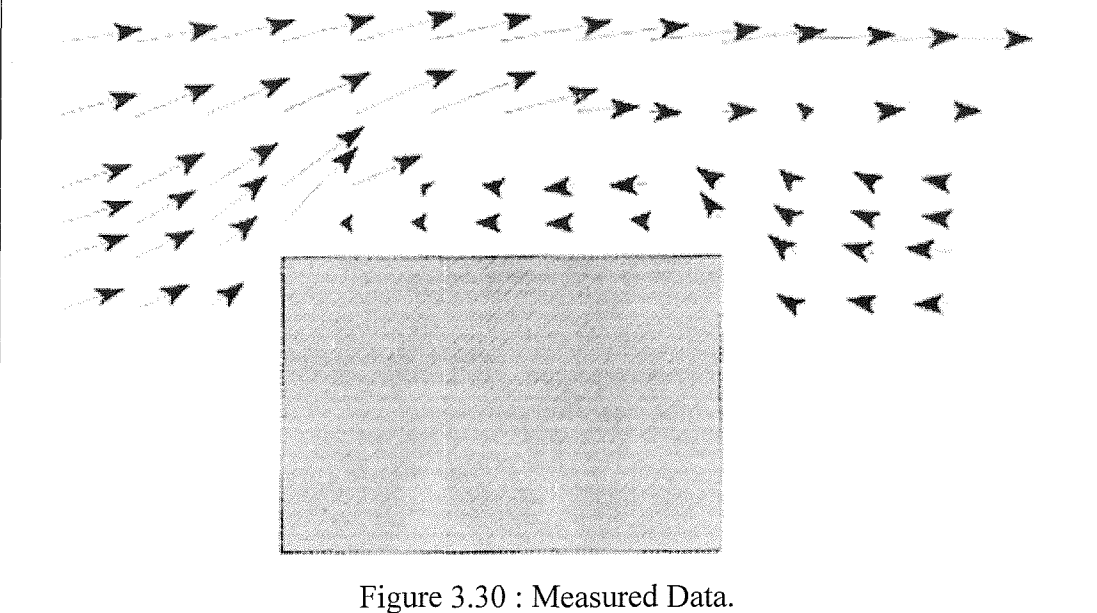


Figure 3.30 : Measured Data.

The experimental and computational results are compared quantitatively in Figure 3.31 and Figure 3.32. Three vertical axes were chosen along which the velocities are measured. All three axes lie on the block's centreline, the first is above the leading or windward edge, the second extends upwards from the centre of the block and the final axis lies above the leeward edge of the block. Figure 3.31 shows the longitudinal velocities. The axis over the windward edge is shown by the square symbols. The measured data is shown as discrete points whereas the CFD solution is shown as a continuous line. In general the CFD solution agrees quite well with the measured data.

The flow over the centre of the block is shown by the triangles. The experimental results predict a sharper transition between the recirculation region and the shear layer. At a height of 0.62m the experimental flow is 5.7m/s which is greater than the freestream whereas the CFD solution gives a velocity of 4.4m/s. Above the leeward edge of the block, denoted by the circles, there is very good agreement within the recirculation but at a height of 0.73m the CFD solution predicts 17% smaller flow velocity.

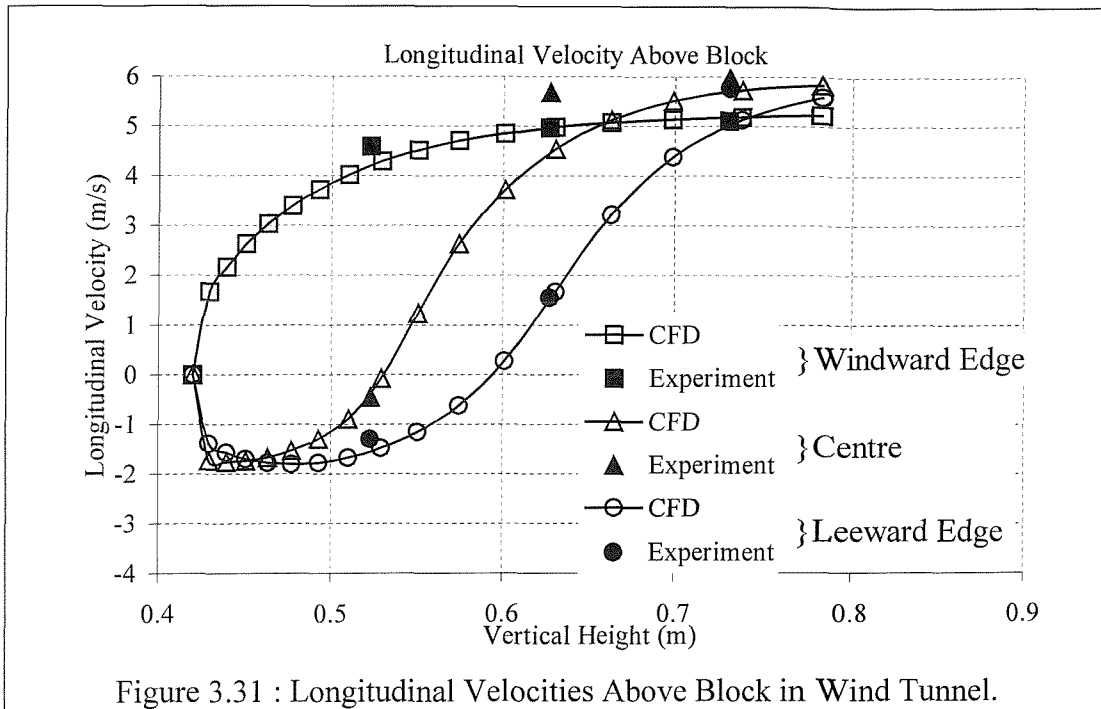


Figure 3.31 : Longitudinal Velocities Above Block in Wind Tunnel.

The experimental and computational vertical velocities are shown in Figure 3.32. The data along the axis above the block's windward edge is shown by the squares. The solutions agree to within 8% of the freestream velocity. The flow above the block's centre is shown by the triangles. As with the longitudinal velocity, the solutions are the same at the upper and lower heights but vary by 0.5m/s (10% of the freestream) at a height of 0.63m.

The circles denote the flow above the leeward face. The computational results are similar (within 2% of the freestream velocity) to the measured results at the upper locations, however there is a discrepancy of over 1m/s at a height of 0.52m. The experimental results indicate the recirculating fluid travels upwards along the back face of the block and then horizontally over the block in the opposite direction to the free stream. However, the CFD solution shows the fluid in the recirculation region reaches the block horizontally from downstream.

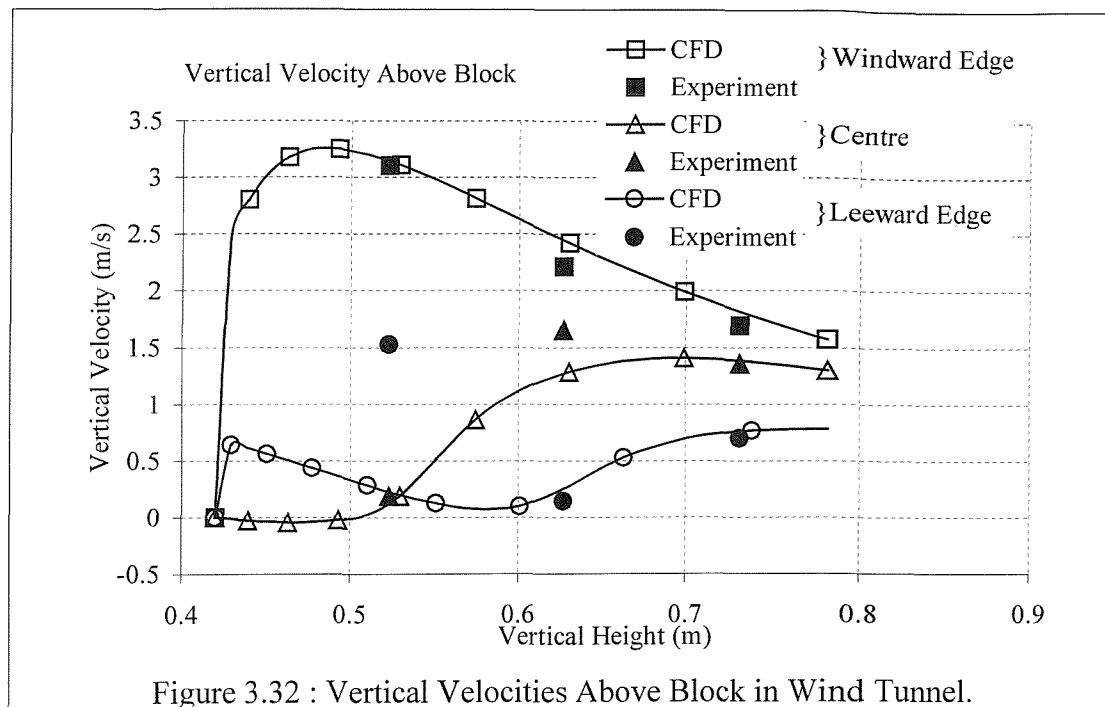


Figure 3.32 : Vertical Velocities Above Block in Wind Tunnel.

Only one velocity component of one measured data point is significantly different from the computational solution, the vertical velocity immediately above the aft edge of the block. A Laser Doppler Anemometer (LDA) was used to take the wind tunnel measurements. This method relies on seeding the flow, which is difficult in a region of recirculation such as this point. In this case the source of seeding particles was placed downstream of the block. The flow of these particles was weaker and hence inaccuracies crept into the results.

The CFD solution predicts a less sharp transition between the separated shear layer and recirculation region than the experimental results. This is most apparent for both velocity components over the centre of the block at a height of 0.63m.

This section has shown that a well constructed CFD geometry can provide a flow solution which exhibits all the characteristics of experimental results. In this case the quantitative comparison has shown the accuracy of CFD.

### 3.11 Conclusion

This chapter contains a considerable amount of information which is carried forward to further studies presented below. Aspects of achieving a generally correct CFD solution without unnecessary computing resources are covered.

The various solvers and pressure correction schemes are considered. As demonstrated, employing the wrong solution strategy is costly with respect to computing time taken, and can more than double required resources. The location of the boundaries is also discussed and it is shown that these must be distant from the body in order to not affect the solution. The upper boundary for an external flow problem can be either an imposed flow condition or a symmetry plane. Applying the pressure condition at this boundary gives spurious results.

The grid was separated into two regions, the volume around the perturbation, in this case a block, and the outer region, which covers the volume out to the boundaries. Care must be taken to ensure that there are enough cells around the body, however the outer region required few cells. One method tested within this chapter to reduce the number of cells is using a C-grid around the block instead of the H-grid. This degraded the solution slightly but reduced computing resources greatly.

In order to investigate the effects of turbulence model, solutions were found using all the models available within CFX 4 and compared to measured data. The RNG K-Epsilon model performs best with good agreement to the measured results.

CFD is an established tool for predicting flows around aerodynamic bodies. This chapter has demonstrated that careful definition of a flow solution geometry and turbulence parameters can provide a good bluff body flow solution.

## **4 Modelling a Helicopter Using CFD.**

### **4.1 Introduction**

There are several methods by which the aerodynamics of a helicopter rotor operating in hover or forward flight can be modelled. These are of varying complexity and ultimately provide a compromise between the realistic representation of a helicopter and the practical limitations of time and software available. There are three main features of a helicopter, which are discussed here, namely the main rotor, tail rotor and fuselage.

Boundary conditions usually lie at the edge of the geometry. At these points there is some condition imposed that does not vary with the iteration process. As previously discussed, these imposed conditions take several forms, examples being flow values, flow symmetry planes, walls, or pressure values. They are all readily accessible in most commercially available CFD software

Most problems can be modelled accurately using some or all of the boundary conditions given above. However, there are certain specific problems that will yield meaningless solutions if this procedure is followed. Examples are the helicopter rotor in hover and ships' propellers operating at zero advance. These problems are inherently different because flow throughout the physical space is induced from its centre, not from any of the boundaries. This chapter describes a general boundary condition, that when applied around a helicopter in hover, gives a physically justifiable flow solution without imposing any flow conditions at the boundaries.

Comparisons between the computational solutions and established momentum theories are used to verify the novel boundary condition.

## 4.2 The Helicopter Model

For the purpose of this section, the helicopter model is divided into three parts, the main rotor, tail rotor and fuselage. The fuselage includes all parts of the helicopter other than the rotors. It is assumed the helicopter rotor configuration consists of one main rotor and one tail rotor.

### 4.2.1 The Main Rotor

Three methods of representing the main rotor are discussed below. The most obvious method of representing the rotor is to model each blade rotating around the hub. There are several drawbacks to this approach.

The angle of the blades must be known as they move around the azimuth. This may be relatively simple to assume for a hovering helicopter distant from the ground, ships or other structures. Unfortunately the area of greatest interest is in exactly these locations. If an erroneous assumption is made when calculating the blade angles, the helicopter thrust exerted within the flow solution may be different in magnitude to the helicopter weight and the centre of thrust may not act through the helicopter's centre of mass.

There are other difficulties associated with moving rotor blades within CFX. Most importantly, a huge number of cells are required to calculate the thrust exerted on the fluid. A satisfactory grid around a typical aerofoil is shown in Figure 4.1. The other shortcomings of this method pertain to the flow solver. The outer regions of the blades are travelling at Mach numbers greater than 0.5, thus the fluid cannot be assumed incompressible. This complicates the solution process because density has to be solved at every location. The forces exerted on the fluid are not time independent. Flow solutions that vary with time require huge computing time to achieve. Related to this problem is the fact that as the blades move the grid will have to move with them. Moving grids also require extremely large amounts of computing time.

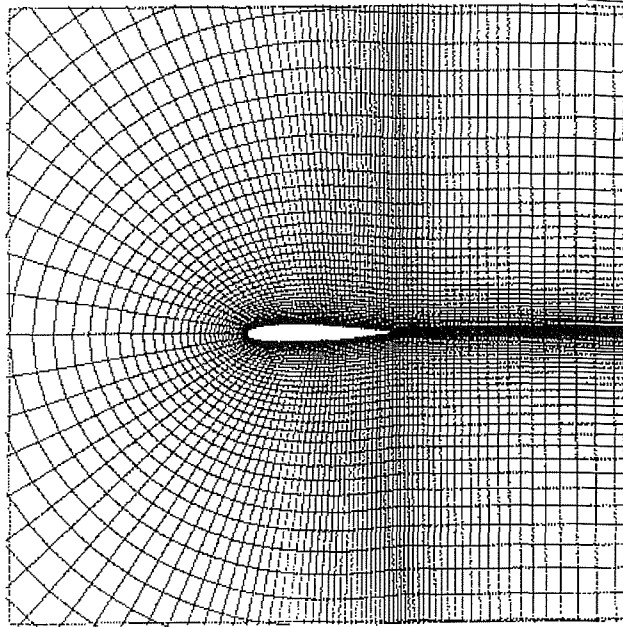


Figure 4.1 : CFD Grid Around An Aerofoil.

Another option to represent a helicopter main rotor within a fluid domain is to define the velocity components at the plane of the rotor, as depicted in Figure 4.2. The velocity defined at the location of the rotor blades is found from simple momentum and power principles; these velocities can vary across the rotor radius or remain constant. The fluid flow throughout the rest of the domain is allowed to vary. The advantages of this method are that the geometry requires fewer grid cells and the solution is faster to solve, indeed many orders of magnitude faster than modelling the individual blades. The rotor will occupy zero thickness as shown in Figure 4.2. The key disadvantage of this method is that the fluid flow at the location of the rotor must be predetermined. At present there is no established method for choosing these flow parameters. Therefore the solution, although interesting, would provide only a limited insight into the helicopter handling difficulties. The pressure disturbance at the rotor will not necessarily represent the helicopter mass.

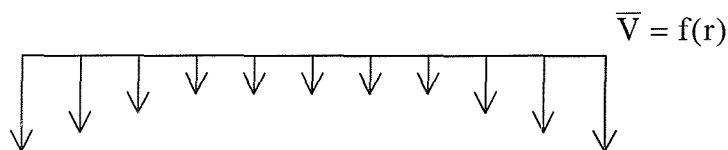


Figure 4.2 : Velocity Representation of a Main Rotor.

The third viable method is to exert forces onto the fluid at the plane of the rotor blades, as shown in Figure 4.3. This method is very simple in terms of grid

structure. Provided the necessary grid cells can be located within the grid, the appropriate force can be applied to the fluid. The key advantage is that the magnitude of the vertical and horizontal forces applied to the fluid is equal to the helicopter thrust exerted by the rotors. This force does not depend on the velocity of the surrounding fluid. Using this method the velocity components at the rotor can vary freely, as they vary throughout the rest of the domain. The only evidence of the rotor is a pressure discontinuity at the plane of the rotor, which remains constant regardless of the local velocities.

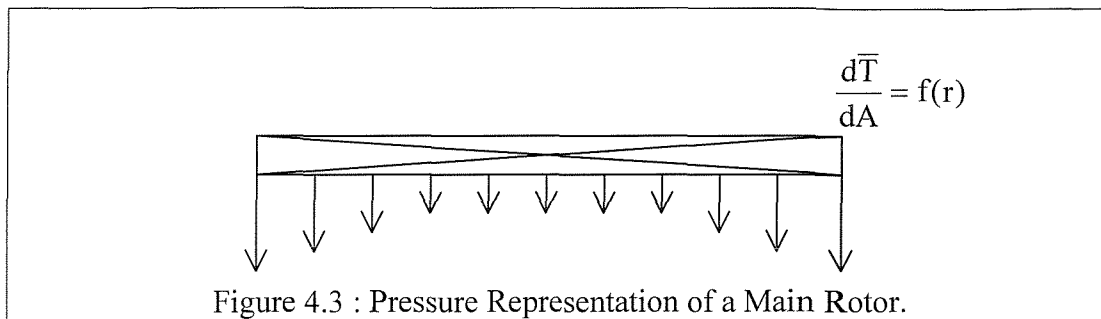


Figure 4.3 : Pressure Representation of a Main Rotor.

The thrust per area exerted on the fluid is not necessarily constant across the rotor radius. A more realistic thrust distribution, for example based on experimental data or blade element theory can be used. These forces can be defined as constant with respect to time, modelling an actuator disc, or vary periodically. However a time dependant solution is computationally very expensive. The flow solver CFX uses a finite volume method, therefore the forces must be exerted over a finite thickness rotor, as shown by the hatched regions in Figure 4.3.

Consideration of the vertical velocity components at the plane of the rotor provides information about the power exerted at the rotor. Further analysis using blade element theory yields information about the cyclic, lateral and longitudinal pitch that the pilot inputs to remain in a certain position. These theories are discussed in more detail below.

Of these options the final method provides a means to generate a flow solution using minimal computational resources. Using this method, the thrust exerted on the fluid is known and is an input to the solution, rather than being a product of the flow solution.

### **4.2.2 The Tail Rotor**

The modelling options for the tail rotor are identical to those outlined for the main rotor. Modelling each of the individual blades would be as impractical as modelling each blade of the main rotor.

Defining the velocity at the tail rotor has the same deficiencies as with the main rotor. The solution is somewhat predetermined and hence provides limited information.

The tail rotor can also be modelled by applying forces to the fluid at the location of the rotor. The disadvantages are that the rotor occupies a finite thickness and the magnitude of the force applied at the rotor must be known. The force at the tail rotor counteracts the torque applied to the main rotor blades. In order to know the torque at the main rotor, the induced power exerted must be found, which relies on the flow solution. This problem leads to an iterative solution method in order to input a realistic tail rotor thrust to the model and hence find the power and control used by the tail rotor.

Despite the iterative nature of defining the tail rotor thrust, this method is preferable to the previous two methods and will be adopted for further studies. The tail rotor will not be included in any 2D or axisymmetric models.

### **4.2.3 The Fuselage**

The fuselage model can be as simple or complex as defined. In all cases the principles are identical. The region of space occupied by the fuselage must be defined, and within this space there is no fluid. At the walls of the fuselage the no slip condition is applied, such that all the fluid velocity components are zero. Outside of the fuselage the pressure and velocities are unconstrained and vary. The grid around the fuselage must be chosen carefully in order to model the flow accurately. The presence of a body such as the fuselage complicates the grid greatly. New blocks are introduced which would not otherwise have been necessary, and even a simple representation greatly complicates the grid. If the grid around the fuselage is insufficiently defined the flow will not be resolved satisfactorily and hence may not exhibit important flow features or accurately predict loads.

In reality the main rotor exerts a downward force on the helicopter fuselage. This is known as blockage and has the effect of increasing the power requirements. Modelling the fuselage accurately would also yield information about blockage.

This chapter is primarily concerned with verifying the rotor models and that boundary conditions within the CFD model are operating correctly. For this reason the fuselage has been ignored.

### **4.3 Verification of Rotor Model**

The purpose of this section is to ensure that the force exerted on the fluid by the rotor model is equal to the force intended to be exerted on the fluid. This force is exerted on the fluid by the 'body forces' function within CFX, which is designed to model porous media, for example sponges. This section determines that the 'body forces' function can be applied to actuator disc problems.

A simple 2D geometry has been used, as shown in Figure 4.4. The upper boundary is an inlet, at which the velocity is defined as 10m/s. The side boundaries are symmetry planes, convenient because there is no flow across them and zero friction exerted on the fluid. The lower boundary is a pressure boundary, at which the pressure is defined as a datum, in this case zero. The domain is 4m wide and 20m tall, the rotor is placed at the mid-height of the domain. The grid cells are 0.1m by 0.1m in size.

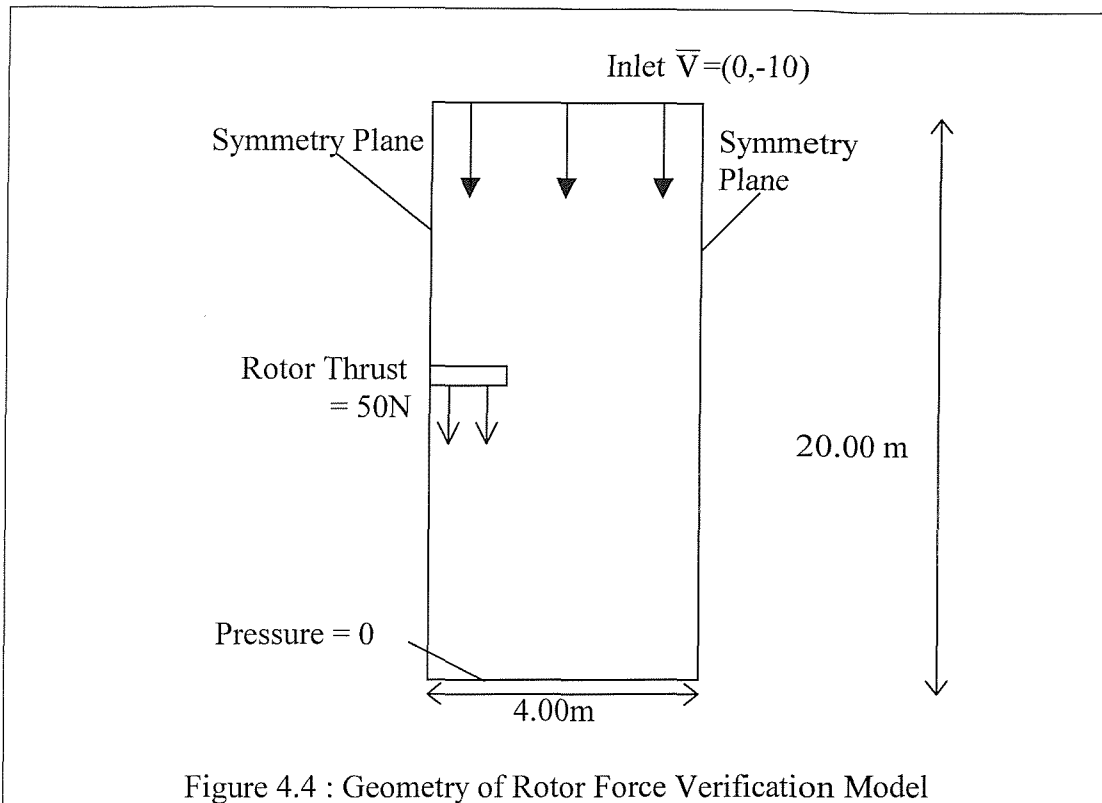


Figure 4.4 : Geometry of Rotor Force Verification Model

The thrust exerted by the rotor is distributed over a volume, as shown by the hatched areas in Figure 4.5. The force  $B_Y$ , which is the quantity ultimately entered into the flow solver, has units of force per unit volume. In order to define  $B_Y$ , the thrust per area must be divided by the rotor depth  $H$ , as shown in equation (4.1).

$$\Delta p = \frac{dT}{dA} = B_Y \cdot H \quad (4.1)$$

In this case the thrust per area was defined as 50N, and hence the total thrust,  $T$ , is 50N because the rotor has an area,  $A$ , of  $1\text{m}^2$ .

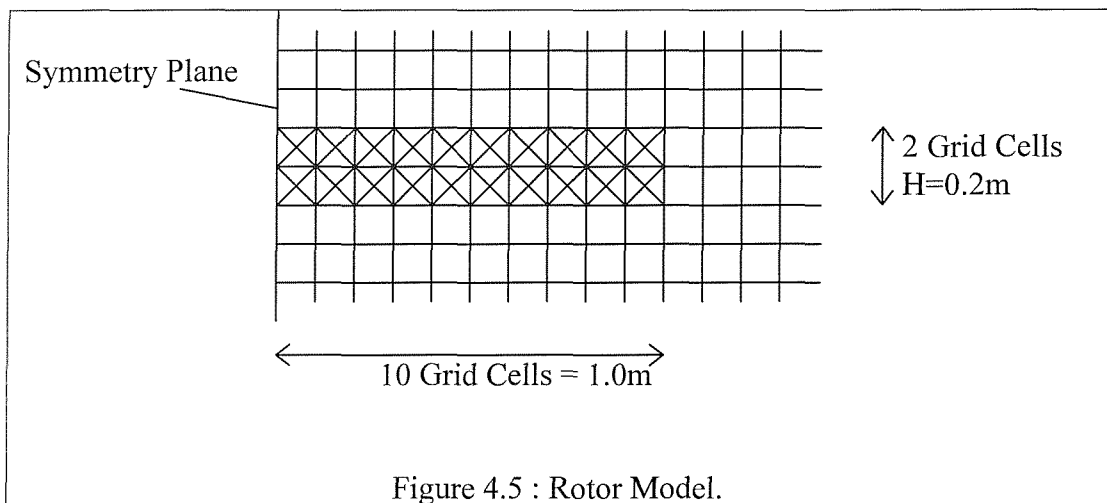


Figure 4.5 : Rotor Model.

In order to evaluate the flow solution an imaginary box is drawn around the rotor and the momentum in and out considered. As the only forces acting on the fluid

inside the control volume are the forces acting around the perimeter and the rotor forces equation (4.2) is applicable.  $\overline{F}_p$  is the force acting on the outer surface of the box.  $\overline{T}_{APP}$  is the force exerted by the actuator disc.

$$\overline{\Phi} = \rho \int_A \overline{V} (\overline{V} d\overline{A}) = \sum \overline{F} = \overline{F}_p + \overline{T}_{APP} \quad (4.2)$$

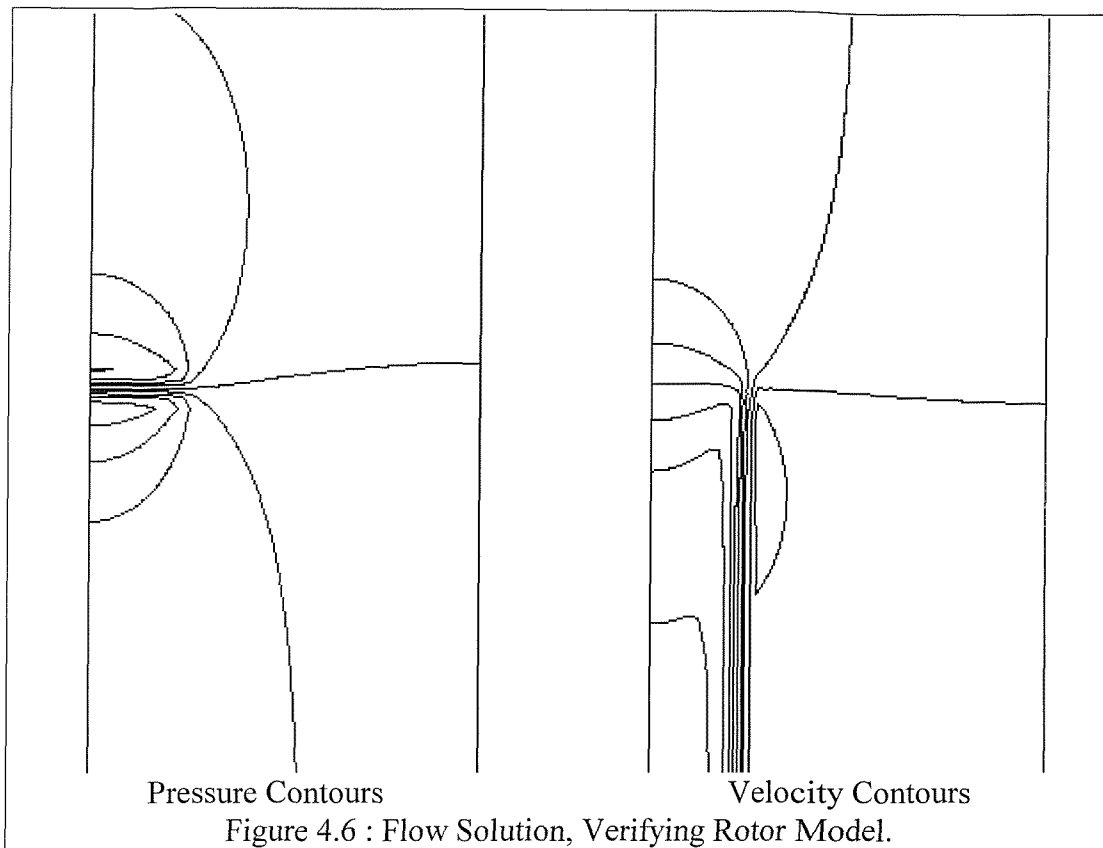
The force exerted on the box,  $\overline{F}_p$ , is found by integrating the static pressure around the outside of the control volume, as shown in equation (4.3). The frictional forces exerted on the box are ignored. The vertical sides of the box are bounded by symmetry planes along which there are, by definition, no frictional forces. The frictional forces exerted on the horizontal faces of the control volume at the top and bottom of the box do not affect the vertical forces or momentum flow.

$$\overline{F}_p = \oint p d\overline{A} \quad (4.3)$$

The net momentum flux moving out of the control volume is given in equation (4.4). The area vector  $d\overline{A}$  points perpendicularly out of the control volume.  $\overline{V}$  is the velocity vector.

$$\overline{\Phi} = \rho \int_A \overline{V} (\overline{V} d\overline{A}) \quad (4.4)$$

Two aspects, pressure contours and velocity contours, of the flow solution of the advancing actuator disc is shown in Figure 4.6, where the rotor model is located at the mid-height of the figures on the left. The pressure contours are spaced at 5Pa, showing the lowest pressure immediately above the rotor model and the greatest immediately below. The speed contours are spaced at the 0.5m/s, the flow is fastest in the downwash and slowest adjacent to the downwash.



In order to analyse the solution flow data was recorded at two horizontal planes; 10m below and above the rotor. The static pressure across these planes was integrated to find the force exerted on the control volume. The momentum travelling vertically down across the planes was also found, as shown in Table 4.1. The differences between the momentum and the force are shown in the fourth column.

Horizontal Plane (m)	Vertical Force acting on Plane (N)	Momentum Flux (kg.m/s/s)	Momentum Flux - Force (N)
y=10m 'IN'	-38.474	-449.600	-411.126
y=-10m 'OUT'	0.000	-461.042	-461.042

Table 4.1 : Analysis of Rotor Verification Model.

Equation (4.2) is rearranged to include just two planes as shown in equation (4.5). The apparent thrust can be evaluated from Table 4.1, where the plane below the rotor model is the 'OUT' plane and above is 'IN' planes.

$$\bar{T}_{APP} = -461.042N + 411.126N = -49.916N \quad (4.5)$$

The apparent thrust is -49.92N. Recalling that the thrust defined at the rotor was 50.00N downwards, the discrepancy is less than 0.1N, a magnitude of 0.2%.

Such a small discrepancy can be attributed to rounding errors in the integration process or approximations within flow solution process. A difference of 0.2% between the defined thrust and apparent thrust proves that the 'body forces' function within CFX works and that an actuator disc or rotor can modelled in this way.

#### **4.4 Deficiencies of Existing Boundary Conditions.**

There are three boundary conditions which define flow into, or out of a geometry, they are inlets, mass flow and pressure boundaries. Other boundary conditions such as walls and symmetry planes concern the treatment of the flow at solid boundaries.

The inlet condition defines velocity components and turbulence parameters; this is known as the Dirichlet condition. This condition is used only when the velocity vector is known. The pressure gradient at the inlet is zero; this is the Neumann condition.

At a pressure boundary the pressure is defined; this is the Dirichlet condition. The velocity and turbulence parameters are solved, however the gradient is zero (the Neumann boundary condition). One such example is the downwind side of a domain modelling yachts' sails in the atmosphere. We know that at a plane distant from the sails the pressure must be atmospheric. An example of a hover flow solution found using pressure boundaries is shown in Figure 4.7. The rotor is placed at the left of the figure, exerting a force vertically downwards. The chief inaccuracy of this flow solution is the region of fluid travelling upwards in the right of the figure. This is physically unrealistic and conflicts with established momentum principles because a hovering actuator disc induces flow in the downwards direction and the flow into the disc is drawn in from all around.

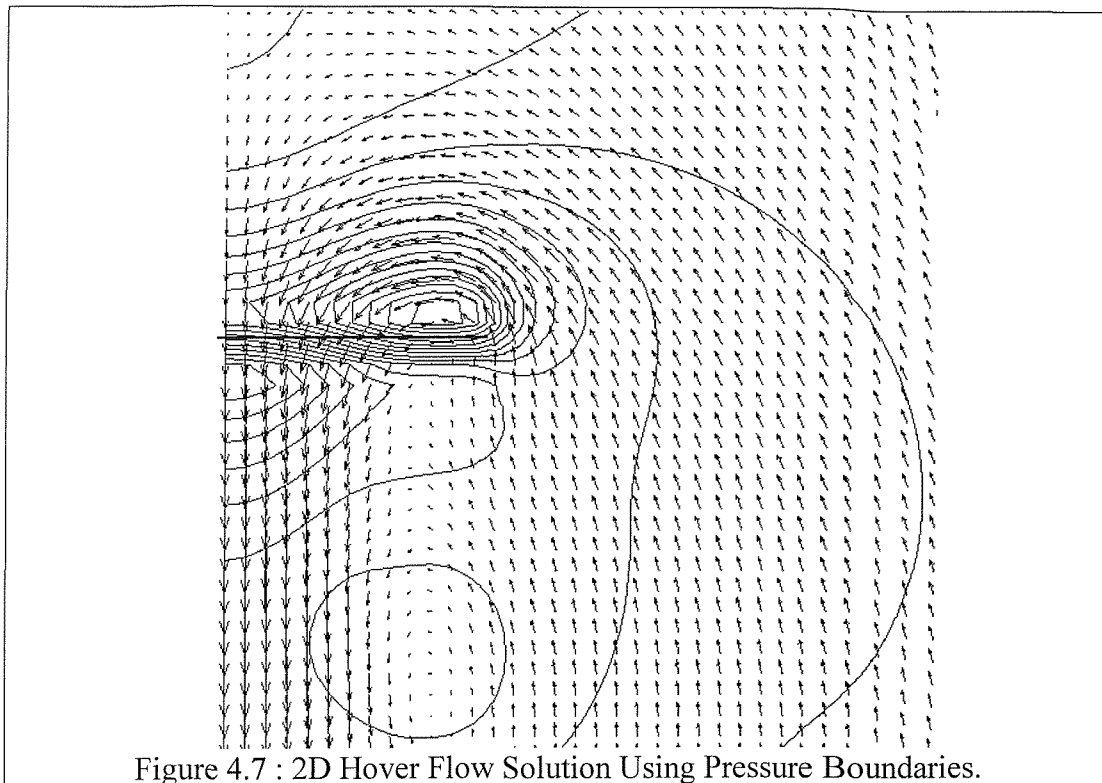


Figure 4.7 : 2D Hover Flow Solution Using Pressure Boundaries.

A mass flow boundary is used across boundaries at which the pressure is not known but the mass flow rate is. This is also known as a Neumann boundary condition and can be used in internal flow problems such as pipe networks.

All of the above three conditions require the flow to have a freestream velocity. There are established theories which give the flow solution of a helicopter hovering from actuator disc and annulus theory. Both of these use inviscid flow and are published in many references, for example Newman [4.1].

It would be possible to incorporate known flow values, found from actuator disc theory, into a CFD flow solution. The known values would have to applied at the boundaries using the Dirichlet condition.

It would be ill advised to use this method for anything other than the simplest flows; this would be wholly inaccurate for complex helicopter geometry being modelled in viscous flow. The user would require knowledge of blockage or drag exerted on the fuselage, which is one of the main outputs one would hope to yield from a CFD model.

The pressure and mass flow Neumann conditions outlined above also require precalculated values to be imposed at the boundaries. By the same argument this

would give a solution determined by the input values that may be inaccurate for the model being considered

#### 4.5 Theory of The New Boundary Condition

The existing Neumann boundary conditions require either the velocity or the pressure to be defined, the remaining variables are then found using the iterative calculation method. Any basic relationship between pressure and velocity is abandoned. One such pressure/velocity dependence is given in Bernoulli's Equation.

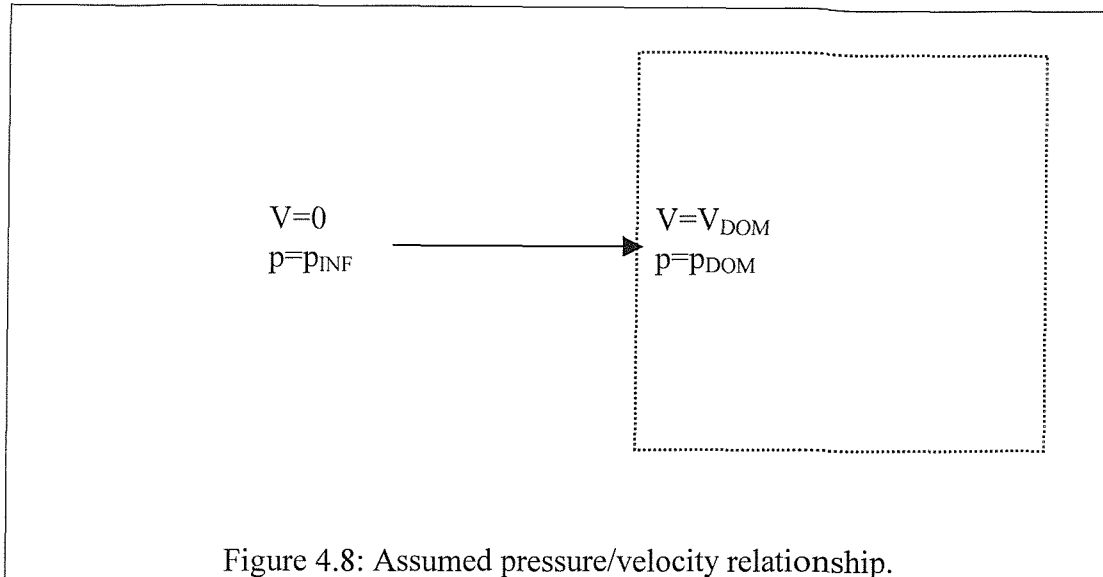
The new boundary condition leaves both pressure and velocity undefined but couples them using Bernoulli's equation. As the solver iterates, both the pressure and velocity vary and tend to a limit. This is achieved using the 'body forces' function within CFX 4.1 around the extremities of the domain. Forces are exerted on the fluid thus inhibiting the fluid flow out of and into the domain, these forces are proportional to the square of velocity. Using this method fluid can flow in and out of the domain but at the penalty of a pressure change.

The proof is outlined briefly below. It is assumed that at an infinite distance from the domain the fluid is at rest. At this distance the fluid also has a datum pressure  $P_{INF}$ , which is atmospheric pressure. As defined in Bernoulli's Equation as the fluid accelerates towards the domain the total pressure remains constant but the static pressure reduces as described in equation (4.6). In this equation  $V$  represents the fluid speed and  $P$  is the corresponding pressure.

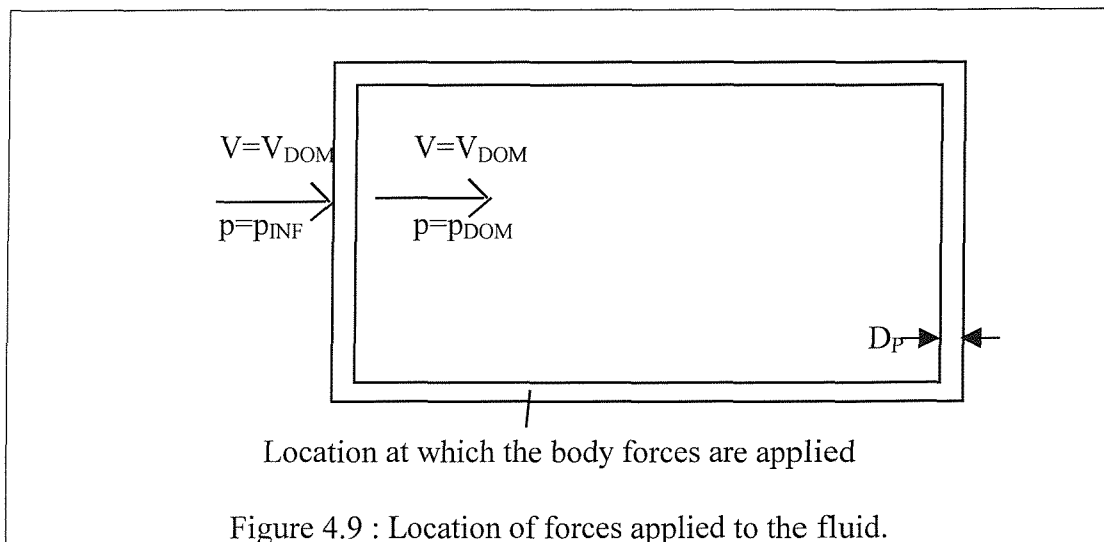
$$P_{INF} = p + \frac{1}{2}\rho V^2 \quad (4.6)$$

When the fluid enters the domain it must therefore have a lower pressure than the datum pressure, as described in equation (4.7).  $P_{DOM}$  is the pressure upon entry to the domain and  $V_{DOM}$  is the velocity upon entry to the computational domain. For the computational model  $P_{INF}$  is the datum pressure, which is set to zero. This is shown graphically in Figure 4.8, where the dotted line represents the domain boundary.

$$P_{DOM} = P_{INF} - \frac{1}{2}\rho V_{DOM}^2 \quad (4.7)$$



Unfortunately this pressure drop cannot be instigated upon entry into the domain when using CFX 4.1, since the fluid enters the extremity of the domain at the datum pressure and experiences a pressure change over a finite distance. Forces are applied to the fluid inside the cells around the periphery of the problem. As CFX uses a finite volume method these forces are added easily into the governing Navier-Stokes equations. Figure 4.9 shows the method by which this is achieved. The body forces are exerted upon the fluid at the periphery of the domain.



The derivation of the forces applied to induce the pressure drop is given below. The body forces function adds the term  $\bar{B}$  into the Navier-Stokes equations, as shown in equation (4.8), from [4.2]. This term can also be used to model buoyancy, centripetal or electrostatic forces. This term has units of force per volume.

$$\frac{\partial \rho \bar{V}}{\partial t} + \nabla \cdot (\rho \bar{V} \otimes \bar{V}) = \bar{B} + \nabla \cdot \sigma \quad (4.8)$$

The components of  $\bar{B}$  are specified in the CFX command module, the three components,  $B_x$ ,  $B_y$ , and  $B_z$  are defined, as in equation (4.9).  $u$ ,  $v$  and  $w$  are the velocity components.

$$\bar{B} = \begin{bmatrix} -B_x \cdot u \cdot |u| \\ -B_y \cdot v \cdot |v| \\ -B_z \cdot w \cdot |w| \end{bmatrix} \quad (4.9)$$

These body forces are exerted over a layer of cells with thickness  $D_p$ , as shown in Figure 4.9. Therefore the pressure drop as fluid enters the domain along the x axis is described in equation (4.10).

$$\Delta p = \text{Force} / \text{Area} = \text{Force} \cdot D_p / \text{Volume} = B_x \cdot u \cdot u \cdot D_p \quad (4.10)$$

Combining equations (4.7) and (4.10) we obtain values for  $B_x$ . In practice  $B_y$  and  $B_z$  are also defined with the same values in order to prevent large flows occurring tangential to the walls of the domain, as shown in equations (4.11) and (4.12).

$$B_x = B_y = B_z = \frac{\rho}{2D_p} \quad (4.11)$$

$$\bar{B} = \begin{bmatrix} -u \cdot |u| \cdot \frac{\rho}{2D_p} \\ -v \cdot |v| \cdot \frac{\rho}{2D_p} \\ -w \cdot |w| \cdot \frac{\rho}{2D_p} \end{bmatrix} \quad (4.12)$$

The coefficients  $B_x$ ,  $B_y$  and  $B_z$  are defined at all external boundaries to the problem, as indicated in Figure 4.9. Within CFX these body forces are defined as constant values throughout the peripheral blocks. Therefore it is necessary to place an individual block at every boundary. These blocks are described as ‘peripheral’ blocks, containing peripheral forces. The geometry is described in Section 4.6.3.

In summary the forces exerted on the fluid at the periphery of the model represent the forces required to accelerate the fluid to the inside of the domain from an infinite distance. The magnitude of these forces has been determined from Bernoulli’s Equation and are introduced into the model using the body forces function within CFX.

## **4.6 Verification of Boundary Conditions**

### **4.6.1 Introduction**

There are no analytical flow solutions of the viscous flow through a propeller or rotor, however actuator disc theory provides a solution for an inviscid flow. A model has been generated that will parallel an actuator disc as closely as computationally possible. The key measure of the accuracy of the model and effectiveness of the boundary conditions is a comparison of the thrust applied within the domain and the resulting momentum change, this is explained in more detail in the following sections.

A computational actuator disc was modelled using the CFD package CFX 4.1. There are many conceivable geometries that can be used to model an actuator disc. Even the simplest geometries provide many parameters that can be varied. A general geometry was selected as described in the next section. Certain parameters were varied in turn, for example, domain size, grid coarseness, fluid viscosity, domain shape, rotor size and thrust exerted.

### **4.6.2 Flow Solver**

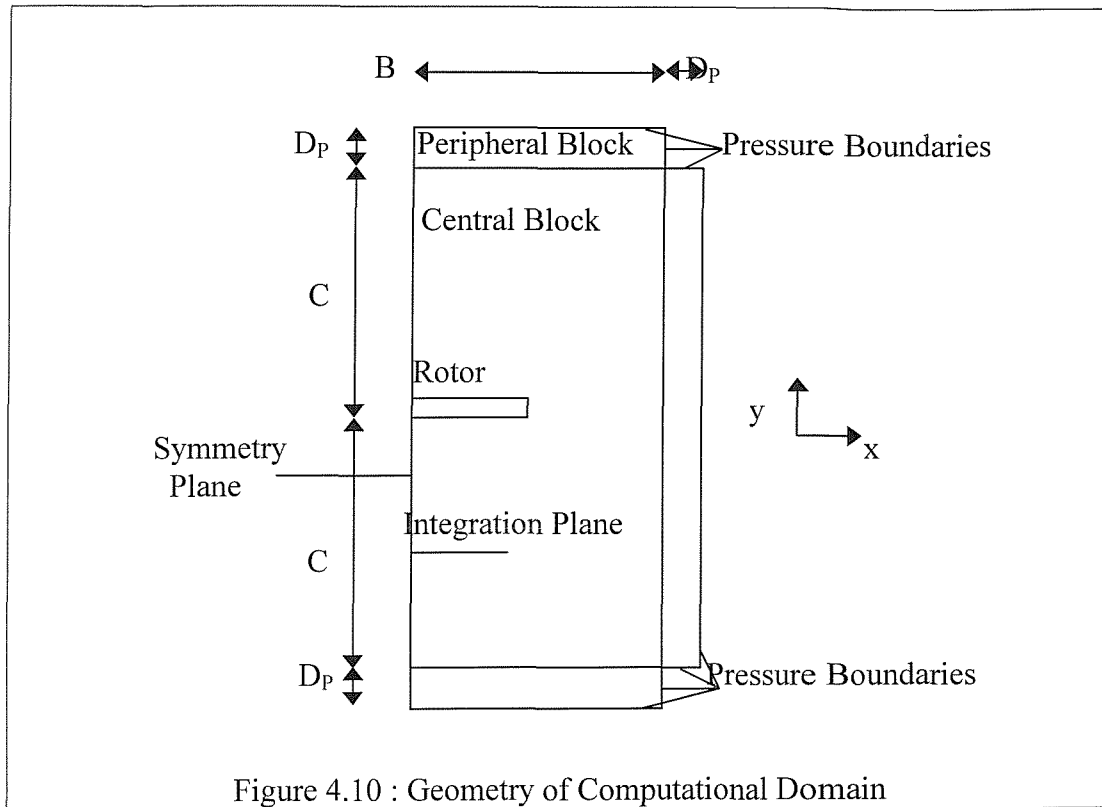
CFX 4.1 uses a finite volume method solution, therefore each block has to be divided into cells. The problem was simplified into two dimensions initially, where the beneficial effects are twofold. Firstly this reduces the number of velocity components to be determined from three to two, and secondly the number of cells within the domain can be reduced whilst maintaining the grid definition.

Since it was considered essential that the boundary conditions were verified initially, certain flow characteristics were ignored, namely, turbulence, temperature and compressibility.

### **4.6.3 General Geometry of Verification Model**

An example of the geometry is given in Figure 4.10. The three outer blocks have the additional force terms as described in the previous section. This problem is two dimensional in the z plane. The computational time and power required to solve each problem is halved by employing a symmetry plane. The principal dimensions of the problem are indicated on the diagram. The distance C is

measured from the edge of the central block to the mid-height of the rotor. The length  $B$  is the width of the central block in the  $x$  direction. The three peripheral blocks that provide the extra forces used identical thickness,  $D_p$ .



The method of subdividing the blocks of the domain into cells is shown in Figure 4.11. For this study all of the cells in the central block have identical size, or alternatively the edges of the block are divided uniformly. Therefore, the central block was subdivided using only two parameters,  $N_x$  and  $N_y$ .  $N_x$  divides the upper and lower peripheral blocks along their length.  $N_y$  divides the vertical peripheral block. The width of all three peripheral blocks are divided using the parameter  $N_p$ . The rotor is always at the midheight of the geometry.

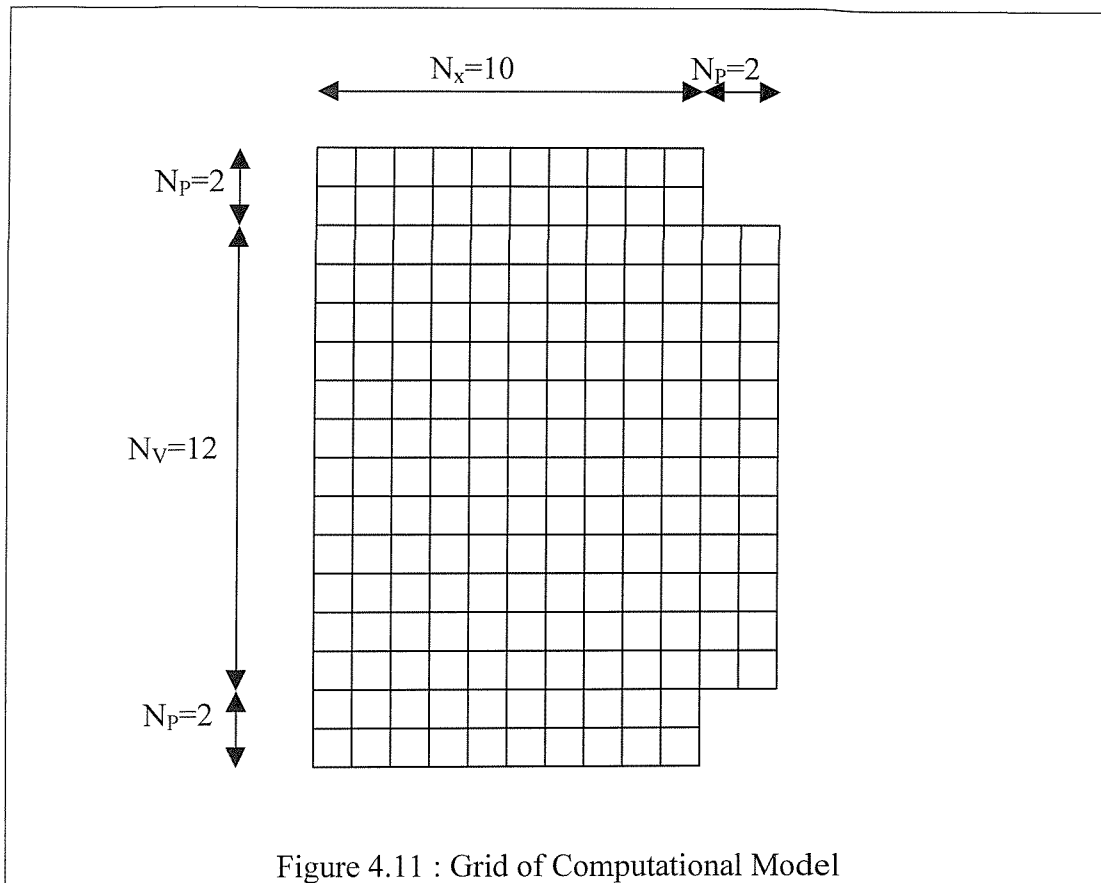


Figure 4.11 : Grid of Computational Model

#### 4.6.4 Evaluation of Flow Solution

Actuator disc theory for a helicopter in hover is relatively simple, the only variables being thrust, downwash velocity, disc area and air density. With any three of these variables known the fourth can be calculated. The CFD model uses a realistic value for air density ( $1.124 \text{ kg/m}^3$ ). The 2D rotor has a radius of 1m, and despite the two dimensional nature of the model the rotor had a depth of 1m in the z direction. All variables are invariant in the z direction, the rotor therefore has an area ( $A_R$ ) of  $1\text{m}^2$ . A downwash velocity ( $V_2$ ) is the third variable defined, which is equivalent to the fluid velocity within the downwash at an infinite distance from an actuator disc. From these three values CFX calculates the total thrust applied to the fluid at the disc using actuator disc theory. The relationship between these variables is given in equation (4.13). CFX then converts this thrust into equivalent body forces that are distributed evenly amongst the relevant cells as shown in Figure 4.5.

$$T_{DEF} = \frac{1}{2} \cdot \rho \cdot A_R \cdot V_2^2 \quad (4.13)$$

In order to verify the physics of the flow the momentum flux needs to be determined. Actuator disc theory dictates that the downwash has greatest

momentum at an infinite distance from the rotor. In the CFD model we have to choose an arbitrary plane at which to integrate across in order to find a value of maximum momentum flow. The plane chosen was at the midpoint between the rotor and lower edge of the domain. It is assumed that the fluid travelling through this plane was initially at rest, hence equation (4.14) yields a value for the apparent thrust that the fluid experiences. The integration is performed across the cross section of the downwash.  $v$  is the velocity component acting parallel to the thrust of the disc.

$$\overline{T_{APP}} = \rho \int_{A_{DW}} v^2 dA \quad (4.14)$$

The thrust defined at the disc and apparent thrust in the downwash can be compared as shown in Equation (4.15). This provides a quantitative measure of the how well the overall flow solution satisfies Newton's 2<sup>nd</sup> Law.

$$EF\% = \left( \frac{T_{APP}}{T_{DEF}} - 1 \right) * 100 \quad (4.15)$$

As can be seen from Figure 4.10 and Figure 4.11, even the simplest model has many parameters that can be varied. To determine the effect of these, each is varied in turn whilst holding the others constant.

#### 4.6.5 Parameters Varied

Various parameters within the general geometry were varied to determine the effect on the flow solution and validity of the boundary condition. These parameters were disc depth, number of cells in peripheral block, peripheral block thickness, thrust, grid coarseness, domain size relative to disc, domain shape, overall domain size, and fluid viscosity.

##### 4.6.5.1 Effect of Peripheral Block Depth

The depth of the peripheral blocks,  $D_p$ , as shown in Figure 4.10, can be set to any positive value. The 'body forces' or peripheral forces exerted upon the fluid in the outer blocks are adjusted automatically by CFX to be consistent with the block thickness. This is important as these forces have units of force/volume.

For these cases the rotor radius is 1m and the total thrust defined is 56.2N. The grid is relatively coarse, 30 cells horizontally and 60 cells vertically. The number

of cells in the thickness of the peripheral blocks remains 1 throughout the four cases. Only the thickness of the peripheral block varies. In order to minimise viscous forces, the dynamic viscosity is set as  $1.8 \times 10^{-10} \text{Ns/m}^2$  (i.e.  $10^{-5}$  times less than typical value for air).

The results are outlined below in Table 4.2. The variation of the vertical velocity component  $V$  is plotted in Figure 4.12. The velocity is considered at the plane of  $y = -1.5\text{m}$ ; this plane was chosen as it is at the midpoint between the disc and the domain periphery. The rotor has a span of  $1\text{m}$  and the domain extends  $3\text{m}$  laterally, vertically above and below the rotor. Variation of the flow pattern downstream of rotor can be seen in Figure 4.12.

Peripheral Block Thickness (m)	0.5	0.25	0.125	0.05
Convergence	No	Yes	Yes	Yes
Thrust Defined (N)	56.2	56.2	56.2	56.2
Thrust Apparent(N)	57.7	57.8	57.8	59.3
EF%	+2.6%	+2.8%	+2.8%	+5.5%

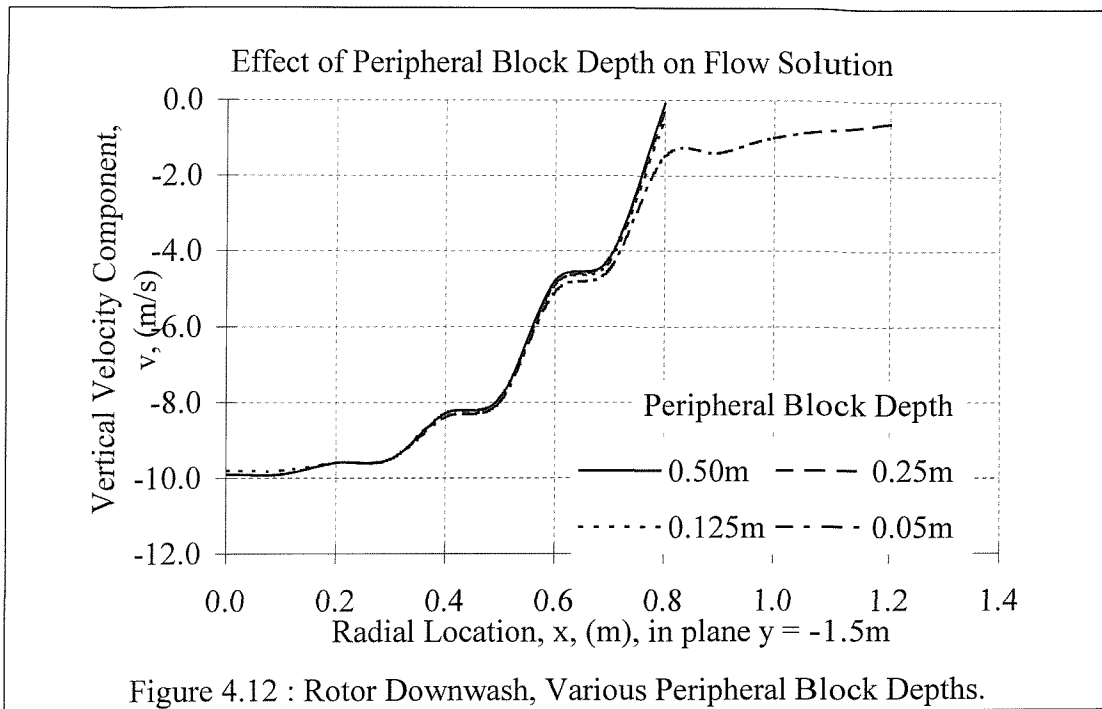
Table 4.2 : Effect of Peripheral Block Thickness

The flow patterns exhibit all the salient features of a classical actuator disc. These are acceleration of the flow both upstream and downstream of the disc and a sharp change in the pressure across the disc. For a quantitative evaluation of the disc, the momentum in the downwash is calculated and compared to the thrust exerted at the disc. All four cases show agreement to within two and six percent.

This study reveals that wide peripheral blocks are required to give a flow solution which corresponds to the physical problem. The variation of induced velocity is similar for the first three cases but markedly different for the fourth case. The flow solution has not converged using the widest outer blocks. This may be a result of the cells within these blocks having large aspect ratios.

Figure 4.12 also shows a somewhat disconcerting velocity distribution which does not exhibit the smooth curve that would be expected. This can be attributed to grid coarseness as demonstrated in Section 4.6.5.4. The grid was kept coarse for

these cases to save both computing time and computer resources during the validation process.



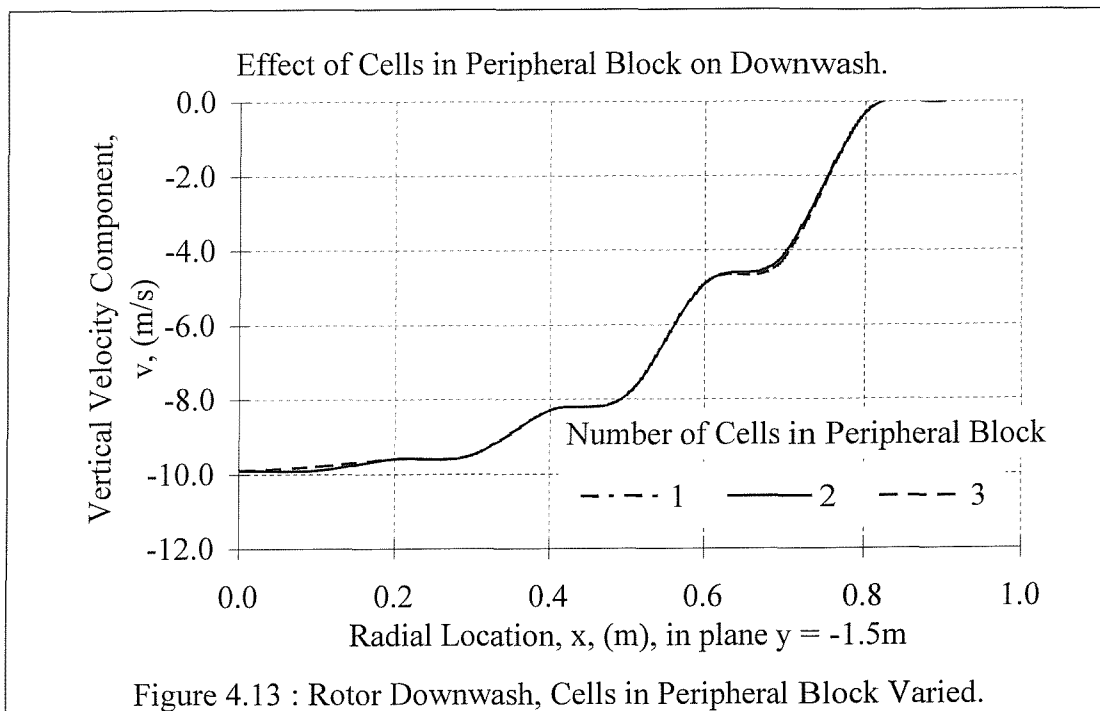
#### 4.6.5.2 Effect of Number of Cells in Peripheral Blocks.

Three solutions are presented, with only the number of cells across the depth of the peripheral blocks,  $N_p$ , is varied. An arbitrary geometry and grid has been considered, identical to the grid used in the previous section. The viscosity is defined as an artificially small value to minimise viscous forces. In all three cases the thrust defined at the rotor is 56.2N. The peripheral blocks have a thickness of 0.25m.

Cells Across Depth of Peripheral Blocks.	1	2	4
Depth of Peripheral Block (m)	0.25	0.25	0.25
Thrust Defined (N)	56.20	56.20	56.20
Thrust Apparent(N)	57.8	57.8	57.6
EF%	2.8%	2.8%	2.5%

Table 4.3 : Effect of Number of Subdivisions in Peripheral Blocks

The variation of downwash at the integration plane can be seen in Figure 4.13. The difference between the three cases is negligible. We can therefore conclude that the number of cells in this region has a very limited influence on the flow solution.



#### 4.6.5.3 Effect of Total Thrust Exerted

Two cases have been considered using various thrusts, with all the other variables in the geometry remaining constant. As mentioned previously, this study was instigated to verify that the boundary conditions worked for various thrusts and resulting downwash velocity. The parameter  $V_2$  takes two values, 5m/s and

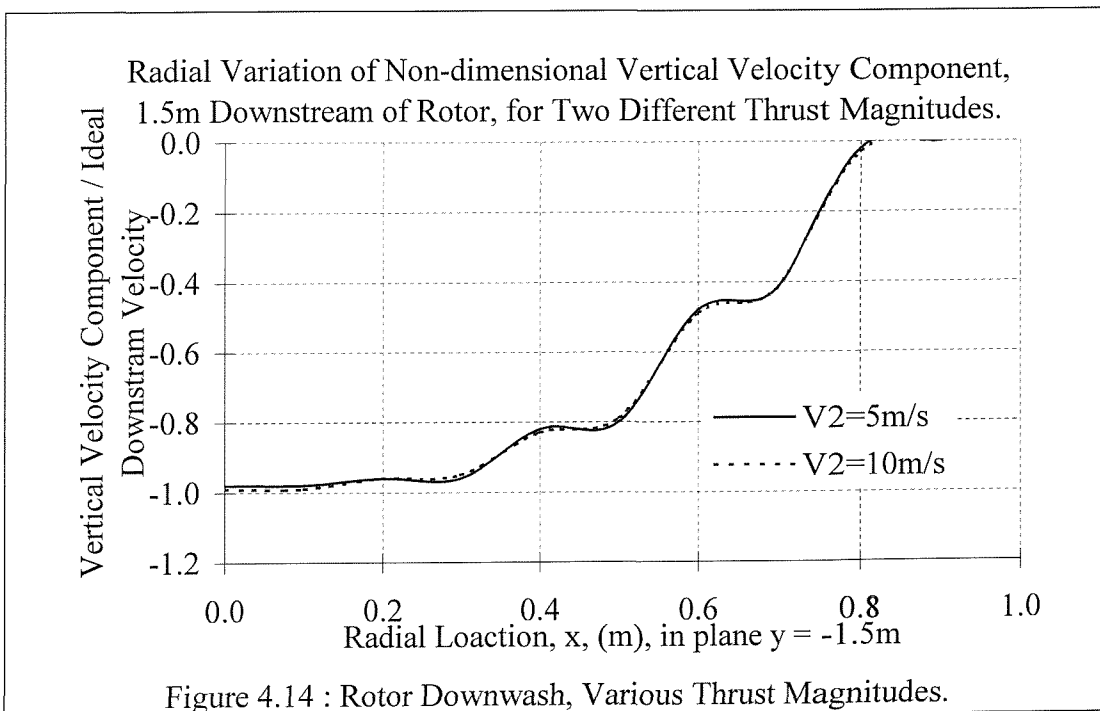
10m/s. The resulting total thrusts are then found and exerted evenly across the disc.

Thrust Defined (N)	14.1	56.2
$V_2$ (m/s)	5	10
Thrust Apparent (N)	14.4	57.8
EF%	+2.7%	+2.8%

Table 4.4 : Effect of Total Thrust

The resulting momentum in the downwash has been calculated for each thrust. As shown in the Table 4.4, in both cases these are slightly larger than the defined thrust. More importantly, in both cases the defined thrust and the apparent thrust vary by similar ratios. The variation of downwash velocity at the ‘integration plane’ can be seen in Figure 4.14. The velocities have been non-dimensionalised by dividing by  $V_2$ . The graph shows that non-dimensional velocities are almost identical.

This clearly demonstrates that the boundary conditions can be used for a variety of thrusts and induced velocities.



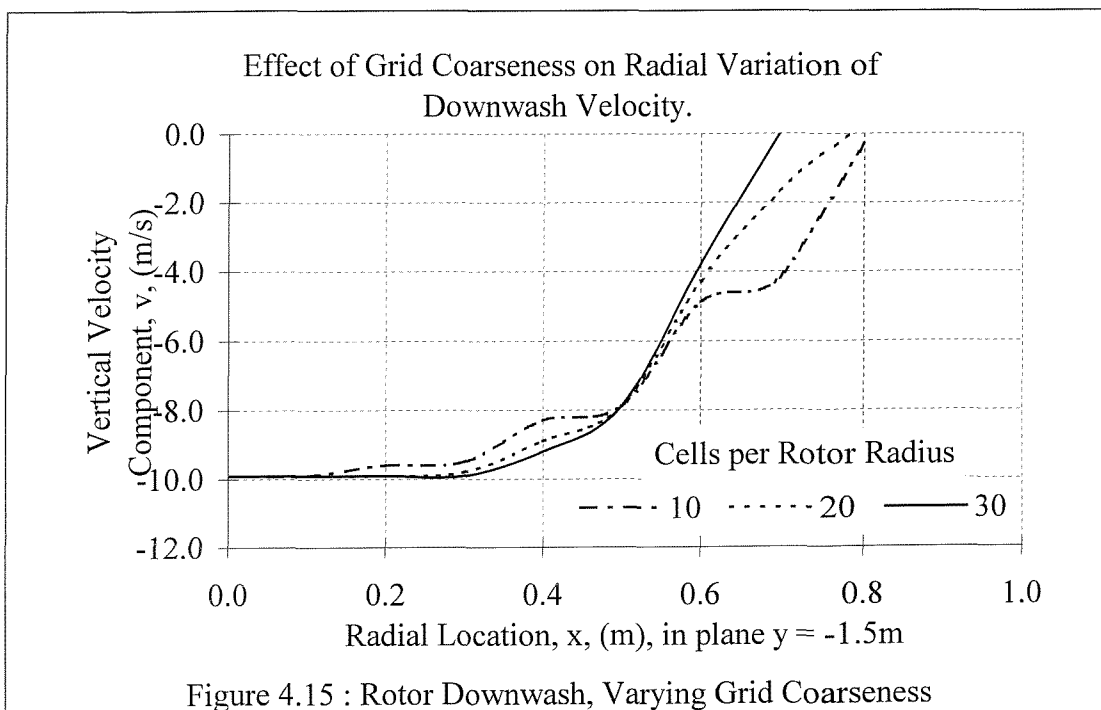
#### 4.6.5.4 Effect of Grid Coarseness

The geometry of the rotor and domain were kept constant whilst only the cell size was varied. In each case the cells remain square throughout the central block. The peripheral blocks are subdivided such that these cells are as close to square and the same size as the central block as is possible. Three different cell sizes have been used, which give 10, 20 and 30 cells across the span of the rotor.

Cells per Rotor Radius	10	20	30
Total Cells in Domain	30 * 60	60 * 120	90 * 180
Thrust Defined (N)	56.2	56.2	56.2
Thrust Apparent (N)	57.8	57.2	57.4
EF%	+2.8%	+1.8%	+2.2%

Table 4.5 : Effect of Grid Coarseness

The induced velocity across the downwash for the three cases is shown in Figure 4.15. It can be seen clearly that as the number of subdivisions is increased the flow variation becomes smoother. As with the other cases the defined thrust and apparent thrust are only fractionally different. The number of grid cells determines the shape of the downwash, not the momentum contained within it.



#### 4.6.5.5 Effect of Domain Size

For this study the rotor radius and cell size were kept constant but the dimensions of the domain were increased. Graphs of both the downwash velocity and the downstream pressure variation are shown in Figure 4.16 and Figure 4.17. Table 4.6 displays the parameters used; dimensions B, C and  $D_p$ , as defined in Figure 4.10 are varied. The numbers of subdivisions in the domain are varied proportionally.

Cells in Domain	60 * 120	80 * 160	120 * 240
Depth of Peripheral Blocks, ( $D_p$ ) (m)	0.25	0.33	0.5
Cells in Peripheral Block. ( $N_p$ )	1	5	8
Domain Height (2C) (m)	6	8	12
Domain Width (B) (m)	3	4	6
Thrust Defined ( $T_{DEF}$ ) (N)	56.2	56.2	56.2
Convergence	Yes	Yes	No
Thrust Apparent ( $T_{APP}$ ) (N)	57.2	57.4	55.4
EF%	+1.8%	+2.1%	-1.4%

Table 4.6 : Effect of Domain Size.

The first two flow solutions converged, however the third case did not converge to a mass source residual of  $10^{-6}$  kg/s. In spite of this the results have been included, but should be treated accordingly. Figure 4.16 shows the downwash velocity distribution. The solutions that have converged are very similar.

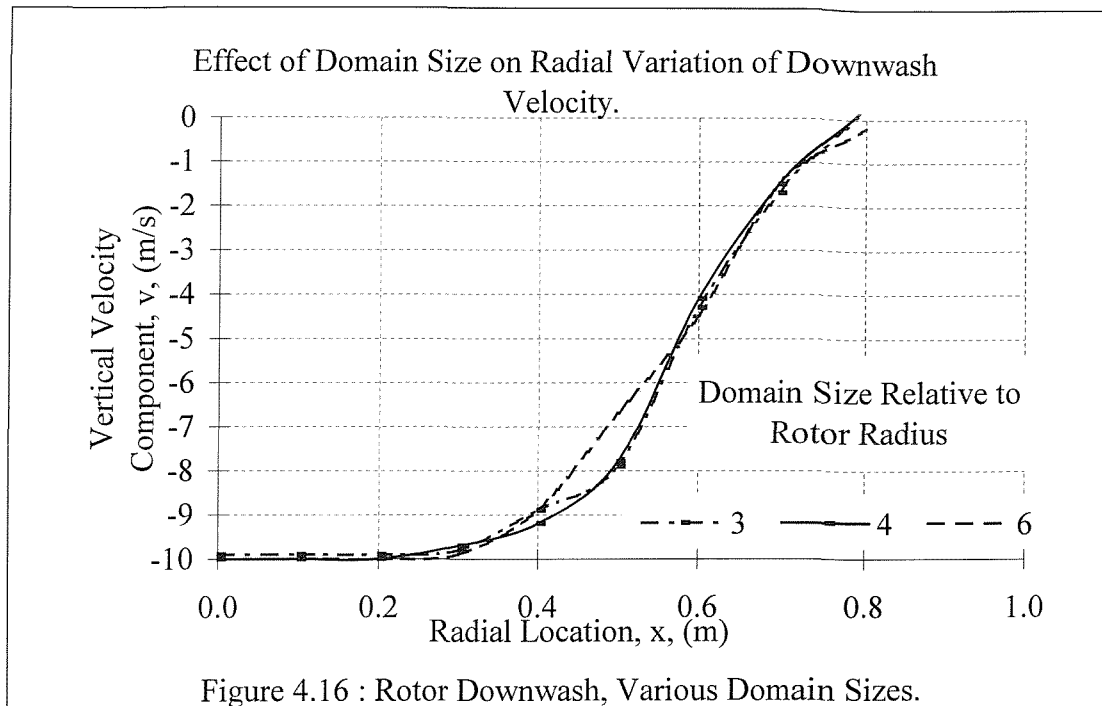
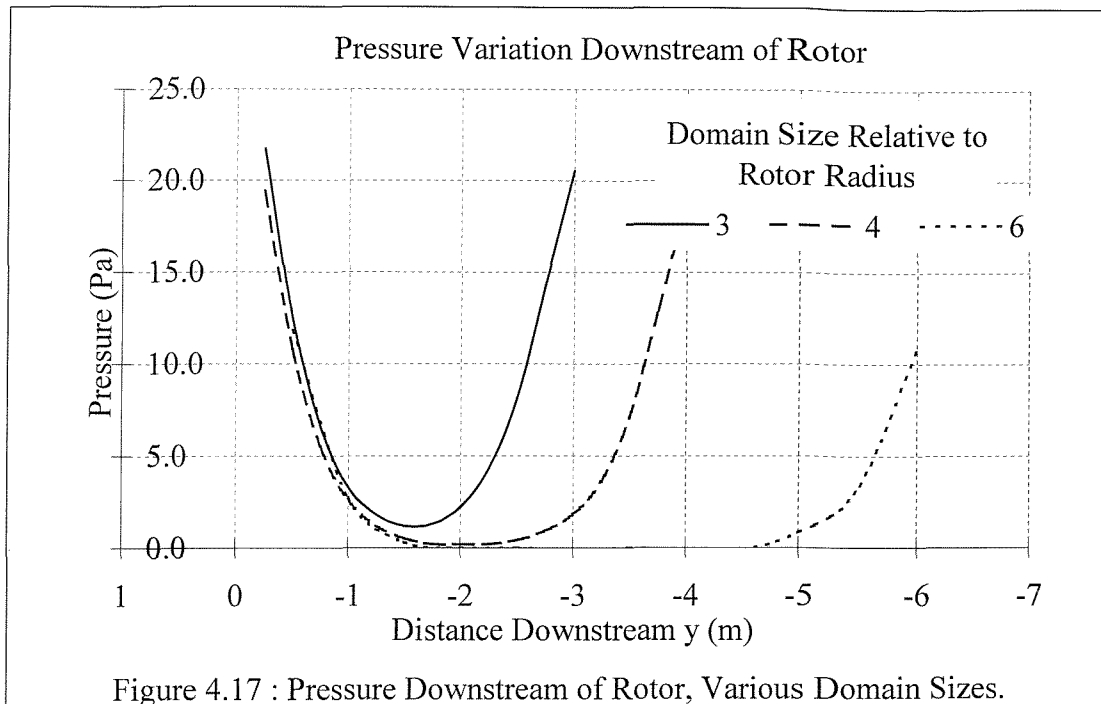


Figure 4.16 : Rotor Downwash, Various Domain Sizes.

Figure 4.17 shows the pressure variation along the negative  $y$  axis. It should be noted that in the cases of the two larger domains there is a complete pressure recovery downstream of the rotor. The pressure then rises again as the fluid reaches the boundary. In the smaller case the fluid never reaches zero pressure downstream of the rotor.

We can conclude from this that if a complete pressure recovery is required, a rotor of radius 1m must be at least 4m from the domain boundary. This complete pressure recovery in the larger cases also results in the downwash velocity reaching a maximum of 10.0m/s, whereas it only reached 9.9m/s for the smaller domain.



#### 4.6.5.6 Effect of Domain Shape

The purpose of these solutions was to determine whether the overall shape of the computational domain would influence the result in any way. A previous flow solution for a rectangular domain was compared to a semicircular domain. With the addition of a vertical symmetry boundary the domain was, in essence, circular.

A diagram of the circular domain is presented in Figure 4.18. It should be noted that in both cases, the peripheral blocks have the same thickness and number of subdivisions. Four central blocks in the circular case replace the main block in the rectangular domain. At the location of the rotor in the circular domain the grid sizing is identical to that of the rectangular domain. This enables the rotor in both cases to be identical.

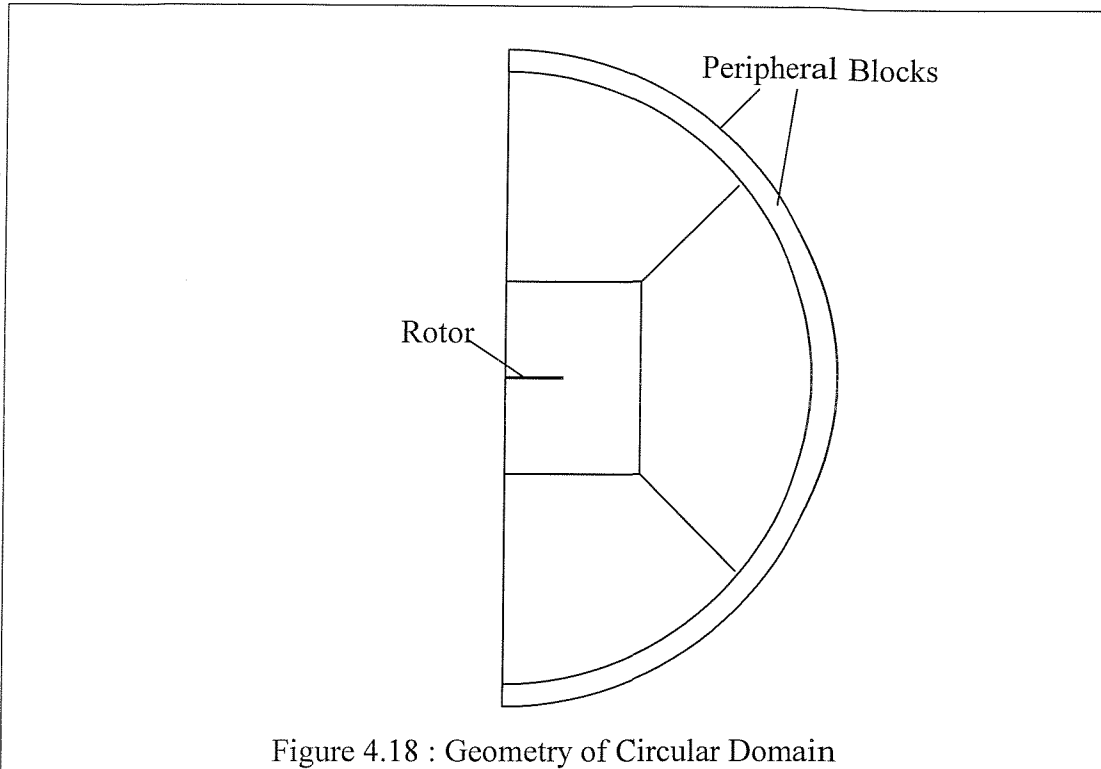


Figure 4.18 : Geometry of Circular Domain

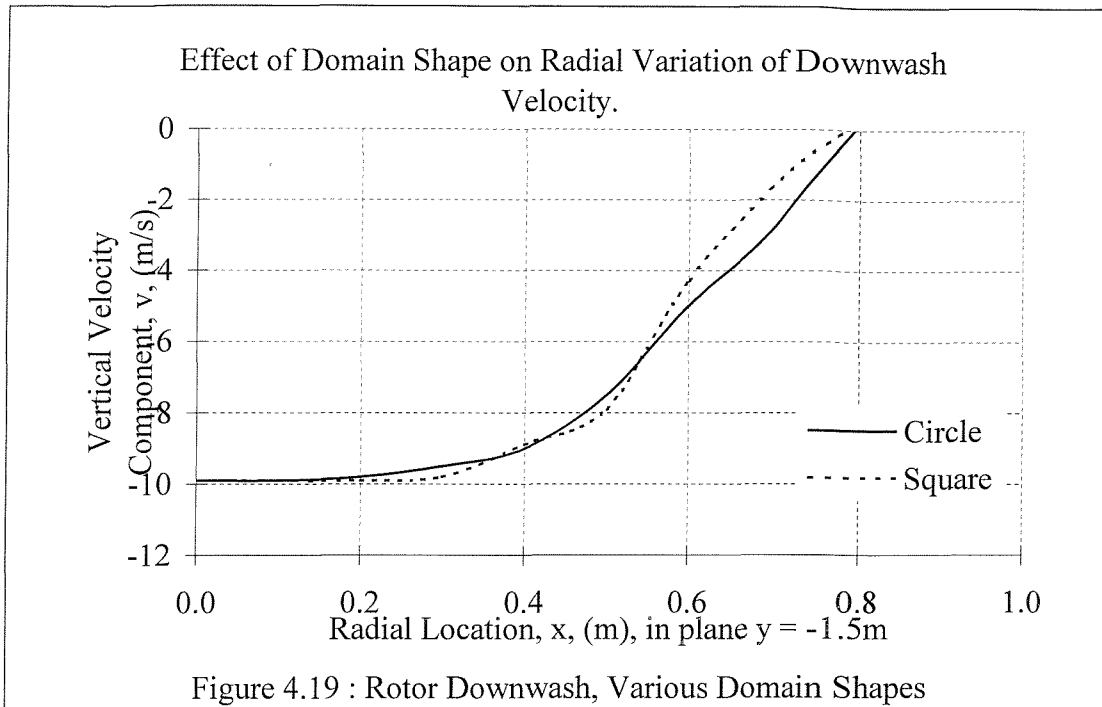
A summary of the geometries and output are presented in Table 4.7.

Domain Shape	Circle	Square
Thrust Defined (N)	56.2	56.2
Thrust Apparent (N)	56.7	57.2
Error (EF)	+0.9%	+1.8%

Table 4.7 : Effect of Domain Shape

Figure 4.19 shows the downwash velocity at the plane  $y = -1.5\text{m}$ . The two flow solutions are similar but not identical. The discrepancies are attributable to the difference in grid cell shape and size at this location. However, the momentum within the downwash, in both cases, is similar to both the defined thrust to and each other.

From this comparison it is possible to conclude that the domain shape does not significantly affect the solution.



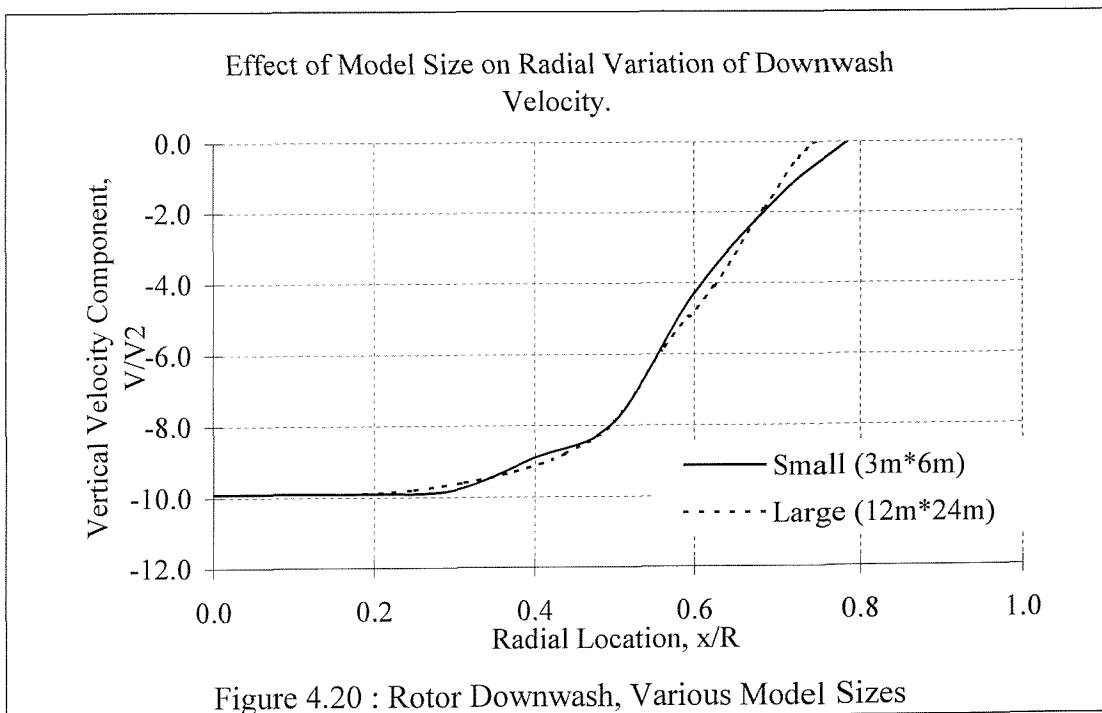
#### 4.6.5.7 Effect of Overall Model Size

For the studies so far the flow solutions have been derived for domains of dimension 6m vertically and 3m horizontally, the rotor having a 1m radius. For this study the whole domain and cell size is increased by a factor of 4. The two solutions are then compared to determine the effects of scaling. Table 4.8 gives a summary of the domain geometries; it should be noted that whilst the dimensions vary the subdivisions remain constant. The rotor model is now larger and therefore the rotor thrust is scaled accordingly.

Rotor Radius (m)	1	4
Domain Width (B) (m)	3	12
Domain Height (2C) (m)	6	24
No cells/radius	20	20
Cells in Domain	60 * 120	60 * 120
Thrust Defined $T_{DEF}$ (N)	56.2	224.8
Thrust Apparent $T_{APP}$ (N)	57.2	227.5
EF%	+1.8%	+1.2%

Table 4.8 : Effect of Overall Model Size

Figure 4.20 shows the downwash velocity at the plane  $y = -1.5\text{m}$  for the smaller case and  $y = -6.0\text{m}$  for the larger case. The radial location has been non-dimensionalised with respect to the rotor radius. The distributions are similar but not identical, although the momentum in the downwash only varies by 0.6%. The results indicate that the flow solutions can be scaled correctly when this boundary condition is employed.



#### 4.6.5.8 Effect of Fluid Viscosity

The flow solver is capable of using various fluid viscosities, either laminar or turbulent. The three cases below all used the laminar flow option but varied the viscosity. Table 4.9 shows the values of viscosity. The first solution uses a negligible viscosity, thus making the model as close to an actuator disc as possible. The second case uses a realistic value for air, and the final solution uses a value that is ten times the realistic value. The fluid domain used is 6m by 3m. In all parts of the domain the grid contains 20 cells per metre. The peripheral blocks are 0.25m thick.

Thrust Defined $T_{DEF}$ (N)	56.2	56.2	56.2
Viscosity ( $Ns/m^2$ )	$1.79*10^{-10}$	$1.79*10^{-5}$	$1.79*10^{-4}$
Thrust Apparent $T_{APP}$ (N)	57.2	57.2	57.2
EF%	+1.8%	+1.8%	+1.8%

Table 4.9 : Effect of Viscosity

The change in viscosity made no discernible difference to the solution. The vertical velocity component at the measurement plane was identical for all three flow solutions. We can conclude that laminar viscosity makes negligible difference for this problem.

#### 4.6.5.9 Effect of Number of Cells in Disc Depth

An actuator disc exerts thrust upon the fluid over the area of a disc. However this is not possible to model computationally using a finite volume based flow solver. The thrust within the model is exerted upon the fluid over a finite volume and hence the modelled disc has a depth.

To ensure that the model corresponds to the disc theory it is desirable to keep the finite height as small as possible. The three cases below use identical geometry but the number of grid cells that the thrust is spread over vertically is varied from one to three. The rotor model is shown in Figure 4.5. The fluid domain used is 6m by 3m. In all parts of the domain the grid contains 20 cells per metre. The peripheral blocks are 0.25m thick. A negligible viscosity has been used ( $1.8*10^{-8}Ns/m^2$ ).

Vertical Cells over Depth of Disc ( $N_v$ )	1	2	3
Thrust Defined $T_{DEF}$ (N)	56.2	56.2	56.2
Convergence	No	Yes	Yes
Thrust Apparent $T_{APP}$ (N)	-	57.2	57.2
EF%	-	+1.8%	+1.8%

Table 4.10 : Effect of Vertical Cells over Depth of Disc.

The flow solver diverged for the first case that uses one vertical grid cell over which to spread the thrust forces. The CFX solver does not indicate why the solution diverged but it is probably due to resolving excessive pressure gradients numerically.

The other cases that use two and three vertical cells give identical momentum and velocity variations within the downwash. It should however be noted that the second case required more iterations to achieve the convergence limit than the solution using three vertical cells.

#### 4.6.6 Detailed Analysis of Momentum and Power

This analysis was performed using the information found from Section 4.6.5 in order to model a disc that would match the physical problem as closely as possible. Specific attention was paid to ensure that the grid cells were fine enough, the boundaries were sufficiently far from the disc and that the peripheral blocks were such that the solution would converge efficiently.

The geometry of this problem was chosen such that the rotor would be sufficiently far from the boundary that there would be a complete pressure recovery in the downwash. The grid cells are also small to resolve the flow in great detail.

The rotor radius is 1m and there are 40 grid cells across its span. All the boundaries are 4m from the rotor. Within the central block the grid cells are no longer square but rectangular with aspect ratio 0.75. This enables the rotor to have 40 cells across its span without a prohibitively large total number of cells for the flow solver. The outer blocks are 0.33m thick and contain six cells across this thickness. The viscosity used was  $1.7 \cdot 10^{-10} \text{Ns/m}^2$ .

The flow solution converged successfully and is shown in Figure 4.21. Figure 4.21 shows qualitative variations of velocity, depicted with vectors and pressure shown by contours. The location of the disc can be determined by the sharp pressure variations. This graph clearly displays all the flow characteristics of an actuator disc, namely the pressure drop upwind of the disc, the sharp pressure step across the disc and high pressures just downwind of the disc.

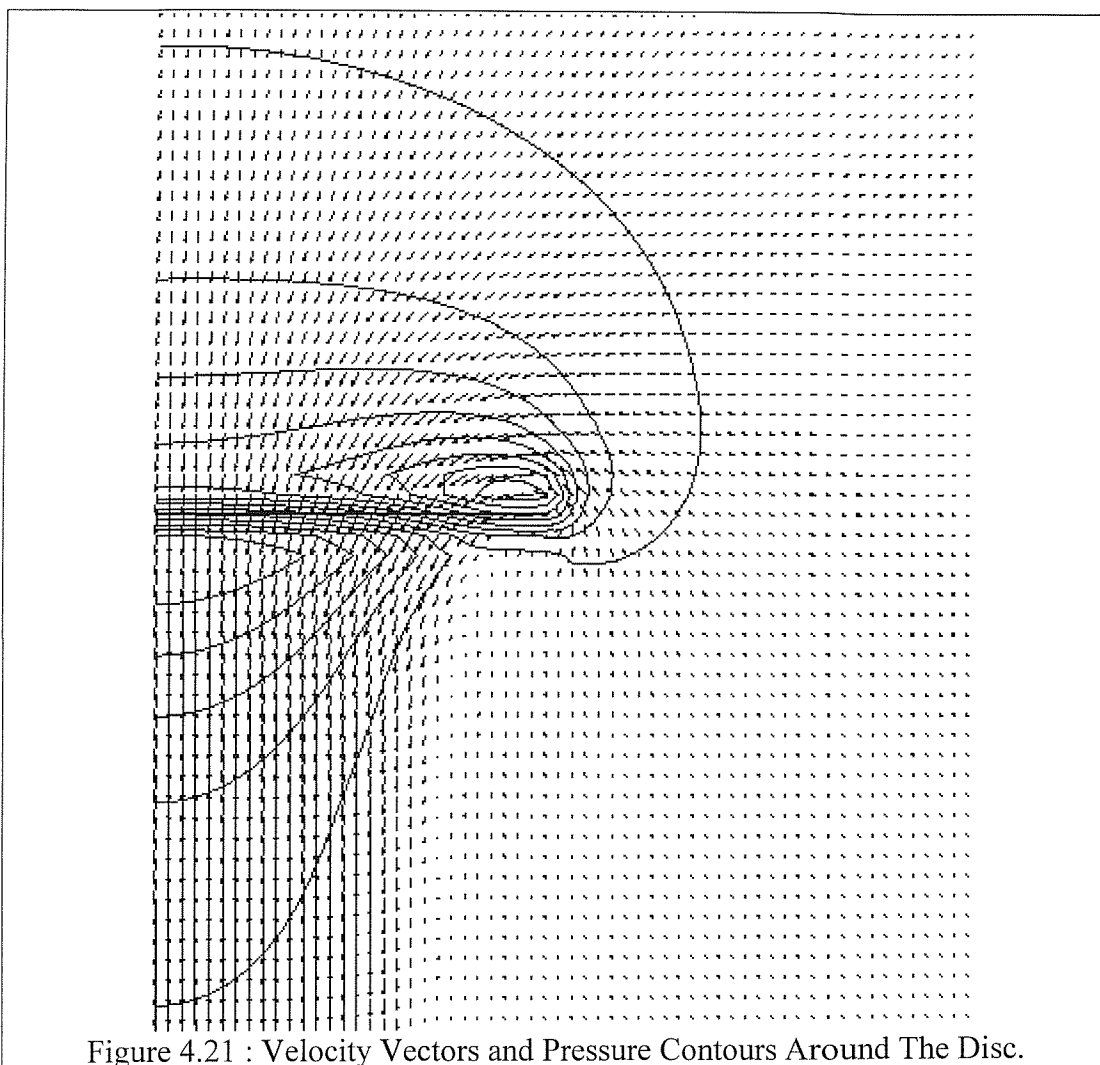


Figure 4.22 shows the downwash velocity along the axis  $x=0$  or symmetry plane;  $y=0$  corresponds to the disc,  $y= -4\text{m}$  corresponds to the horizontal lower boundary of the central block. It can be seen that the flow continues accelerating downstream of the disc and reaches a maximum at  $y= -1.5\text{m}$ . The flow remains at this speed until  $y=-2.5\text{m}$ , after which the flow decelerates as it approaches the boundary. The maximum flow velocity achieved is  $10\text{m/s}$ , which corresponds exactly to actuator disc theory.

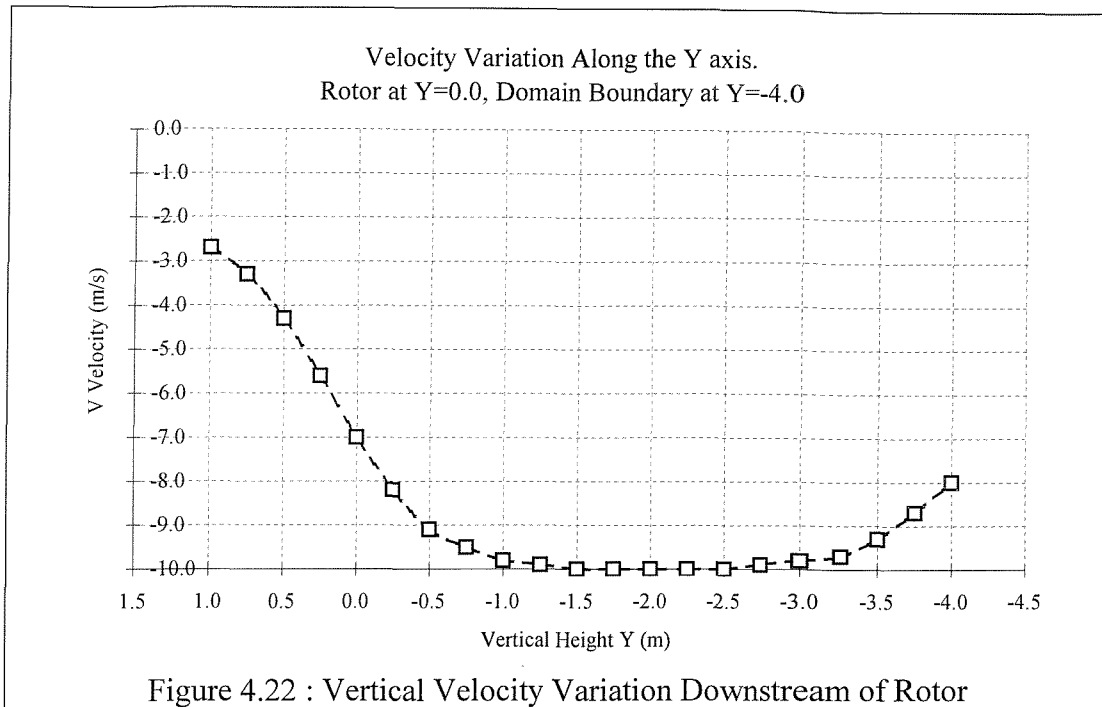


Figure 4.23 shows the pressure variation along the symmetry plane. There is a large step in the pressure at  $y=0$ , which corresponds to the forces exerted by the disc itself. Downstream of the disc the pressure remains positive, except at  $y=-1.5\text{m}$  where the pressure reduces to zero. The pressure remains zero until  $y=-2.5\text{m}$ , at which point it rises as the boundary is approached.

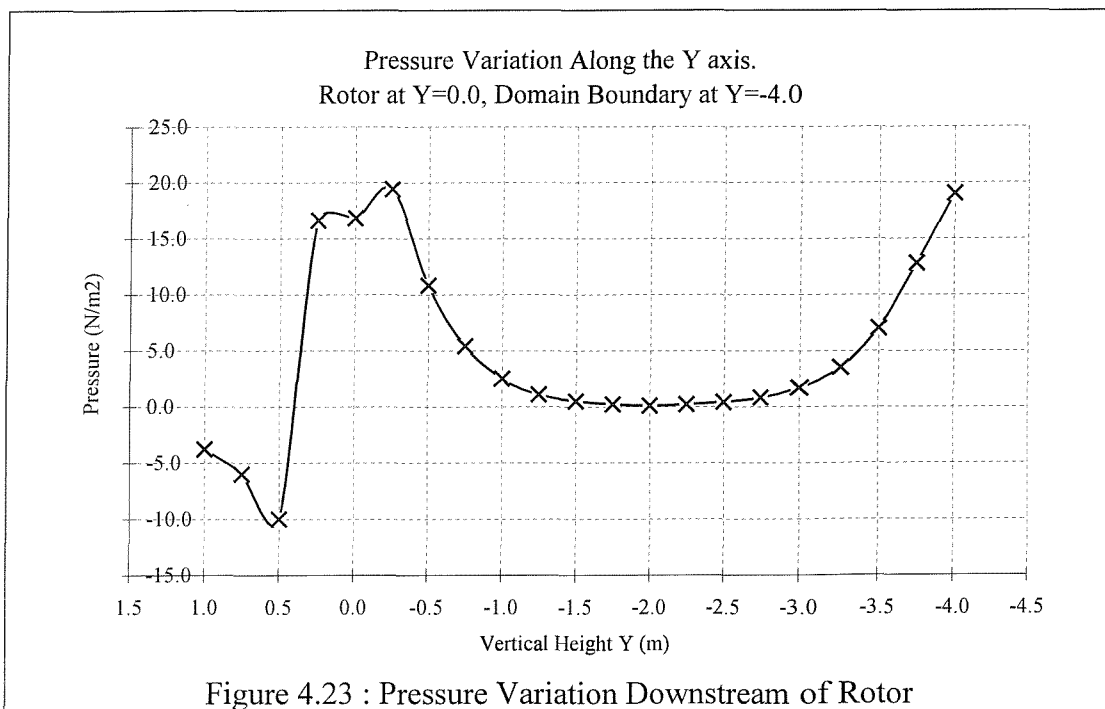


Figure 4.24 shows the vertical velocity component  $v$ , at various horizontal planes. This again displays the fact that the downwash velocity is greatest across the plane  $y=-2\text{m}$ . Table 4.11 shows the momentum across each of these planes.

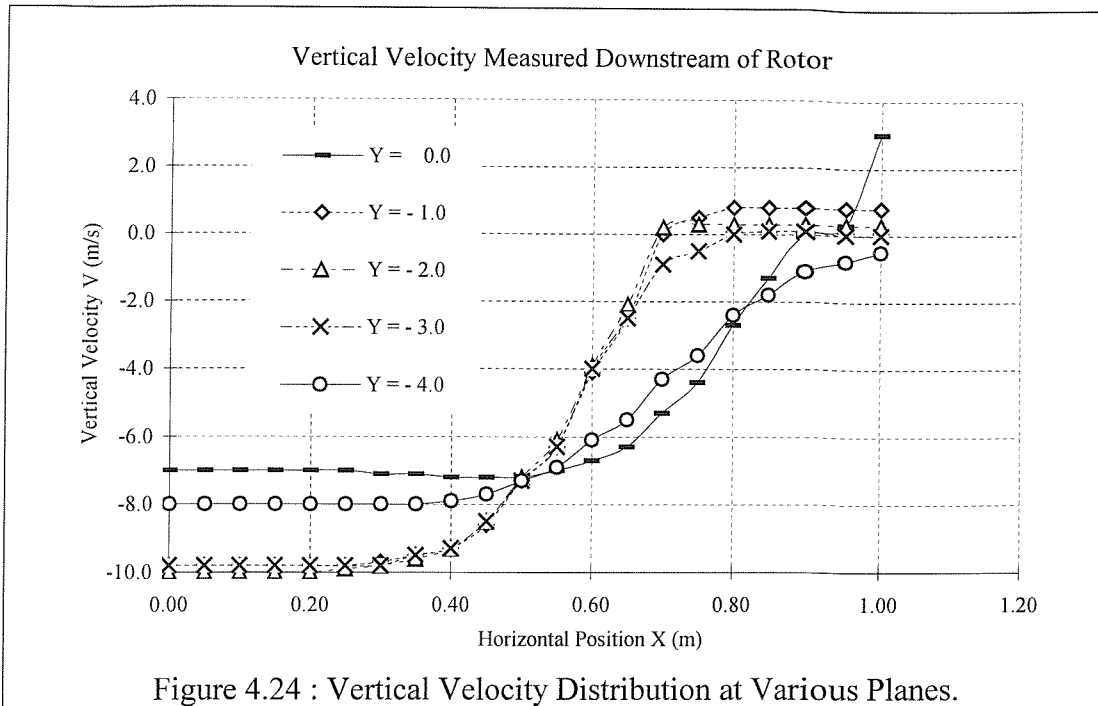


Figure 4.24 : Vertical Velocity Distribution at Various Planes.

y(m)	0	-0.5	-1.0	-2.0	-3.0	-4.0
Apparent Thrust T <sub>APP</sub> (N)	40.3	52.6	55.7	56.5	55.7	45.8
EF%	-28.3%	-6.3%	-0.8%	0.5%	-0.9%	-18.5%

Table 4.11 : Momentum Variation Downstream of Rotor.

As can be deduced from Table 4.11, the greatest downwash momentum occurs at the plane  $y = -2$ ; this has only a 0.5% discrepancy from the thrust defined at the disc.

The power exerted at the disc can be calculated using the relationship given in equation (4.16).

$$Power = \sum Force * v = \iint \Delta p \cdot v \cdot dA_R = \Delta p \iint v \cdot dA_R \quad (4.16)$$

This can be compared to power prediction from actuator disc theory as shown below in equation (4.17)

$$EP = \frac{PowerModel}{PowerActuatorDisc} = \frac{\Delta p \iint v \cdot dA_R}{2 \cdot \rho \cdot V_1^3 \cdot A_R} = \frac{\Delta p \iint v \cdot dA_R}{\frac{1}{4} \cdot \rho \cdot V_2^3 \cdot A_R} \quad (4.17)$$

For this model the power exerted at the disc is 303 Watts, and the theoretical power is 281 Watts. Thus EP is 1.08 or 7.8%. This discrepancy is caused by the

non-uniform induced velocity through the rotor. The idealised actuator disc does not predict this.

## **4.7 3D Rotor Model**

### **4.7.1 Introduction**

The previous sections within this chapter have validated the rotor model and verified that the power exerted at the rotor is consistent with the thrust. This section considers more specific models which correspond closely to a helicopter rotor. The data from these rotor models will be carried forward to studies considering flight over a ship's flight deck.

The thrust models described below do not model the rotor blades themselves but the forces exerted on the fluid, as described in Section 4.3.1. The presence of three dimensions allows more intricate thrust variations to be defined, whereas previously the thrust per unit area has been constant. Two models are considered to define radial variation of vertical and swirl forces.

The first model described as the 'constant thrust model' uses a constant thrust across the whole area of the rotor blade. This model is simple and provides an easy comparison with actuator disc theory.

The second model is described as the 'blade element thrust model'. The vertical thrust exerted on the fluid per unit area is obtained from a blade element analysis. Swirl forces created by the blade drag are exerted on the fluid in a horizontal direction perpendicular to the blade element radius. Analysis of the induced velocities provides information about the collective pitch input to provide the necessary thrust. This analysis also reveals power considerations.

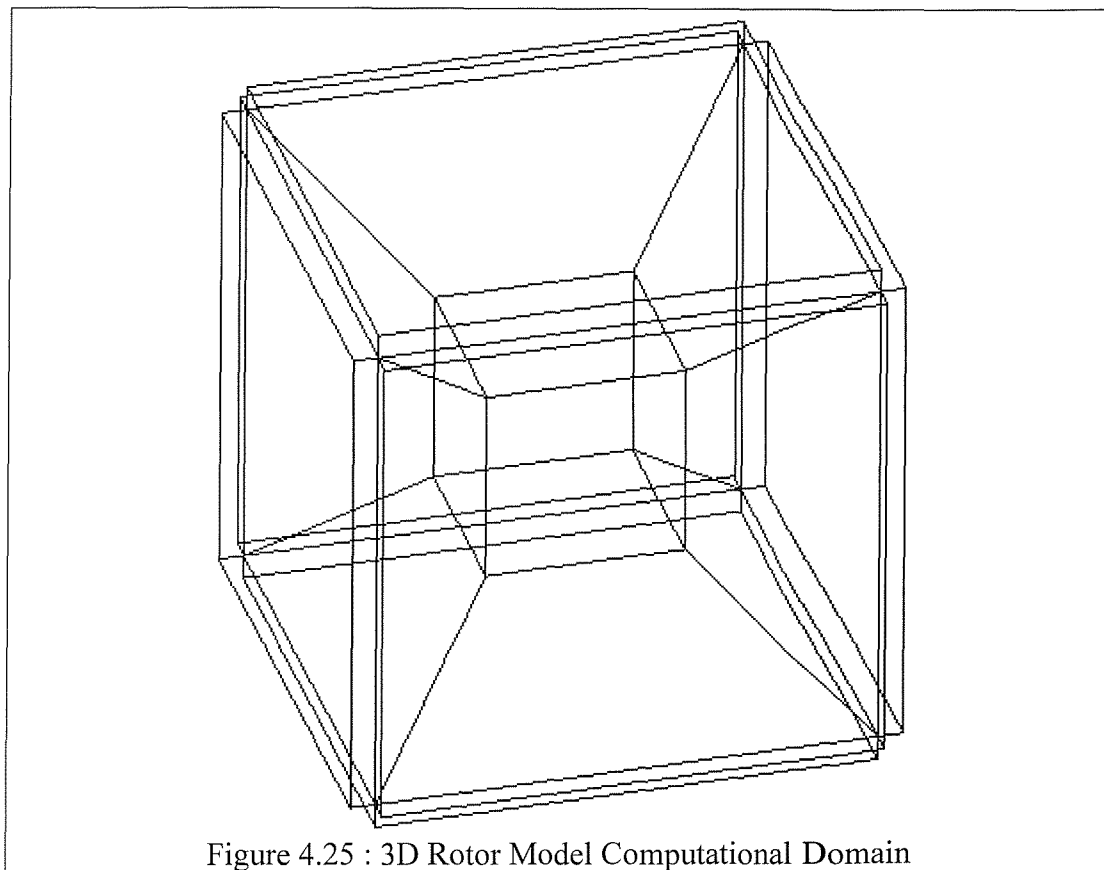
The rotor radius and thrust were defined to reflect the Westland Lynx aircraft.

### **4.7.2 Grid and Turbulence Parameters**

Two turbulence parameters, turbulent energy and energy dissipation rate, were defined at the boundaries of the domain. At all other locations these values were allowed to vary according to their governing equations [4.2]. The value of these parameters at the boundary was found to make negligible difference to the final

flow solution achieved. However the solution failed to converge if these parameters were left undefined. The turbulent kinetic energy was defined as  $0.001\text{m}^2\text{s}^{-2}$  and the turbulent dissipation rate was defined as  $0.001\text{m}^2\text{s}^{-3}$  at the boundaries. The RNG k- $\epsilon$  model was used. These values are consistent with the results in Chapter 3.

The computational domain was cubic in shape surrounded by six peripheral blocks as shown in Figure 4.25. The central cube had dimensions of 50m, and the peripheral blocks are 2.5m in thickness. The rotor was placed at the centre of the region. The grid cells immediately surrounding the rotor are exactly cubic. For both the constant thrust model and the blade element thrust model three different grid cell sizes were employed. The cell edge lengths were 1.0m, 0.67m and 0.50m. Whilst these cell sizes only vary by a factor of two the total number of grid cells within the domain varies by the cube of the cell size, and hence the total grid size was varied by a factor of eight.



As described previously the CFX4 flow solver requires a structured grid, which consists entirely of hexahedral or cuboid cells. This poses a somewhat fundamental problem, namely how can a grid, which is essentially square, be used to model a circular rotor. For ease of modelling the circular rotor was placed

directly over the square grid as shown in Figure 4.26. There are alternative grids, which allow the grid cell boundaries to match the rotor boundary, however these are more time consuming to define. As demonstrated within Sections 4.8.3.2 and 4.8.4.2 using a square grid to model a circular rotor provides a solution with limited detrimental effects.

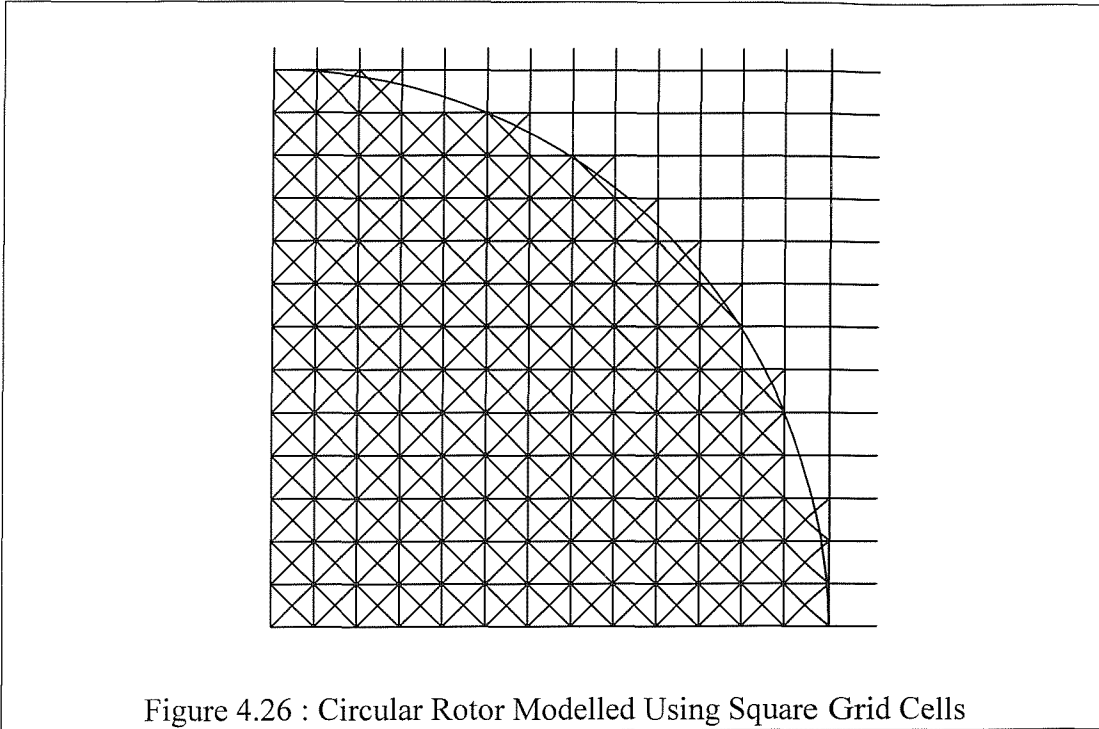


Figure 4.26 : Circular Rotor Modelled Using Square Grid Cells

### 4.7.3 Constant Thrust Model

#### 4.7.3.1 Thrust Definition

The constant thrust model is defined according to equation (4.18). This allows no radial variation of thrust. It assumes the weight of the helicopter is spread evenly over the rotor area. There is no root cutout at the rotor centre and no swirl forces applied to the fluid. This force is applied to grid cells whose centre lies within the radius of the rotor.

$$\Delta p = \frac{dT}{dA} = \frac{m \cdot g}{\pi R^2} \quad (4.18)$$

For the case of the Lynx the mass has been assumed to be 5200kg and the radius of the rotor 6.4m. The thrust per unit area is therefore 396.4Pa.

### 4.7.3.2 Constant Thrust Model Flow Analysis

An example of the flow solutions achieved is shown in Figure 4.27. These results are from the most detailed grid, which used grid cells of 0.5m. The flow solution in Figure 4.27 has the features associated with an actuator disc, namely the sharp pressure gradient at the plane of the disc and greatest velocities occurring in the downwash beneath the rotor.

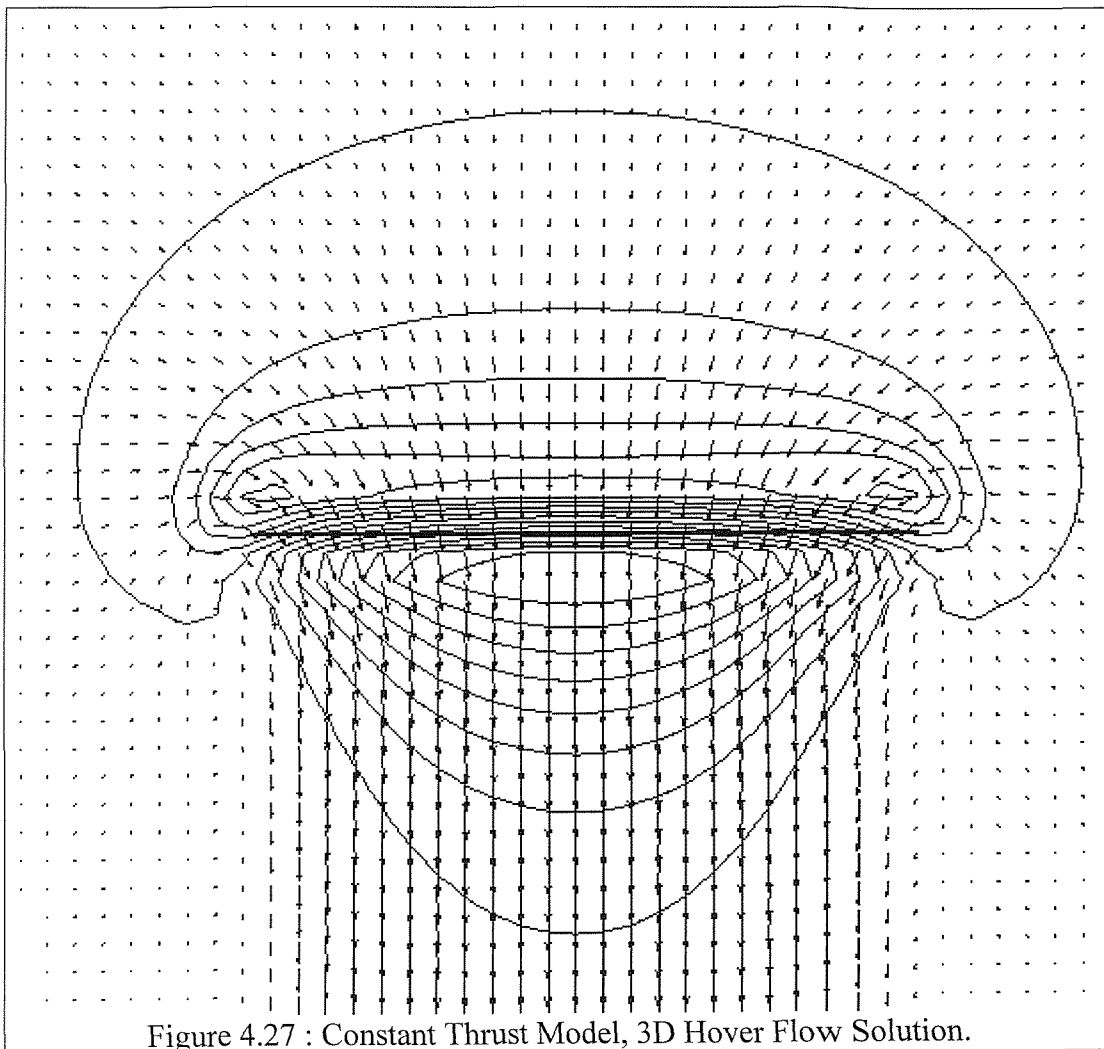
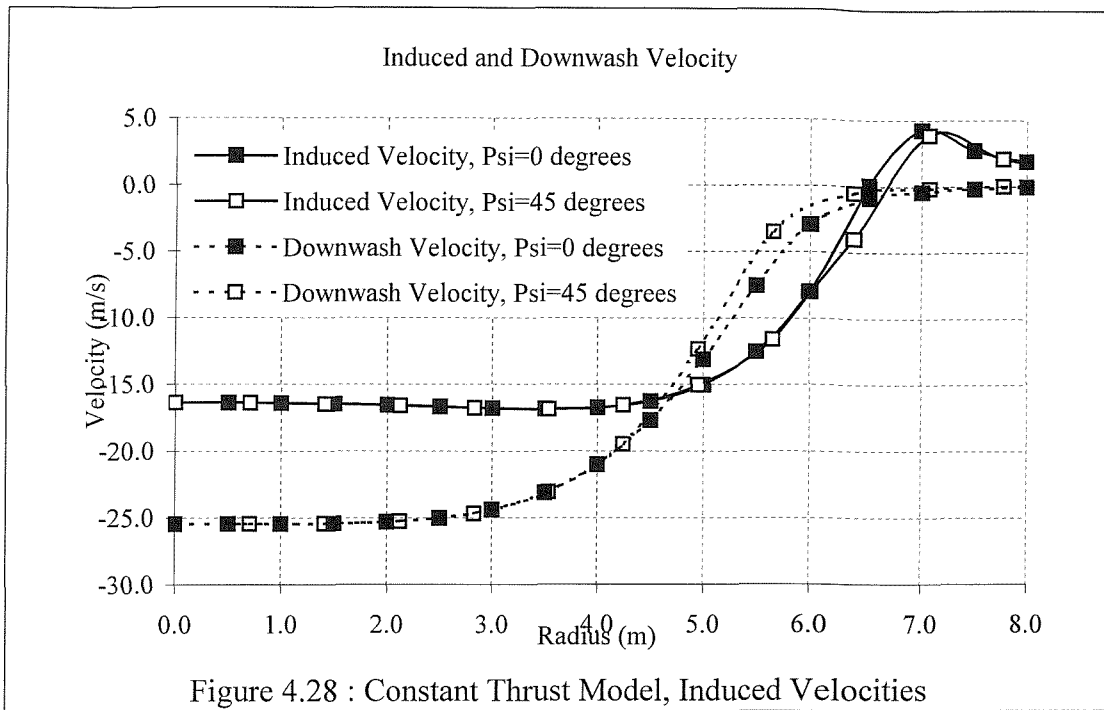


Figure 4.27 : Constant Thrust Model, 3D Hover Flow Solution.

The induced velocities, both at the plane of the rotor disc and at the plane 10m below the rotor are shown in Figure 4.28. The induced velocity is shown at azimuth angles of  $0^\circ$  and  $45^\circ$ , denoted by the solid lines. The slight variation of the velocities at these angles is attributed to the grid cells, whose boundaries lie along the azimuth axes of  $0^\circ$  and  $90^\circ$ . The induced velocity is approximately 17m/s across the majority of the rotor disc. The downwash is narrower and concentrated in a region with a radius of approximately 4.5m.



The analysis of the constant thrust model is limited to power considerations alone. The power exerted at the plane of the rotor is found from the integration in equation (4.19). The integral is evaluated numerically in eight 45° segments as indicated in equation (4.20). The angle  $\psi$  adopts the values zero to 315° in increments of 45°. The calculated powers are shown in Table 4.12. The three values vary by approximately 5%. This variation can be attributed to the difference in the grids. These values are all slightly greater than the power prediction from actuator disc theory [4.1], which predicts 656kW.

$$Power = \int_0^{2\pi} \int_0^R \Delta p \cdot v(r, \psi) \cdot r \, dr \cdot d\psi \quad (4.19)$$

$$Power = \Delta p \frac{2\pi}{8} \sum_{i=1}^8 \int_0^R v(\psi_i, r) \cdot r \, dr \quad (4.20)$$

Grid cell size	Power
0.50m	710kW
0.67m	677kW
1.00m	709kW
Ideal – Actuator Disc	656kW

Table 4.12 : Induced Power, Constant Thrust Model.

#### 4.7.4 Blade Element Thrust Model

##### 4.7.4.1 Thrust Definition

The method below combines blade element theory and annulus theory to provide a more realistic blade loading, referred to as the blade element thrust model. The total thrust per radius can be described approximately according to Equation (4.21). For a given helicopter operating in air all the quantities are known except the induced velocity,  $v_i$ , and the blade element angle  $\theta(r)$ .

$$N \frac{dT}{dr} = \frac{1}{2} \cdot \rho \cdot (\Omega r)^2 \cdot N \cdot c \cdot a \cdot \left( \theta(r) - \frac{v_i(r)}{\Omega r} \right) \quad (4.21)$$

The rotor blades often have a linear twist over their length, such that the angle can be described according to equation (4.22).  $\kappa$  is the angle of twist over the entire length of the blade, and a linear twist distribution is assumed.

$$\theta(\psi, r) = \theta_0(\psi) - \kappa \frac{r}{R} \quad (4.22)$$

Considering each annulus individually, momentum theory gives equation (4.23). Equating (4.21) and (4.23) gives a quadratic in  $v_i(r)$ . An assumed value of  $\theta_0$  gives the radial thrust variation, which gives the total thrust when integrated across the radius.

$$N \frac{dT}{dr} = 2 \cdot \rho \cdot v_i(r)^2 \cdot 2 \cdot \pi \cdot r \quad (4.23)$$

For the rotor model used within this section, it is assumed that the thrust exerted is equal to the weight of the helicopter. Therefore  $\theta_0$  must be adjusted such that these two values are equal, in practice this is easiest to perform in a spreadsheet.

The helicopter model considered within this chapter is broadly based around the Westland Lynx. The rotor radius is 6.4m, the mass is 5.2 tonnes. It has four blades with a chord of 0.394m, the tip speed is 218.69m/s and the lift curve slope is assumed to be 5.8 radians. The blades have a 15% root cut out; there is no thrust applied to the air within this area at the centre of the rotor. The linear twist along the length of the blades is  $8^\circ$ . The air density is assumed to be  $1.2\text{kg/m}^3$ .

Equations (4.21) to (4.23) are solved using these parameters to find a predicted radial variation of blade loading. This is shown in Figure 4.29. The blade loads have been solved twice, using the same parameters but discretising the radius a various number of times. The graph demonstrates that these equations are not sensitive to the number of discretisations used in the solution process. The blade pitch at the root of the blades is determined as  $17.3^\circ$ .

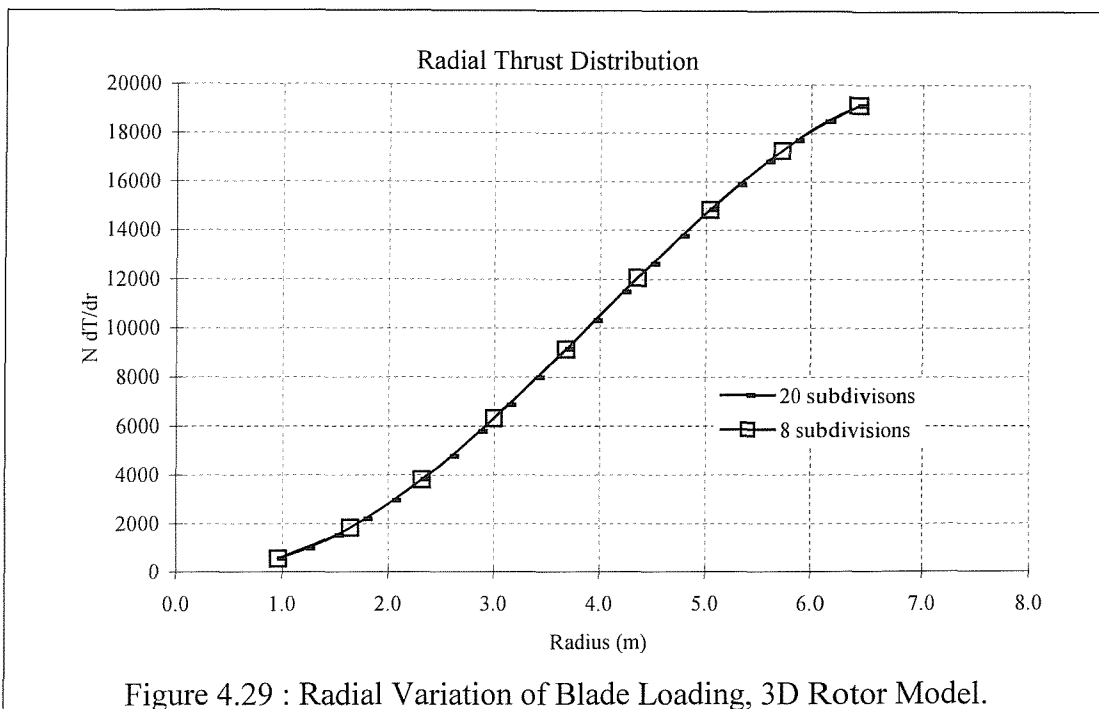
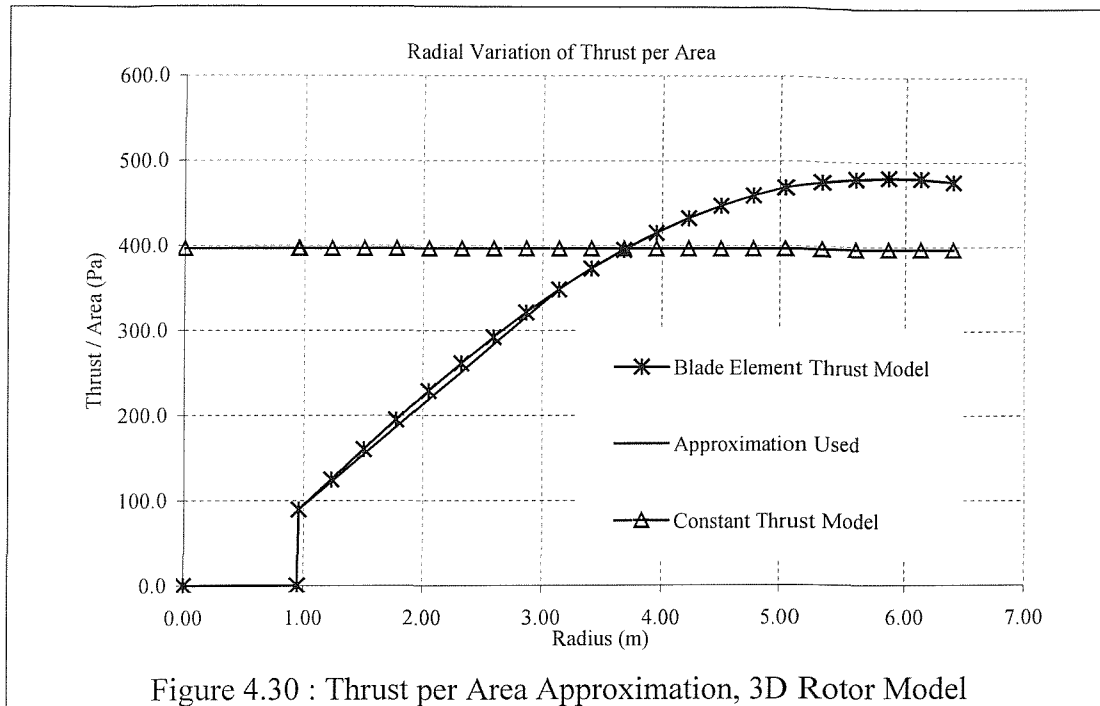


Figure 4.29 : Radial Variation of Blade Loading, 3D Rotor Model.

The predicted blade loads are converted into thrust per area and are shown in Figure 4.30; these are the values which are used within CFX. It is convenient to have an approximation in order to simplify the FORTRAN algorithm in CFX. This approximation has two sections, in the region where the radius is less than half the rotor radius the variation is assumed linear. In the outer half of the rotor radius, the variation of loading is assumed quadratic. This approximation is shown in Figure 4.30. The thrust used within the constant thrust model is also shown in Figure 4.30. These two models provide characteristic loading distributions.



The addition of the third dimension also allows swirl forces to be added to the rotor thrust model. These forces can be defined in conjunction with the constant thrust model or the blade element thrust model. However it is inconsistent to use these forces with the constant thrust model, and therefore the swirl forces are only defined when the blade element thrust model is employed.

The drag a blade element experiences is described approximately in Equation (4.24).

$$\frac{dD}{dr} = \frac{1}{2} \cdot \rho \cdot (\Omega r)^2 \cdot C_d \cdot c \quad (4.24)$$

The forces that the blade element experiences are equal to the forces exerted on the fluid. If the force the fluid experiences is summed for all the blades, averaged around the annulus and resolved in to a Cartesian co-ordinate system, Equation (4.25) is found. The angle  $\psi$  is the azimuthal position of the element  $dA$  relative to the rotor hub, hence the force acts perpendicular to the radius  $r$ . The method outlined above assumes the rotor is rotating in an anticlockwise direction when viewed from above.

$$\frac{d\bar{F}_{SW}}{dA} = \frac{1}{4\pi r} \cdot \rho \cdot (\Omega r)^2 \cdot C_d \cdot N \cdot c \cdot \begin{bmatrix} -\sin \psi \\ \cos \psi \end{bmatrix} \quad (4.25)$$

$$\sin \psi = \frac{y}{r} \quad (4.26)$$

$$\cos \psi = \frac{x}{r} \quad (4.27)$$

#### 4.7.4.2 Blade Element Thrust Model Flow Analysis

The three flow solutions exhibited the features of a stationary actuator disc. An example is shown in Figure 4.31. This figure shows the flow solution found from the most detailed grid cells, using grid cells which were 0.5m in length. The flow diagram shows the root cut-out at the centre of the disc. Within this region there is little fluid flow, however there is a large pressure difference, as indicated by the pressure contours.

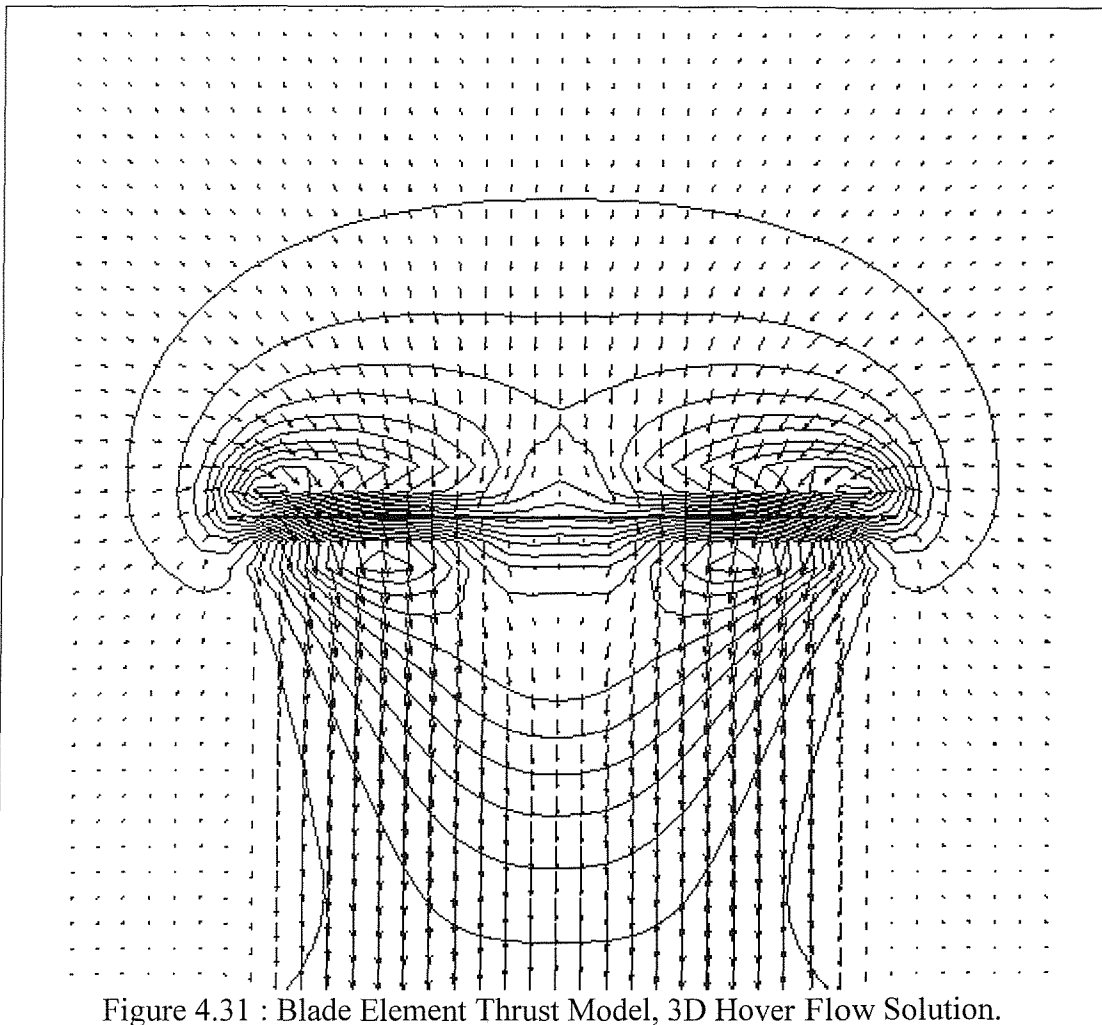


Figure 4.32 shows the induced velocities at the plane of the rotor blades. The Cartesian grid produces a flow solution with rotational symmetry of order four. Hence the flow at azimuth angles  $0^\circ$ ,  $90^\circ$ ,  $180^\circ$  and  $270^\circ$  are identical; likewise  $45^\circ$ ,  $135^\circ$ ,  $225^\circ$  and  $315^\circ$  are the same.

The induced velocities at  $0^\circ$  and  $45^\circ$  are shown in Figure 4.32. These differ marginally because the grid varies between the angles. However both flows have zero velocity at the rotor hub and reach a maximum induced velocity of 18m/s at a radius of 4m. Also shown within this figure is the velocity in the downwash 10m below the rotor disc. The flow directly below the rotor centre has a velocity of 15m/s, however the maximum is 25m/s at a radius of 3m from the centreline.

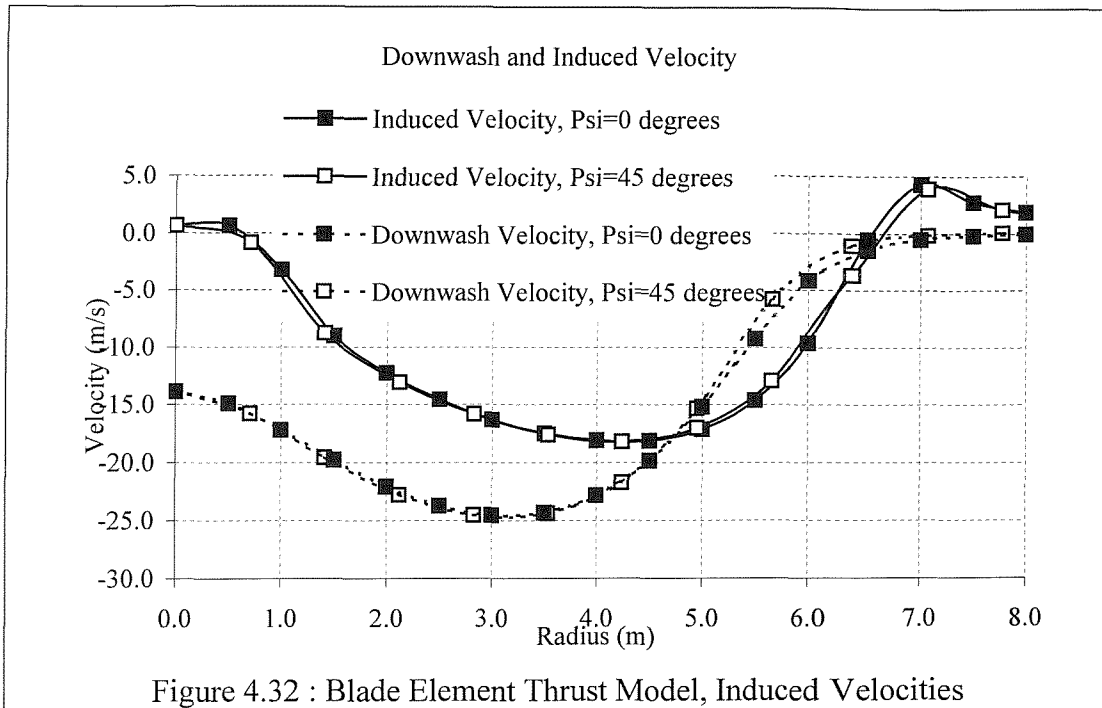


Figure 4.33 shows the radial variation of the rotational component of velocity at the rotor disc; this velocity component acts in the same direction as rotor blades and is sometimes referred to as swirl velocity. The velocity is zero at the rotor hub, increasing to 0.55m/s immediately inside the rotor radius. The velocity is zero outside the extremity of the rotor disc. These velocities are small and hence do not greatly affect the overall performance of the rotor blades.

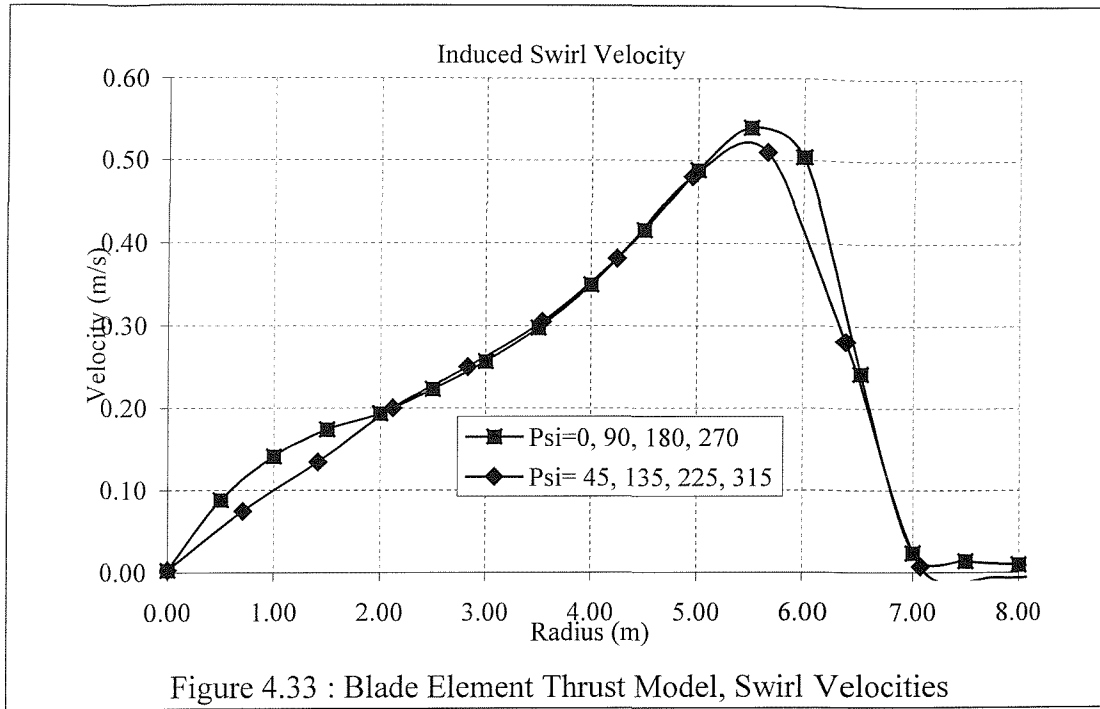


Figure 4.33 : Blade Element Thrust Model, Swirl Velocities

The more detailed composition of the blade element thrust model allows information about the collective and cyclic pitches to be obtained. These give information about the power requirements. The first part of the flow solution analysis determines the pitch angle at the eight azimuthal positions. The rotor speed and flow components are known so the relative speed between the blade element and the fluid,  $U_T$ , is determined from Equation (4.28). Note that the swirl velocity,  $V_\theta$ , is included. This velocity has the effect of reducing the relative velocities. The angle of the flow through the rotor disc is determined using Equation (4.29).

$$U_T = \sqrt{(r\Omega - V_\theta)^2 + (v_i)^2} \quad (4.28)$$

$$\phi = \tan^{-1}\left(\frac{v_i}{r\Omega - V_\theta}\right) \quad (4.29)$$

The lift and drag a blade element experiences are given Equations (4.31) and (4.32). The forces can be integrated along the blade length to find the total thrust exerted, as shown in Equation (4.32). The only unknown in these equations is the blade angle. Therefore these equations can be solved relatively easily using a spreadsheet. The value of  $\theta_0$  is varied until the thrust exerted by the rotor is equal to the thrust defined within the flow solution. The root blade angles for each of the three grids is shown in Table 4.13. A value of  $\theta_0$  is found at each 45° segment.

Theoretically the blade angles obtained from these analyses should be identical to the value found from the previous section which was used to determine the radial thrust distribution. There is a slight discrepancy between the values below and the original value of  $17.3^\circ$ , which can be attributed to two factors, the discretisation process inherent within CFD that introduces numerical errors and the swirl forces present within the CFD but absent in the blade element theory. However the values are in fact very similar which verifies the model.

$$\frac{dL}{dr} = \frac{1}{2} \cdot \rho \cdot U_T^2 \cdot c \cdot a \cdot (\theta(r, \psi) - \phi) \quad (4.30)$$

$$\frac{dD}{dr} = \frac{1}{2} \cdot \rho \cdot U_T^2 \cdot c \cdot C_d \quad (4.31)$$

$$T = N \int_{R^{IN}}^R \left( \frac{dL}{dr} \cos \phi - \frac{dD}{dr} \sin \phi \right) dr \quad (4.32)$$

Once the blade pitch angles are known the torque exerted to maintain the rotor rotation can be determined. Using small angle approximations for  $\phi$ , the torque for all blades can be found from Equation (4.33) and hence power from Equation (4.34). The results of these power calculations are shown in Table 4.13. The average power prediction is 812kW, which is 24% greater than the power prediction from actuator disc theory. The power requirements vary between the three grids used; these variations are around 5% and can be attributed to the numerical errors incurred when discretising a physical space into a finite number of grid cells. The variations in power are consistent with the collective pitch, that is the power increases as the collective pitch increases.

$$Q = N \int_{R^{IN}}^R \left( \frac{dL}{dr} \phi + \frac{dD}{dr} \right) \cdot r \cdot dr \quad (4.33)$$

$$Power = \Omega Q \quad (4.34)$$

For steady flight or hover the azimuthal blade pitch distribution is often described as shown in Equation (4.35), taken from Newman [4.1].  $\theta_0$  is the collective pitch angle,  $A_1$  is the longitudinal cyclic variation and  $B_1$  is the lateral cyclic variation. Equations (4.36) to (4.38) describe a method of determining these terms from a flow solution using a method consistent with the first terms of a Fourier series. Also shown is a numerical method of determining these values, which has been

employed in these cases. As mentioned previously  $\theta_0$  is determined at eight azimuthal locations spaced at  $45^\circ$ . This section has considered hover and hence the flow solutions are axisymmetric, therefore the terms  $A_1$  and  $B_1$  are zero. The collective pitch for the three flow solutions are shown in Table 4.13.

$$\theta(r, \psi) = \theta_0 - \kappa \frac{r}{R} - A_1 \cos \psi - B_1 \sin \psi \quad (4.35)$$

$$\theta_0 = \frac{1}{2\pi} \int_0^{2\pi} \theta_0(\psi) d\psi = \frac{1}{8} \sum_1^8 \theta_{0i} \quad (4.36)$$

$$A_1 = \frac{-1}{\pi} \int_0^{2\pi} \theta_0(\psi) \cdot \cos \psi d\psi = \frac{-1}{4} \sum_1^8 \theta_{0i} \cos \psi_i \quad (4.37)$$

$$B_1 = \frac{-1}{\pi} \int_0^{2\pi} \theta_0(\psi) \cdot \sin \psi d\psi = \frac{-1}{4} \sum_1^8 \theta_{0i} \sin \psi_i \quad (4.38)$$

Grid Cell Size	$\theta_0$ (Collective Pitch)	Power
0.50m	17.6°	831kW
0.67m	17.1°	785kW
1.00m	17.4°	816kW
Ideal – Actuator Disc	-	656kW

Table 4.13 : Power and Control Parameters, Blade Element Thrust Model.

These results show that simple forces can be applied to a fluid to model a rotor. The lift and drag force that rotor blade elements experience can be averaged over a circular annulus and applied to the fluid. The CFD solution generated is not exactly as predicted from annulus theory and blade element theory and does vary slightly according to the grid definition, however the solution bears all the salient features of the predicted induced velocity distributions. Thus the resultant analysis of the velocities yields a plausible collective pitch value. These values will be carried forward to studies of forward flight and flight around ships' superstructures.

#### 4.8 Conclusion

This chapter began by discussing the methods of modelling a helicopter main and tail rotor. The 'body forces' method allowed a simplification of the rotor models, which was necessary to bring the computational space and time requirements

within the available resources. This method also allows the thrust of the helicopter to be defined without predetermining any velocity components.

Section 4.4 briefly verified that the CFX 'body force' function was acting as specified and the force exerted on the fluid was equal to the force defined.

Unfortunately none of the default boundary conditions within commercial flow solvers are applicable to actuator discs operating at zero advance ratio. Section 4.6 describes a novel boundary condition, based on Bernoulli's Equation. Within Section 4.7, many parameters are varied within a 2D computational domain to assess their influence on the clarity of the resultant flow solution. It is found that none of these had a significant influence on the fidelity of the results. All the flow solutions were analysed by comparing the thrust defined at the rotor plane to the momentum in the downwash. In all cases these two values were very similar and often within one percent of each other. Finally the induced power exerted at the plane of the rotor was compared to the power predicted by actuator disc theory. It was found that the measured power at the rotor was approximately 8% greater than the ideal predicted value. This difference, although small, can be attributed to velocity variations across the disc, which are not predicted in the idealised solution.

Section 4.8 showed that these boundary conditions and rotor model could be applied to a full-scale helicopter, in this case a Lynx. Whereas previously the thrust per unit area within the rotor disc had been constant, the thrust was now a function of the radius from the rotor centre. This distribution was determined from a blade element analysis, and then used as an input into the flow solution. The resultant flow solution was analysed to derive information about collective and cyclic pitch variations. The solutions compared very favourably with data input into the flow solver. Whilst this process appears time consuming, these results prove that the simple 'body forces' function can be used to model blade elements and these results will provide a valuable comparison when considering more complex flow solutions, which include cross winds, turbulence and ground effect from ship structures.

This chapter has shown that a simple function within CFX can be manipulated to model the complex problem of helicopter flight and simultaneously derive information about control and power parameters.

## **5 Power Requirements of Helicopter Hovering in Ground Effect**

### **5.1 Introduction**

This study models a stationary actuator disc using hovering at various heights above the ground. CFX 4.1 is the commercial CFD software used. The actuator disc is modelled by adding extra terms to the governing Navier-Stokes equations over a small volume at the centre of the domain. The thrust is evenly distributed across the area of the disc. The height at which the disc is placed is varied and the resultant power exerted upon the fluid is determined.

The resultant height/power curve is plotted and compared to an existing analytical curve and measured data. This new curve compares favourably with the existing data.

### **5.2 Description of Geometry and Boundary Conditions.**

The domain models a three dimensional actuator disc. In order to save considerably on computational resources only a  $10^\circ$  segment of the problem was modelled. This enforces an axisymmetric flow solution.

The domain used had a height of 5m and radius of 5m. The disc was placed horizontally at the centre, and the height was varied. This geometry was divided using two grids. The first used grid cells of uniform height; this was used for the disc hovering at the greater heights. The second grid had a greater concentration of cells at the base of the domain; this grid was used for the lower heights.

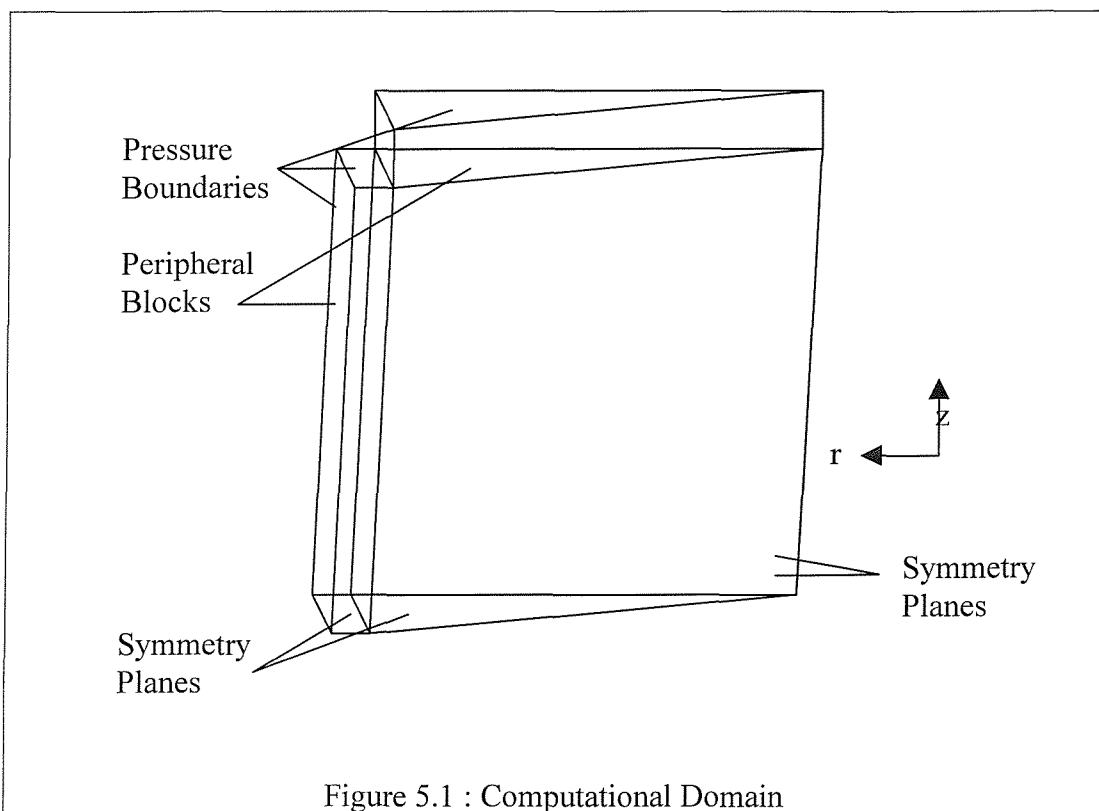
One further study was performed using a smaller domain. This ensured that the domain was sufficiently large and well defined that it was not predetermining the flow solution obtained. A schematic of the domain is shown in Figure 5.1.

The lower boundary was defined as a symmetry plane. This gives the property of enabling tangential flow without exerting frictional forces. This also avoids the development of a boundary layer, which requires a detailed local grid to resolve accurately.

The novel boundary conditions, described in Chapter 4, were used at the edges of the domain. These enforce a velocity/pressure relationship as described in equation (5.1).

$$p + \frac{1}{2} \cdot \rho \cdot V^2 = 0 \quad (5.1)$$

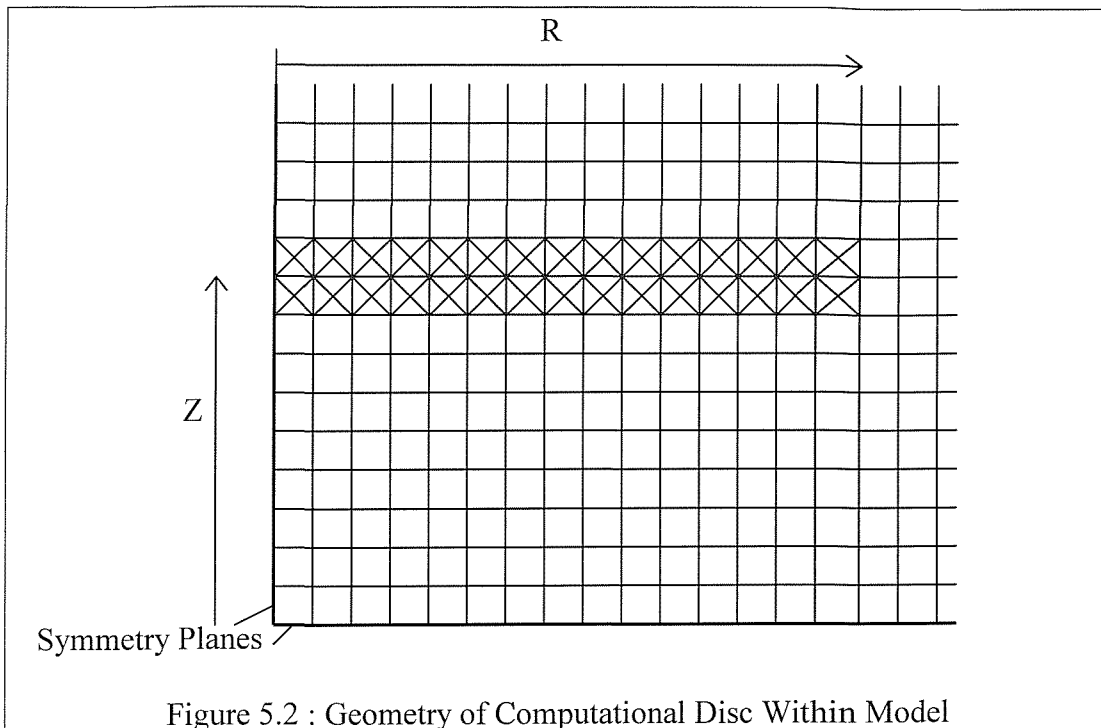
To determine the power exerted upon the fluid whilst out of the ground effect a series of control runs were performed which modelled a hovering disc at infinite height. The power determined from these was used as the infinite height power value ( $P_{INF}$ ). The computational domain used for this study has the same dimensions and grid cell size as the domain used by the model hovering over the ground.



### 5.3 Description of Actuator Disc

An actuator disc is generated by exerting force upon the fluid, which is divided equally over two layers of cells, as shown in Figure 5.2. In reality most rotors occupy very little vertical height; the rotor would be more accurately modelled if the thrust forces were exerted upon the fluid over one layer of cells. This is not possible as the flow solution diverges, due to excessive pressure gradients, and for this reason thrust is distributed evenly throughout the hatched area within Figure

5.2. In this example the disc spans 15 cells. The rotor radius is approximately 1m in all examples; the size varies according to the grid cell boundaries.



The thrust adopted for this study was  $2\rho A*(1\text{m/s})^2$ . This was chosen such that the ideal induced velocity at the disc would be 1m/s and the ideal velocity magnitude would be 2m/s downstream of the disc.

#### 5.4 Flow Solver

The commercial software CFX 4.1 was used to generate these flow solutions. In order to keep computing resources to a minimum the laminar, isothermal and incompressible options were adopted. These options removed the variables, density, temperature and the turbulence parameters  $k$  and  $\epsilon$  from the calculations.

The density and viscosity were defined as  $1.124\text{kg/m}^3$  and  $1.8*10^{-4}\text{Ns/m}^2$  respectively. The relaxation factors used to vary velocity and pressure between iterations were initially 0.3, but reduced to 0.1 to aid convergence.



## 5.5 Results

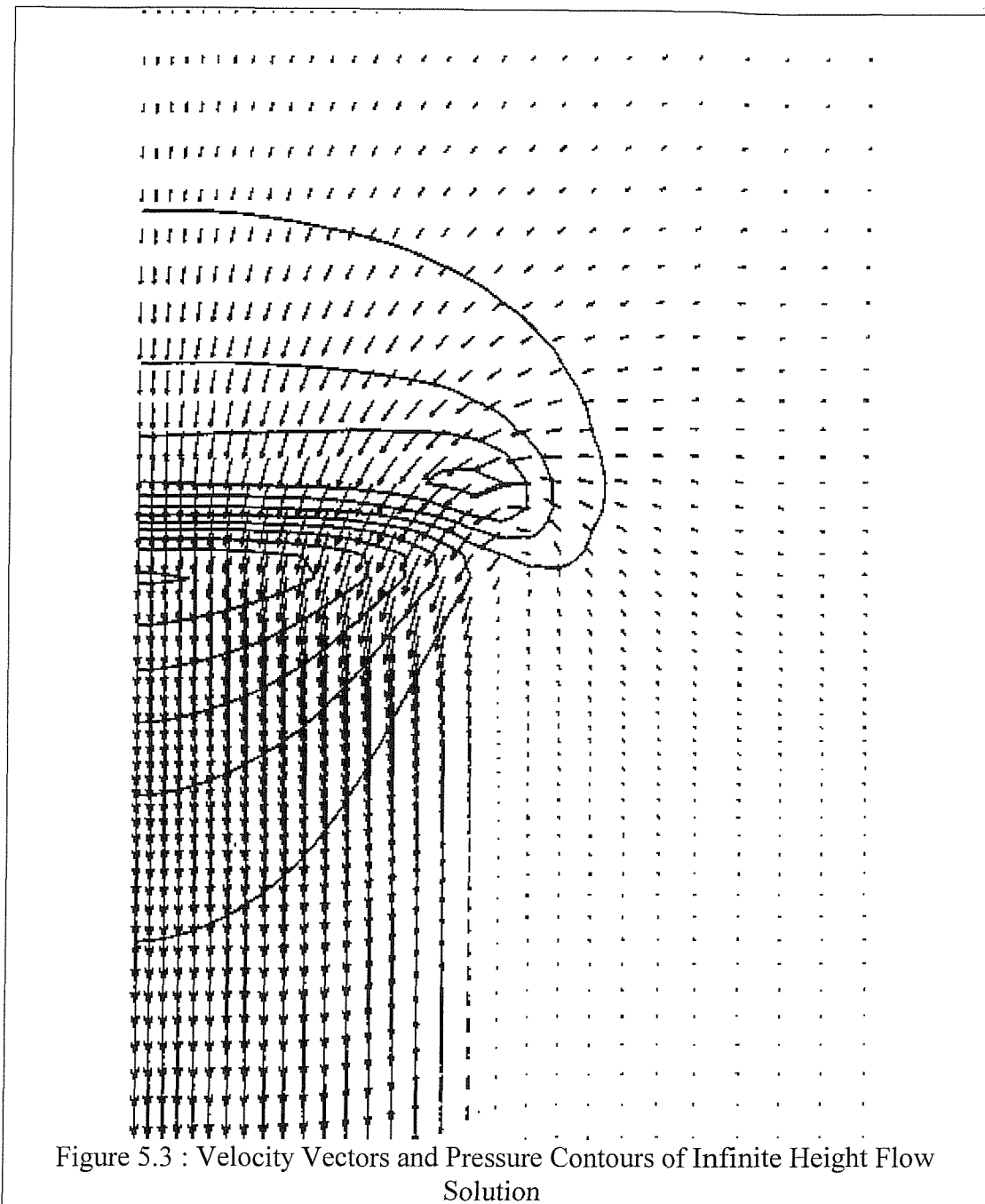
### 5.5.1 Infinite Height

A disc was modelled at an infinite height in order to obtain a value of  $P_{INF}$ . A peripheral block replaced the ground plane at the lower edge of the computational domain. This flow solution has also been compared to an ideal value obtained from actuator disc theory. These results are shown in Table 5.1, along with results from two other flow solutions with slightly different geometries.

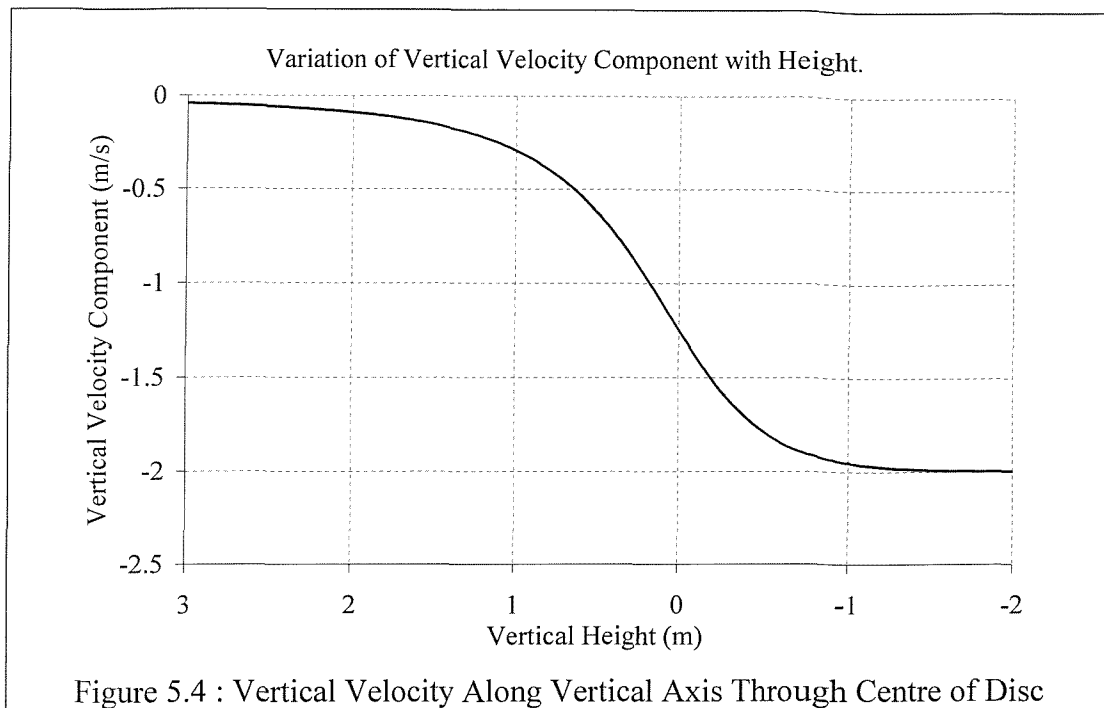
Case	Control case	Geometry 1	Geometry 2
Domain Radius (m)	5.0	5.0	4.0
Domain Above Disc (m)	5.0	5.0	3.0
Domain Below Disc (m)	5.0	5.0	4.0
Rotor Area (m <sup>2</sup> )	3.389	3.225	2.964
Thrust/Area (Pa)	2.248	2.248	2.248
Thrust Defined (N)	7.618	7.250	6.662
Momentum Measured (N)	7.566	7.226	6.612
Difference	-0.7%	-0.3%	-0.7%
Ideal Power (Watts)	7.618	7.250	6.662
Power Exerted (Watts)	7.919	7.526	6.899
Difference	4.0%	3.8%	3.6%

Table 5.1 : Flow Solutions, Hover at Infinite Height.

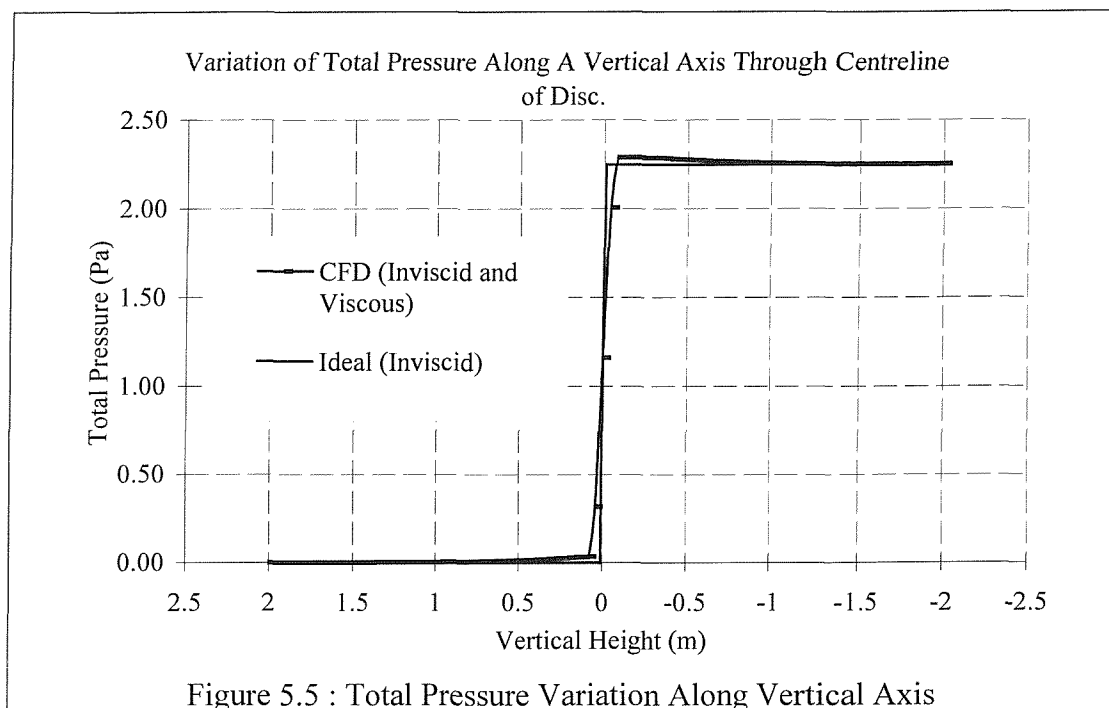
$P_{INF}$  was taken as 7.919 Watts. The geometry used to create this flow solution uses the same grid cell size as the flow solutions generated over ground. The lower plane of the computational domain was replaced by a peripheral block containing body forces, as described in Chapter 4, to model an infinite height.



One flow solution is shown in Figure 5.3 , where the arrows represent the velocity vectors and the contours show pressure. This figure demonstrates that the pressure variations caused by the rotor are localised. All pressure variations occur within one diameter of the rotor's centre.



The variation of the vertical velocity component,  $w$ , is shown in Figure 5.4, the velocity downstream is  $-2\text{m/s}$ , which corresponds exactly to the thrust applied at the plane of the disc. The flow speed through the rotor centre, at a height of zero, is  $1.25\text{m/s}$ . This is slightly greater than the flow speed predicted by actuator disc theory which is  $1\text{m/s}$ .

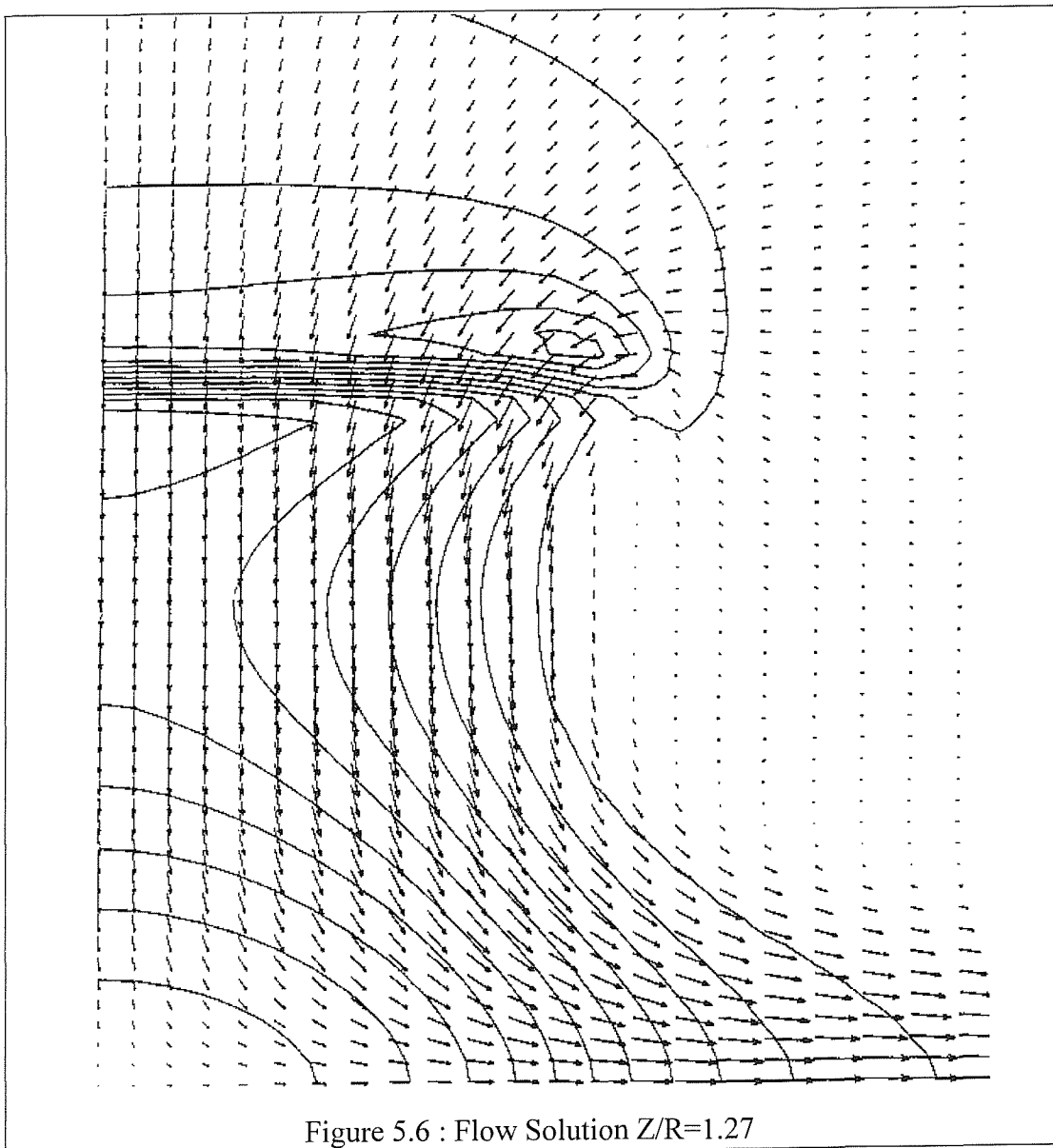


The total pressure variation through the centre of the disc is shown in Figure 5.5. The value at  $2.5\text{m}$ , above the disc, is zero. This should remain zero, as the fluid moves towards the disc and has a step to  $2.248$  at the disc. The figure shows that

immediately above and below the disc, the total pressure does vary from the ideal, however this discrepancy diminishes downstream of the rotor.

### 5.5.2 Ground Effect

Flow solutions were obtained at a range of heights using the geometry described in Section 5.2. Figure 5.6 shows the flow solution obtained for the disc hovering at 1.32m. The figure shows velocity vectors and pressure contours. The contours show the sharp pressure discontinuity at the disc. They also show the high pressure at the surface of the ground.



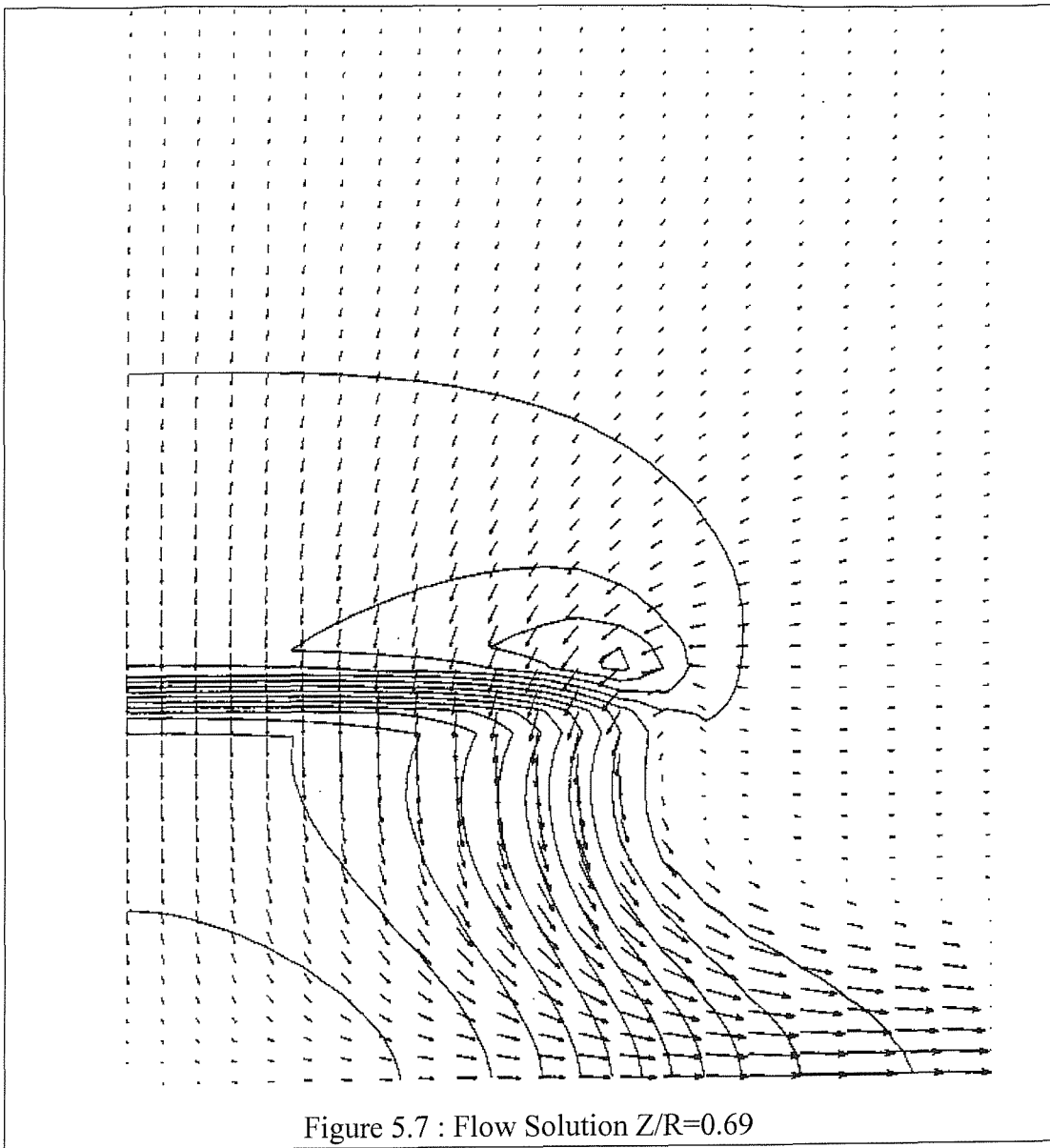


Figure 5.7 shows a disc at 0.72m. Comparisons of these two flow solutions clearly indicate reduced velocity through the plane of the disc at the lower height.

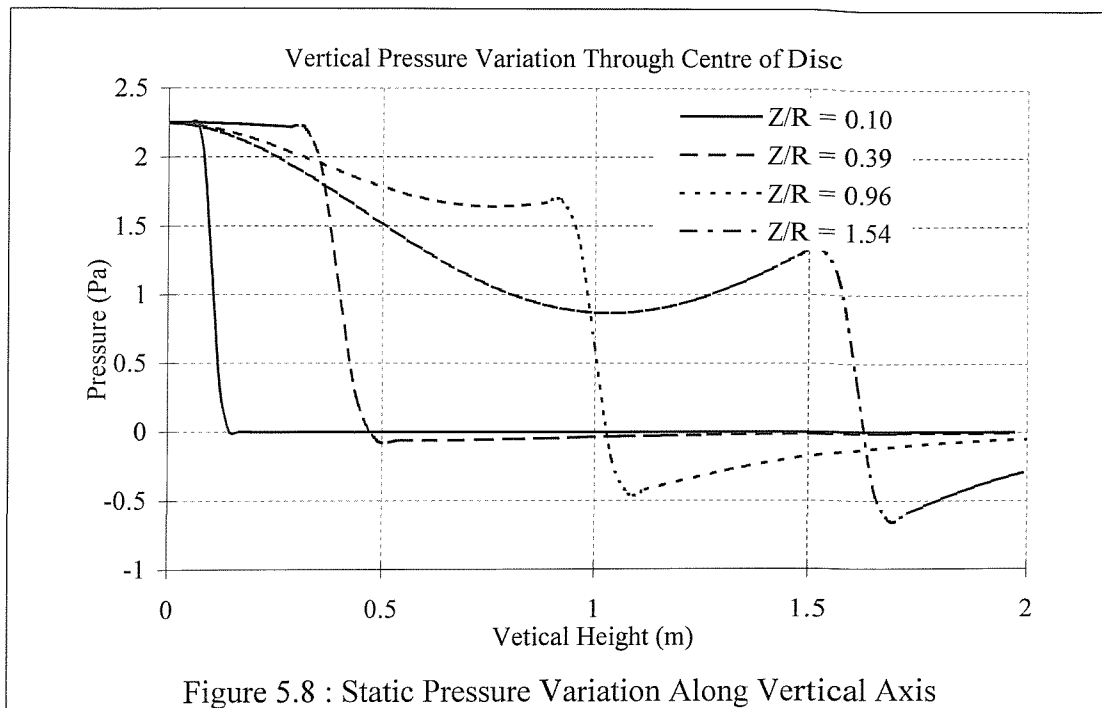


Figure 5.8 shows the vertical variation of static pressure through the centreline of the disc. The four lines correspond to various heights of hover. The vertical height of zero shows the pressure at ground level; this point is also a stagnation point directly below the centre of the disc, where the pressure is 2.248Pa which is  $2\rho*(1\text{m/s})^2$ . This shows that the thrust defined at the disc,  $2\rho/A$ , is applied correctly to the fluid and also there are no pressure or velocity losses through the boundaries of the domain. This figure shows that at the greater heights, there is a low pressure above the disc and a high pressure below the disc, whereas at lower height there is only a high pressure above the disc.

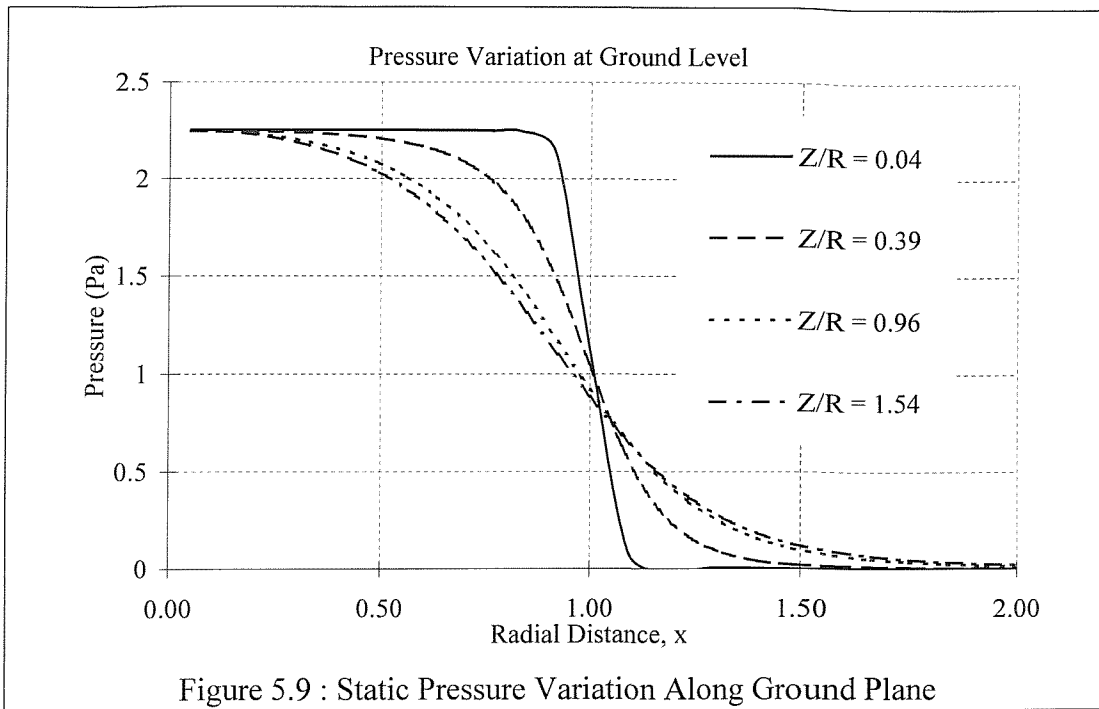


Figure 5.9 shows the pressure exerted upon the ground plane. This figure also shows the stagnation point occurring below the centre of the disc. The total force exerted on the ground is  $2\rho A$  in all cases. The only variation in this force is spread over a greater area when the disc is hovering at a greater height, and concentrated when the disc is close to the ground.

Figure 5.10 shows the induced velocity at the plane of the disc. The series of plots indicate that the induced velocity reduces with height. Since the induced velocities determine the power exerted, the power requirements also reduce with height.

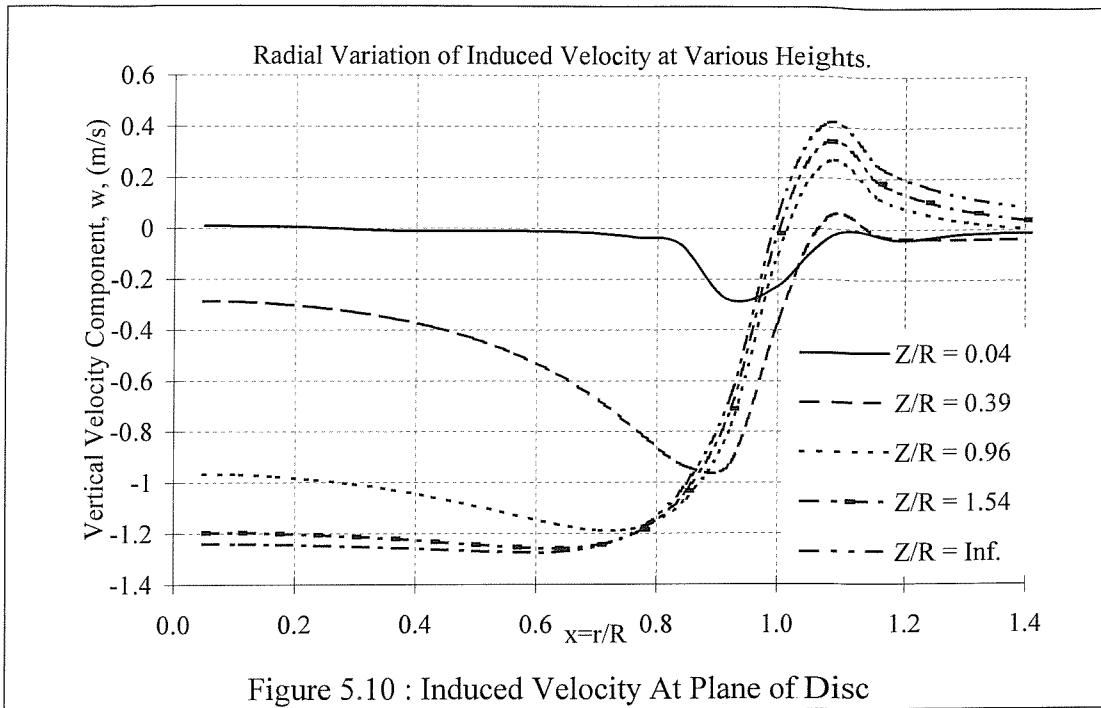


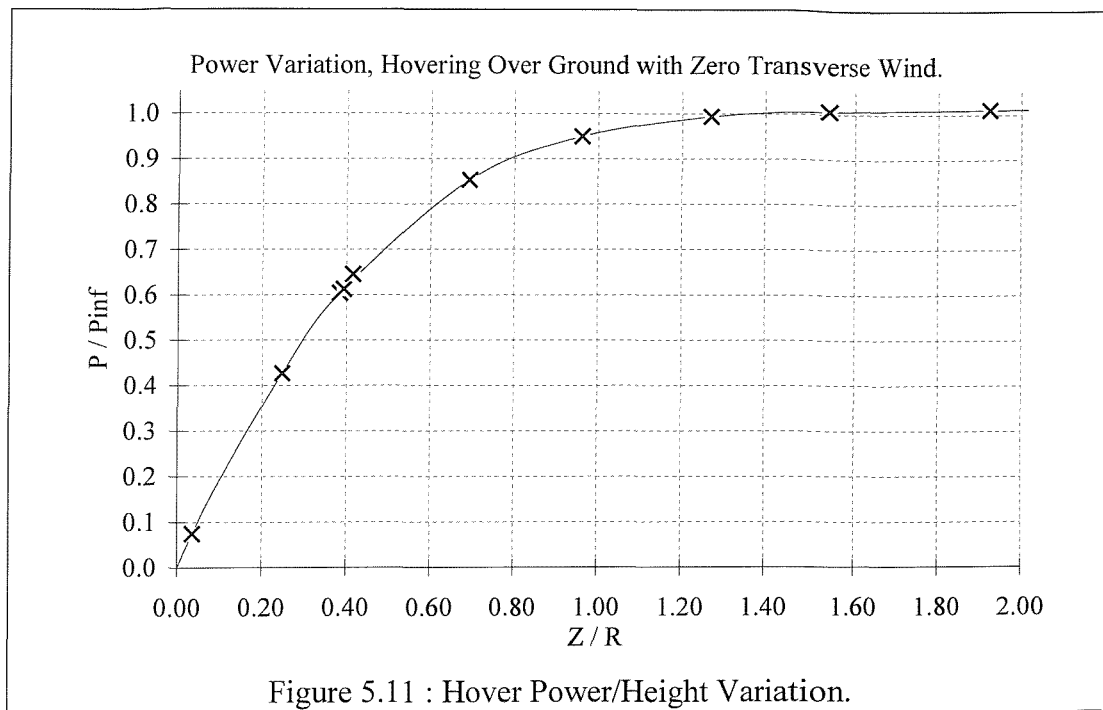
Table 5.2 shows the heights at which the disc was placed, and the resulting power exerted on the fluid.

Run	Height Z, (m)	Radius r (m)	Z/r	P(z)	P/P <sub>INF</sub>
1	2.000	1.0398	1.92	7.99	1.01
2	1.600	1.0398	1.54	7.95	1.01
3	1.320	1.0398	1.27	7.85	0.99
4	1.000	1.0398	0.96	7.50	0.95
5	0.720	1.0398	0.69	6.74	0.85
6	0.4104	0.9889	0.42	4.61	0.64
7	0.3954	1.0047	0.39	4.52	0.61
8	0.400	1.0398	0.38	4.77	0.60
9	0.2489	1.0047	0.25	3.15	0.43
10	0.1017	1.0047	0.10	1.42	0.19
11	0.0366	1.0047	0.04	0.55	0.07

Table 5.2 : Power Requirements at Various Heights.

All the runs used identical geometry except Run 6, which used a reduced domain size, to ensure the results were not adversely influenced by a geometry of insufficient size.

Two grids were used. The first grid was used for the rotor operating at heights equal to and greater than 0.4m; the cells within this grid had uniform size. The second grid utilised smaller cells around the ground plane and was used for the heights less than .42m. Runs 7 and 8 have a similar Z/r and used each grid; these solutions demonstrate that the results can be generated regardless of the grid used. These results are shown graphically in Figure 5.11.



## 5.6 Conclusion

The relationship between height/power is shown in Figure 5.11. The graph clearly indicates the established trend experienced by pilots hovering over ground. The ground effect experienced is only significant below  $Z/R=1.0$ . The only anomaly amongst the results is the power required at the greater finite heights,  $Z/R=1.96$  and  $1.54$  (101%) which is greater than the power required out of the ground effect. This indicates that the control cases do not reflect the grid or geometry used to determine flow solutions over ground. To eliminate this 1% discrepancy would require further investigation and time consuming CFD runs. This has not been attempted because 1% can be considered acceptable.

## 5.7 Comparison

There is little published data that can be compared directly to the results found within this study. This is largely due to the nature of experiments undertaken. In this study the thrust remained constant and only the power varied. Blade element theory dictates that the thrust exerted by a rotor is a function of many parameters, namely, induced velocity, blade angle, and blade chord, as described in equation (5.2).

$$T = \frac{1}{2} \cdot \rho \cdot \Omega^2 \cdot \frac{dC_L}{d\theta} \cdot c \cdot N \int_0^R \left( \theta(r) - \frac{v_i}{\Omega r} \right) \cdot r^2 \cdot dr \quad (5.2)$$

Much of the experimental work has taken measurements for a rotor operating out of the ground effect and moved it closer to the ground whilst holding the angular velocity constant. Inspection of equation (5.2) indicates that as the rotor moves closer to the ground, the induced velocity decreases, increasing thrust. However the angle of attack of the blade elements also increases as the induced velocity increases, thus increasing drag and creating more torque and hence power.

If we neglect the increases in torque and hence power, data from [5.1] can be plotted using the relationship given in equation (5.3). This is shown in Figure 5.12. This paper also notes that the fuselage experiences a download at  $Z/R > 1.0$ , but experiences an upload at in ground effect,  $Z/R < 1.0$ .

$$\frac{P(Z)}{P_{INF}} = \frac{C_{T_{INF}}}{C_T(Z)} \quad (5.3)$$

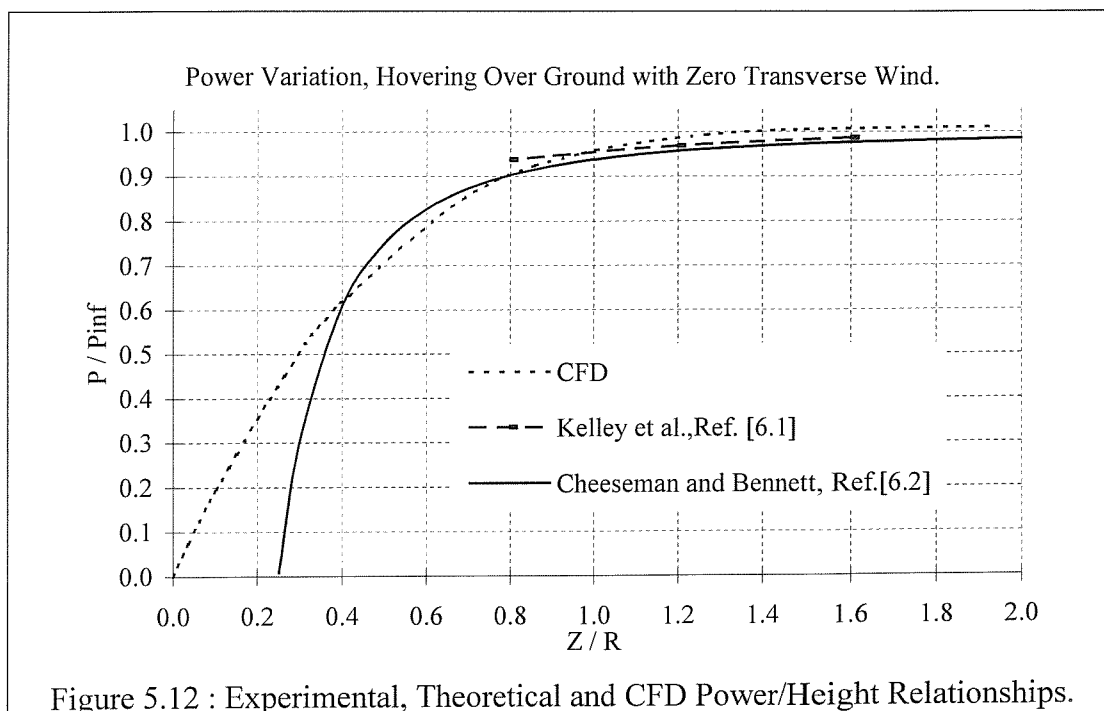


Figure 5.12 : Experimental, Theoretical and CFD Power/Height Relationships.

Cheeseman and Bennett, [5.2], proposed a solution using an actuator disc modified by the addition of a source placed below the disc. This image source creates a virtual upwash that reduces the induced velocity at the plane of the disc and thus reduces power. The constant thrust relationship is given below. This relationship is also plotted on Figure 5.12.

$$\frac{P(z)}{P_{INF}} = 1 - \frac{R^2}{16Z^2} \quad (5.4)$$

The three power variations are shown in Figure 5.12. Only the CFD and modified actuator disc extend to zero height. The CFD solution intersects the origin. This point corresponds to a disc resting on an infinitesimally thin cushion of air with negligible fluid flow through the disc. The modified actuator disc [5.2] reduces to zero power at  $Z/R=0.25$ , which implies that no power is required whilst hovering at this height. This part of the curve is recognised as erroneous within the reference, but it is emphasised that in reality this region is not used because the helicopter fuselage prevents this.

The experimental data is somewhat incomplete. The three heights for which data are available are  $Z/R=0.8, 1.2$  and  $1.6$ . This data does not provide a conclusive trend that can be compared against the other analytical and computational plots.

This study indicates that these novel composite boundary conditions provide a complete and plausible solution that has not previously been achieved either numerically or analytically.

## 6 2D Helicopter Flight Over a Frigate Helideck

### 6.1 Introduction

The contents of this chapter were presented at two conferences, [6.1] and [6.2]. All the results presented within this chapter are 2D in nature. A 2D study is less realistic than using three dimensions, however qualitative comparisons are made of the flow solutions and the influence on both power and control discussed.

### 6.2 The Rotor Model

A simple theoretical model of the helicopter main rotor was constructed within the computational domain. The method solves the governing Navier-Stokes equations as shown in equation (6.1). The main rotor was designed to reflect the loading and geometry of a Westland Lynx, that is the rotor radius is 6.5m and the mass is 5.2 tonnes. The thrust exerted by the rotor was evenly distributed across the disc. The force was exerted within the computational domain as shown in Figure 6.1. The figure indicates that the rotor thrust is exerted within the hatched areas. In these regions, the Navier-Stokes equations are modified by the addition of the vector  $\bar{B}$ , as shown in equation (6.1); elsewhere  $\bar{B}$  is zero.

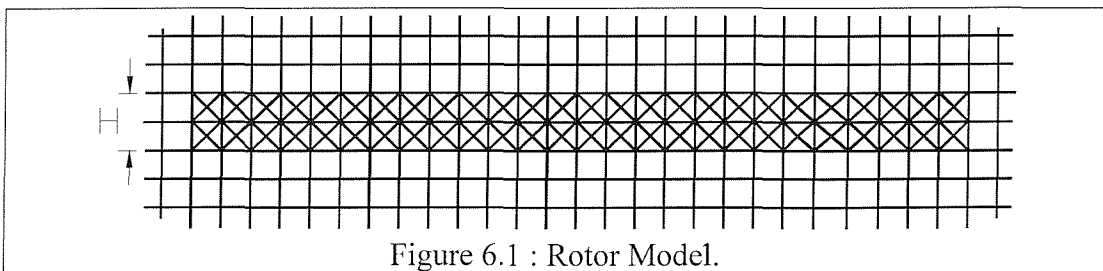


Figure 6.1 : Rotor Model.

$$\frac{\partial \rho \bar{V}}{\partial t} + \nabla \cdot (\rho \bar{V} \otimes \bar{V}) = \bar{B} + \nabla \cdot \sigma \quad (6.1)$$

The vector term  $\bar{B}$  has units of force per unit volume, therefore to exert the required thrust to the fluid,  $\bar{B}$  was defined as in equation (6.2).

$$\bar{B} = \begin{bmatrix} 0 \\ 0 \\ Thrust / Area / H \end{bmatrix} \quad (6.2)$$

The rotor is only manifested by the pressure step caused by the thrust; this has two implications. Firstly, the flow is in no way predetermined at the location of the rotor; the velocity and pressure are solved in exactly the same way as they are

throughout the rest of the domain. Secondly, the resultant vertical velocity component determines the induced power exerted across the rotor whilst the thrust always remains constant and acting through the centre of the rotor.

In all the flow solutions described within this paper the grid cell dimensions are 0.50m\*0.50m. The rotor is therefore 26 cells wide. Ideally the rotor would be one cell deep, but the flow solver can not resolve the sharp pressure gradients, and making the rotor two cells deep alleviates this problem.

This method of modelling a rotor within CFD has been discussed and verified in more detail in Chapter 4.

### **6.3 Modified Boundary Conditions**

The default boundary conditions available within CFX 4.1 and other commercial CFD software packages are applicable to external flows which comprise a free stream velocity and some body causing a perturbation, for example a wing or a building.

The air flow around a hovering helicopter is fundamentally different because there is no free stream velocity and all fluid flow is induced by the helicopter rotor itself. For this reason, applying any of the available boundary conditions such as an imposed velocity or pressure is unjustifiable and gives physically incorrect flow solutions. The novel boundary conditions, described in Chapter 4, are used in all the flow solutions below.

### **6.4 Rotor In Hover**

To verify that both the boundaries employed and the rotor model work as intended a test case was run to model the rotor in hover with no cross wind. Both two and three dimensional cases were obtained. In each case the fluid used was air with a density  $1.2\text{kg/m}^3$  and viscosity  $1.8 \cdot 10^{-5}\text{Ns/m}^2$ . The fluid was considered isothermal, incompressible and turbulent.

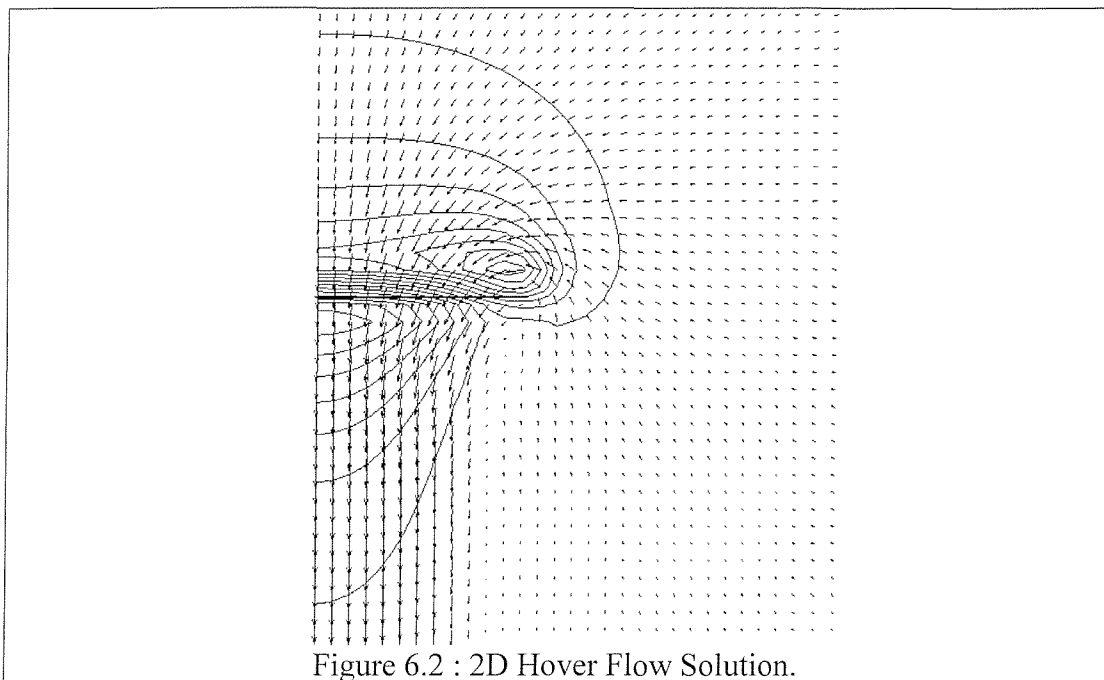
The two dimensional case modelled a disc of diameter 13m and unit thickness. The thrust per unit area used is described in equation (6.3); these values were chosen to reflect the Westland Lynx. The total thrust exerted was 4996.2N. Half

of the flow solution is shown in Figure 6.2. The contours represent pressure variations of 25Pa.

$$\text{Thrust / Area} = 5200 * 9.81 / (\pi * 6.5^2) = 384.3 \text{Pa} \quad (6.3)$$

In order to gauge the validity of the flow solution, momentum and energy principles from existing actuator disc theory were compared to the computational results.

The momentum in the downwash was obtained, as described in equation (6.4). This integral was evaluated 20m below the plane of the disc, across the downwash.



$$\Phi = \rho \int_{A_{DW}} w^2 dA = 4980N \quad (6.4)$$

The discrepancy between the momentum in the downwash and the thrust exerted at the rotor is 0.3%. This indicates that momentum has been effectively conserved within the system and Newton's equation is satisfied.

The power exerted by the rotor was evaluated as described in equation (6.5). This integral is performed across the plane of the rotor itself. The power derived is per unit depth, and thus is not comparable to the power exerted over the whole rotor plane.

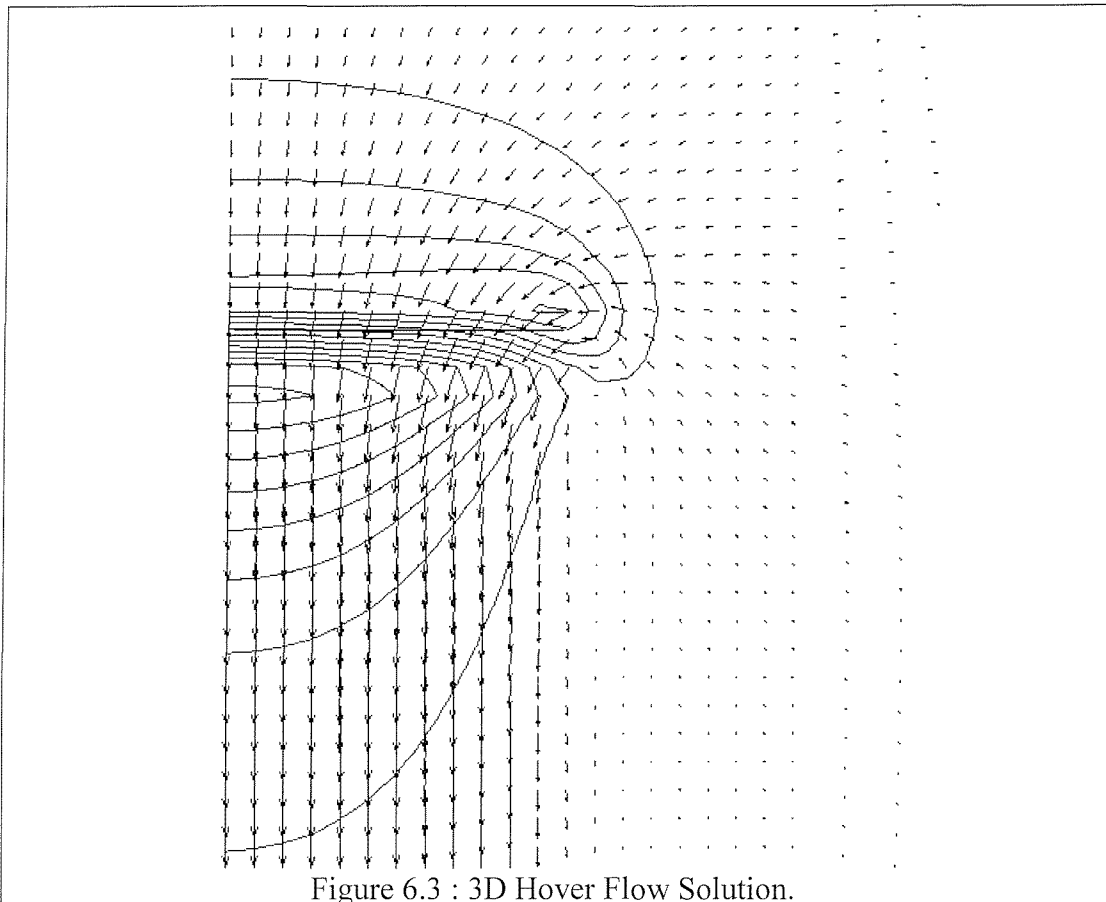
$$P_H = \int w \cdot \Delta p \cdot dA = 67.4kW \quad (6.5)$$

The ideal power as found from standard actuator disc theory is shown in equation (6.6). The difference between the predicted ideal power and the measured power is 7%.

$$P_{IDEAL} = T \cdot \sqrt{T / (2 \cdot \rho \cdot A)} = 63.2kW \quad (6.6)$$

The 7% discrepancy between the two values can be attributed to variations in the induced velocity across the rotor that are not permitted within actuator disc theory. Such a difference is realistic since 10-15% is a typical range used in the helicopter industry. The calculated power 67.4kW is carried forward to studies of the flow around the ship helideck.

A further study of a three dimensional rotor was performed, with the thrust per unit area kept constant. The flow solution is shown in Figure 6.3. The solution is axisymmetric; Figure 6.3 corresponds to an azimuth angle of  $0^0$ . The vectors represent speed and the contours pressure variations of 25Pa.



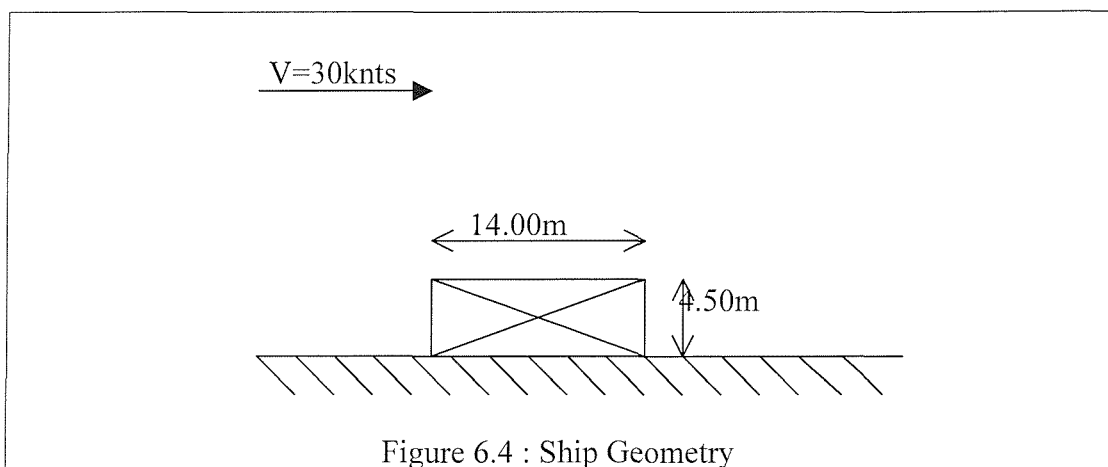
Comparison of momentum in the downwash and thrust applied yielded a 0.2% discrepancy. The power exerted at the plane of the disc was 3% greater than the ideal value predicted by actuator disc theory.

## 6.5 Ship Airwake

Apart from operational and performance calculations, the airflow around the ship in the absence of the helicopter thrust is of interest for other reasons, such as helicopter blade strike predictions during rotor engagement and disengagement.

A flow solution was obtained for a 2D model of a helideck. The geometry of the ship is shown in Figure 6.4. The domain extended 75m upwind, downwind and above the centre of the ship. A horizontal free stream velocity of 30 knots was imposed. The dimensions of the helideck are those used by the TTCP Nations for their research into the Helicopter Ship Dynamic Interface<sup>1</sup>.

Both the sea and ship were modelled as walls; zero flow was imposed at these surfaces. The k- $\epsilon$  turbulence model was used and the flow was assumed to be turbulent, incompressible and isothermal. Plate [6.3] was used to determine the turbulent kinetic energy imposed at the windward edge of the domain. Veersteg [6.4] was used to determine a realistic mixing length for the initial turbulence dissipation constant, epsilon.

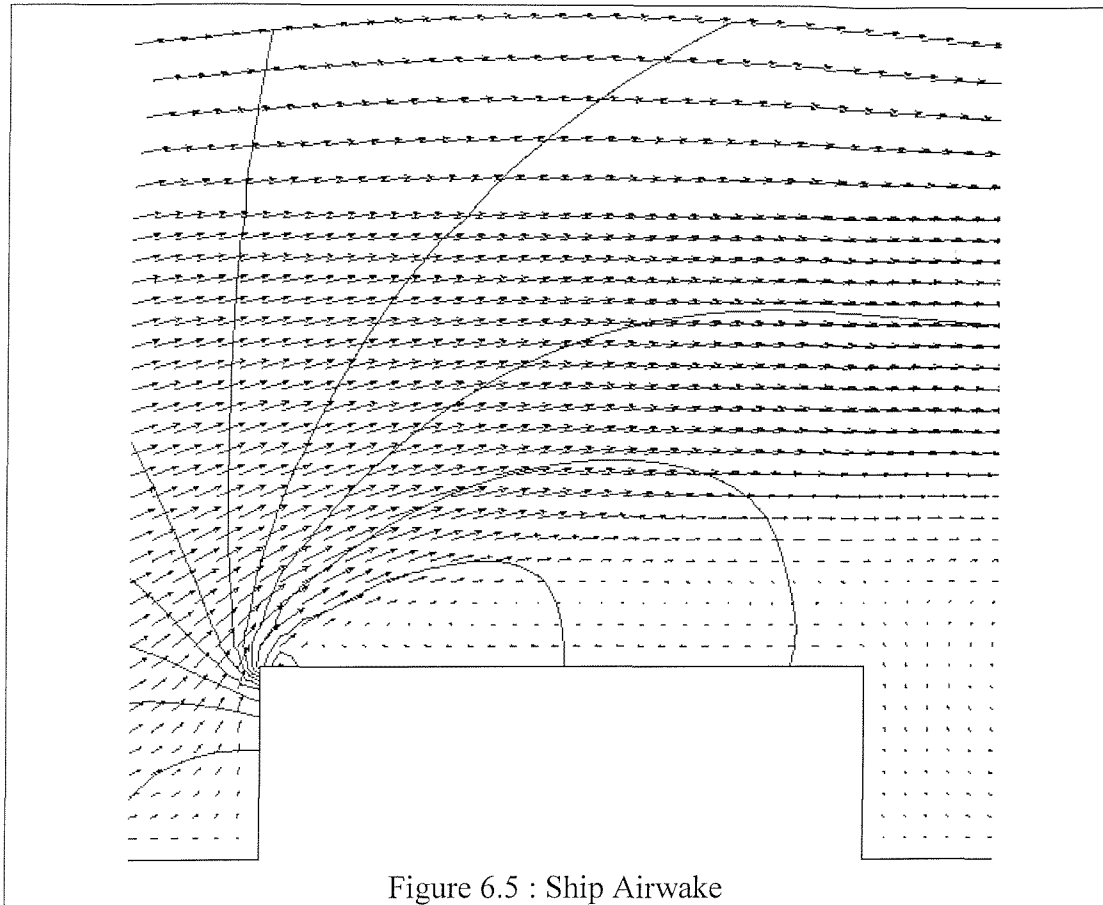


The flow solution is shown in Figure 6.5. The arrows represent the velocity vectors, and the contours are pressure contours at 25Pa intervals. The figure

---

<sup>1</sup> Tripartite Technical Co-operation Program, national defence research organisations from, UK, USA, Canada and Australia.

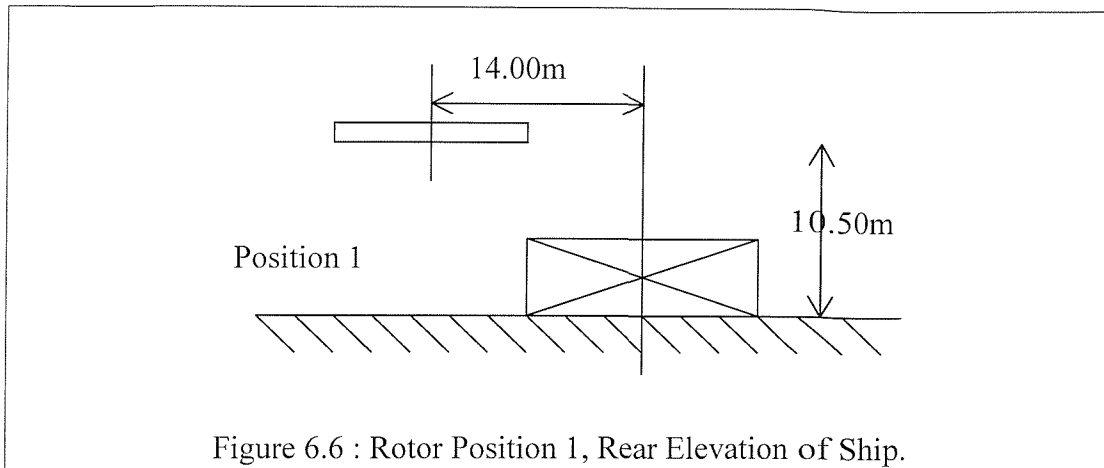
shows the flow separating at the windward edge of the helideck and a large region of recirculation both above and downwind of the ship. This flow pattern agrees with experimentally measured data published by Newman [6.5].



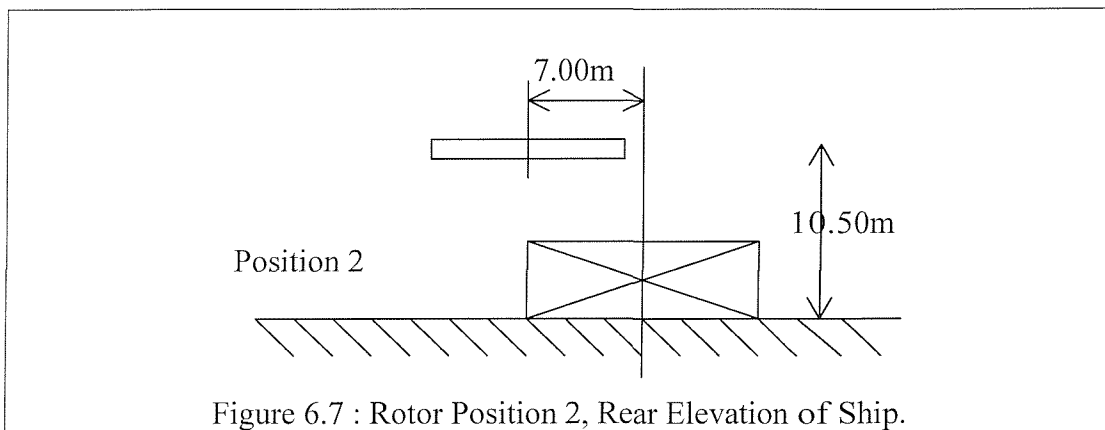
## 6.6 Ship/Helicopter Interaction

The geometry of the ship used is the same as that described in Section 6.5. Three positions for the main rotor were chosen, which broadly reflect the final part of a conventional flight path the helicopter traces as it approaches the ship to land. The helicopter approaches the ship from astern on the port side. The pilot traverses the side of the ship to a position above the landing spot before putting down on the deck.

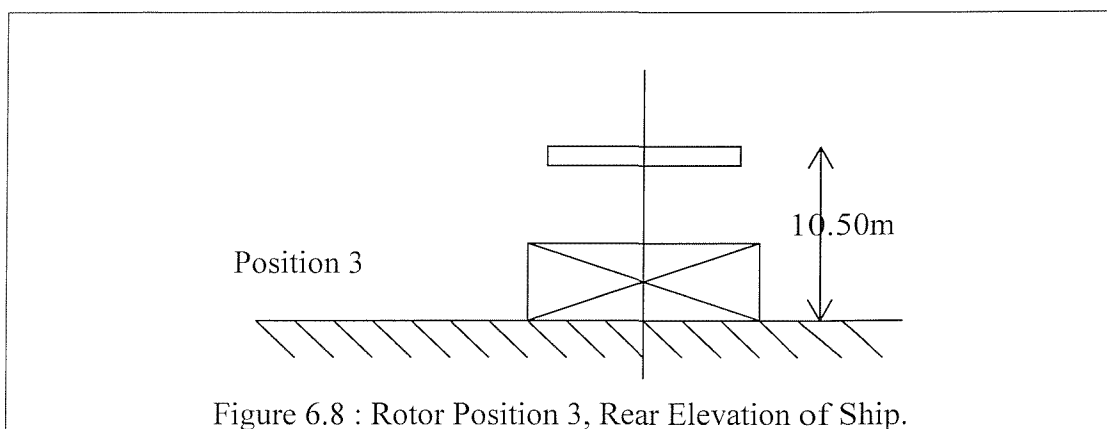
The first position is shown in Figure 6.6; the rotor is at a height of 10.5m above sea level and 14m to port of the centreline of the helideck. The second position is 7m to port of the centreline as shown in Figure 6.7, and the rotor is placed over the centreline of the ship in Position 3 shown in Figure 6.8.



Four wind velocities were chosen relative to the ship, zero, 30 knots port to starboard, 30 knots starboard to port and 60 knots port to starboard. Flow solutions were obtained for all of these wind velocities, with the rotor at each of these positions.



The flow solution was solved as incompressible, isothermal and turbulent. The  $k-\epsilon$  turbulence model was used, the turbulent kinetic energy and energy dissipation parameters were determined as described in Section 6.5.



The solver could not achieve a steady state solution for any of the problems due to the turbulent unsteady nature of the flows; the solutions were obtained using a time-stepping approach. The results presented in the following sections are

therefore instantaneous and represent a snapshot of the flow solution, after the rotor has been stationary in the given location for at least 30 seconds.

There are two factors that limit helicopter operations in adverse weather conditions, namely power and control. The pilot must have adequate quantities of both in order to perform manoeuvres. As outlined in Section 5, the power required to hover out of ground effect in still air is 67.4kW. The power to hover in a stationary position with the given cross winds was calculated using equation (6.7). For each of the flow solutions generated the corresponding power was calculated accordingly.

$$P = \int w \cdot \Delta p \cdot dA \quad (6.7)$$

The lateral wind that the rotor experiences was also quantified.  $V_{AV}$  is the average lateral velocity component across the entire span of the rotor.

Whilst the power required to maintain a certain hover position is important, control requirements are as significant. For this reason the vertical flow velocities have been recorded near the extremities of the rotor.  $W_P$  and  $W_S$  correspond to the vertical flow 5m to port and 5m to starboard of the rotor centre respectively. (5m is approximately 75% of the rotor radius.) These values not only indicate the velocity gradients across the rotor but also provide a measure of control demanded.  $\Delta W$  is the difference between the vertical components  $W_P$  and  $W_S$ .

For future development, a three dimensional analysis could be extended to include blade element theory and inverse simulation. Vertical velocity components would provide an estimate of cyclic and collective pitch variations that achieve the required thrust magnitude and distribution. This has not been attempted to date because these flow solutions are two dimensional and provide a qualitative understanding of the flow regimes. The techniques are under development and 2D cases are much less demanding of time during the validation phases of the model.

### 6.6.1 Zero Wind

The flow solutions for hover in each of the three positions are shown in Figure 6.9 to Figure 6.11. The arrows represent velocity vectors and the contours are spaced

at 100Pa in the first two flow solutions and 40Pa in the final flow figure. The computed power requirements are shown in Table 6.1.

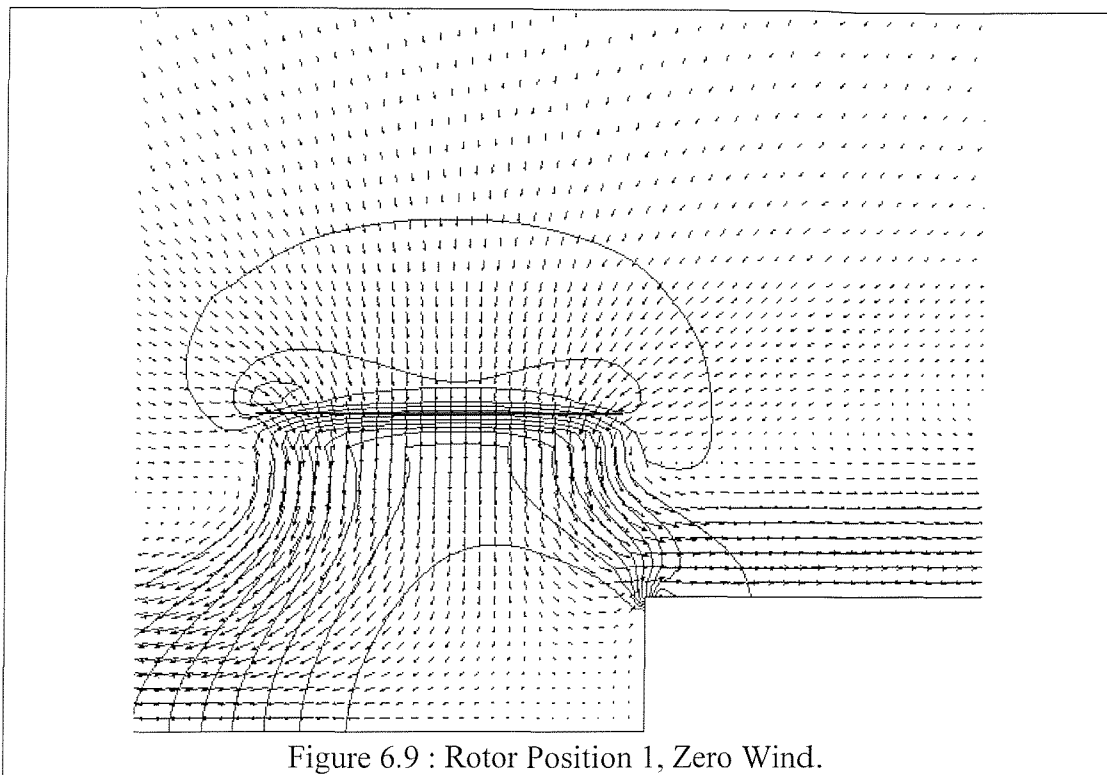


Figure 6.9 : Rotor Position 1, Zero Wind.

In Position 1 the rotor downwash divides into two parts. One part travels over the ship and the other part moves away over the sea surface. The flow through the rotor itself is approximately vertical.

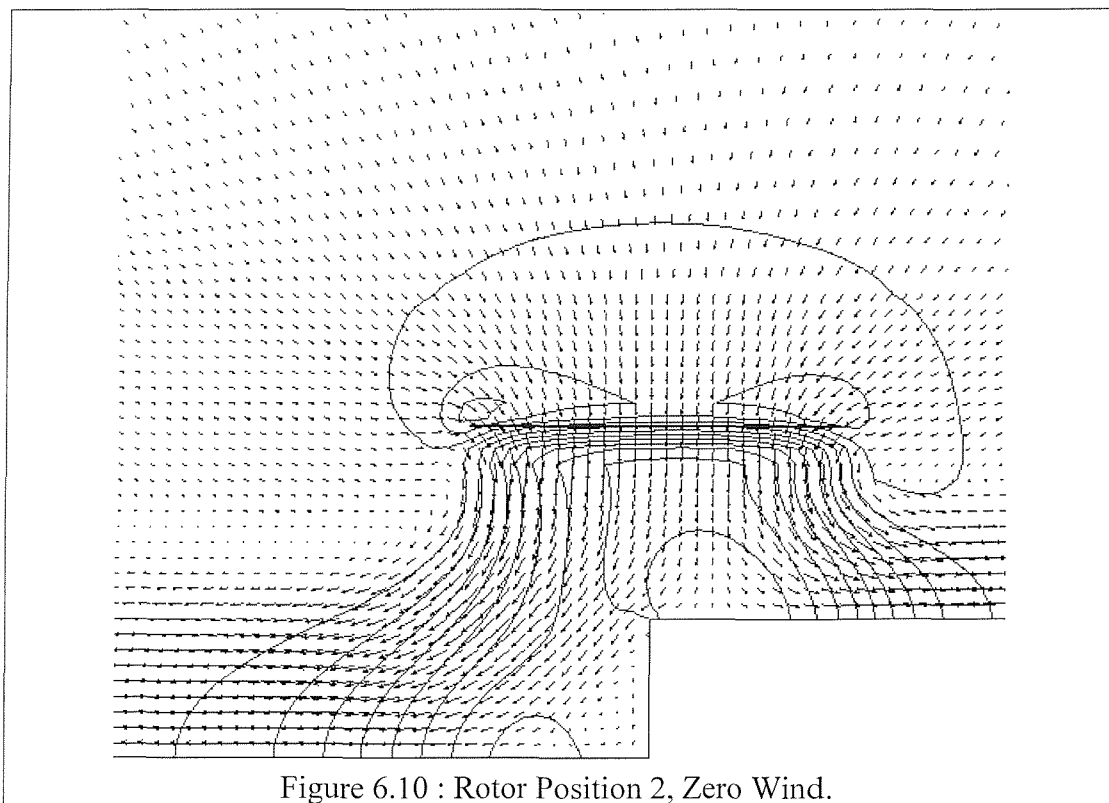


Figure 6.10 : Rotor Position 2, Zero Wind.



Position	1	2	3
P (kW)	62.1	59.8	49.9
%P <sub>H</sub>	92	89	74
V <sub>AV</sub> (ms <sup>-1</sup> )	0.8	0.5	0.0
W <sub>P</sub> (ms <sup>-1</sup> )	-14.2	-14.3	-13.9
W <sub>S</sub> (ms <sup>-1</sup> )	-14.9	-14.5	-13.9
ΔW(ms <sup>-1</sup> )	0.7	0.2	0.0

Table 6.1 : Power and Control Requirements, Zero Wind.

The values V<sub>AV</sub> are the average lateral velocities across the rotor span. The rotor in position 3 has V<sub>AV</sub> of zero consistent with symmetrical flow. The other two positions have small lateral flows across the rotor. The difference in vertical flow across the span is also small in all three positions.

### 6.6.2 Wind 30 Knots, Port to Starboard.

These three flow solutions were determined with a 30 knot free stream velocity acting from port to starboard, which appears left to right in the figures. The pressure contours are spaced at 40Pa.

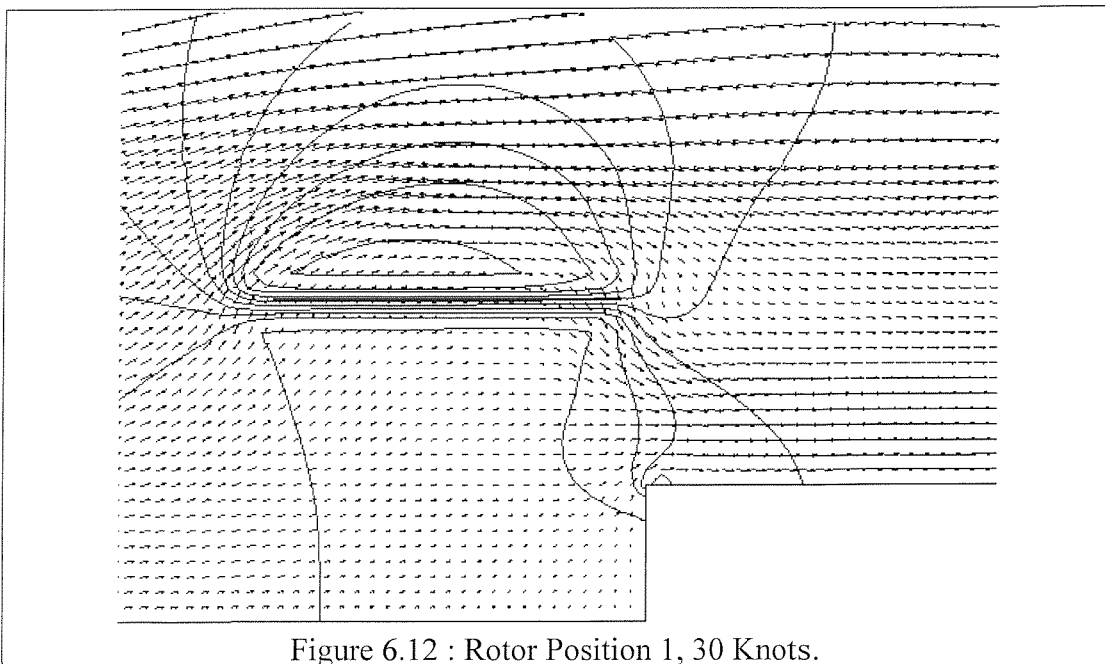


Figure 6.12 : Rotor Position 1, 30 Knots.

The flow solution for the outboard position is displayed in Figure 6.12. This figure shows a large low pressure region above the rotor and a weaker high

pressure region below the rotor. However there is little vertical flow through the rotor itself. The model shows the balancing of the rotor downwash with the upflow generated by the ship. This is reflected in the power exerted, as shown in Table 6.2. There is however a large vertical velocity gradient across the rotor. The fluid is passing upward through the rotor on the port side and downward at the starboard side. This represents increased control requirements.

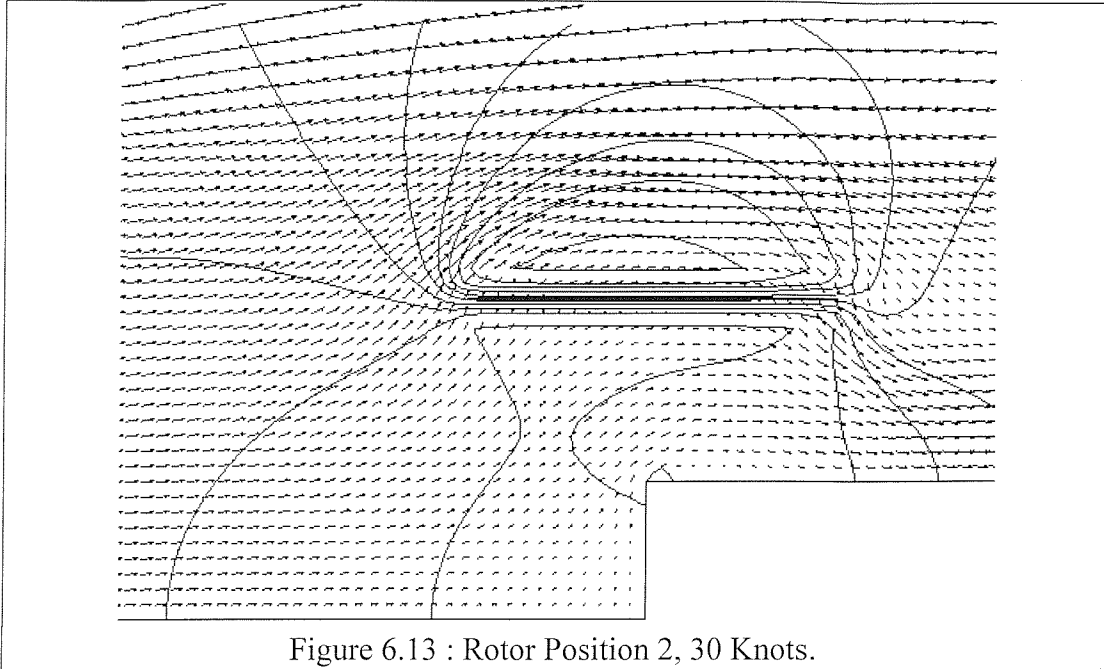


Figure 6.13 : Rotor Position 2, 30 Knots.

Figure 6.13 shows the flow solution with the rotor over the side of the ship. At this position the helicopter is resting in the upflow generated by the blockage of the ship. The power requirements are negative as shown in Table 6.2. This indicates an autorotative state. The lateral velocity the rotor experiences is 4.6m/s or 9 knots. This is in fact less than the undisturbed free stream velocity of 15 knots. This flow also exhibits a large vertical velocity variation across the span, 10.9m/s with correspondingly high resulting control demands.

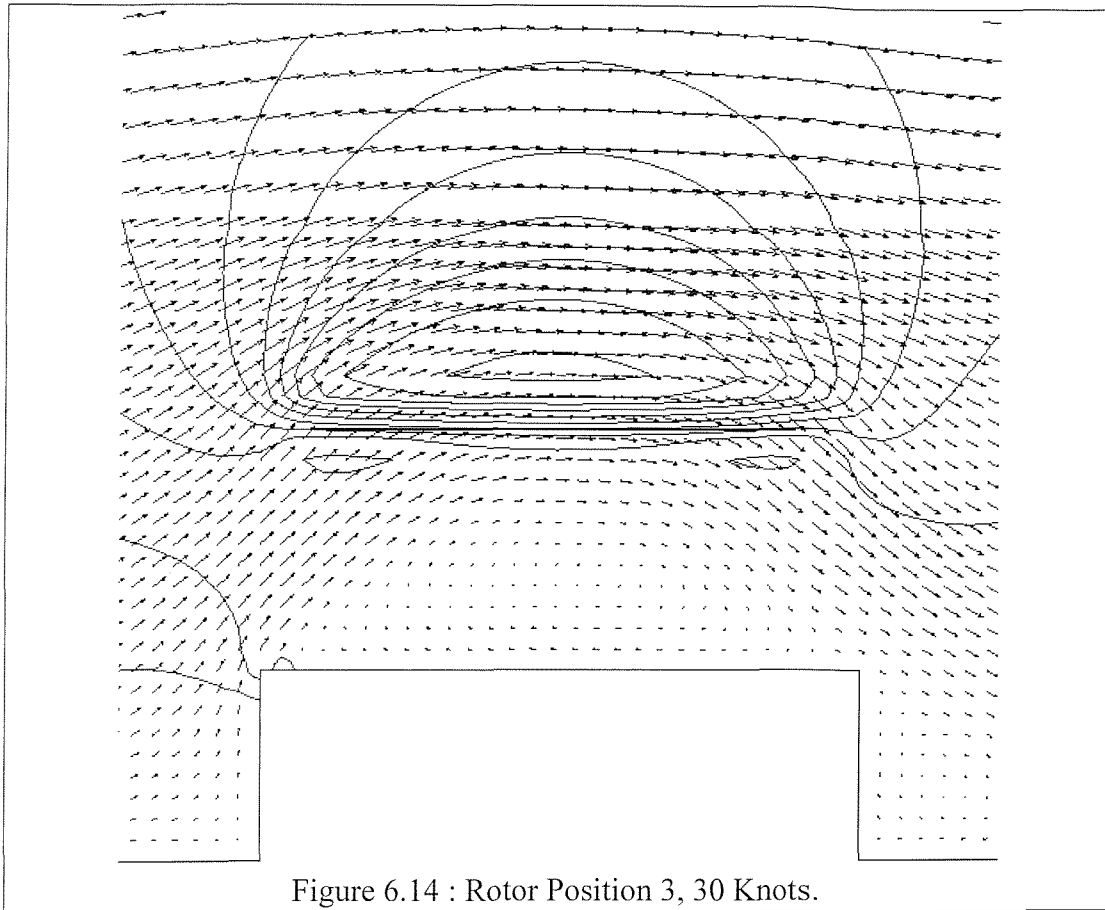


Figure 6.14 : Rotor Position 3, 30 Knots.

The rotor over the ship's centreline is shown in Figure 6.14. Similar to the other positions the induced power is small due to the upflow across the rotor. The most noticeable feature of the flow solution is the lateral velocity the rotor experiences, 10.9m/s or 21knots. This is more than double the other two positions caused by only a small change in position of the rotor. As with the other two positions the fluid is flowing upwards through the rotor on the port side and downwards on the starboard side.

Position	1	2	3
P (kW)	-0.2	-1.0	0.0
%P <sub>H</sub>	0	-1	0
V <sub>AV</sub> (ms <sup>-1</sup> )	3.5	4.6	10.9
W <sub>P</sub> (ms <sup>-1</sup> )	3.9	4.2	6.1
W <sub>S</sub> (ms <sup>-1</sup> )	-7.0	-6.6	-7.6
ΔW(ms <sup>-1</sup> )	10.9	10.8	13.7

Table 6.2 : Power and Control Requirements, 30 Knots Port to Starboard.

Table 6.2 shows that in these cases there is little power exerted at the rotor and the rotor is operating in significantly less lateral wind than the free stream of 15.4m/s. However the rotor is experiencing widely varying flow vertical flow across its span. In reality this would necessitate large cyclic pitch variations to trim the helicopter.

### 6.6.3 Wind 60 Knots, Port to Starboard

These three flow solutions were generated using a free stream velocity of 60 knots acting from port to starboard. The pressure contours are spaced at 75Pa.

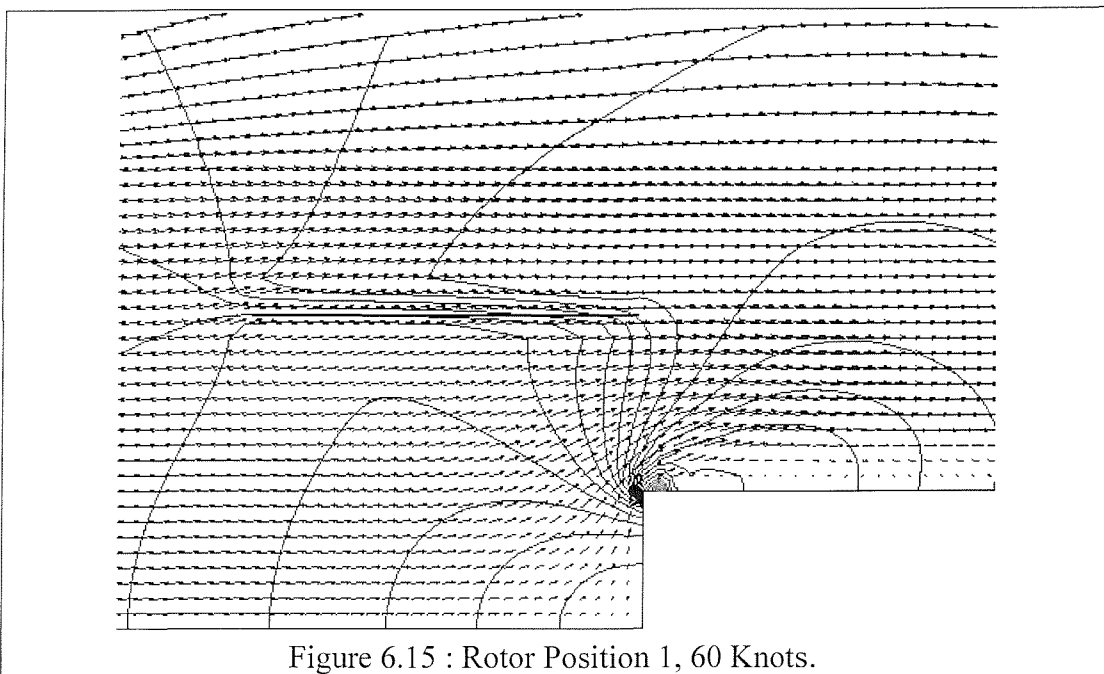
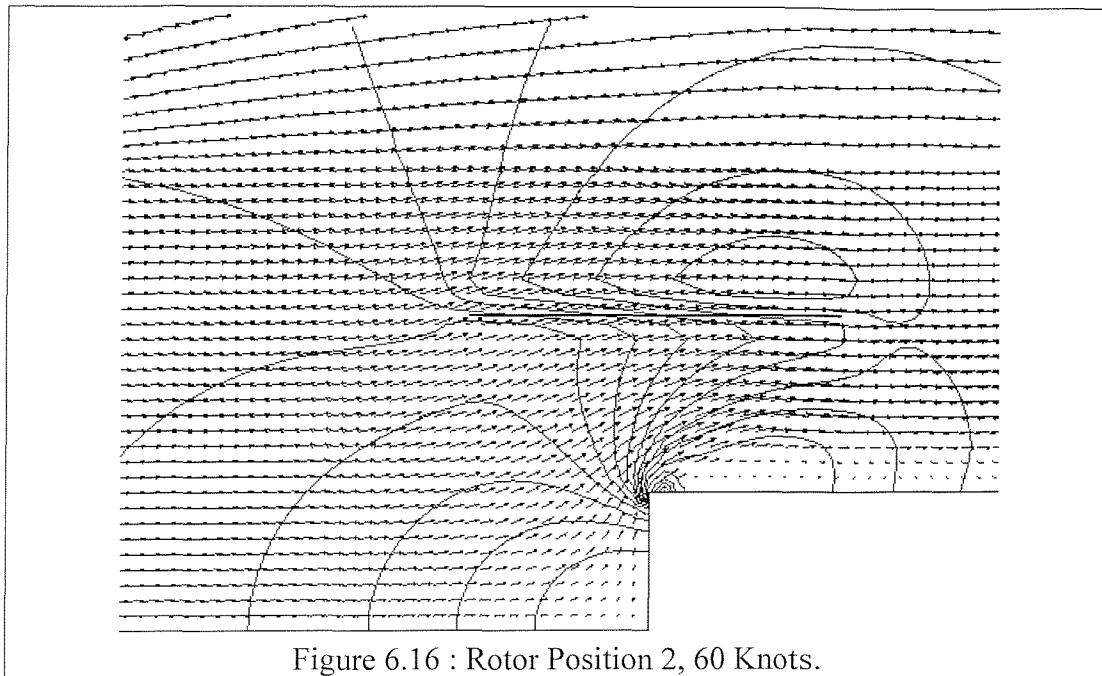


Figure 6.15 : Rotor Position 1, 60 Knots.

Figure 6.15 shows that the flow around the rotor in Position 1 is largely influenced by the free stream and the presence of the ship's helideck. The greatest pressure

gradients occur at the windward edge of the deck, not at the rotor. The rotor is operating in a strong upflow resulting in a negative power requirement, as shown in Table 6.3. The lateral wind speed across the rotor is 23.8m/s which is less than the undisturbed free stream velocity.



The flow solution for the rotor above the side of the ship is shown in Figure 6.16. In many respects this is similar to the rotor in the outboard position. The rotor is operating within an upflow greater than the outboard position, shown in Figure 6.15, resulting in a larger negative power at the rotor. The rotor is operating in 28.2m/s cross wind flow, which is similar to the case of free stream velocity of 60 knots.

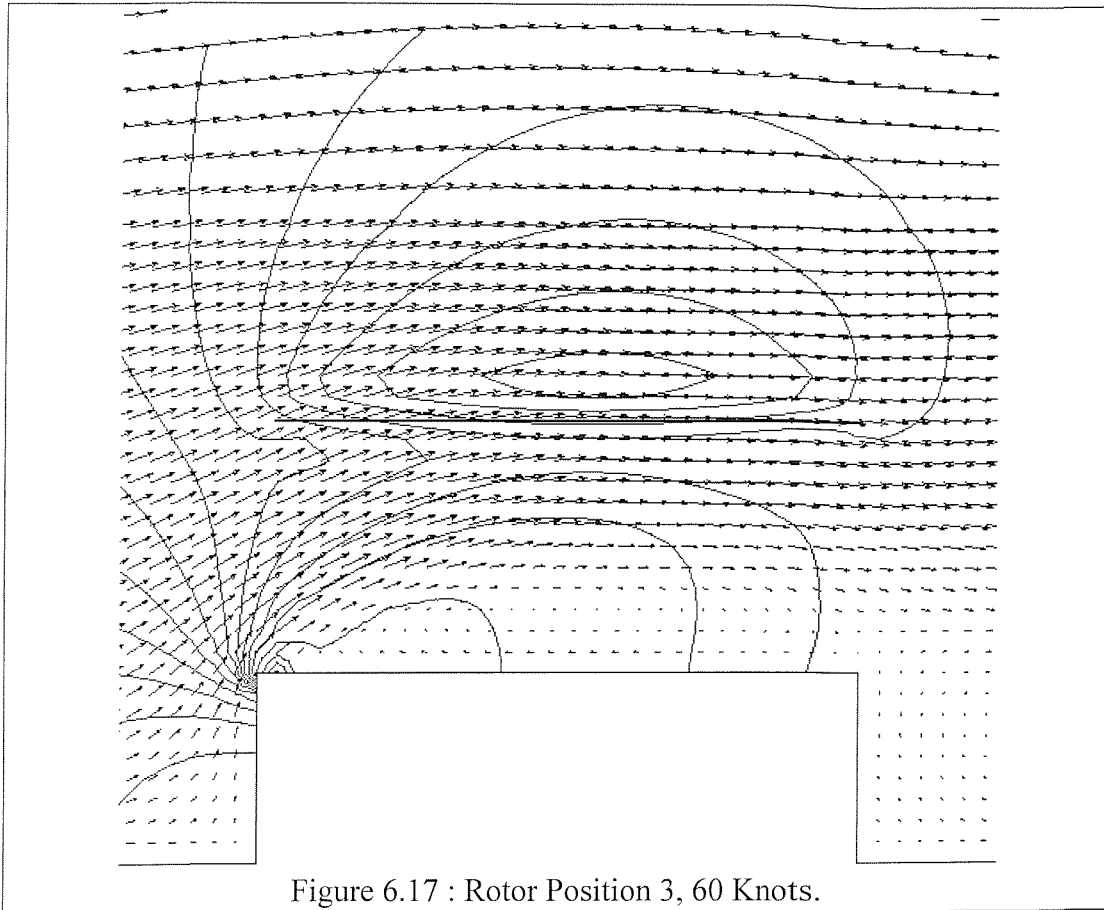


Figure 6.17 : Rotor Position 3, 60 Knots.

The flow solution for the rotor over the centreline of the ship is shown in Figure 6.17. The airflow and pressure variations are clearly dominated by the ship. The rotor is operating in an upflow generated from the ship, causing a large negative power requirement. The lateral wind speed across the rotor is 65 knots, which is greater than the free stream velocity. The vertical flow of fluid through the rotor varies by 13.3m/s between the port and starboard reference points.

Position	1	2	3
P (kW)	-21.8	-26.1	-20.1
%P <sub>H</sub>	-32	-39	-30
V <sub>AV</sub> (ms <sup>-1</sup> )	23.8	28.2	33.3
W <sub>P</sub> (ms <sup>-1</sup> )	5.8	7.9	10.5
W <sub>S</sub> (ms <sup>-1</sup> )	3.4	0.9	-2.8
ΔW(ms <sup>-1</sup> )	2.4	7.0	13.3

Table 6.3 : Power and Control Requirements, Wind 60 Knots, Port to Starboard.

These flow solutions indicate that although power requirements are small or negative the helicopter has to contend with accelerated side winds and large velocity gradients across the span of the rotor.

#### 6.6.4 Wind 30 Knots, Starboard to Port

The flow solutions within this section were obtained with a free stream velocity of 30 knots, which therefore appears right to left in the figures.

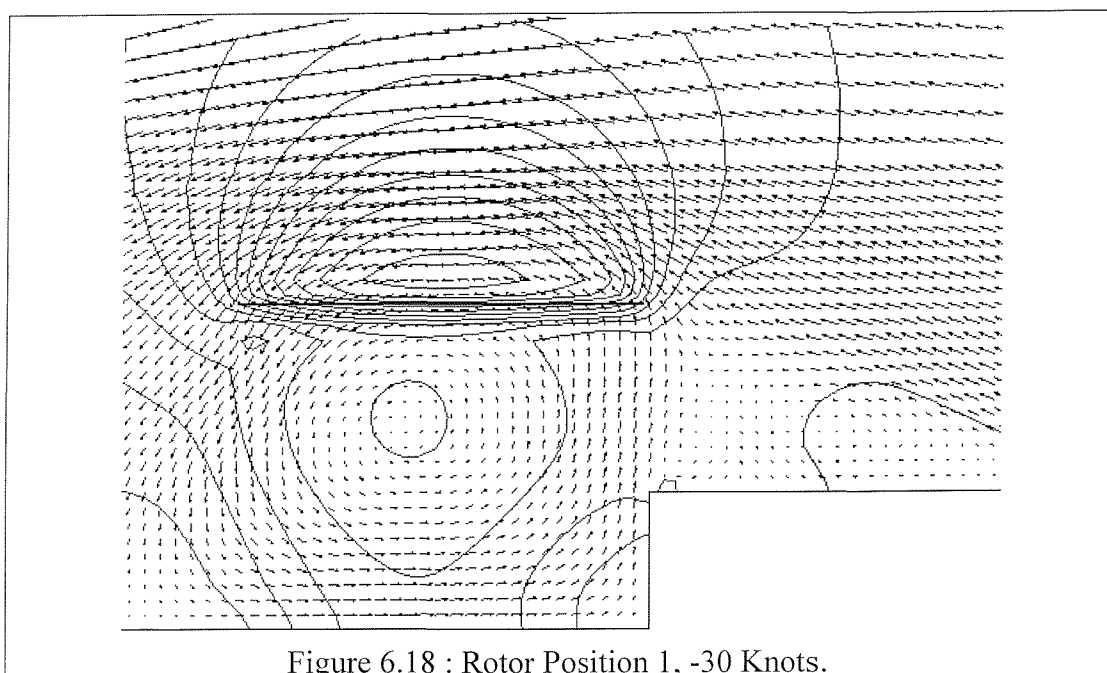
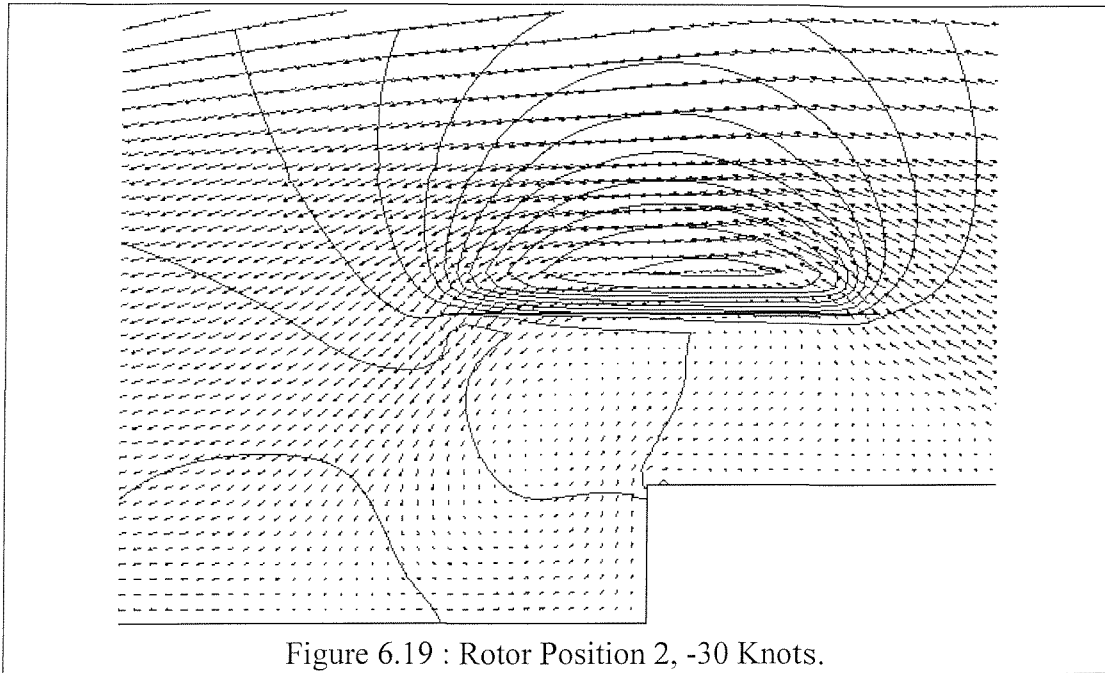


Figure 6.18 : Rotor Position 1, -30 Knots.

The rotor operating in the outboard position is shown in Figure 6.18 . The solution shows that the flow separates at the windward edge of the helideck and the deck is covered in an area of recirculation. There is another recirculation region downstream of the ship, where the downwash of the rotor travels down to

the sea surface and upwind to the ship, and finally up towards the rotor. This vortex appears to be small and does not contribute adversely to the power requirements as given in Table 6.4. The power exerted at the rotor is only a fraction of the power exerted in the simple hover case. The flow across the rotor is a 8m/s, this is less than the free stream velocity. The variation between the vertical velocity component at the port and starboard end of the rotors is large, 16.8m/s.



The flow pattern corresponding to the rotor in Position 2 is shown in Figure 6.19 above. The rotor has a large region of low pressure above the rotor whereas there is little pressure increase below the rotor. The angle of the separation at the windward edge of the deck is greater than that found in the previous flow solution, indicating the rotor downwash being ‘fed’ into the separation region above the deck. The power exerted by the rotor within the solution is only 8.8kW, which is only 14% of the power required in hover.

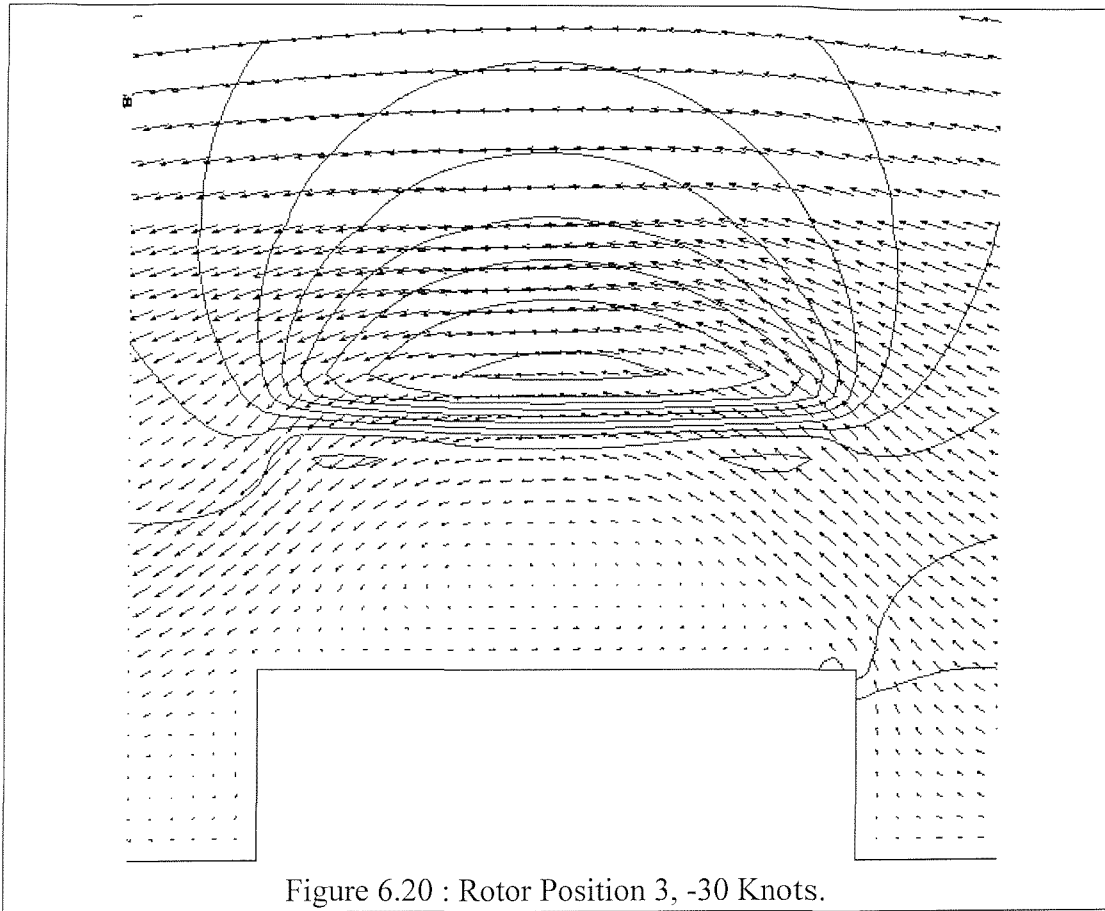


Figure 6.20 shows the flow solution for the rotor over the ship centreline, which is an exact reflection of Figure 6.2 . The upflow of the air over the ship causes the air to flow upwards through the rotor at the windward end. At the leeward end of the rotor the air is flowing downwards. The net effect of the up and down flow is a zero power requirement. The lateral wind speed across the rotor, shown in Table 6.4, is 10.9m/s, this is less than the free stream velocity.

Position	1	2	3
P (kW)	8.7	6.8	0.0
%P <sub>H</sub>	13	10	0
V <sub>AV</sub> (ms <sup>-1</sup> )	-8.0	-6.0	-10.9
W <sub>P</sub> (ms <sup>-1</sup> )	-11.5	-9.0	-7.6
W <sub>S</sub> (ms <sup>-1</sup> )	5.4	3.3	6.1
ΔW (ms <sup>-1</sup> )	-16.8	-12.3	-13.7

Table 6.4 : Power and Control Requirements, Wind 30 Knots, Starboard to Port.

These three flow solutions exhibit limited power requirements and lateral flow speeds but large velocity gradients across the rotor span.

## 6.7 Conclusions

These results combine the ship airwake and the helicopter induced flow and from the results clear indications of power and control requirements are evident. With no side winds the helicopter rotor experiences slight power increases, but there are negligible lateral flows to contend with. The vertical flow is approximately constant across the span of the disc so the control requirements are limited.

The three cases that considered the 30 knot wind from the port side all exhibited net power of around zero. However the large velocity gradients across the rotor indicate high demands on pilot and rotor control.

The 60 knot wind cases indicated that the ship airwake was predominant and the helicopter thrust caused small disturbances by comparison. In these cases the net power was negative. The helicopter over the ship's centreline experienced local wind speeds greater than the free stream velocity. In these cases the variation of vertical velocity flow across the span was actually less than those in the 30 knot cases.

Regarding wind from the starboard side of the ship, that was shown in Section 6.6.4, once again the power requirements were minimal compared to that of the hover. However the rotor experiences the most dramatic vertical velocity gradients across the rotor in these cases.

This study indicates that the control requirements of the helicopter are more likely to limit safe operations than the power limitations. The vertical velocity variations evident in the flow solutions are not found in any other normal operations, such as hover or forward flight.

The geometries considered have only dealt with a lateral wind relative to the ship and therefore do not include any downflows due to the influence of the ship's superstructure.

These results provide a qualitative measure of the flow variations around the ship and helicopter because of the two dimensional nature. In reality the flow is far from two-dimensional and some of the features exhibited in these solutions will be less prominent, for example, the upflow through the rotor when the rotor is upwind of the ship. In a three dimensional solution, the air can travel laterally around the rotor, rather than remaining in the same plane and being forced through the rotor. This will, in turn, affect the power predictions which are predicted from induced velocities at the rotor plane.

The boundary conditions and rotor model employed for a three dimensional case are identical to those used for the two dimensional study. The computational resources for a three dimensional study far exceed those of the two dimensional study undertaken presently. However this study demonstrates the viability of CFD in order to predict accurate flow solutions and resultant power and control requirements.

## **7 3D Forward Flight Inflow Models.**

### **7.1 Summary**

The airflow through helicopter rotor blades in forward flight is highly complex. There are various rotor wake models which provide some insight into the flow regime. The most simple is actuator disc theory which uses momentum principles to balance flow variations with external thrust and drag force considerations. This theory assumes a uniform thrust and does not allow for any variations of induced velocity over the rotor radius or azimuth.

This chapter compares the flow through the computational rotor, discussed in Chapter 4, with established theories. The ‘constant thrust’ rotor model is flown at various speeds and the resultant solutions are compared to the inflow predicted by Castles and DeLeeuw [7.1]. The ‘blade element thrust’ model solution is compared to the work of Mangler and Squire [7.2].

No CFD result can be justified without an extensive sensitivity study, this is performed in Section 7.6.

### **7.2 Description of Geometry and Boundary Conditions.**

The domain was cubic in shape with sides of length 60m, with the rotor placed at the centre. The grid at the centre was orthogonal; all the grid cells in the central region are cubes of length 1m. The free stream velocity was introduced using the boundary conditions developed in Chapter 4, which couple pressure and velocity. The freestream direction was horizontal acting along the y axis. The rotor was horizontal, in the x-y plane. The computational domain is shown in Figure 7.1.

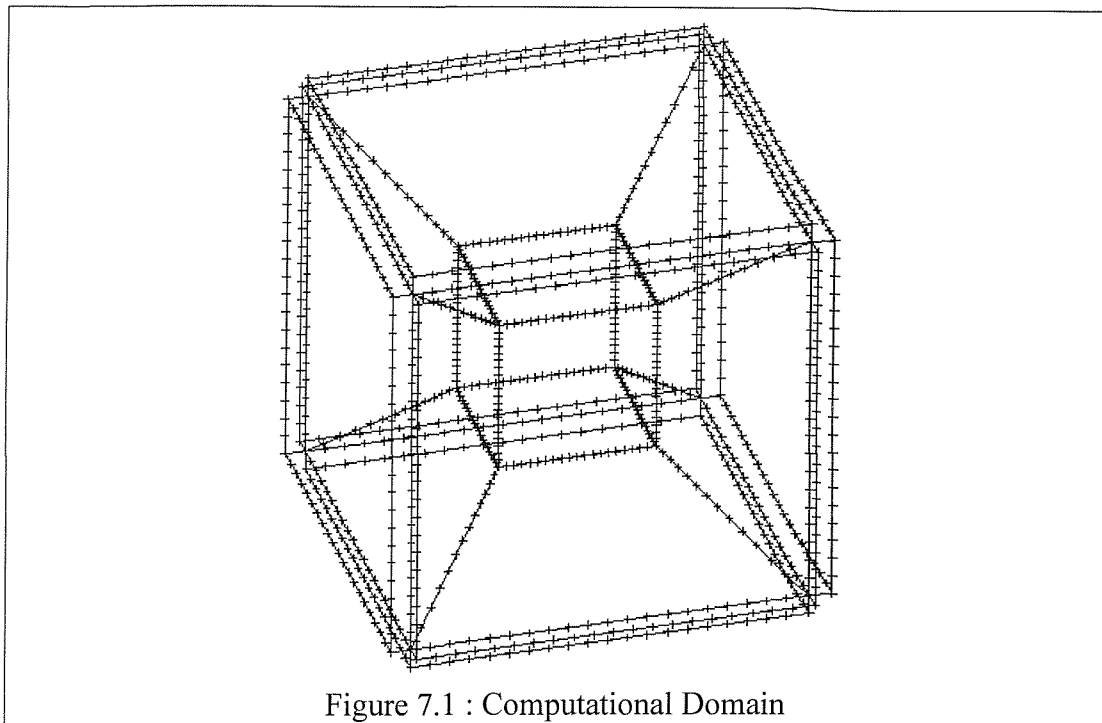


Figure 7.1 : Computational Domain

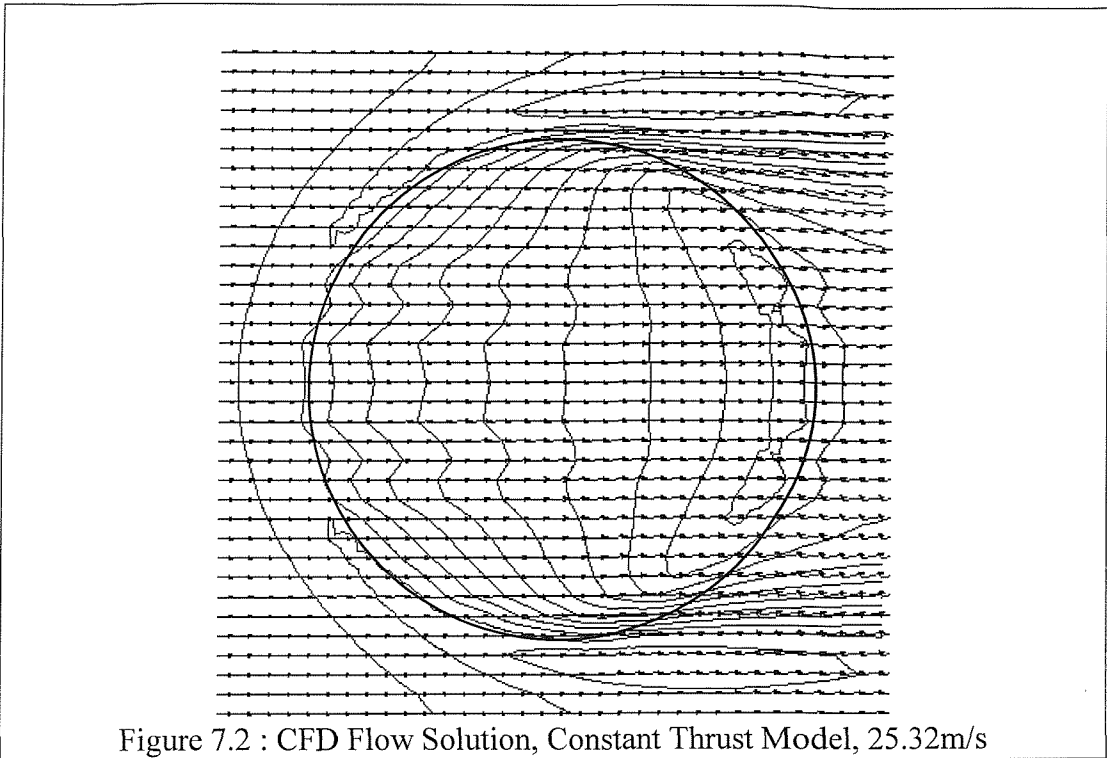
The two rotor models are described in detail in Chapter 4.

### 7.3 Constant Thrust Model, Forward Flight

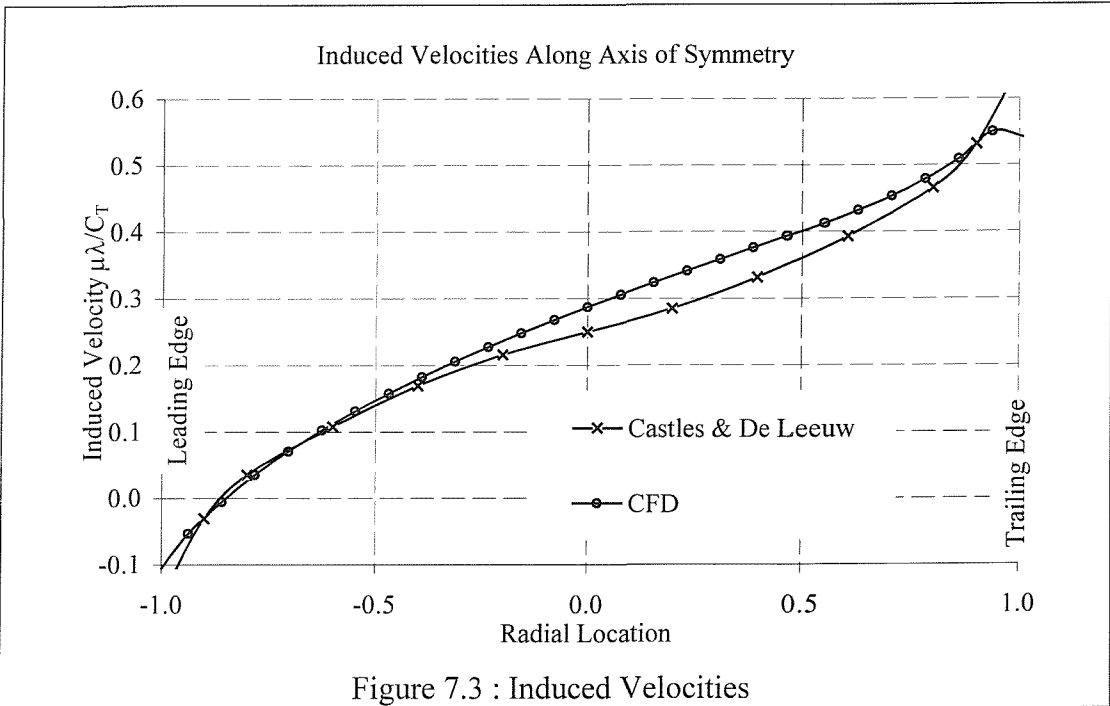
#### 7.3.1 Induced Velocity Along Rotor Centreline

Castles and DeLeeuw [7.1] assumed that the wake was ‘formed by a uniform and continuous distribution of vortex rings of infinitesimal strength, lying in planes parallel to the tip-path plane and extending downstream to infinity’. In addition to the Glauert factor,  $E$ , the induced velocity at all points over the rotor disc can be ascertained, but this involves extensive numerical calculations.

One comparison between CFD and Castles and DeLeeuw [7.1] is presented below. Using momentum theory and the ‘constant thrust’ rotor model, a forward speed of 25.32m/s gives an induced velocity of 6.33m/s. This gives the ratio of forward velocity and induced velocity as 4.0.



The CFD flow solution is shown in Figure 7.2; the vectors represent flow velocity and contours show 2m/s variations in induced velocity. The region of greatest induced velocity is at the aft edge of the rotor disc. The contours are approximately evenly spaced which is consistent with the Glauert model.



The induced velocities along the axis of symmetry are extracted from the flow solution and shown in Figure 7.3; these have been non-dimensionalised with respect to the advance ratio  $\mu$ , inflow ratio  $\lambda_i$  and coefficient of thrust  $C_T$ . Also

shown in this figure are the induced velocities found by Castles and DeLeeuw [7.5].

The comprehensive Castles and DeLeeuw relationship is roughly linear in the central regions but varies sharply at the extremities of the rotor disc.

The CFD inflow has overpredicted the average inflow velocity. The variation of the inflow with respect to the symmetry axis is approximately linear in the central region of the rotor disc. At the forward and rear edges of the disc the induced velocity is not linear but follows the Castles and DeLeeuw prediction.

### 7.3.2 Glauert Inflow Factor

#### 7.3.2.1 Introduction

Experimental observations indicate that the induced velocity does indeed vary both radially and azimuthally. H. Glauert proposed an inflow model [7.6], based on the induced flow generated by a skewed vortex tube, shown in equation (7.1). Thus the inflow is skewed such that the induced velocity is increased at the rear of the rotor and reduced in the leading half of the disc. The extent by which the inflow is skewed is determined by  $E$  which is known as the Glauert factor. The simplicity of the inflow model allows it to be implemented as the next step beyond a uniform downwash velocity. This model does not however include the presence of any discrete vortices.

$$v_{iG} = V_I \left( 1 + E \frac{r}{R} \cos \psi \right) \quad (7.1)$$

Castles and DeLeeuw [7.1] found that although the variation of induced velocity was not exactly linear, the Glauert model was a good approximation. They also discovered that the inflow factor,  $E$ , does vary according to forward velocity and their work has been used to derive the relationship in equation (7.2), as stated by Payne [7.5]. The inflow factor,  $E$ , is determined by the ratio of the forward velocity to the average induced velocity, which is normal to the rotor. These factors dictate the angle,  $\chi$ , at which the rotor wash is skewed from the vertical.

$$E = \frac{4}{3} \frac{\mu}{\lambda} \left( 1.2 + \frac{\mu}{\lambda} \right) \quad (7.2)$$

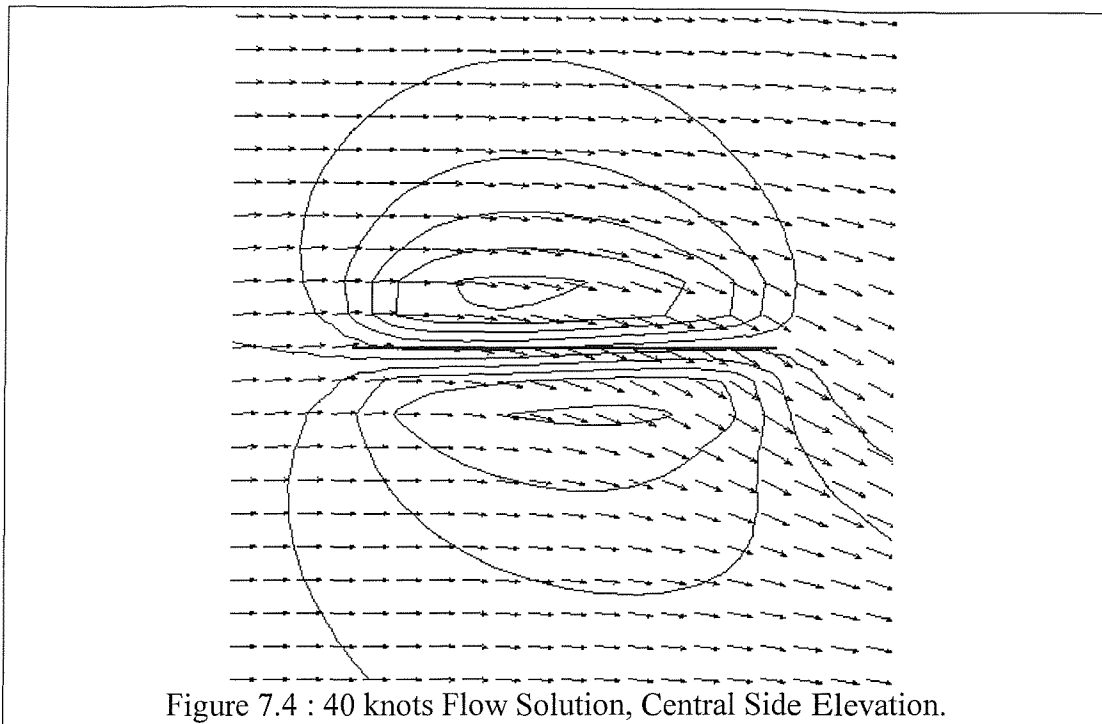
$$\tan \chi = \frac{\mu}{\lambda} = \frac{V_F}{V_I} \quad (7.3)$$

### 7.3.2.2 CFD Prediction and Analysis

Using the grid and boundary condition described in Section 7.2 and the constant thrust model described in Chapter 4, a series of flow solutions at various horizontal forward speeds was found. The forward speeds are given in Table 7.1; also shown are the inflow velocities found from momentum theory [7.3].

Forward Speed (knots)	Forward Speed (m/s)	Mean Induced Velocity $V_{i0}$	Inflow Ratio $\mu/\lambda$
0	0.0	12.85	0.0
5	2.6	12.72	0.2
10	5.1	12.35	0.4
20	10.3	10.98	0.9
30	15.4	9.19	1.7
40	20.6	7.54	2.9
60	30.9	5.27	6.4
100	51.4	3.20	17.8
150	77.2	2.14	40.2
225	115.7	1.43	90.4
300	154.3	1.07	159.9

Table 7.1 : Glauert Factor Forward Velocities.



The flow solution found at 40 knots is shown in Figure 7.4, Figure 7.5 and Figure 7.6. Figure 7.4 shows a side elevation, where the vectors represent velocity and the contours show pressure variation. The location of the disc is depicted by the solid horizontal line. The figure shows a region of low pressure above the disc and high pressure below the disc. The diagram shows that the flow is almost horizontal at the front edge of the rotor, however at the back the flow is faster and has a large downward component.

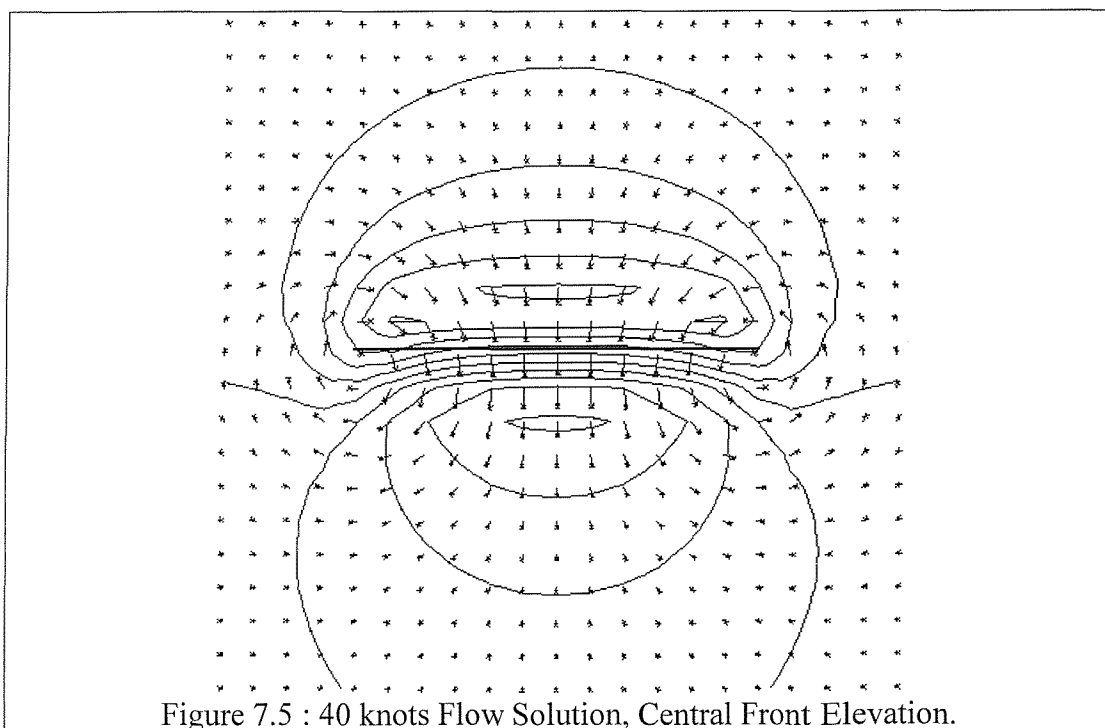
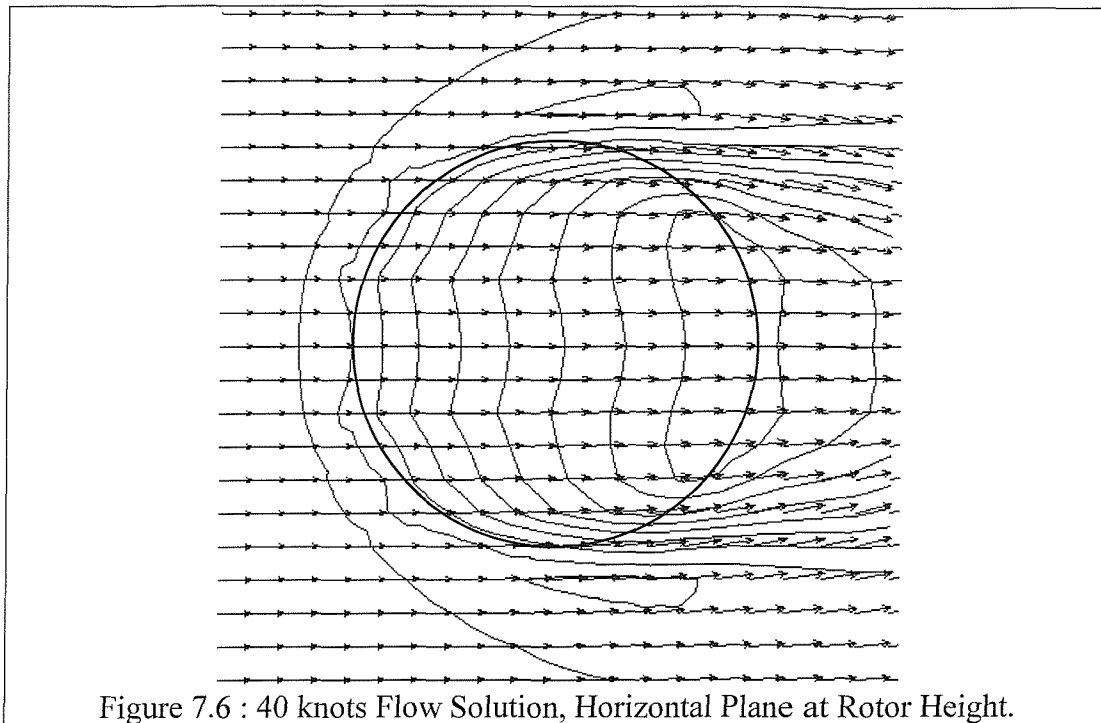


Figure 7.5 shows an elevation view of the rotor from in front of the helicopter. This plane traverses the rotor at its centre in a direction lateral to the free stream. The velocity vectors show low pressure above the rotor and high pressure below the rotor. The vectors show downwash through the rotor. Beyond the edges of the rotor plane there is upflow consistent with tip vortices.



A further representation of the flow is shown in Figure 7.6. This is a plan view of the rotor plane. The vectors are flow velocity and the contours show vertical velocity component. This figure shows the increased vertical component at the rear of the disc, which is the right hand side of the diagram. The contours are not straight across the width of the disc but draw closer together at the sides of the rotor disc. This feature has implications when calculating the Glauert factor as discussed below.

The flow solution contains many variables known at each grid cell vertex. These known values must be used to find one unknown factor, the Glauert inflow factor. Therefore the problem lends itself to a regression analysis, within which a gradient can be determined.

There are 129 grid cell vertices within the rotor plane. The vertical velocity component is used in two regression analyses to find a Glauert factor; one uses the

whole rotor disc and the second only the flow data found along the disc's centreline.

From these a linear relationship between location,  $y$ , and vertical velocity component,  $w$ , will be derived as shown in equation (7.4), and hence the Glauert inflow factor will be found, equation (7.5).

$$v_l(y) = my + v_{l0} \quad (7.4)$$

$$E = \frac{mR}{V_{l0}} \quad (7.5)$$

$$\sum_1^N \frac{r}{R} \cos \psi = \sum_1^N y = 0 \quad (7.6)$$

$$\sum_1^N w = w_1 + w_2 + \dots + w_N \quad (7.7)$$

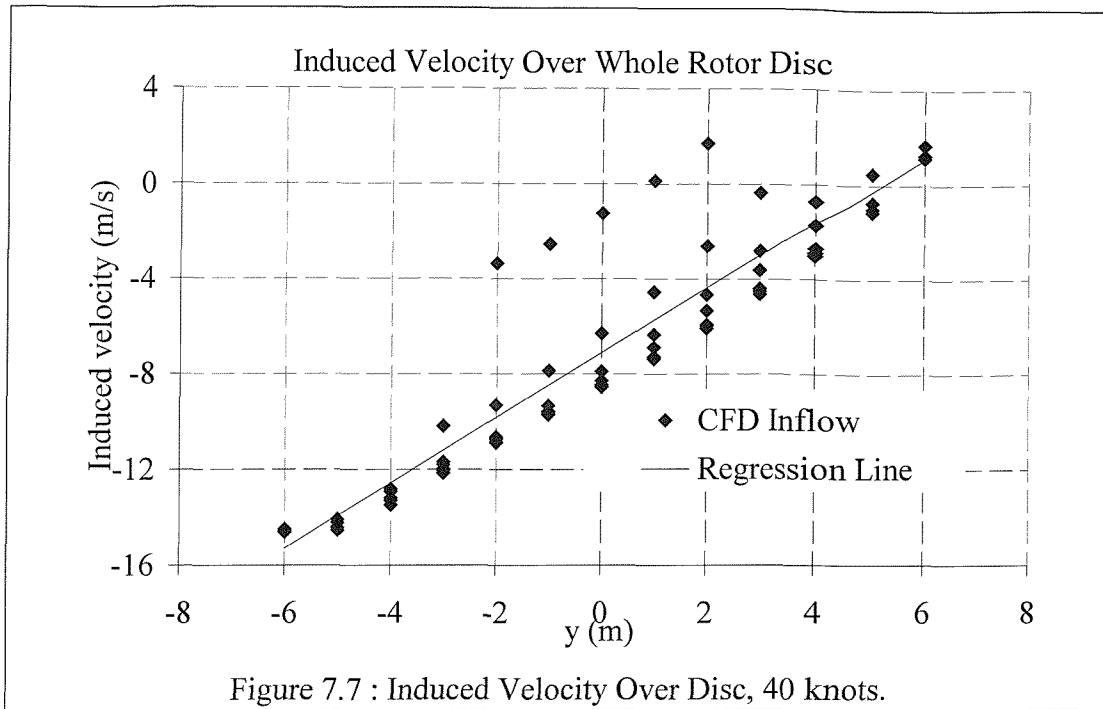
$$\sum_1^N yw = y_1w_1 + y_2w_2 + \dots + y_Nw_N \quad (7.8)$$

$$\sum_1^N y^2 = y_1^2 + y_2^2 + \dots + y_N^2 \quad (7.9)$$

$$m = \frac{\sum wy}{\sum (y^2)} \quad (7.10)$$

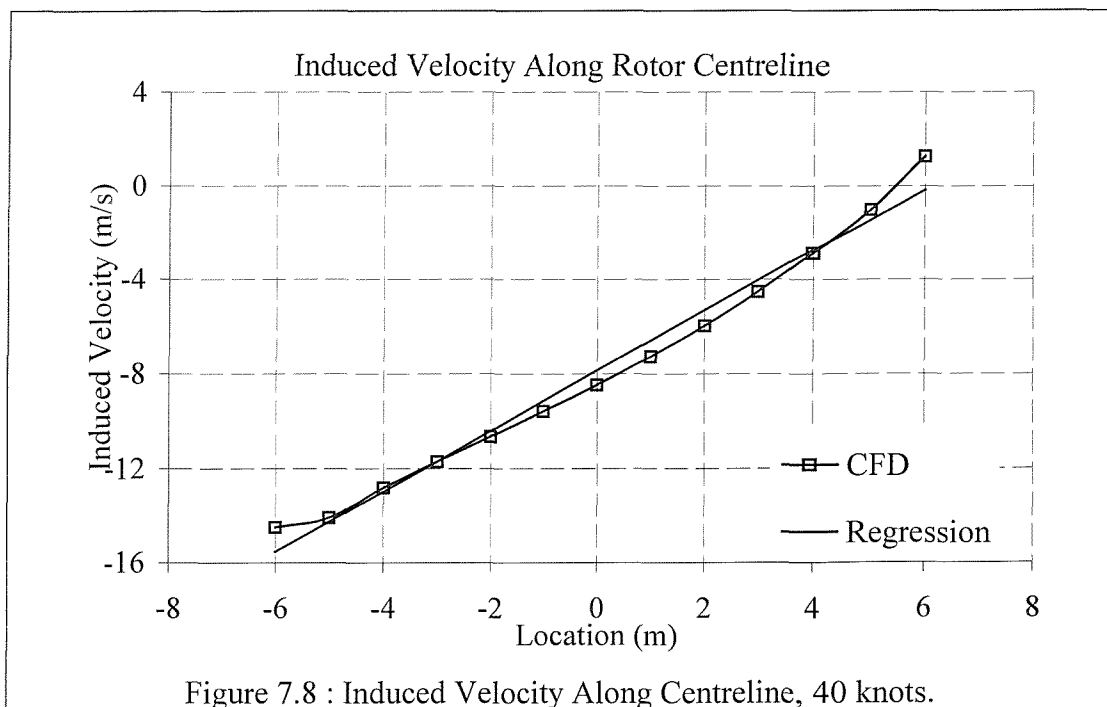
$$v_{l0} = \frac{\sum w}{N} \quad (7.11)$$

The regression method is shown in equations (7.6) to (7.11), and is taken from [7.4].



An example of the data used in a regression analysis of the whole disc is shown in Figure 7.7, this corresponds to the 40 knot flow solution. The data taken from each cell vertex is represented as a diamond on the chart. The regression line appears to successfully characterise the trend of the scatter graph.

The vast majority of the points lie very close to the calculated regression line. However, there are a few which lie significantly above the regression line. These vertices are from the outer edge of the rotor disc. The data points found from the front and rear edge of the disc lie very close to the regression line.



The induced velocities along the rotor centreline are shown in Figure 7.8. The variation is approximately linear and hence all the points lie close to the line found from the regression analysis.

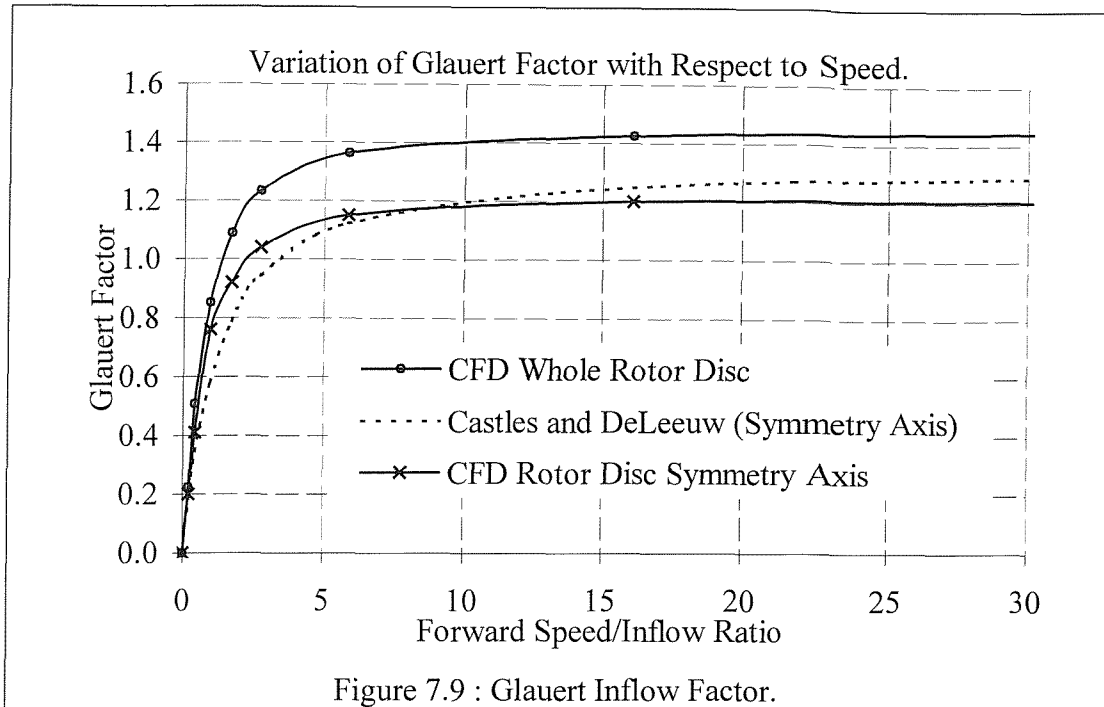


Figure 7.9 : Glauert Inflow Factor.

Each flow solution was analysed to find a prediction of the Glauert factor both along the centreline and across the whole disc. The results are shown in Table 7.2 and Figure 7.9.

Inflow Ratio $\mu/\lambda$	Glauert Factor (CFD Centreline Only)	Glauert Factor (CFD Whole Disc)	Glauert Factor (Castles and DeLeeuw)
0.0	0.0	0.0	0.0
0.2	0.20	0.22	0.18
0.4	0.41	0.51	0.34
0.9	0.76	0.85	0.58
1.7	0.92	1.09	0.79
2.9	1.04	1.23	0.94
6.4	1.15	1.36	1.12
17.8	1.20	1.42	1.25
40.2	1.21	1.44	1.29
90.4	1.22	1.45	1.32
159.9	1.22	1.45	1.32

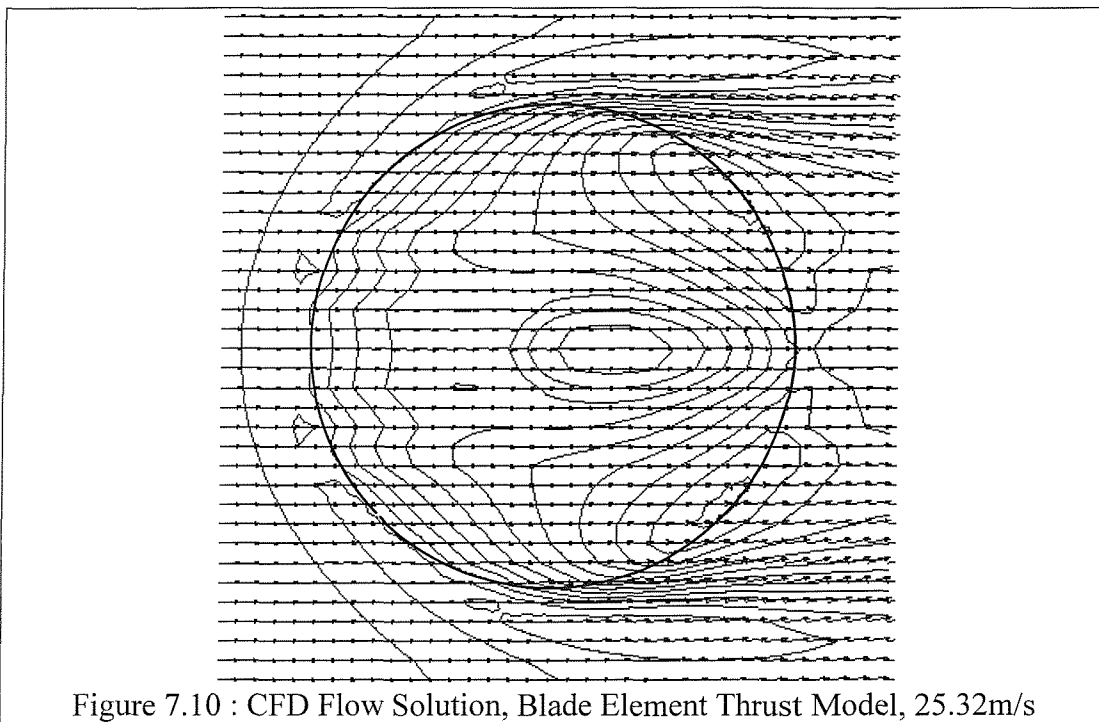
Table 7.2 : Glauert Inflow Factors for Given Non-dimensional Speeds

## 7.4 Blade Element Thrust Model, Forward Flight.

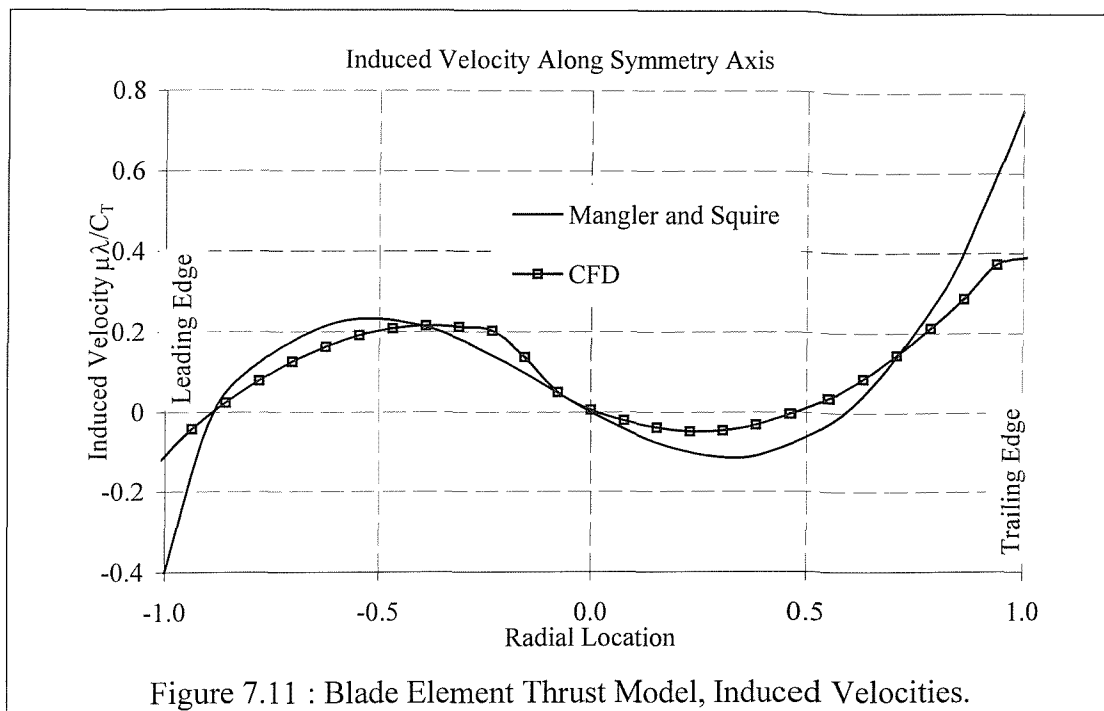
### 7.4.1 Comparison to Theoretical Inflow

Mangler and Squire [7.2] advanced the theory of Castles and DeLeeuw to include a rotor disc within which the thrust exerted was not uniform across the whole disc but varied with radius, a characteristic of helicopter rotor blades. The inflow velocities found by Mangler and Squire are given by Payne [7.5]. The ratio of forward velocity to the mean inflow velocity considered here is 4.0.

The blade element thrust model described in Chapter 4 uses a radially varying disc load. A CFD solution was obtained which included this rotor model flying at a forward speed of 25.32m/s. At this speed the mean induced velocity found from momentum theory is 6.33m/s which gives ratio of forward velocity to inflow velocity of 4.0.



The resultant CFD flow solution is shown in Figure 7.10; the vectors represent the velocity and the contours are variations in vertical velocity of 2m/s. The azimuth variation is described conventionally, namely zero lying along fuselage, in this case downstream, and increasing in an anticlockwise direction. The figure shows that the greatest induced velocities are at the azimuthal locations of 45° and 315°.



The induced velocities are extracted from the flow solution and non-dimensionalised with respect to the advance ratio, inflow ratio and coefficient of thrust. A comparison of these induced velocities and the velocities predicted by Mangler and Squire [7.2] are shown in Figure 7.11.

#### 7.4.2 40 Knots Forward Flight

Presented within this section is an overview of the helicopter rotor wake. This flow solution represents a helicopter in forward flight at speed of 40 knots, distant from the ground or any other solid boundaries. The rotor model is described in detail in Chapter 4. The flow solution presented below is used for comparison with flight in the ship airwake presented in Chapter 8.

Figure 7.12 shows a front elevation of the rotor in a vertical plane through the rotor hub. The figure shows velocity vectors and pressure contours. The contours show the low pressure region above the rotor and the high pressure below the rotor. The rotor exerts more thrust at the outer regions of the disc than in the centre. The vectors only show vertical and lateral flow; the longitudinal flow acts directly into the page. There is evidence of tip vortices at the outer edges of the rotor. A vertical component is present across the span of the rotor but elsewhere the flow is largely acting in the direction of the freestream.

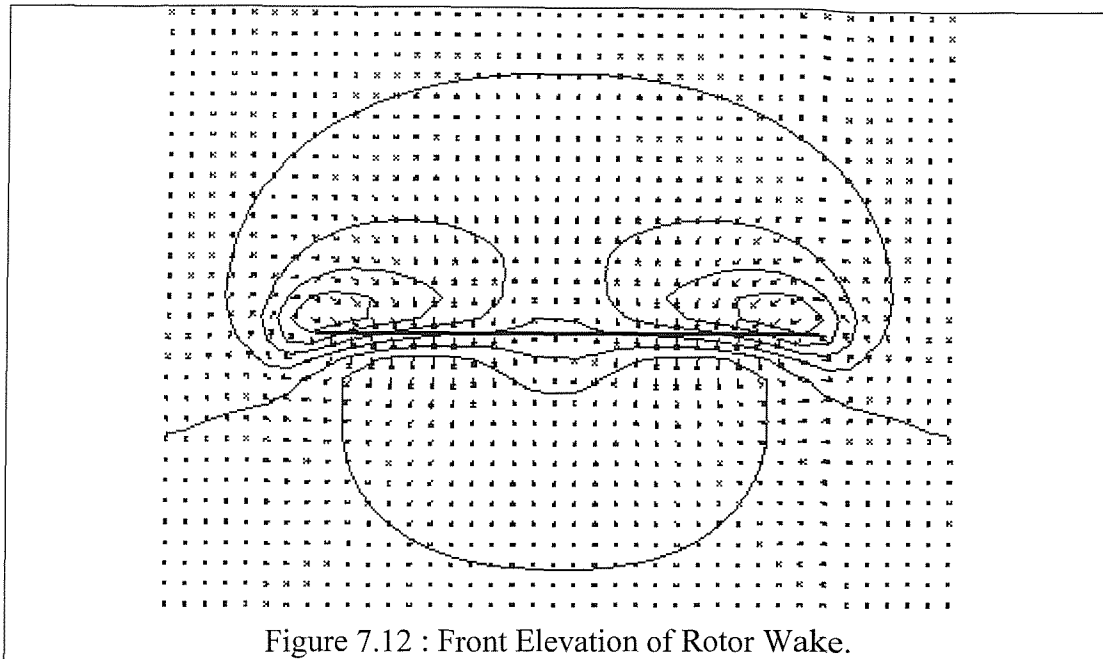


Figure 7.12 : Front Elevation of Rotor Wake.

A side elevation of the rotor along the centreline is shown in Figure 7.13, where again the vectors represent velocity and contours lines are pressure. The rotor lies at the region of the high pressure gradient. The air is clearly flowing down at the region of the high pressure gradient. The flow at the centre is roughly horizontal indicating the modelling of the rotor cut out is accurate.

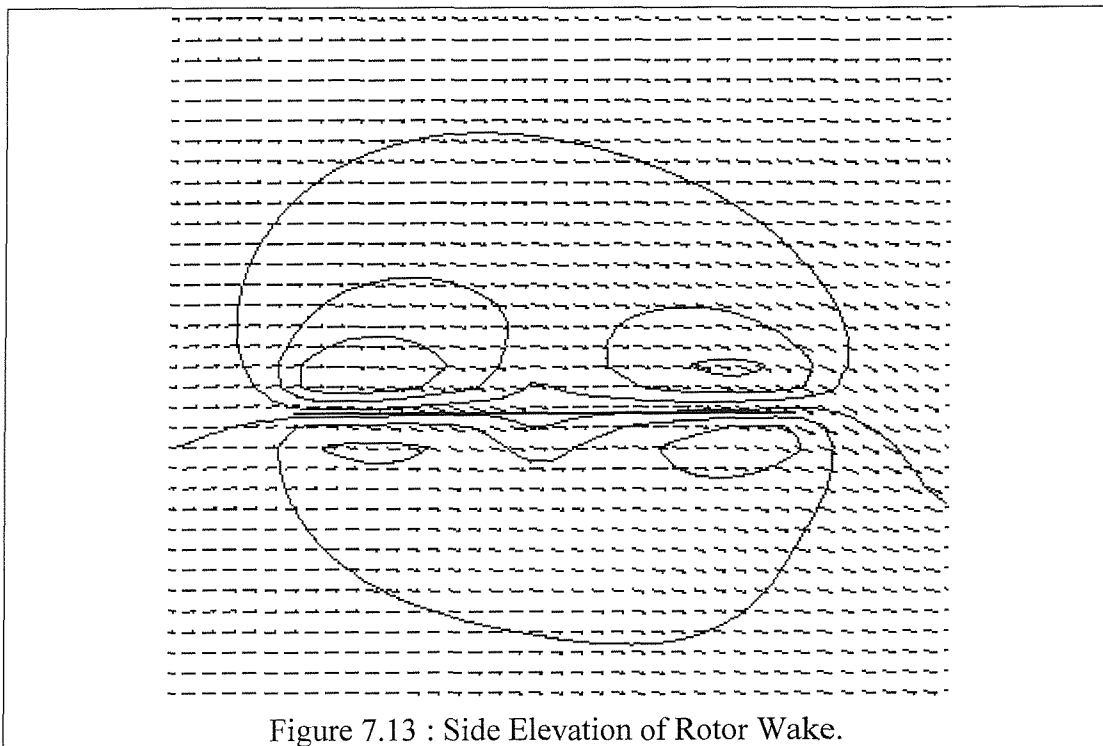


Figure 7.13 : Side Elevation of Rotor Wake.

Figure 7.14 shows a plan view of the rotor. The contours show variation of the vertical component of the flow velocity. There are some slight asymmetries in the solution, which are caused by the swirl forces exerted on the fluid which model the rotor blades rotation. Using a conventional notation for azimuthal location,

namely zero lying along fuselage, in this case downstream, and increasing in an anticlockwise direction, the greatest induced velocities lie at  $45^\circ$  and  $315^\circ$ . The front half of the rotor disc experiences less induced velocity than the rear half of the disc. The greatest upward vertical velocities occur outside the rotor disc and are caused by the tip vortices seen in Figure 7.12. The flow appears to be largely in the free stream direction except outside the rotor disc extremity at the rear where the flow is being drawn inwards.

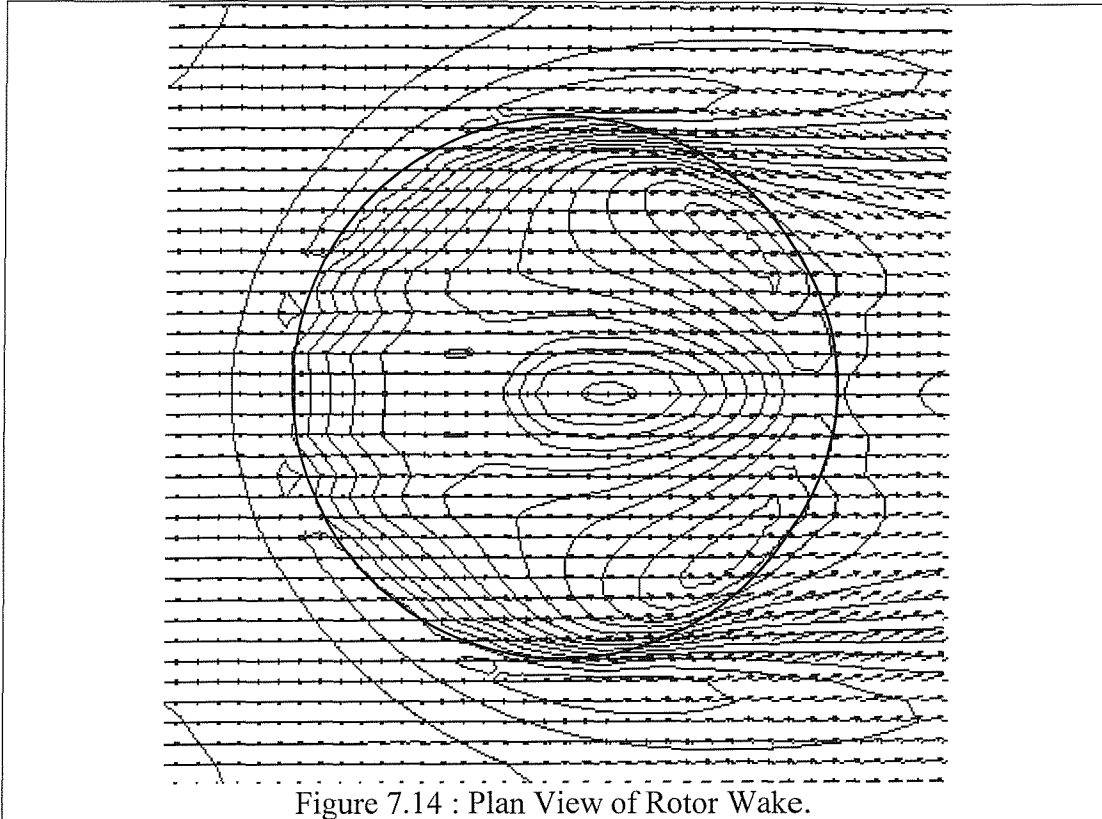


Figure 7.14 : Plan View of Rotor Wake.

The vertical velocities extracted from the flow solution are shown in Figure 7.15. As the flow solution is almost symmetrical only the angles in the first two quadrants are shown. At  $45^\circ$  azimuth the induced velocity is largest; the induced velocities reduce as the azimuth increases to  $180^\circ$ . The induced velocities at  $0^\circ$  are anomalous to this trend, being less in magnitude than the velocities at either side,  $45^\circ$  and  $315^\circ$ . This is also contrary to wake models such as the Glauert model, however the Glauert model does not include the rotor hub.

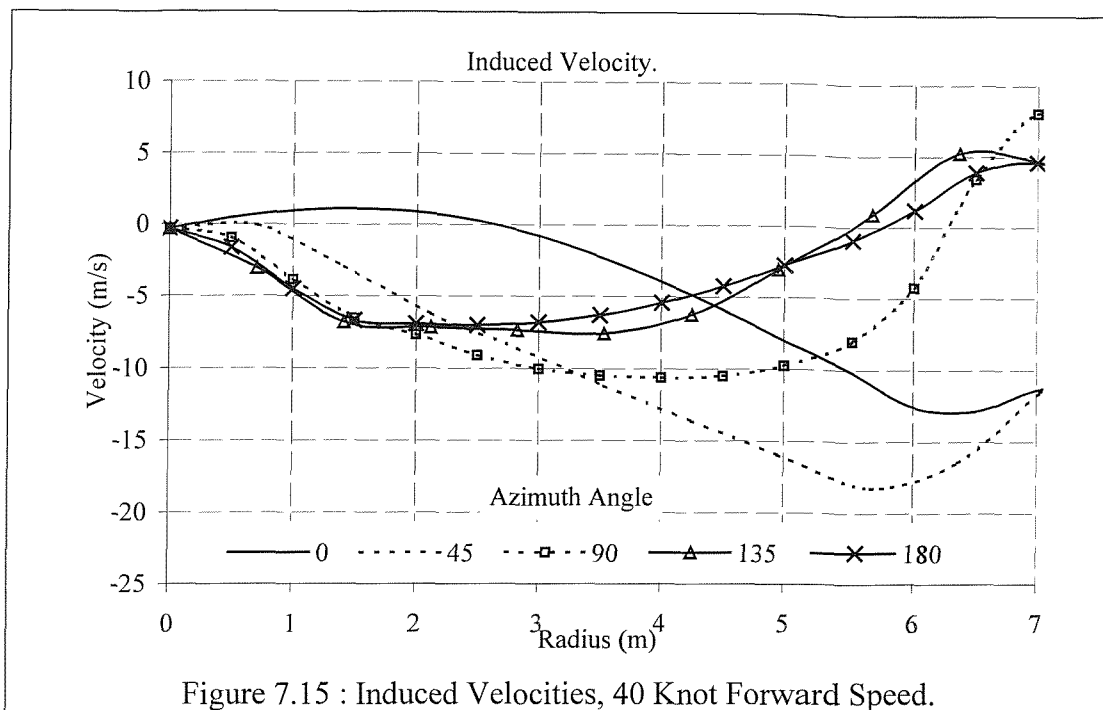


Figure 7.15 : Induced Velocities, 40 Knot Forward Speed.

Using a simple blade element method it is possible to consider each 45° segment and deduce the necessary blade pitch to achieve the thrust defined at the onset at the problem. The exact method is detailed in Chapter 4. The resultant predicted blade pitch around the azimuth is the solid line shown in Figure 7.16.

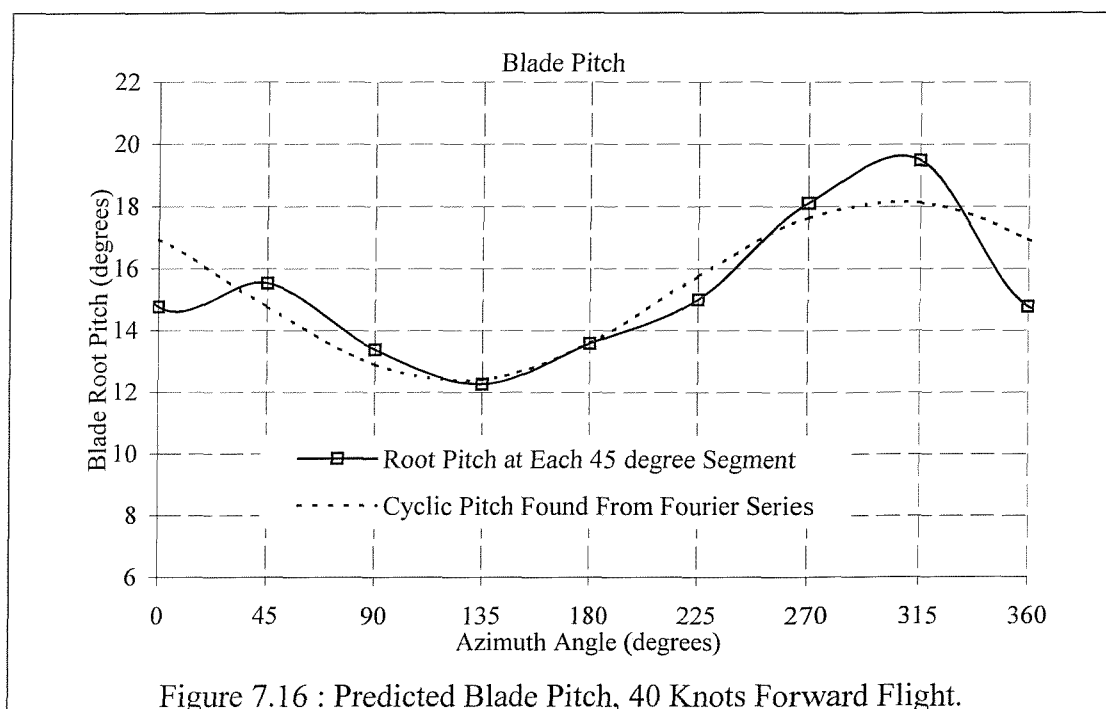


Figure 7.16 : Predicted Blade Pitch, 40 Knots Forward Flight.

The flow solution was approximately symmetrical, however the pitch prediction incorporates the blade motion and hence the pitch is greater on the retreating side, which is azimuth angles 180° through to 360°. The greatest pitch is at the azimuth angle of 315°; in this region the induced velocity is large and the blade is on the

retreating side of the disc. Conversely, at 135° there are minimal induced velocities and the blade is advancing, hence the blades have only 12° of incidence at the root.

Using the calculated pitch it is possible to determine the first two coefficients of a Fourier series and reconstruct the variation of pitch incidence according to this series. These coefficients give the collective and cyclic pitch incidence. This is shown in the broken line in Figure 7.16. The full method of determining the three coefficients in equation (7.12) is shown in Chapter 4.

$$\theta(\psi) = \theta_0 - A_1 \cos \psi - B_1 \sin \psi \quad (7.12)$$

$$\theta(\psi) = 15.3^\circ + 1.7^\circ \cos \psi - 2.4^\circ \sin \psi \quad (7.13)$$

The result of this analysis is shown in equation (7.13); the collective pitch is 15.3° which is less than the collective pitch found in the hover solution which was 17.6°. There are two cyclic pitch components, which are presented as pitch incidence. The longitudinal pitch incidence variation, 1.7°, counteracts the increased induced velocity at the rear of the rotor without this input the rotor would not generate enough thrust at the rear of the disc and the helicopter would pitch nose up and decelerate. The lateral pitch incidence variation, 2.4°, (despite the symmetrical nature of the flow solution) compensates for the reduced local wind speed the blades experienced on the retreating side of the disc.

The rotor flying at 40 knots requires less power than the hovering rotor, which is also reflected in the collective pitch as shown in Table 7.3.

	Hover	40 Knots Forward
Power	842 kW	515kW
Collective	17.6°	15.3°
Longitudinal	0°	-1.7°
Lateral	0°	2.4°

Table 7.3 : Control and Power Requirements, Hover and 40 knots Forward Flight.

## 7.5 Discussion of Results

Both the constant thrust model and blade element thrust model are discussed in this section. Because the theoretical flow solutions are derived from the same theory, the regions of disparity and strengths are similar.

The graphs in Figure 7.7 and Figure 7.8 have shown that the linear variation of the induced velocity distribution predicted by Castles and DeLeeuw [7.1] and hypothesised by Glauert [7.6] can be reproduced by CFD.

At low speeds the CFD solutions predicted greater Glauert inflow factors than the theory. This is due to a weakness of the Castles and DeLeeuw theory, which assumes that the wake is a straight skewed elliptic cylinder extending downstream to infinity. This assumption is not strictly valid at any speed but introduces most inaccuracies at low speeds at which the wake undergoes most direction changes in the region of the rotor. This is demonstrated in Figure 7.4, which shows the wake direction change both at the plane of the rotor disc and further downstream. At greater speeds the inflow velocity is reduced and hence the variations, and therefore this assumption becomes more valid. Likewise, in hover, the wake contracts but does remain straight hence this assumption is valid.

At high forward speeds the theory of Castles and DeLeeuw predicts the Glauert inflow factor,  $E$ , reaches an asymptotic value of 1.33. The CFD also reaches an asymptotic value, 1.22, for the centreline. Also shown in Figure 7.9 is the Glauert factor found from the whole rotor plane area. At all forward speeds this is greater than the prediction which considered just the rotor centreline. The gradient over the outer regions of the disc is greater than the centreline, hence the overall Glauert factor increases once the outer regions are considered. This feature of the induced velocity can be seen in Figure 7.6, shown by the contours of induced velocity being closer together in the outer regions of the disc.

One flow solution was found using the blade element thrust model; this is shown in Section 7.4. The CFD flow solution was compared to the theoretical work of Mangler and Squire [7.2]. The two flow solutions exhibit good correlation around the centre of the rotor but Mangler and Squire predict large induced velocities at the leading and trailing edge of the rotor, as shown in Figure 7.11.

In both cases the CFD has accurately predicted the induced velocities of the central region of the disc, however there are differences at the forward and rear edges of the rotor disc. The skewed vortex tube theory predicts infinite induced velocities at the leading and trailing edge of the disc. The CFD induced velocities increase in magnitude in these regions but remain finite.

The Castles and DeLeeuw theory includes an infinite number of rotor blades and hence an infinite number of weak vortex sheets. This theory predicts induced velocities based on the distance from the vortex centres, which lie at the blade extremity. Hence at the edge of the rotor disc there is zero in the denominator and the induced velocity becomes infinite.

An infinite induced velocity is physically unjustifiable, however discussing the physical justification is inappropriate as both solutions deal with an infinite number of rotor blades having a predetermined load distribution, which is impossible in itself. The CFD may be omitting a flow feature which is lost in either a numerical process or the discretisation process.

The key reason for the disparity lies in the fact that the induced velocities are solutions to two different problems. The Castles and DeLeeuw theory includes an infinite number of rotor blades and hence an infinite number of weak vortex sheets. The induced velocity at any point is found from an integration of all the vortex sheets. This integration determines the variation of the induced velocity from the predetermined initial induced velocity which was chosen at the outset of the problem.

The CFD also commences with rotor disc load distribution but no information whatsoever about induced velocity. The induced velocity is solved over the whole disc in one step. This solution does not include tip vortices caused by a finite or infinite number of blades, hence there are no predicted infinite velocities at the rotor tips.

## **7.6 Scale Dependency Study**

All the results in the previous section use one grid cell size, one domain and one helicopter rotor size and thrust. These results are then reduced to a non-dimensional form. This section demonstrates that these results are independent of

the scales and thrust adopted and the results can be reproduced using alternative grids.

The original case used a rotor flying at forward speed of 40 knots. This rotor model has a thrust per unit area of 396.4Pa and a radius of 6.4m. Four further flow solutions were obtained and compared to this flow solution. All of these have the same non-dimensional speed but different computational domains, rotor size and thrust are used, in order to determine whether the results are repeatable.

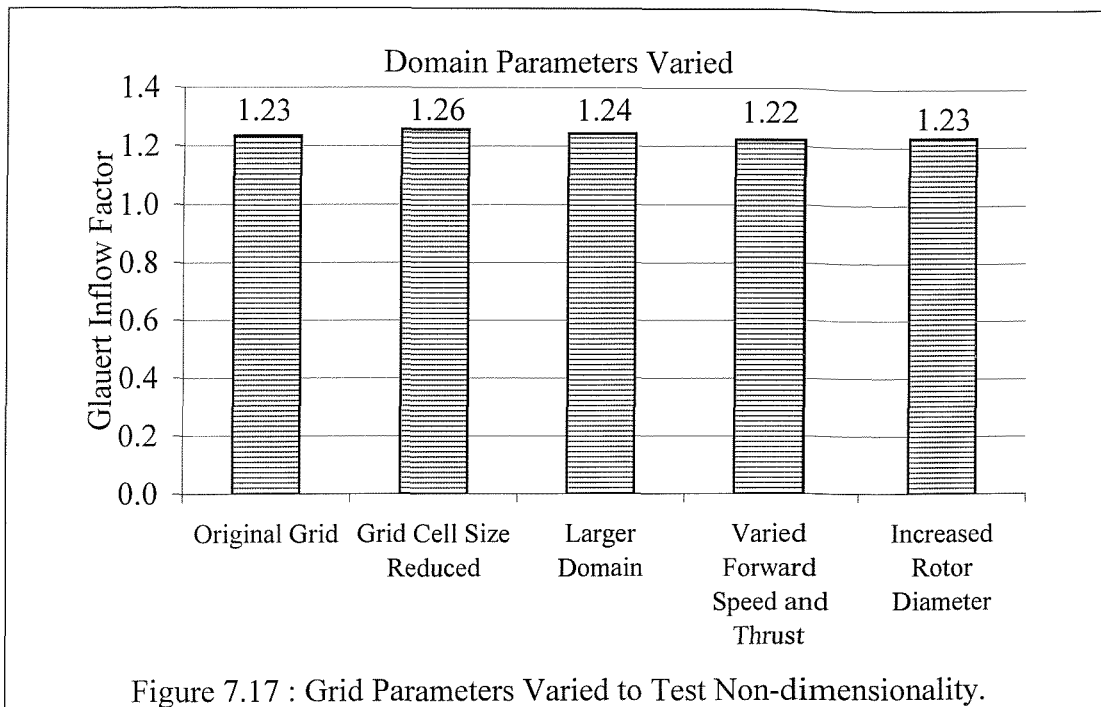
Within any CFD study it is always of paramount importance to determine whether the grid is sufficiently defined, therefore an alternative grid was generated with cubic grid cells of half the length, and hence the domain contained eight times as many cells. The second comparison increased the overall size of the domain but retaining the grid around the rotor. The domain dimensions were doubled, hence the volume increased by a factor of eight. This ascertained whether the domain boundaries were far enough from the rotor to not adversely affect the flow solution.

The third comparison adjusts forward speed of the rotor and the thrust per area is changed such that the non-dimensional speed remains constant. An expression for the thrust is shown in equation (7.14). The forward speed is changed from 40 knots to 20 knots; if the ratio of induced velocity to forward speed remains constant the thrust per area must be reduced by a factor of 4.0 as shown in equation (7.15).

$$T = 2\rho AV_I \sqrt{V_F^2 + V_I^2} \quad (7.14)$$

$$\frac{T}{A} = 396.4\text{Pa} / 4 = 99.1\text{Pa} \quad (7.15)$$

The final comparison uses a larger rotor diameter, however the thrust and forward speed remains the same as the original case. The larger rotor has a diameter of 12.8 metres. The dimensions of the computational domain and grid cells were also doubled to accommodate the larger rotor.



The Glauert factors found for the whole rotor are shown in Figure 7.17. The inflow factor from the original grid and rotor is 1.23. The inflow factors found from the other rotor models and grids all vary from this value, but by no more than 5%. The greatest disparity is shown within the solution utilising the smaller grid cells. This difference can be attributed to the circular rotor being placed over a square grid. The difficulties associated with modelling a circular rotor using a square grid are discussed in Chapter 4.

This sensitivity study proves that the results found in the previous sections are not affected by inadequately defined grids or domains of insufficient sizes.

## 7.7 Conclusion

This chapter has achieved several key objectives. The Glauert inflow factor is based on experimental observations and endorsed by theoretical work. Comparison to the simple CFD model has demonstrated that CFD can be used for modelling rotors of uniform thrust. The blade element thrust model, which includes thrust variations over the disc, also conforms well to the established theory. There are marginal discrepancies in the results which have been introduced by differences in the models and modelling methods themselves, as discussed in Section 7.6. These rotor models can be used with confidence to form part of further flow solutions which do not have theoretical solutions, for example helicopter/ship airwake interaction.

The CFD solution found that the Glauert factor was greater over the whole disc than over the centreline. This feature has not been predicted from theoretical work.

The agreement with theoretical work has validated the rotor model. Only two thrust distributions have been considered but any distribution can be input into model. The model could therefore be used to optimise rotor lift distributions and hence provide minimum induced power requirements for helicopters in forward flight. In comparison to CFD studies in general these models involve relatively few cells, less than 100,000. Therefore each analysis is time efficient, taking less than two hours using a single processor running at 195MHz on a Power Challenge machine. This model can be used as a design tool to determine blade chord and twist distributions.

This model does not include the numerical elegance of analyses such as Castles and DeLeeuw [7.1] but provides a simple method of determining the induced velocity over the whole rotor disc using any rotor thrust distribution.

## 8 3D Helicopter Flight Around A Ship's Superstructure.

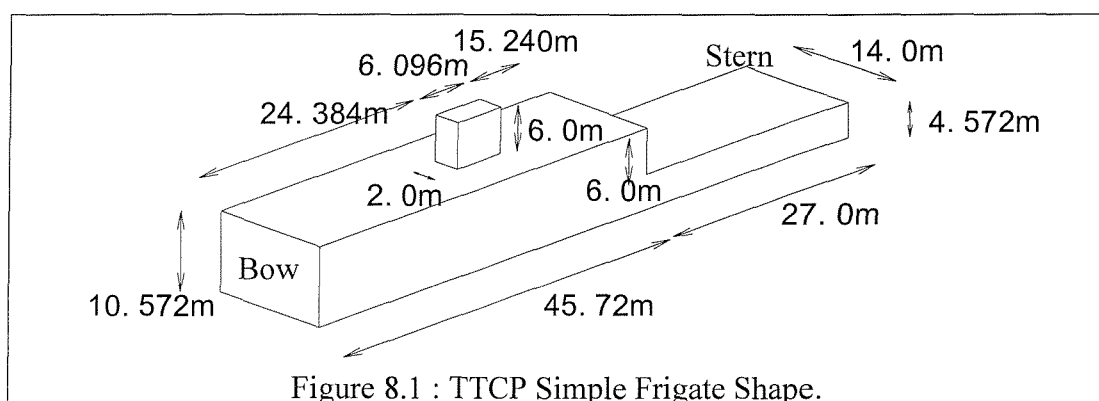
### 8.1 Introduction.

Whilst there are many helicopter/ship combinations worthy of investigation, in order to compare this work with other research efforts the decision was made to study the Lynx helicopter flying over the TTCP Frigate. Details of their specifications are given in the following sections.

This chapter is divided into two sections. Firstly CFD predictions of the ship airwake are compared to wind tunnel data of the same ship. Secondly the CFD model combines the ship and helicopter. The helicopter model is 'flown' above the helideck to simulate hover immediately prior to landing.

### 8.2 Ship Model

Research is presently being performed into ship airwake by various nations worldwide. The TTCP is a collaborative program between Canada, America, UK and Australia. In order to compare CFD and wind tunnel airflow regimes between nations the generic Frigate was developed. The design is simple and allows easy comparison between results from various solver codes from each nation. This original ship model has dimensions in feet. For the purpose of this study, some dimensions have been rounded to the nearest metre, as shown in Figure 8.1.



### 8.3 Ship Airwake

#### 8.3.1 Introduction.

Three ship airwakes are presented within this section all with a wind speed of 40 knots. Three angles are considered; a head wind acting directly over the bow,  $0^\circ$ ,

an oblique angle acting from the starboard side of the bow,  $045^\circ$ , and the wind approaching from abeam of the ship on the starboard side,  $90^\circ$ . These results are compared to experimental data kindly provided by the Canadian NRC [8.1]. Their study considered a scale model of the ship in a wind tunnel, and hence the two studies have two differences, namely Reynolds number and the flow being bounded by a wind tunnel whereas the other models an unbounded flow.

The domain extends 120m away from the ship, upstream, downstream, vertically upwards, to port and to starboard. The flow solutions presented are instantaneous ‘snapshots’. At the upstream and top faces of the domain a flow condition is applied. At the downstream faces a pressure condition is applied. The uniform free stream velocity is 40 knots, and the ship is modelled as full scale. The grid cells around the helideck are cubic of dimension 0.5m. These boundary conditions and grid are consistent and justified by the sensitivity studies performed in Chapter 3.

The sea surface is at the base of the ship and is modelled as stationary. The ship and the sea are modelled as walls and hence a no slip condition is imposed on their surfaces.

### **8.3.2 Zero Degrees.**

The separation over the bow of the ship, found in the Canadian study [8.1], is shown in Figure 8.2 using smoke visualisation. The freestream acts from left to right. In the first part of the figure the smoke probe is placed significantly downstream of the bow, yet the smoke is carried upstream to the bow.

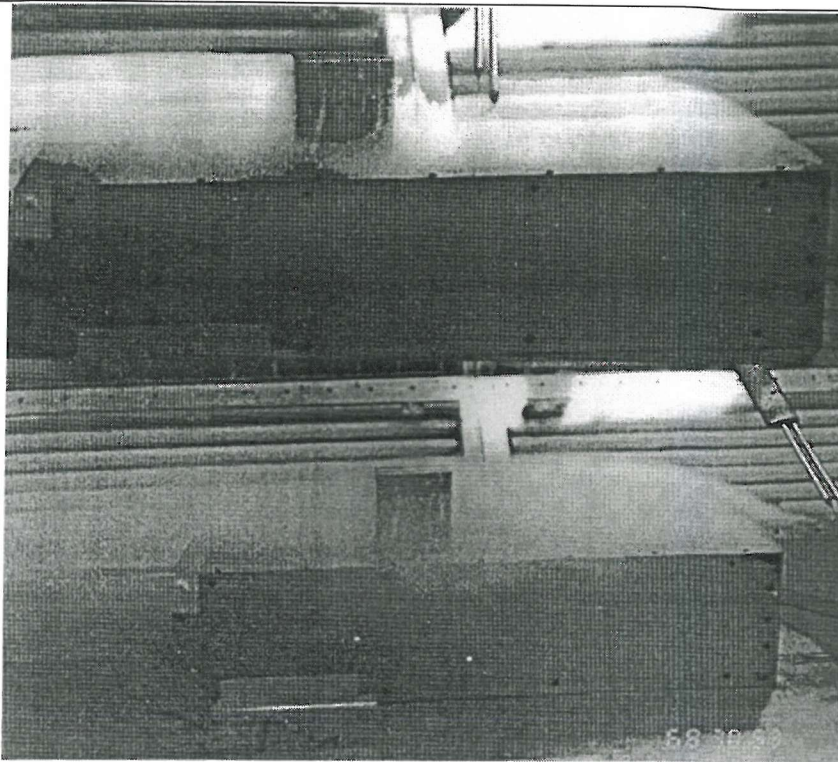


Figure 8.2 : 0°, Smoke Flow Visualisation over the Bow.

The CFD prediction of the flow around the bow is shown in Figure 8.3, the freestream acts from right to left. The separation around the bow is very similar in shape to the experimentally found flow.

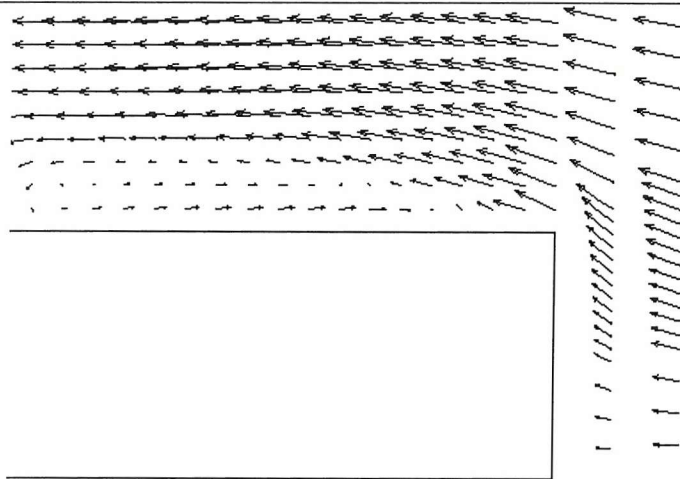


Figure 8.3: 0°, CFD Prediction of flow regime around the bow.

Figure 8.5 shows the CFD prediction of the flow over the centreline of the ship at the helideck and aft face of the hangar. This is equivalent to the experimental results in Figure 8.4.

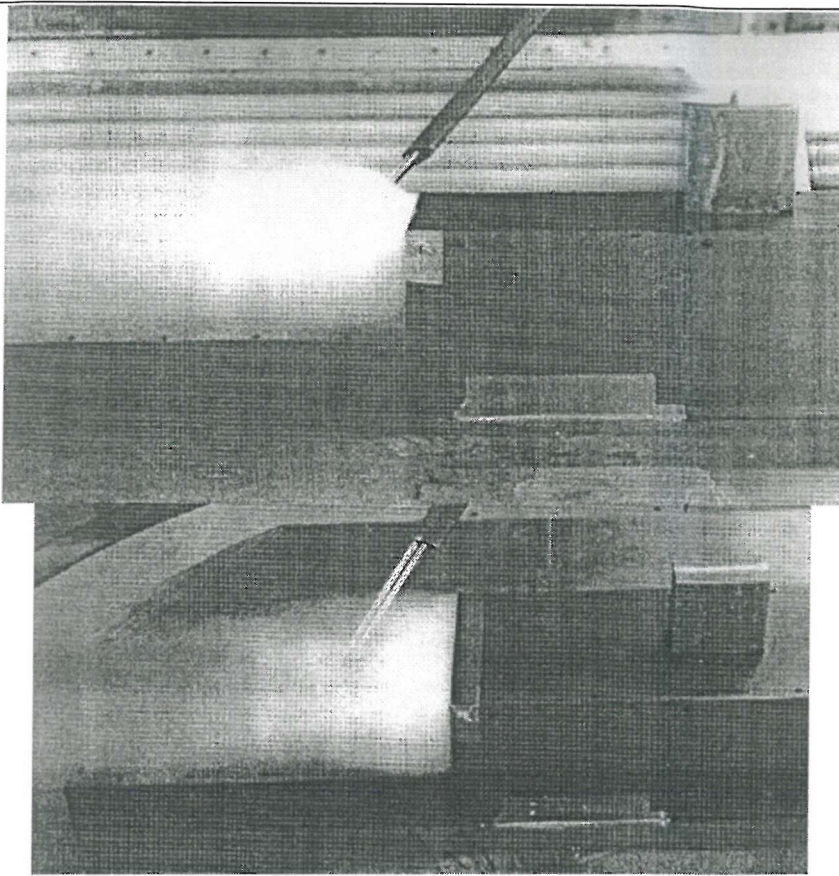


Figure 8.4 : 0°, Experimentally Observed Airflow over the Helideck

In both these figures the flow is attached at the aft edge of the superstructure and detaches at the hangar face. In the CFD solution the vortex is visible at the height of the hangar roof, hence the region of recirculation extends above the hangar roof. This is clearly visible in Figure 8.4.

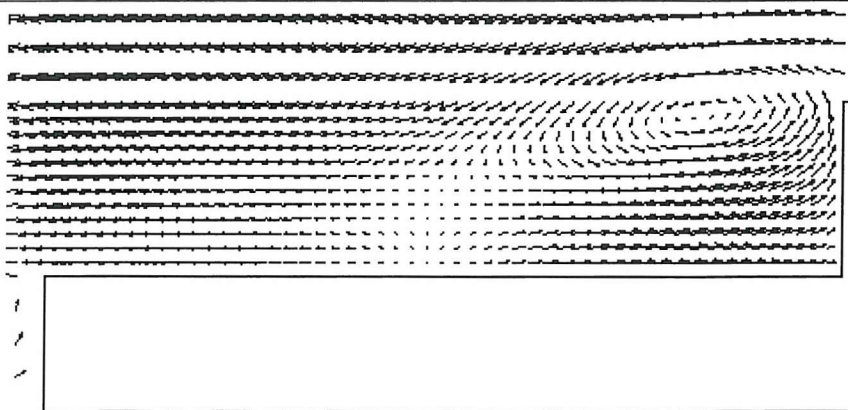


Figure 8.5 : 0°, CFD Airflow over Helideck, Side Elevation.

The CFD predicts a reattachment point approximately 2.3 times the hangar height aft of the hangar. [8.1] states that the reattachment point was not stationary but varied between 1.7 and 2.5 times the hangar height aft of the hangar face.

Oil flow visualisation of the flow on the helideck surface is shown in Figure 8.6, where the free stream velocity acts from right to left and the hangar face can be seen on the right hand side of the figure. There are two vortices near the edges at the front of the helideck, which are caused by the recirculation which covers the hangar face. The reattachment point approximately half way back along the helideck can also be seen.

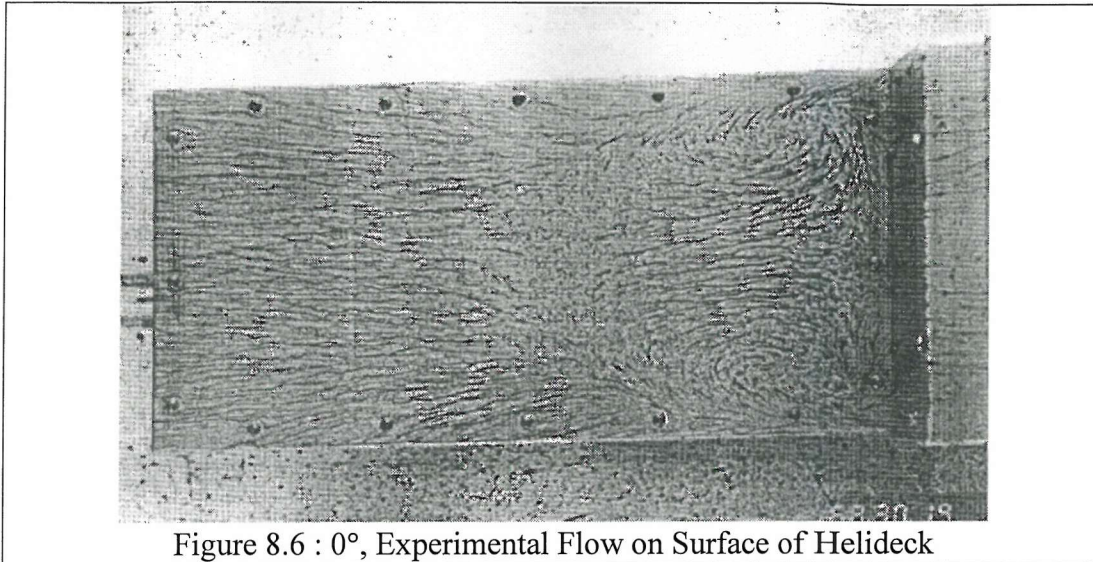


Figure 8.6 :  $0^\circ$ , Experimental Flow on Surface of Helideck

All the features found from the oil flow visualisation are found in the CFD prediction. The oil flow visualisation represents the flow on the helideck's surface. The flow on the deck of the CFD is modelled as zero as a boundary condition of the problem. It is therefore futile comparing the oil visualisation with the velocities predicted on the deck by the CFD because these velocities are zero by definition. However it is possible to consider the velocities at a small height above the deck, in this case 0.3m. This is shown in Figure 8.7. The only discrepancy between the computational and experimental is flow direction at the rear edges. The oil flow visualisation shows the flow splaying outwards whereas the flow remains parallel to the ship's sides at the rear of the helideck in the computationally generated solution.

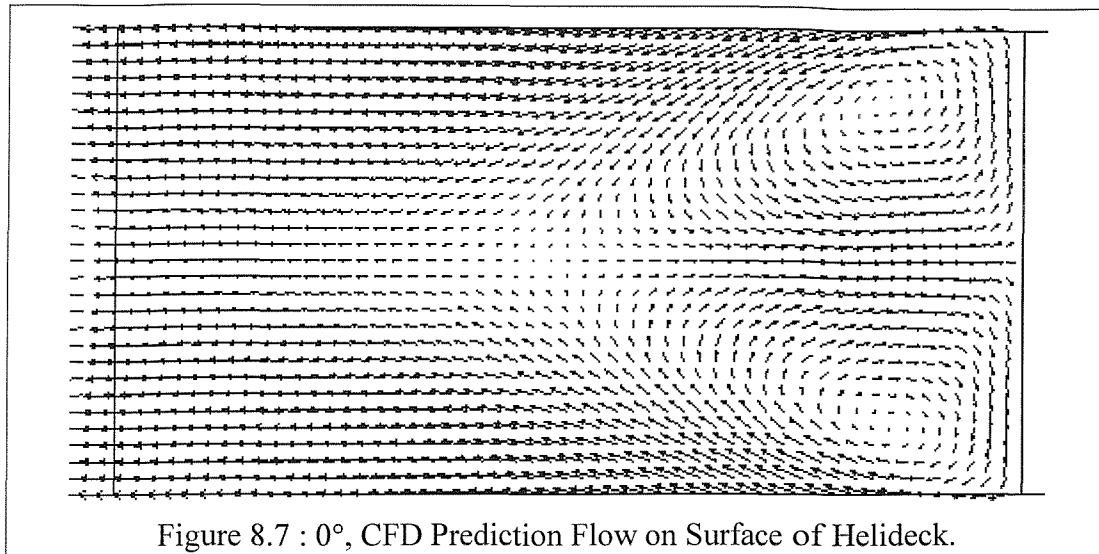


Figure 8.7 :  $0^\circ$ , CFD Prediction Flow on Surface of Helideck.

The Canadians also recorded extensively the pressure on the surface of the model using pressure tappings. Figure 8.9 shows a contour diagram of the pressure over the centre of the helideck. The free stream velocity acts from left to right. The highest pressure is found at the reattachment point which is approximately in the centre of the deck. The lowest pressure is found at the base of the hangar face which is also inside the recirculation associated with the aft face of the hangar.

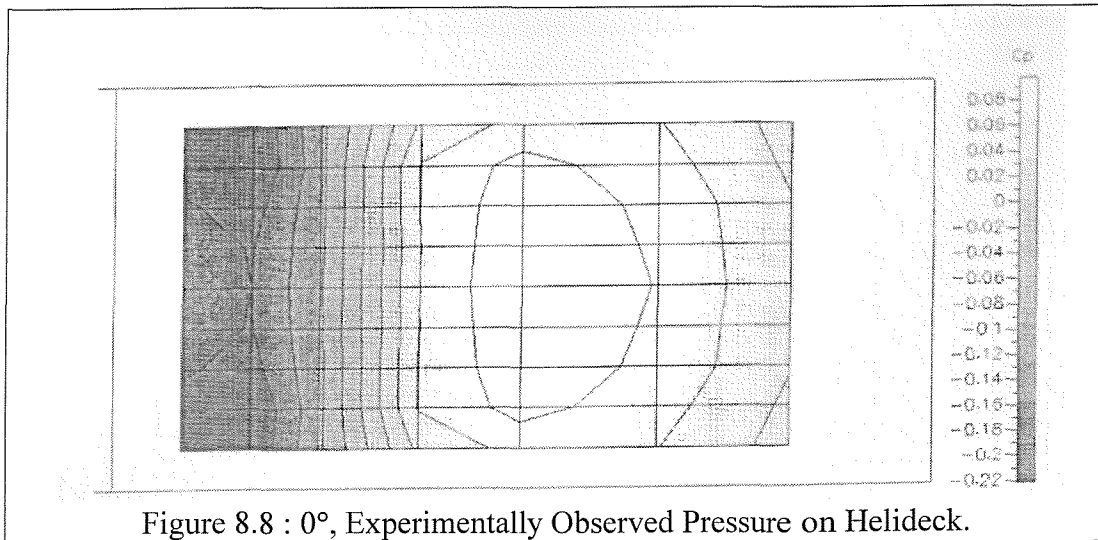
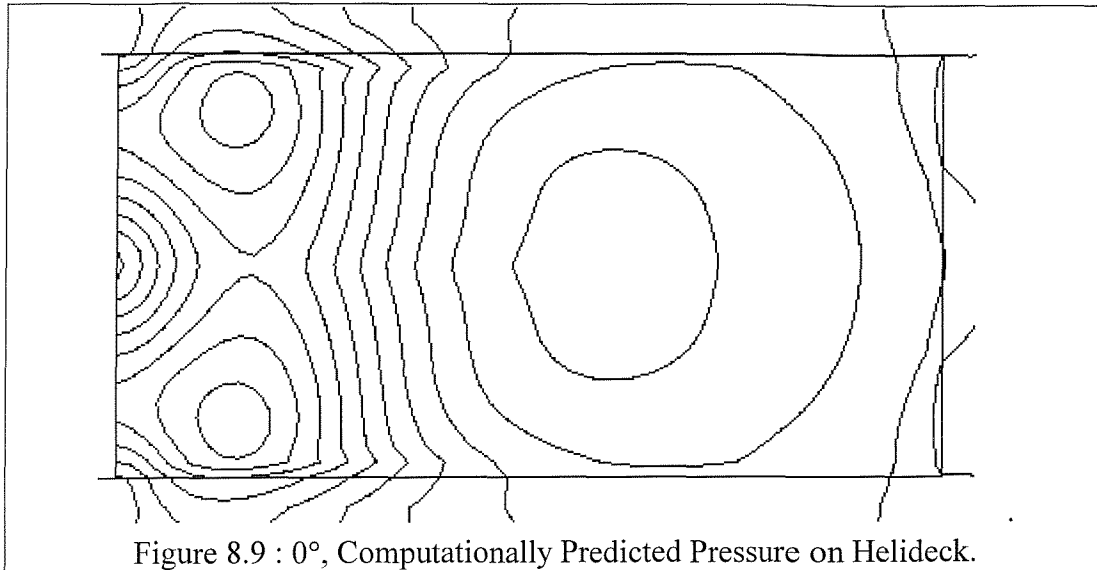


Figure 8.8 :  $0^\circ$ , Experimentally Observed Pressure on Helideck.

The CFD prediction of the pressure on the helideck is shown in Figure 8.9. The high pressure associated with the reattachment is found, however there are two regions of low pressure caused by the vortices emanating from the sides of the hangar. The computational results have predicted these far stronger than they actually appear in reality.



### 8.3.3 45 Degrees

Figure 8.10 shows the flow features along the starboard side of the ship in three parts. The air at the base of the ship is moving aft horizontally, however the airflow at the top of the superstructure moves vertically upwards and aft. This flow pattern is also observed along the whole length of the ship and around the helideck.

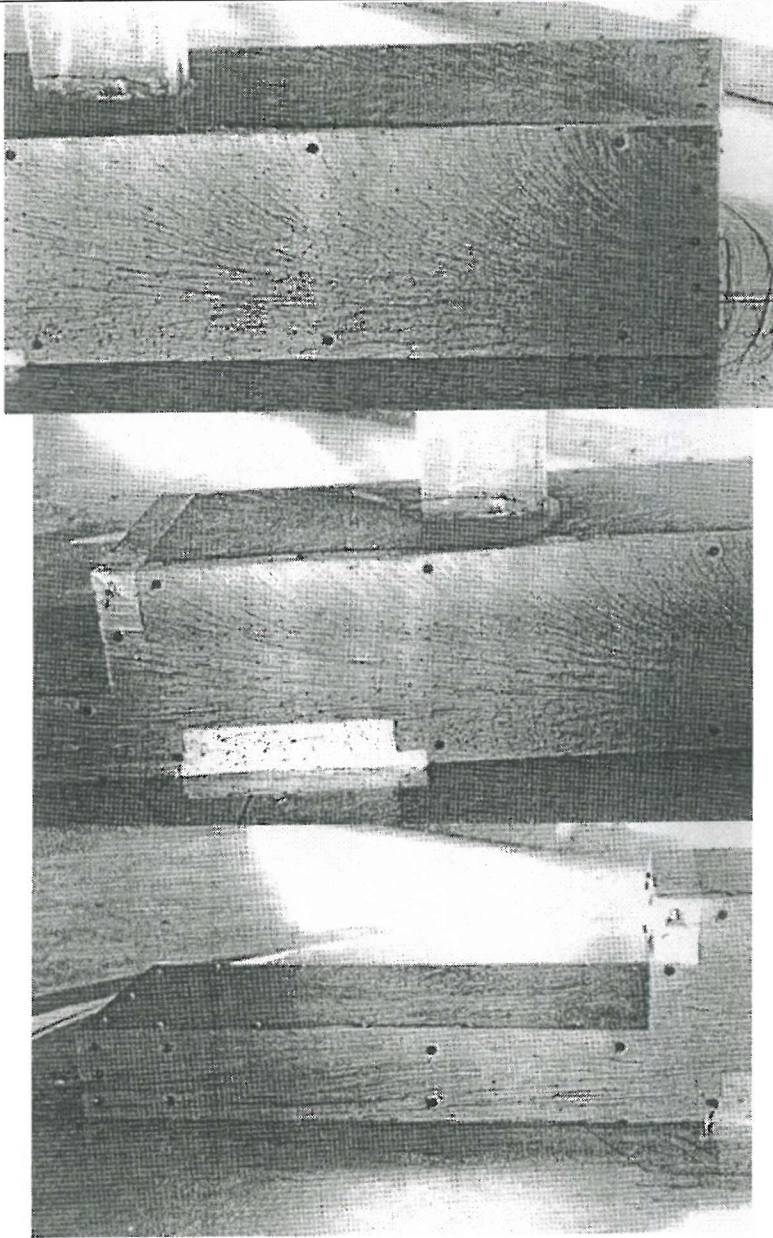
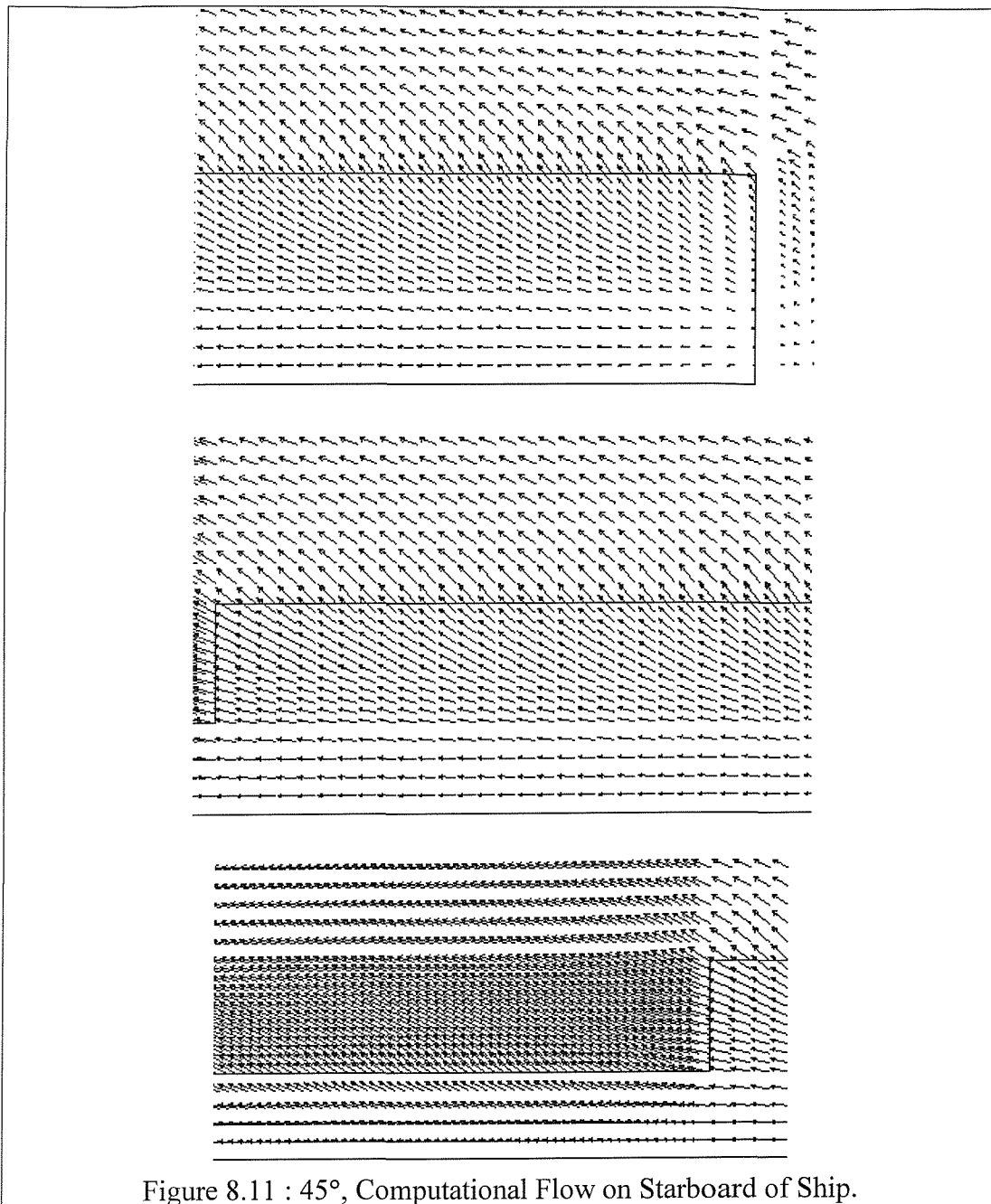


Figure 8.10 : 45°, Experimental Flow on Starboard of Ship.

The computationally predicted flow velocity 0.5m from the starboard side of the ship is shown in Figure 8.11; this figure reflects the experimental results in Figure 8.10.



There were two smoke flow visualisation photos of the recirculation around the hangar door available from [8.1], which are shown in Figure 8.12. The flow remains attached along the starboard side of the ship as shown previously, but detaches at the hangar and surface of the helideck. The angle of separation is particularly large, appearing to be greater than 45°, however this is only the direction of the free stream.

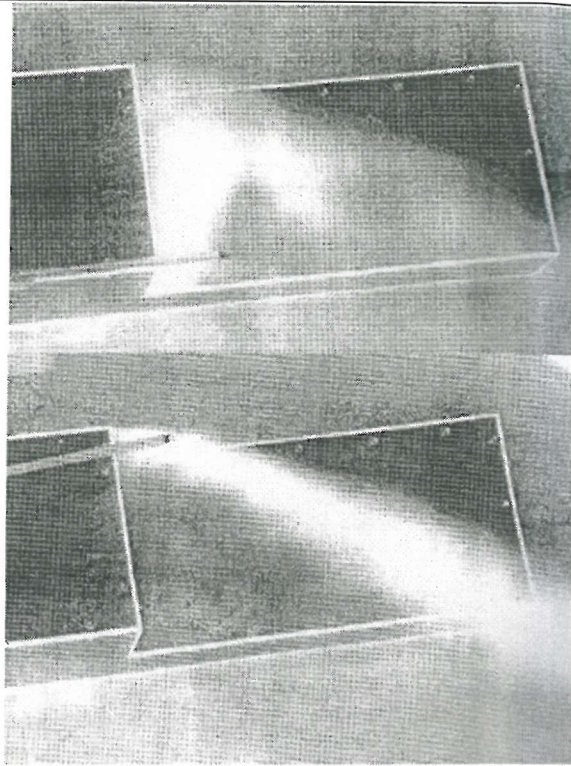


Figure 8.12 : 45°, Experimentally Observed Flow Over Helideck.

Figure 8.13 shows the velocity vectors at a height of ten metres above sea level, 5m above the helideck. The computational prediction of shape of the separation is qualitatively similar to the experimentally observed separation.

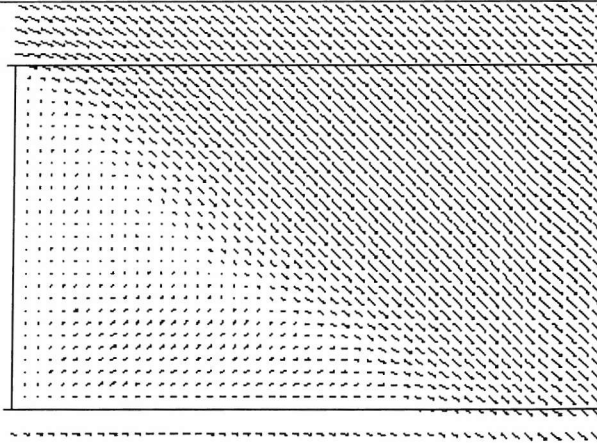


Figure 8.13 : 45°, Computationally Predicted Flow Over Helideck.

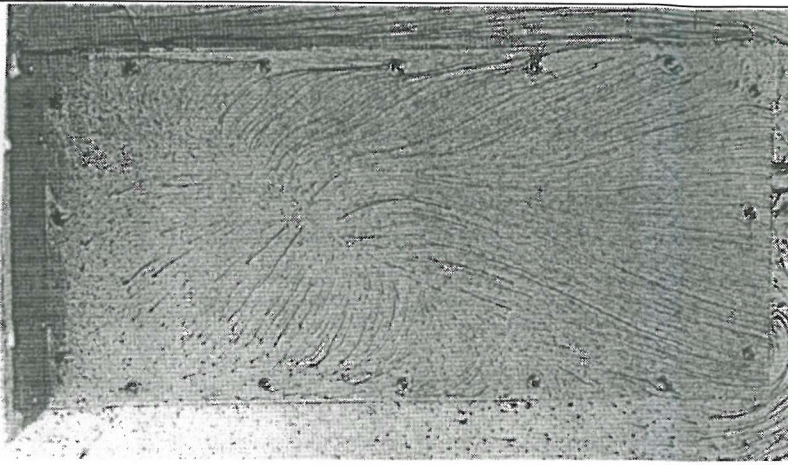


Figure 8.14 : 45°, Experimentally Observed Flow on Helideck.

Figure 8.14 shows an oil flow visualisation of the flow on the surface of the helideck; the comparison is shown in Figure 8.15. These figures show all the same features, for example, the stagnation behind the hangar, from which fluid flows in all directions. The difference lies in the location of the stagnation line; experimentally it is found on the ship's centreline, 40% aft of the hangar towards the transom, whereas the CFD prediction finds this region slightly to port of the centreline and fractionally further aft.

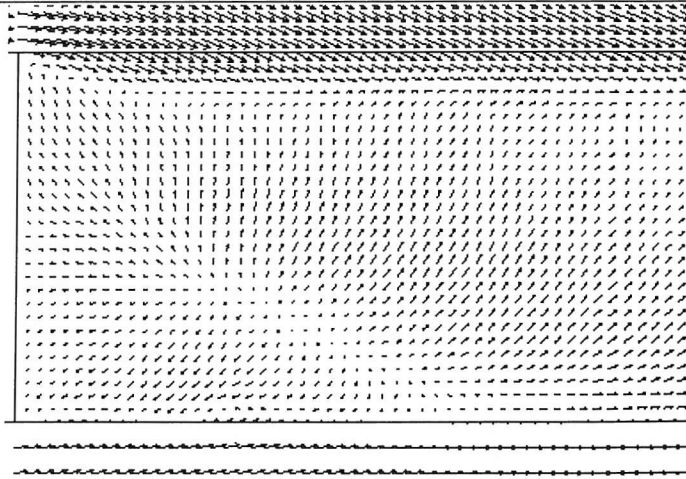


Figure 8.15 : 45°, Computationally Predicted Flow on Helideck.

Extensive data was taken from pressure tappings during the experimental study. The pressure found on the helideck surface is shown in Figure 8.16; this can be compared to the computational results, Figure 8.17. The experimental results show the lowest pressure to exist on the starboard side of the ship's centreline at approximately the mid-length of the helideck. The highest pressure is at the rear of the helideck on the leeward side.

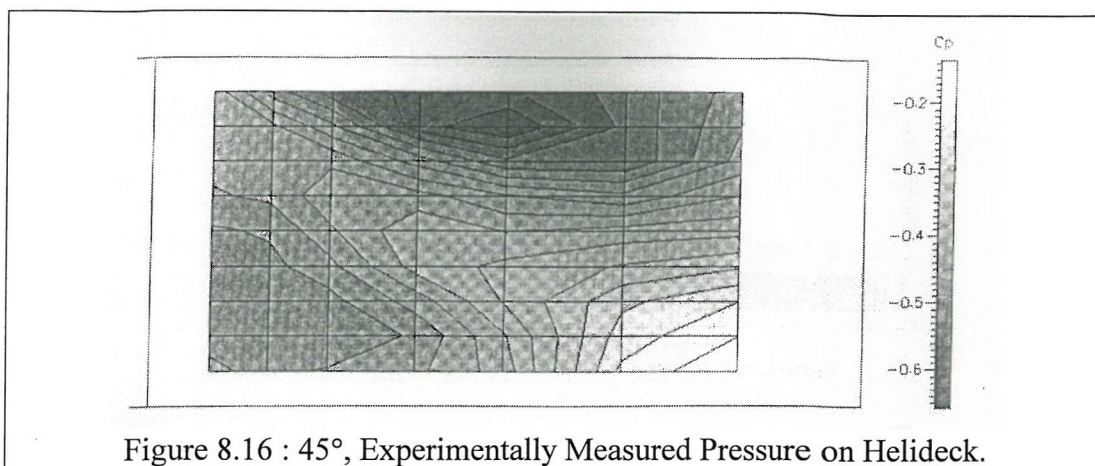


Figure 8.16 : 45°, Experimentally Measured Pressure on Helideck.

The CFD pressure plot, Figure 8.17, covers the entire helideck and the surrounding region. At the windward side of the deck there is a dense cluster of pressure contours, which are caused by the transition between the high pressure on the windward side of the ship and the low pressure beneath the sheared flow above the helideck. The CFD has failed to predict the high suction pressures found along the windward edge of the deck. However the low pressure below the region of recirculation adjacent to the hangar face is present. Also the CFD shows the region of high pressure at the leeward aft corner of the deck.

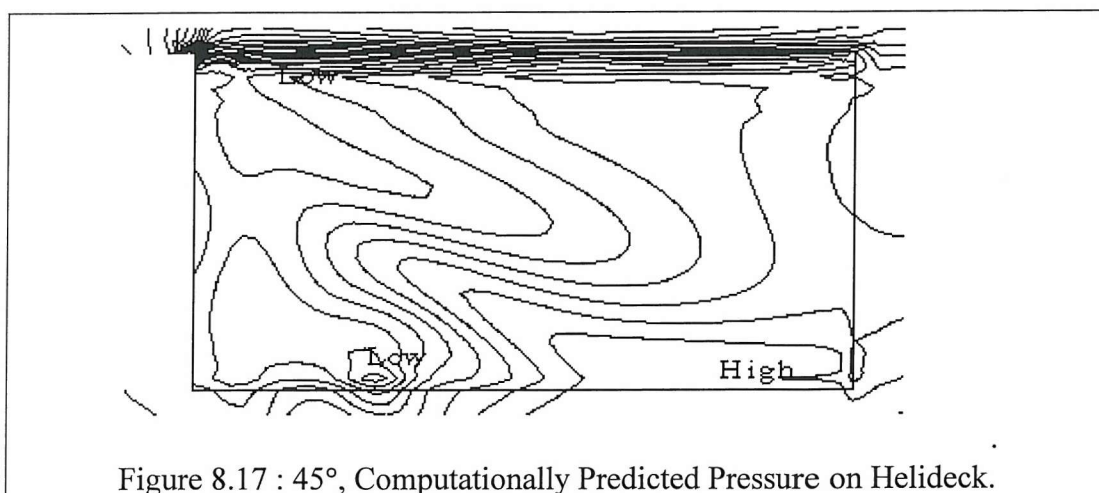


Figure 8.17 : 45°, Computationally Predicted Pressure on Helideck.

### 8.3.4 90 Degrees.

Figure 8.18 shows the shape of the separation and ensuing recirculation at the aft face of the hangar. Note that the smoke probe is placed at the leeward side of the deck and that this location allows the whole recirculation bubble to fill with smoke.

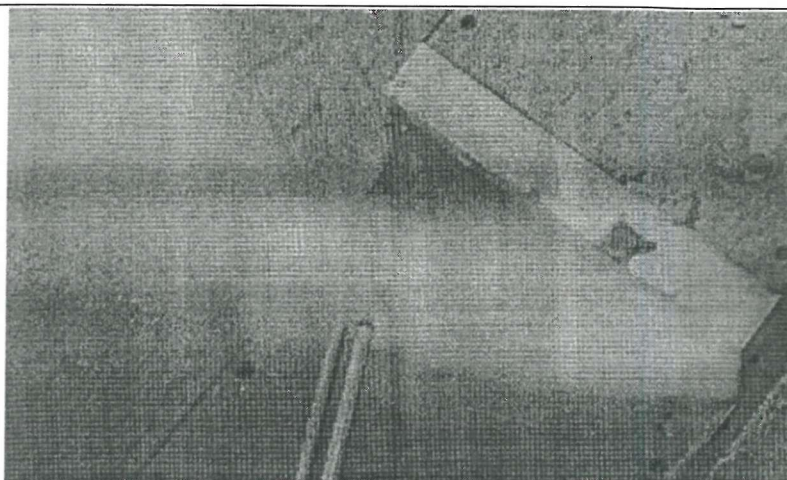


Figure 8.18 : 90°, Experimentally Observed Recirculation Aft of Hangar.

Figure 8.19 shows the computationally predicted separation shape.

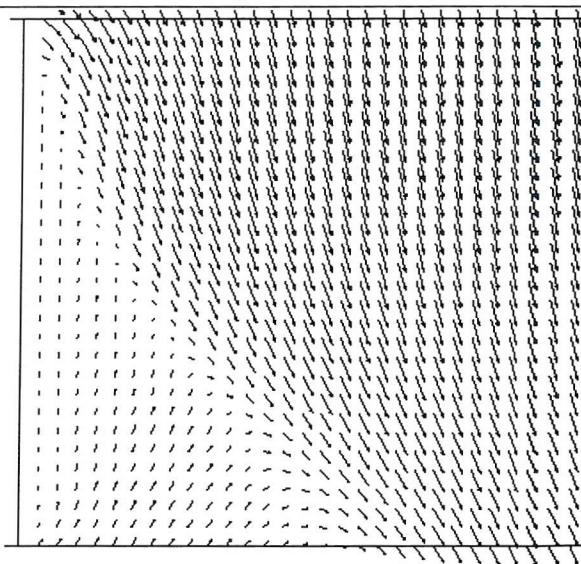


Figure 8.19 : 90°, Computationally Predicted Recirculation Aft of Hangar.

This figure is a plan view of the helideck, the aft face of the hangar is at the left of the diagram and the free stream velocity acts from the top of the page downwards. The ship's transom is out of view on the right of the diagram. The vectors represent the flow at a height of 8m, which is 3.5m above the surface of the helideck. The CFD solution predicts a separation zone similar to that experienced experimentally.

Figure 8.20 shows the oil visualisation of the flow on the front of the helideck; the hangar face is just visible at the left of the picture. The separation from the hangar face is clearly visible at the left of the figure, however the flow does not appear to separate from the deck at the front of the helideck. At the middle and rear of the helideck the flow turns upstream before becoming entrained in the sheared flow from the side of the ship.

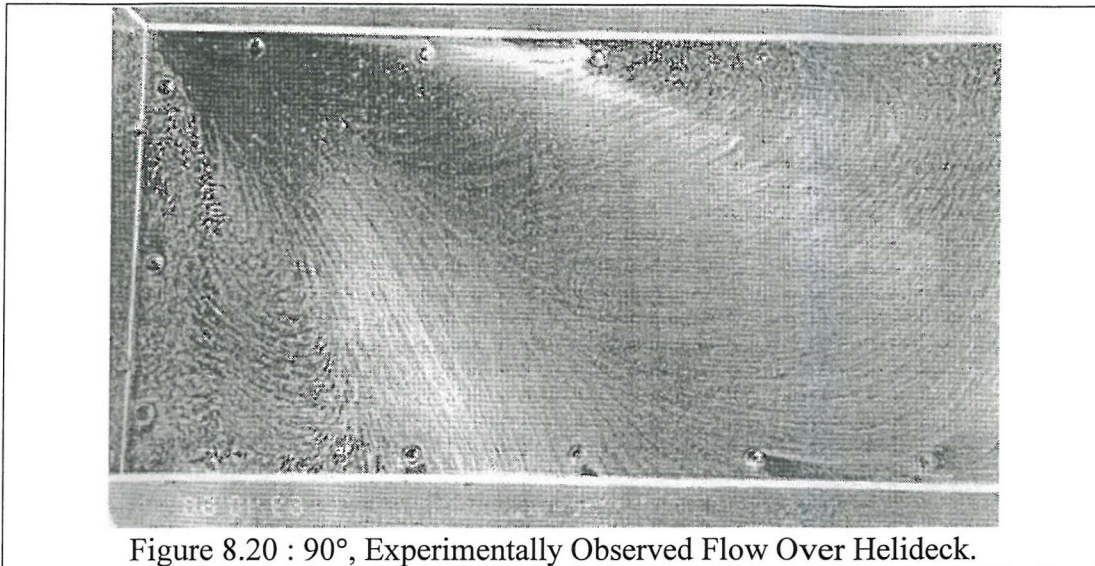


Figure 8.20 : 90°, Experimentally Observed Flow Over Helideck.

Figure 8.21 shows the velocity at a plane 0.3m above the level of the helideck. This figure shows some similarities to the oil trace. Just aft of the hangar the CFD solution correctly predicts a region of reversed flow, which travels against the direction of the freestream from port to starboard; this appears on the left hand side of the diagram.

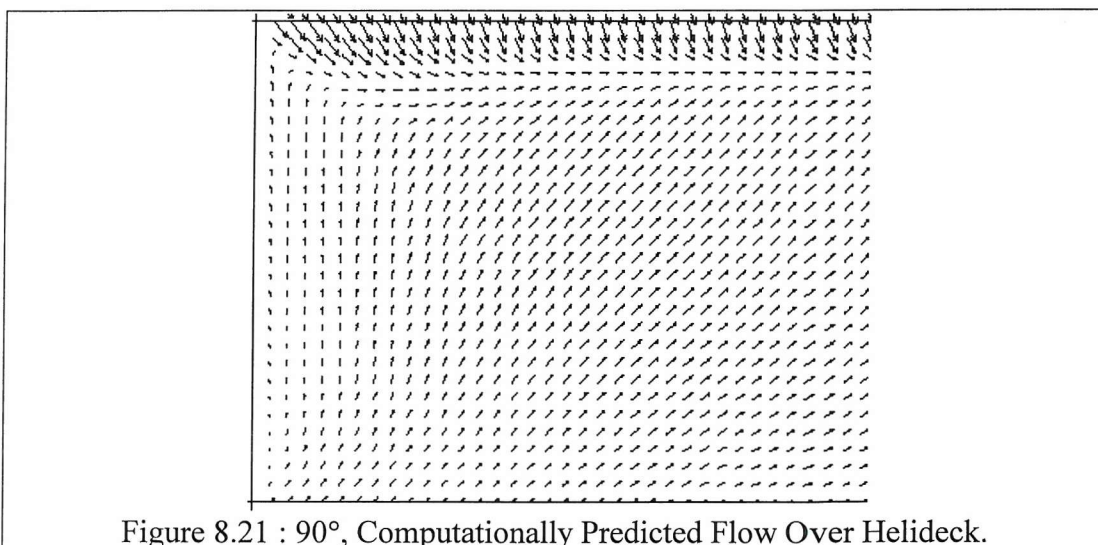


Figure 8.21 : 90°, Computationally Predicted Flow Over Helideck.

The CFD shows the rest of the helideck is covered by flow travelling upstream and aft. This flow is beneath the separated flow and moves upstream before

becoming entrained into the sheared layer at the starboard side of the helideck. This flow feature is largely reflected in the experimental representation, Figure 8.20, however the chief disparity between the experimental and CFD result lies one third of the helideck length back behind the hangar face. The experimental result shows a region of fast moving fluid emanating from the lower starboard corner of the hangar at the helideck surface; this flow does not appear to have separated from the helideck surface. The same region of flow does separate in the CFD solution.

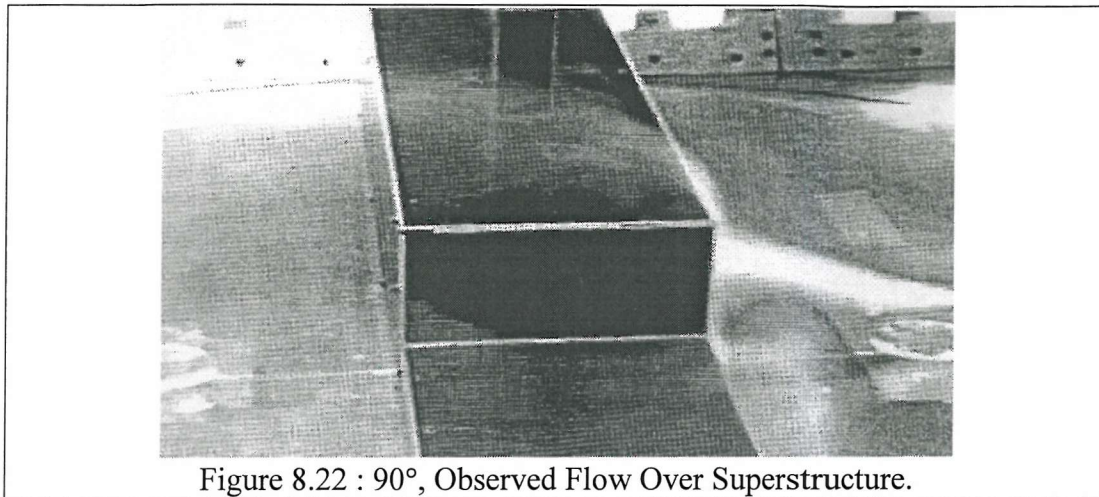
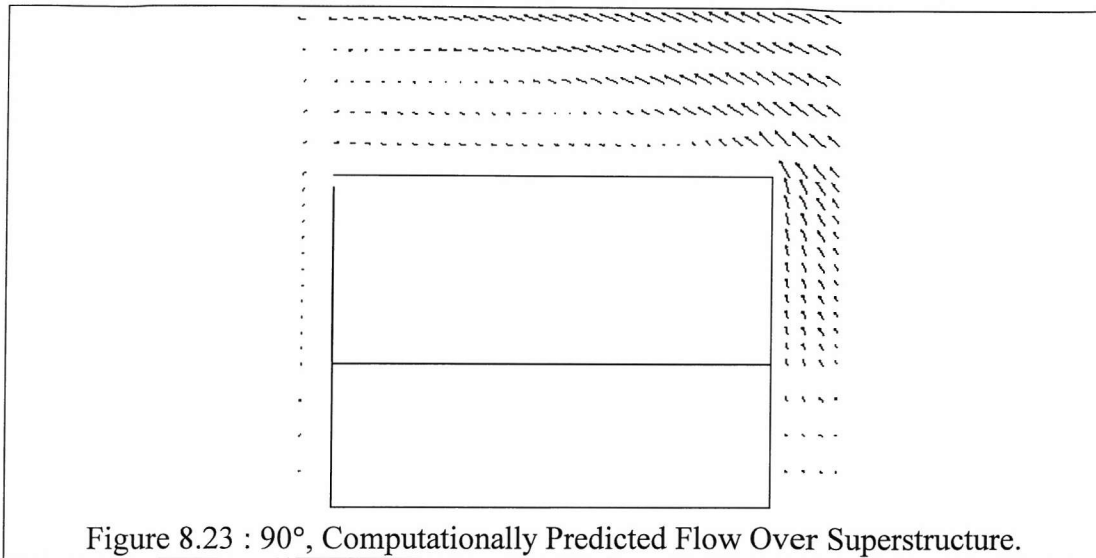


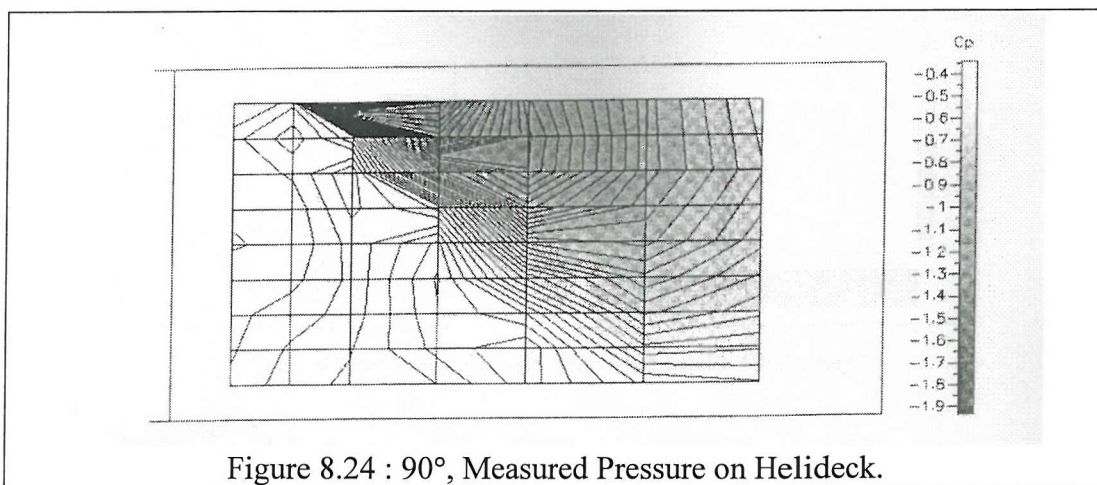
Figure 8.22 : 90°, Observed Flow Over Superstructure.

Figure 8.23 shows a rear elevation of the ship, at a lateral plane 35m from the transom; this is 8m forward of the aft face of the hangar. This flow solution illustrates the flow moving up the starboard side of the superstructure and separating at the top edge. This region of recirculation is huge and extends 1.7 times the superstructure height downstream.

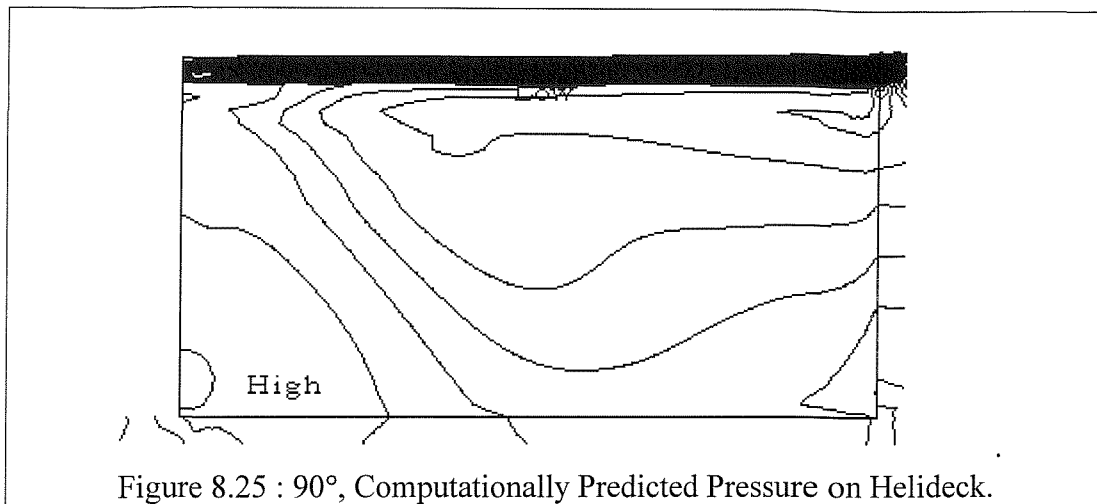


Smoke visualisation of the separation over the superstructure is shown in Figure 8.22. [8.1] states that the region extends at least 1.5 times the superstructure height downstream.

The measured pressure coefficient on the central section of the helideck is shown in Figure 8.24. The lowest pressure is found along the windward edge of the deck approximately half way along the length. The area behind the hangar has a relatively high pressure.



The CFD plot, Figure 8.25, is broadly similar to the experimental equivalent, Figure 8.24, despite the different flow features over the helideck.



### 8.3.5 Conclusion

The CFD modelling has predicted the majority of the flow features found in the wind tunnel modelling. There are however slight discrepancies in magnitude and location of some features such as recirculation zones.

The chief disparity occurs at the front windward corner of the helideck with a freestream of 90°. Experimentally the flow separates from the hangar face but not the helideck itself. The CFD spuriously found the flow to separate from both surfaces.

Some flow features such as reattachment points were predicted at slightly incorrect locations, however the CFD solutions were generally accurate at predicting large scale flow phenomena. This demonstrates that CFD is a viable tool for flow predictions around bluff bodies.

## 8.4 Helicopter Flight

### 8.4.1 Introduction

Ship borne helicopter operations are limited by many factors but it is widely accepted that the airwake is the most influential [8.2]. There have been many studies into ship airwake alone but few of these have attempted to include any helicopter interaction. A notable exception is a study by Syms and Zan [8.3], whose study was divided into two sections. The first section determined the ship's airwake and second section 'flew' a helicopter model in the airwake. Whilst this

produced some interesting results the interaction of the helicopter downwash on the ship airwake was neglected.

To the authors knowledge there is only one other study, by Tattersall [8.4], which uses CFD to model both the helicopter and the ship in one stage. This method has the advantage of directly yielding flow data relevant to the helicopter control and power requirements. As demonstrated in the following sections the control inputs the pilot must use to hold station are far from predictable.

#### **8.4.2 Helicopter Model.**

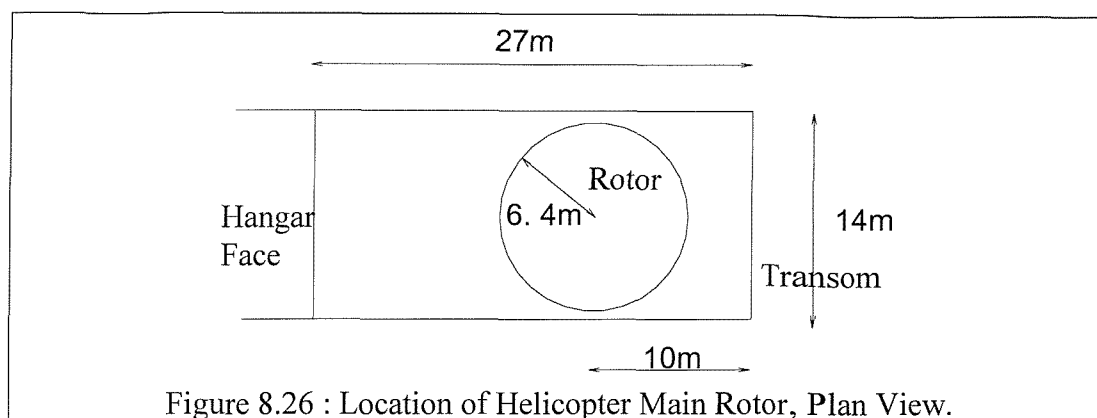
The helicopter is modelled on a Westland Lynx. At the centre of the rotor there is a root cut out, within which the rotor develops no thrust. This region has a radius of 0.96m, which is 15% of the radius and 2% of the disc area. The thrust the rotor exerts on the surrounding fluid is vertical, however the loading varies with radius. Horizontal forces are exerted on the fluid to represent the swirl induced by rotor drag and these are introduced in order to reflect a blade element model. Details of the thrust distribution and method used to achieve it are given in Chapter 4. The rotor thrust distribution is taken to be axisymmetric.

Defining the total rotor thrust and rotor thrust distribution ensures that the thrust is the same magnitude as the helicopter's weight and the centroid of the thrust acts through a predetermined point, in this case the rotor's centre. The assumption that the aerodynamic load is axisymmetric is not necessarily correct. If the blade flapping is large the aerodynamic load that the blades experience will not be completely axisymmetric. The rotor is defined to lie in a horizontal plane. In reality the rotor may have a slight inclination from the horizontal, since a horizontal thrust component is necessary to counteract the fuselage drag. As the fuselage is not modelled, it is valid to ignore the drag associated with it and to assume the rotor plane is horizontal.

#### **8.4.3 Helicopter Location and Flow Directions**

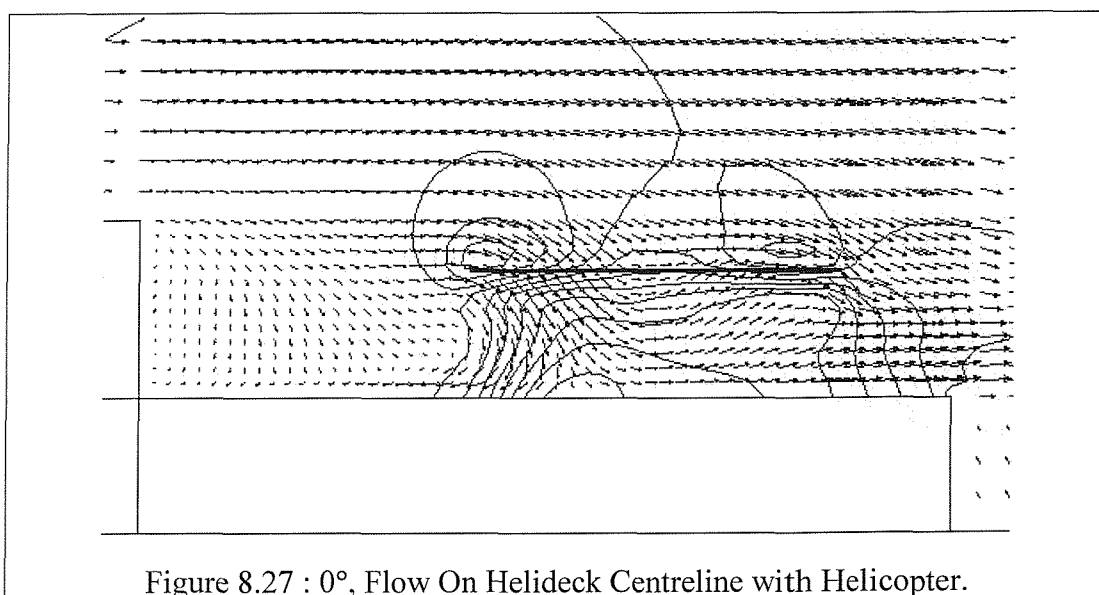
The helicopter main rotor is 3m above the deck. This height was chosen in order to model the helicopter immediately before landing. Three wind directions are chosen;  $0^\circ$  corresponds to the freestream acting from in front of the ship.  $90^\circ$  is

the wind approaching from the starboard side and  $180^\circ$  the wind acts from directly behind the ship. The helicopter thrust is defined according to Chapter 4 and is described in Section 8.4.2.



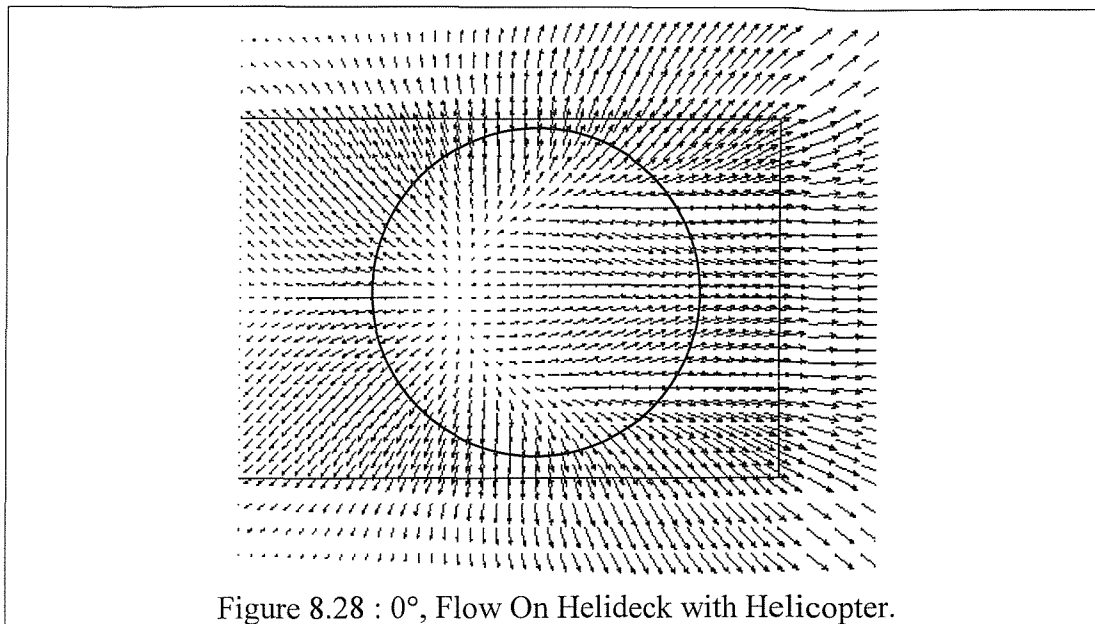
### 8.4.3.1 Zero Degrees

The flow over the centreline of the helideck is shown in Figure 8.27; the vectors represent speed and the contours show pressure variations of 50Pa. The flow is attached at the aft end of the superstructure but separates at the hangar face. The forward half of the rotor disc experiences large air flow velocities with considerable vertical components, which will be discussed later in this section. The rear of the disc experiences air flow with a lesser vertical component. The low pressure regions are above the rotor and the highest pressure occurs at the stagnation point on the deck.

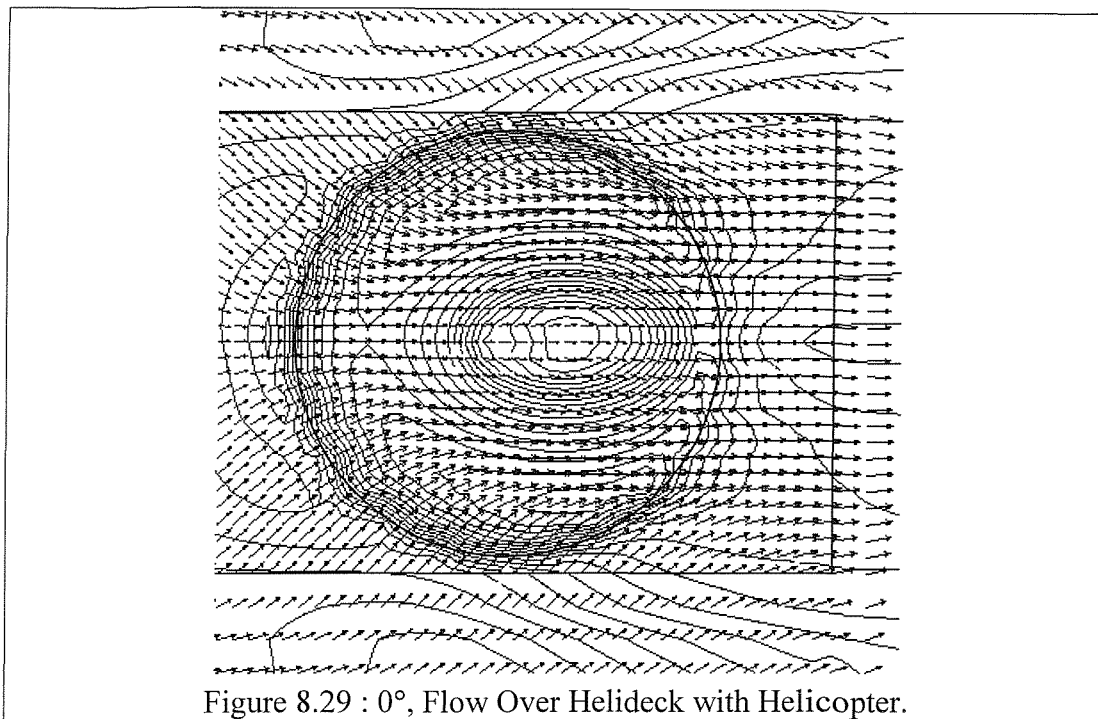


The flow 0.5m above the helideck is shown in Figure 8.28, the hangar is to the left of the diagram and the freestream acts from left to right. There is a stagnation point on the centreline of the ship, which occurs in front of the helicopter hub.

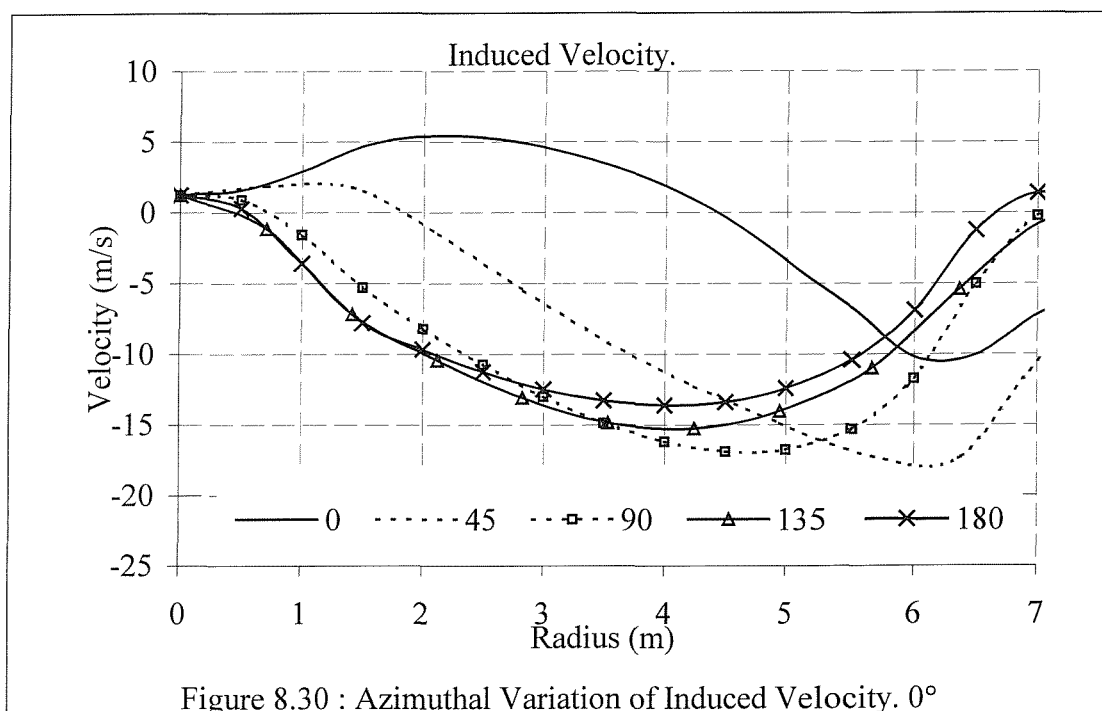
From this point the air is forced out radially in all directions. Therefore there is flow travelling upstream towards the hangar face and out the sides of the helideck.



Another plan view of the flow solution is shown in Figure 8.29; the hangar face is out of view on the left of the diagram and the free stream acts from the left. The vectors are velocity and the contours represent variation in vertical velocity component. The flow diagram is almost symmetrical despite the asymmetry of the helicopter main rotor specification. The thrust forces are symmetrical but the drag forces, which act in the horizontal plane, produce a degree of asymmetry. For this discussion a conventional notation for rotor blade azimuth location will be used, namely the blade is at zero when aligned along the fuselage behind the helicopter and the angle increases as the blade travels in an anti-clockwise direction.



The greatest induced velocity occurs at the azimuthal positions of 90° and 270° and the least at 0°. These variations are shown in Figure 8.30; only the induced velocities in the first two quadrants are shown as the solution is effectively symmetric.



These induced velocities can be analysed to find the blade pitch that must be present to exert the necessary thrust on the fluid. The azimuthal variation of pitch is shown in Figure 8.30. The least root pitch, 13°, occurs at the 0° azimuth; this feature was also found in the forward flight flow solution analysed in Chapter 7.

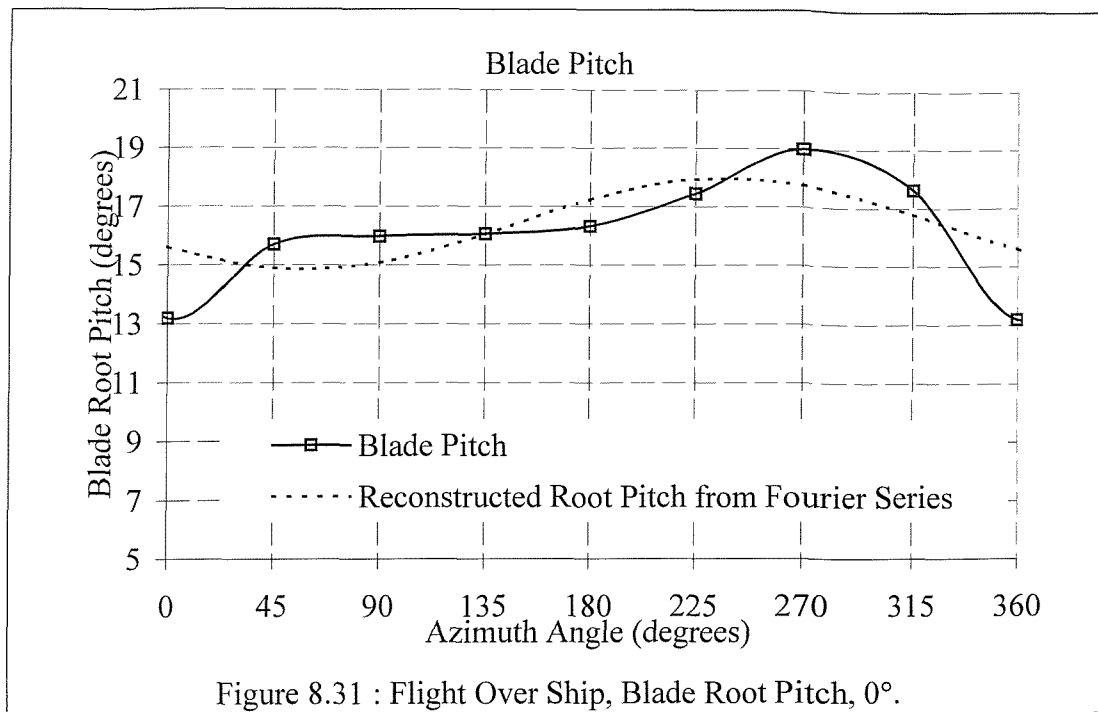


Figure 8.31 : Flight Over Ship, Blade Root Pitch, 0°.

The blade pitch remains approximately constant for the angles 45° through to 180°. The induced velocity the blade experiences during this part of the azimuth does vary widely but the lift force exerted on the blade will remain constant at a constant pitch of 16°.

As the blade passes the 180° location it moves onto the retreating side of the disc. This is considered when calculating blade pitch, thus the blade pitch prediction is not symmetrical and the blade pitch on this side of the disc is greater. The largest root pitch occurs at the azimuth location of 270°, where the blade is moving fastest in the same direction as the free stream. At this location the root pitch required is 3° greater than that at 90° azimuth.

As described in Chapter 4, it is possible to take the blade incidence estimate at the eight azimuthal locations and construct Fourier series based on these. This azimuthal pitch variation consists of only the first three terms of a Fourier series, which are equivalent to collective and cyclic pitch. This is shown in Figure 8.31. The reconstructed pitch variation does not follow the pitch prediction found from considering each 45° segment separately.

#### 8.4.3.2 90 Degrees

A side elevation of the flow over the ship and through the helicopter rotor is shown in Figure 8.32; the freestream is acting from right to left. The contours

represent pressure intervals of 50Pa; the figure not only shows the pressure discontinuity at the plane of the rotor but the pressure increase associated with the stagnation on the upwind side of the ship.

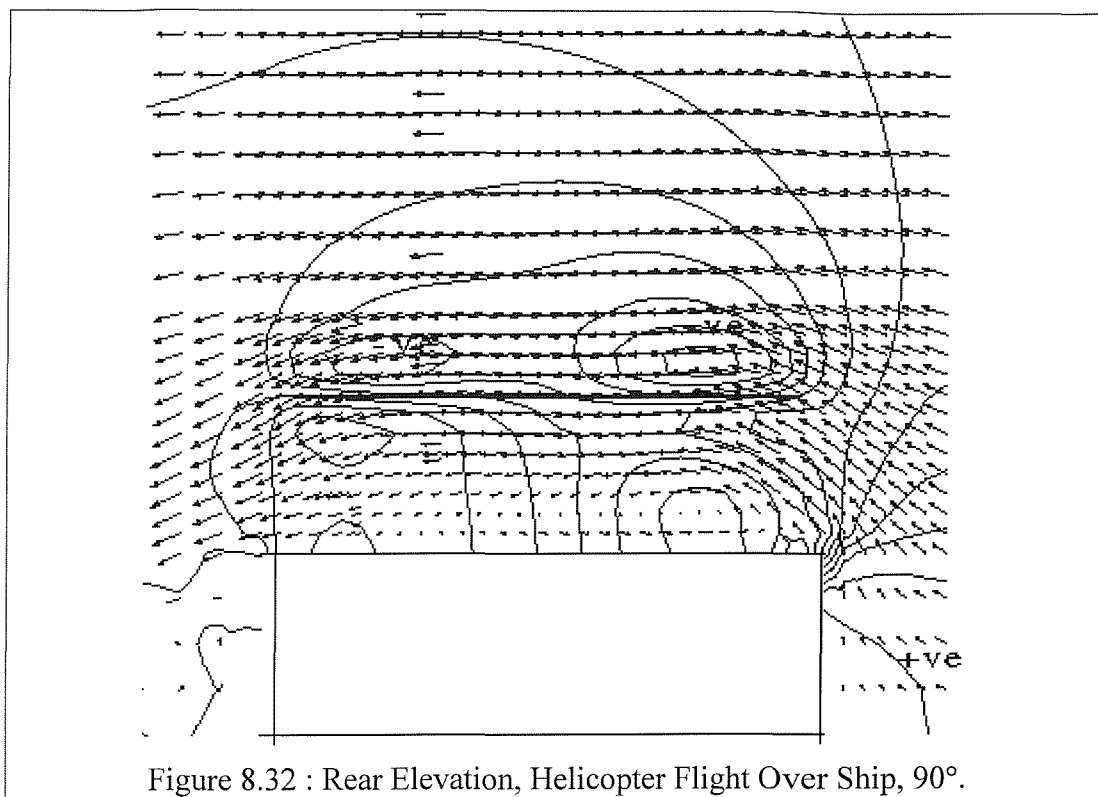


Figure 8.32 shows that the rotor disc experiences upflow through the rotor on the windward side and down flow on the downwind side. There are regions of reverse flow on the helideck surface and immediately downstream of the helideck.

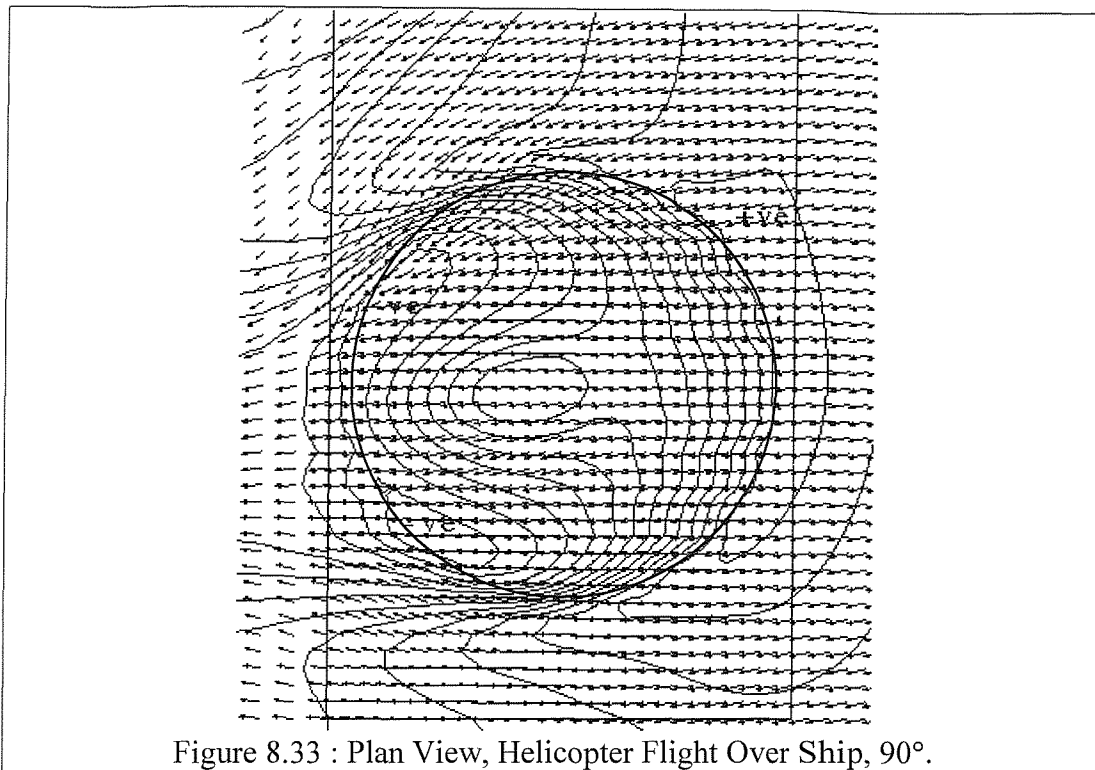


Figure 8.33 : Plan View, Helicopter Flight Over Ship, 90°.

Figure 8.33 displays the plan view of the flow solution at the height of the rotor disc; the free stream acts from right to left. The contours show variation of the vertical velocity component, with positive value indicating vertically upwards. The downstream side of the rotor disc experiences vertical velocities acting down and the upstream side of the disc experiences velocity flowing up through the rotor. The flow solution is not symmetrical; the asymmetries are introduced by the hangar and superstructure which are out of view at the top of the figure.

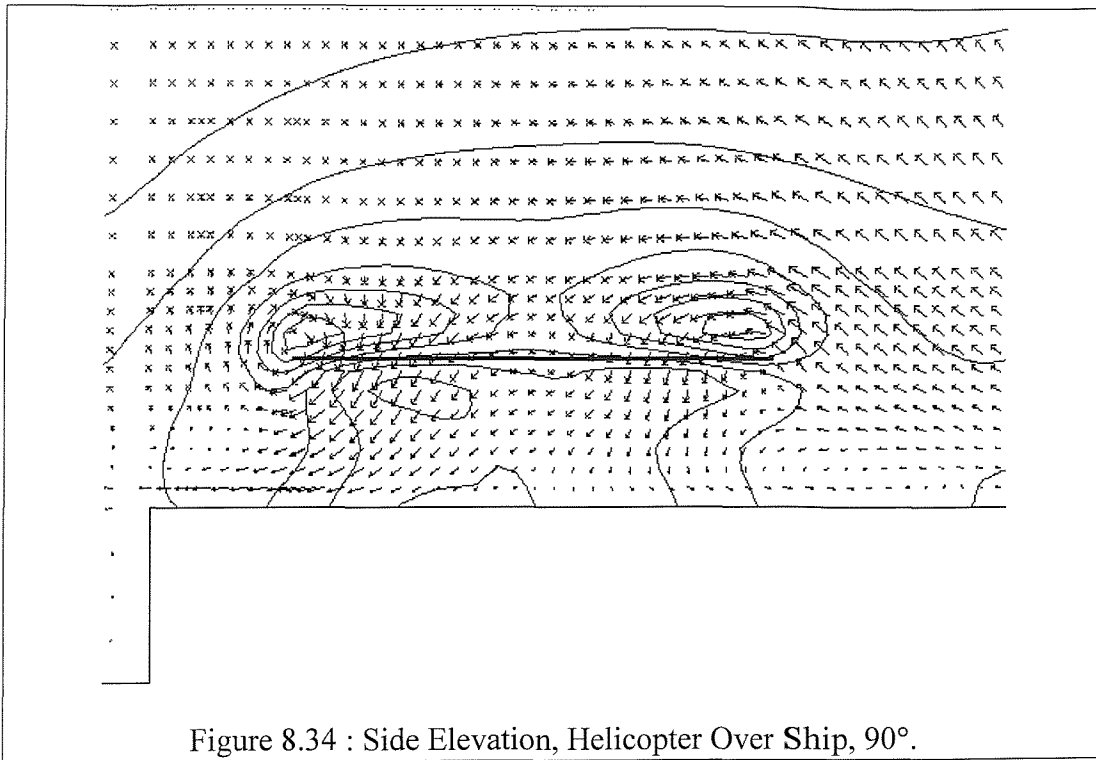
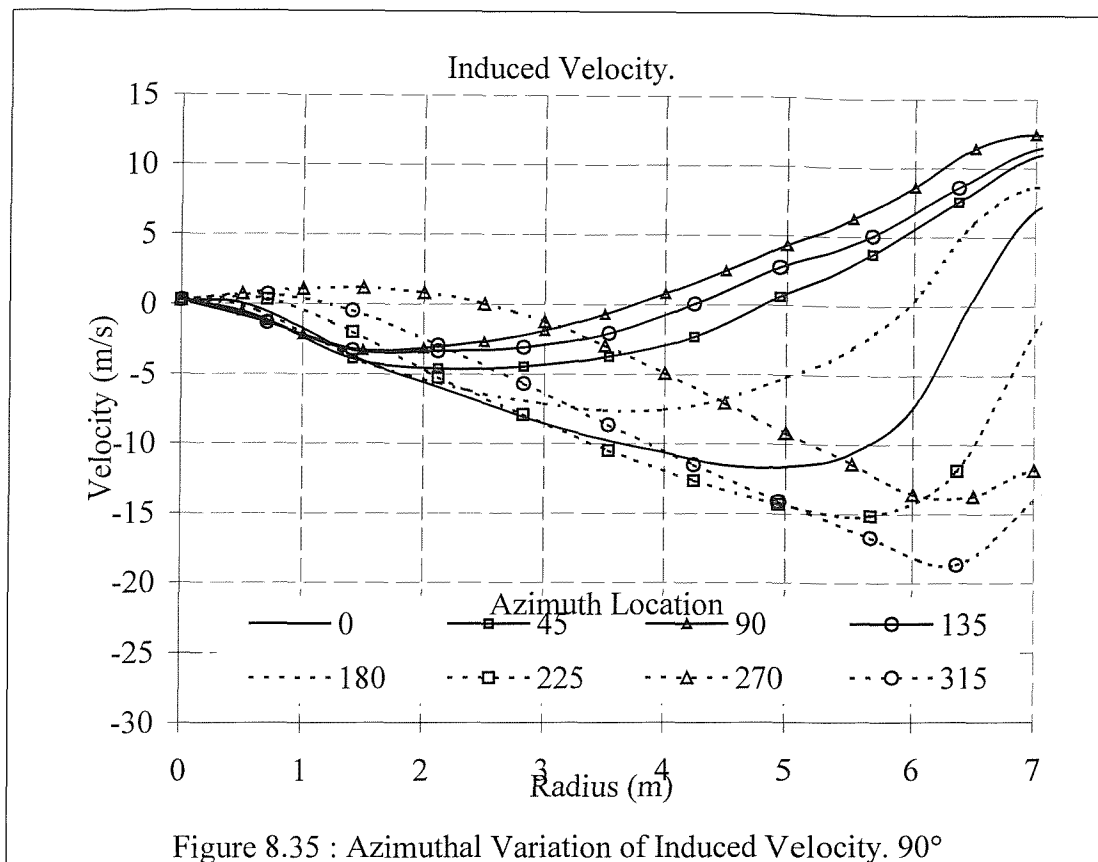
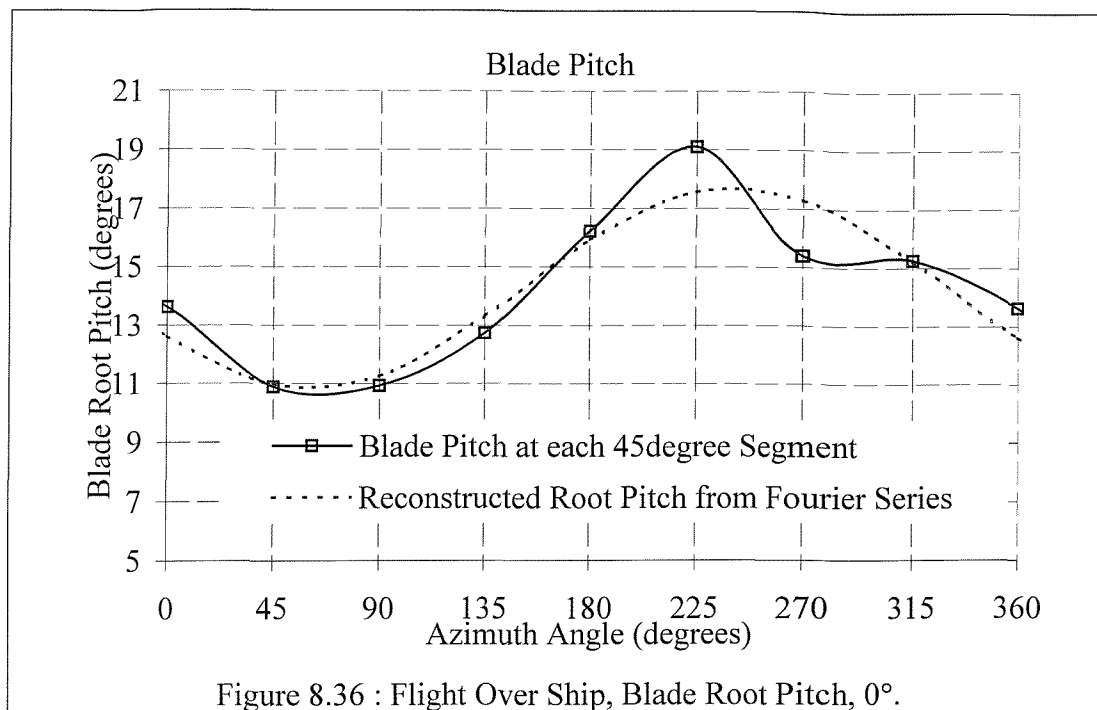


Figure 8.34 : Side Elevation, Helicopter Over Ship, 90°.

Figure 8.34 shows a side elevation of the rear of the flight deck. The freestream is acting into the page, and hence only vertical and lateral perturbations of the flow are shown. The deck area beneath the rotor experiences high pressure as depicted by the pressure contours. The air flow either side of the rotor has components acting vertically up. The flow through the disc itself is predominantly downward.



The induced velocities at each 45 degree segment are shown in Figure 8.35. The azimuth angle remains relative to the ship's coordinate system and has not moved with the freestream direction. Therefore zero degrees azimuth is defined as the location at which the blade is pointing aft along the ship's centreline. This figure indicates that a blade would experience minimal induced velocities as it moves through the first and second quadrants. In fact there would be an upflow through the blade tips in this region. As the blade travels from 180° through to 360° it experiences vastly increased induced velocities.



The induced velocities at each section can be analysed to estimate the necessary incidence to provide a thrust equal to the helicopter's weight. The resultant variation of pitch incidence is shown in Figure 8.36. This pitch incidence also ensures that the rotor thrust acts through the hub. The required rotor pitch is least on the right hand side of the rotor disc because this side of the disc experiences upflow from the side of the helideck. The right hand side of the rotor disc, azimuth angles 180° to 360°, requires increased pitch. The induced velocities at this side of the disc are greater.

Also shown in this figure is a reconstruction of the pitch variation introduced by the first three terms of a Fourier series which are equivalent to collective and cyclic pitch. The method of determining these values are given in Chapter 4. The two pitch distributions are similar throughout the whole azimuth except at 270°. This location is downstream of the rotor hub; the result is consistent with the hover solution analysed in Chapter 7.

### 8.4.3.3 180 Degrees

The 180° wind direction acts from directly astern of the ship; this wind angle is considered most dangerous and most limiting to helicopter operations. Fang [8.5] states 'large helicopter pitch-up angles reduce the pilot's view over the flight deck'. A side elevation of the flow solution is shown in Figure 8.37. The vectors

show velocity and the contours pressure variation of 50Pa. The freestream acts from left to right and the hangar face is on the right of the figure.

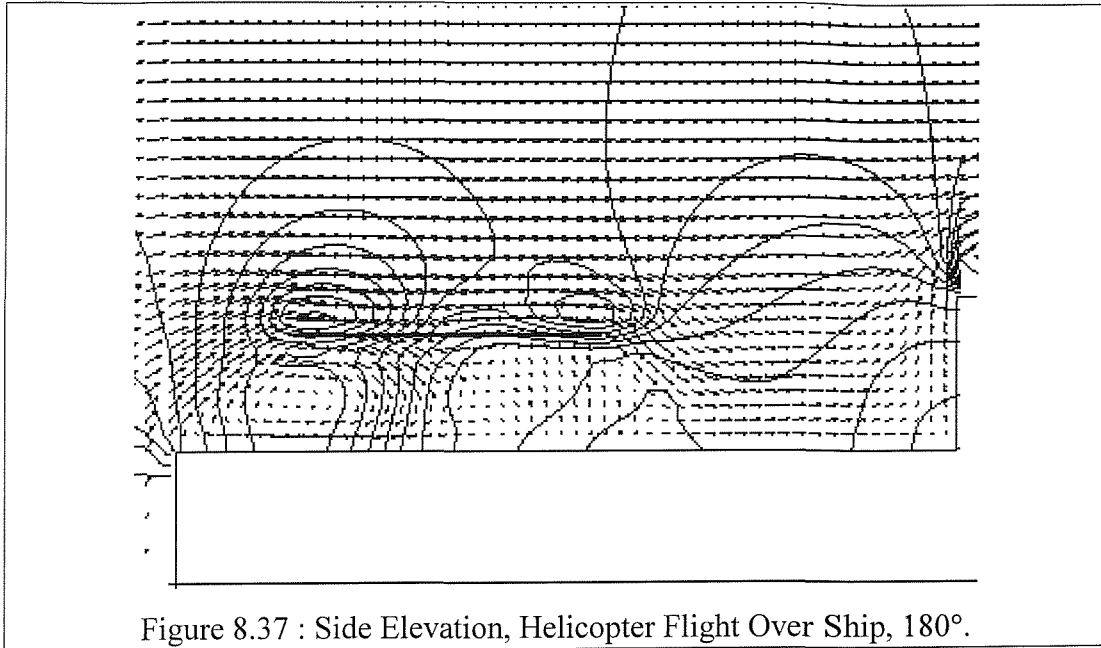
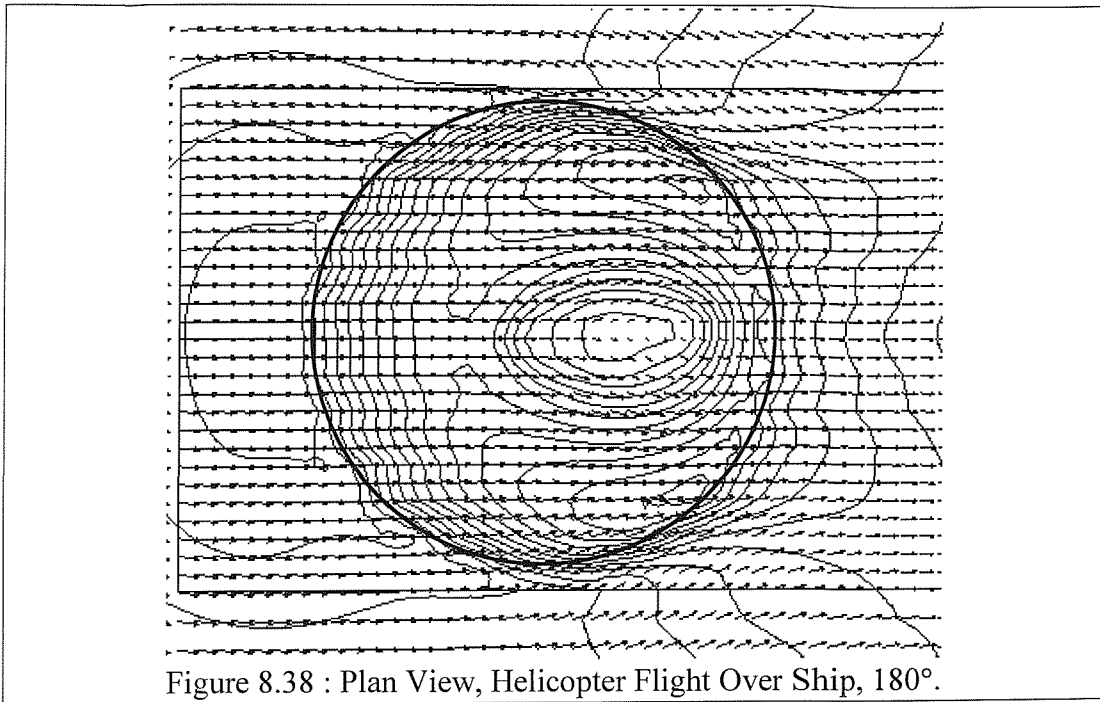
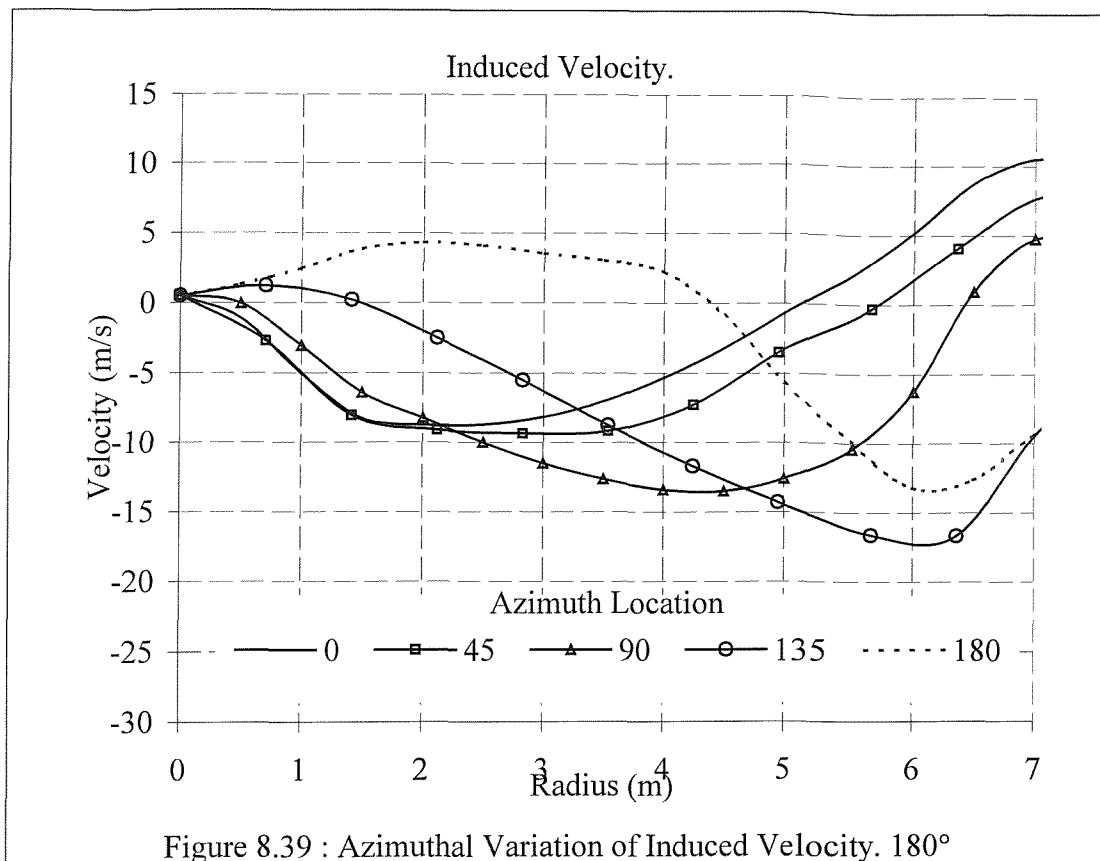


Figure 8.37 : Side Elevation, Helicopter Flight Over Ship, 180°.

Figure 8.38 shows the airflow detaching at the aft edge of the helideck and travelling upwards before turning sharply and moving downwards through the rotor disc and down onto the deck. The flow then turns upstream and flows along the helideck before becoming entrained into the sheared flow from the corner of the helideck. The rear part of the disc experiences upflow near the hub but forces the flow down at the disc extremity. The air flows up and over the hangar face.



A plan view of the flow solution is shown in Figure 8.38; the contours represent variations of vertical velocity component. The velocity acts largely in the direction of the freestream except outside the rotor disc and aft of the hub where the flow is being drawn onto the helideck. The contours display a region of positive vertical velocity just aft of the hub.



The variation of induced velocity around the azimuth is shown in Figure 8.39; the solution is almost symmetrical and hence the angles 225°, 270° and 315° are not shown. At 0° azimuth the blade is pointing aft; at this location the disc experiences upwards vertical velocity at the blade extremity but downward components nearer the hub. This trend is also found at the azimuthal locations 45° and 90°, however the regions of upflow are reduced and there is more flow in a downwards direction. The blade experiences greatest downwards flow velocity at 135°. At 180° azimuth the flow is almost opposite to 0°; near the hub the flow acts upwards and at the outer regions the flow has downwards vertical component.

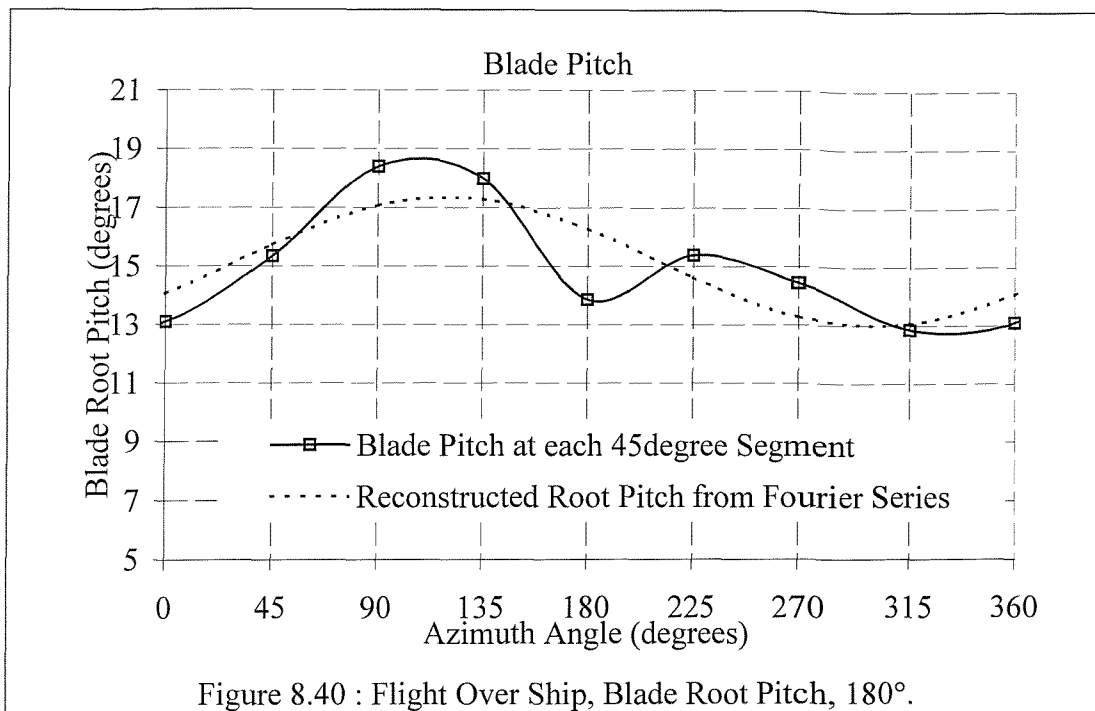


Figure 8.40 : Flight Over Ship, Blade Root Pitch, 180°.

Using the induced velocities shown in Figure 8.39 an estimate of blade root pitch can be made. The pitch is chosen such that the thrust exerted on the fluid found from the induced velocities and blade element theory is equal to the thrust exerted on the fluid within the CFD solution. The resultant pitch variation around the azimuth is shown in Figure 8.40. The helicopter is effectively flying backwards, thus a rotor blade at 90° azimuth is moving in the same direction as the free stream and hence experiencing reduced relative velocities. This is reflected in Figure 8.40; the blade pitch is less between 0° and 180° than 180° and 360°. The pitch is least at 315° azimuth; at this location the blade would be advancing and experiencing the upflow caused by the aft face of the helideck at the transom.

Also shown Figure 8.40 is the blade pitch variation around the azimuth. The reconstructed Fourier series is close to the pitch estimates found from the CFD at all locations except at 180° azimuth.

#### 8.4.4 Analysis and Discussion of Flow Solutions

The power exerted at the rotor disc and the estimates of collective and cyclic pitch are shown in Table 8.1. The 40 knots forward flight case is also shown for comparison.

	40 Knots Flight	0°.	90°.	180°.
Power	515kW	692kW	391kW	477kW
Collective	15.3°	16.4°	14.3°	15.2°
Longitudinal	-1.7°	1.3°	1.7°	1.1
Lateral	2.4°	0.8°	3.0°	-1.9
Local Air Speed	40 knots	28 knots	44 knots	37 knots

Table 8.1 : Control and Power Requirements, Flight Over Ship.

The first interesting feature of these results is the variation in power requirements. The 0° flow case has a high power requirement; it should be noted that although the freestream velocity is 40 knots the rotor is located in a region where the local flow velocity is less, approximately 29 knots. This disparity is caused by the wake of the superstructure. This power requirement is less than the hover power which is 842kW. The power requirements with the wind at 90° and 180° are less than the forward flight. This is due to either the wind accelerating over the helideck or ground effect introduced by the helideck. The predicted collective pitch inputs increase with power increase, which is consistent with blade element theory.

The cyclic pitch predictions were found from the first terms of the Fourier series. These terms give information about the necessary pitch incidence around the azimuth to provide sufficient thrust, as shown in equation (8.1).

$$\theta(\psi) = \theta_0 - A_1 \cos \psi - B_1 \sin \psi \quad (8.1)$$

In all the solutions involving helicopter flight over the ship the helicopter remains orientated in the same direction as the ship and hence is flying sideways in the 90° wind direction and backwards in the 180° case. With the wind from 0° the longitudinal incidence variations counteract the fluctuations of induced velocity over the longitudinal span of the rotor disc. The calculated longitudinal pitch incidence variation is positive implying that there should be greater incidence at the front of the disc than at the rear. This is in marked contrast to the forward flight which predicts a negative longitudinal pitch incidence variation which is consistent with established wake models discussed in Chapter 7. The flow solution is approximately symmetrical, however there is a small amount of lateral

pitch incidence because the retreating side of the rotor requires greater incidence to compensate for the reduced relative velocities.

The helicopter is effectively flying sideways in the  $90^\circ$  wind case. The lateral pitch incidence variation is introduced to compensate for the upflow on the starboard side of the ship and downflow on the port side. The lateral pitch is  $3^\circ$  incidence variation from side to side which is the largest pitch variation of the three solutions. In this case the longitudinal pitch incidence is introduced to give the blades on the retreating side of the disc additional pitch. With this wind direction the flow accelerates over the ship and hence the helicopter experiences wind speeds greater than the freestream velocity.

The wind at  $180^\circ$  corresponds to the freestream acting from directly behind both the ship and helicopter. As the helicopter is flying backwards the advancing side of the rotor is the right hand side, hence the lateral pitch incidence variation is negative. There is also a slight variation in the longitudinal pitch incidence,  $1.1^\circ$ , which compensates for the induced velocity being greater over the front half of the rotor disc. The helicopter is flying in a local airspeed which is marginally less than the freestream velocity.

These results have implications on helicopter control capability. Table 8.1 implies that positive longitudinal pitch incidence is required to hover in all three wind directions yet negative pitch incidence variation is required in steady flight. If the helicopter is travelling onto the helideck the pilot must ensure that there is enough longitudinal stick control to not only arrest the motion of the helicopter but prevent the helicopter flying into the hangar.

The results of this study also indicate a relationship between local air speed, power and control parameters. In all four solutions analysed in Table 8.1, increased local air speed increases the cyclic control parameters but reduces the power requirements.

#### **8.4.5 Conclusion**

The power and control parameters to maintain hover and forward flight are established and understood. As the pilot approaches the deck there is a transition

from these relatively simple predictable flow regimes to flight in the ship airwake. Whilst the pilot negotiates the ship airwake he/she must also prepare to land. Landing on a ship requires accuracy and control but this must also be performed quickly at an opportune moment between large waves.

This study has shown that the helicopter is drawn forwards to the hangar face as it nears the landing spot. This is counteracted by the pilot's use of stick input controls which control the cyclic pitch variations.

Established SHOLs (Safe Helicopter Operating Limits), for example Fang [8.5], are based on pilot workload and show that the operational limits are enforced by a combination of power requirement, control requirements and dynamic inputs. The flow solutions above give us information about the helicopter flight but do not give us any indication of pilot workload. In order to bridge the gap criteria need to be adopted which will ultimately convert a CFD solution into the practicalities and rating of the landing manoeuvre.

## 9 Conclusions and Future Work

### 9.1 Conclusions

The literature review discussed recent research into the helicopter/ship dynamic interface. Whilst advances have been made into understanding the ship airwake from wind tunnel tests and CFD models are recreating the flows with increasing fidelity, these models have overlooked the interactive nature of the problem. The upper limit of wind speed for safe helicopter operations is between 10 and 60 knots, dependent on many factors including wind direction and sea state. The induced velocity through a helicopter rotor in hover is typically 30 knots; it is therefore easy to recognise that the flows will interact and that neither can be neglected.

This study has modelled both the helicopter downwash and the ship airwake in one solution. The first major step in rotor modelling was the decision to simplify the model to the form of an actuator disc. Although a simplification, the disc allows us to glean more data from each flow solution. The alternative method was to model each blade individually, which would firstly involve a considerable increase in number of grid cells and change the solution from steady state to transient and thus increase the computational storage and processing requirements. Such a solution method is impossible at present. Entering the rotor blades themselves into the model would require the definition of the collective and cyclic pitch at the problem onset. There would be no guarantee that the thrust the blades exerted bore any resemblance to the helicopter weight. Definition of the actuator disc generates a flow solution that provides velocity data and thus yields pitch information and power requirements.

The rotor disc was modelled within CFX using functions designed to imitate porous media immersed in fluid. Firstly this function was successfully verified in a freestream before moving onto the hover flow solution. The hover flow solution is unique in that there need not be a uniform freestream velocity and the fluid motion is initiated from the centre of the flow domain. A new boundary condition has been devised that overcomes this problem. This boundary condition couples together pressure and velocity, a technique which to the author's knowledge has not been used elsewhere. The results agree completely with actuator disc theory.

The actuator disc model was flown near a surface plane. The flow solutions yielded a relationship between height and ground effect which manifests itself as an induced power reduction.

A further actuator disc model was developed which, instead of assuming a uniform thrust across the rotor radius, included radial thrust variations and the provision of swirl forces. The flow solutions generated by this model also corresponded to momentum theory. The thrust distribution was assumed axisymmetric and based on a blade element model.

Both rotor models were 'flown' in forward flight and found to agree with the established wake models. All of these results provided the confidence that the rotor model was accurate and could be used to generate flow solutions which are not possible analytically, for example flight in the ship airwake.

The airflow around bluff bodies is characterised by large turbulent areas of separated flow and recirculation. In order to use a CFD program to model these flows, extensive sensitivity and optimisation studies were undertaken. The results of these studies are invaluable for further work as they provide both knowledge that the solutions achieved are both correct and are achieved efficiently. No CFD solution can be treated with any confidence unless sensitivity studies and experimental comparisons back it up. One important discovery was that use of high Reynold's Number turbulence models (RNG k-epsilon model) rather than the default all-purpose model (standard k-epsilon model) was required. The computationally found flow solution of a block in a wind tunnel closely agreed with the wind tunnel measurements.

The parameters derived in the sensitivity study were incorporated into the grids in Chapter 8 used to generate flow solutions around the TTCP Simple Frigate Shape. These solutions demonstrate that CFD can accurately recreate experimental flows. Of the three wind angles considered, all the flow features were resolved at two angles. The only discrepancy occurred in the 90° case; a vortex originating from the hangar base was not predicted computationally.

Armed with the knowledge that the helicopter main rotor and bluff body aerodynamics could both be modelled within CFD they were combined to

consider the helicopter flight at the ship interface. To the author's knowledge this is the only study which combines a ship model, helicopter model and turbulent freestream. From these results the power and rotor blade incidence were estimated. It was found that when the wind comes directly over the bow the helicopter experiences a local wind speed less than the freestream. Also this wind direction required least cyclic pitch variations.

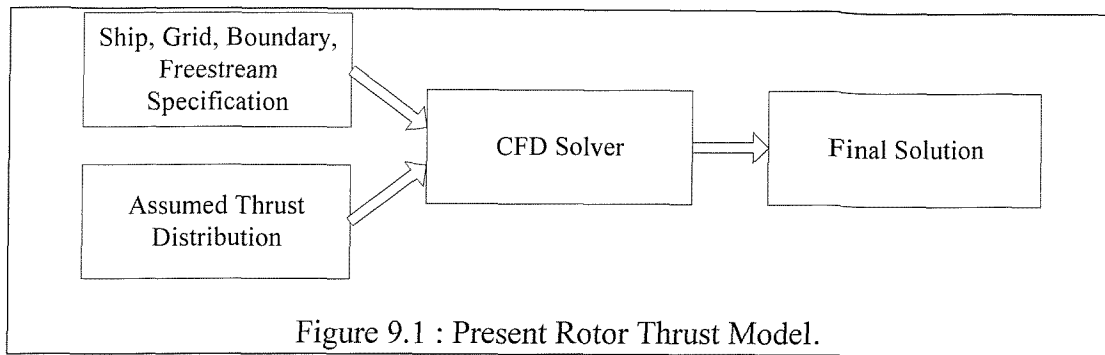
A flow solution was found with the wind approaching the ship at  $90^\circ$ , from the starboard side. At this wind direction the helicopter experiences a greater local wind speed and also requires large cyclic pitch variations to maintain a realistic thrust magnitude and distribution.

A flow solution was obtained with the wind acting from behind the ship,  $180^\circ$ . The CFD showed that hovering over the ship required little power or control requirements, however in reality helicopters endeavour to avoid landing in following winds. This result demonstrates that the CFD model must not be considered in isolation. There are many factors that limit helicopter operations and in this case the helicopter would be hovering with a nose-up attitude which considerably reduces the pilot's deck visibility. Another key factor, beyond the scope of this study is the effect of the tail rotor. High cross winds, perpendicular to the helicopter's direction, introduce high demands on the tail rotor. Fang [9.4] states that inadequate yaw control limits helicopter operations where the ship's relative wind is approximately  $45^\circ$  either side of the bow.

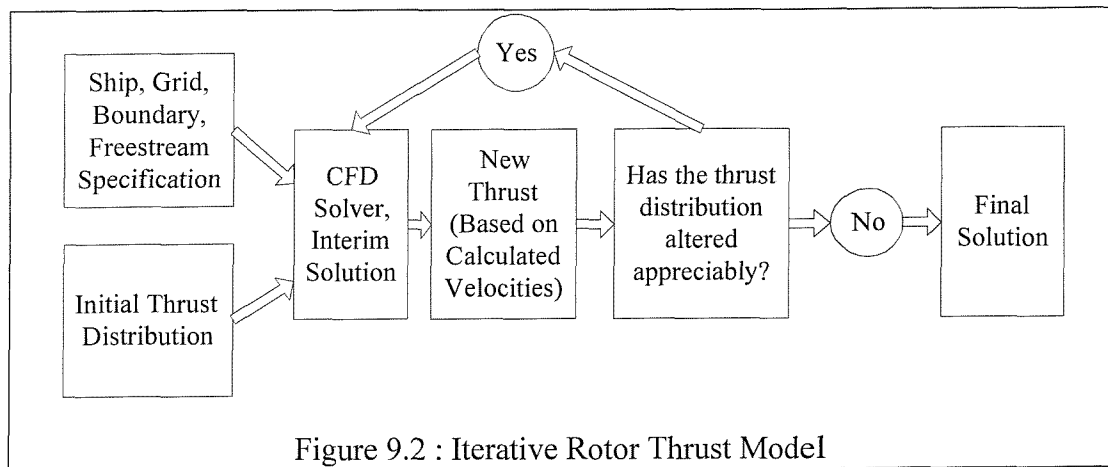
This study has shown that a complex problem can be modelled computationally and realistic results achieved. The model is only limited by the assumptions.

## **9.2 Future Work**

The rotor model has used a basic assumption; the thrust distribution is axisymmetric. Thus the thrust is defined at the onset of the problem, as shown in Figure 9.1. This is realistic in hover but merely an assumption in forward flight.



A rotor, which includes a more complex thrust distribution, could be introduced iteratively. Such a thrust model could be designed to reflect blade flapping motions and the thrust distribution introduced. There are two possible schemes for introducing a thrust distribution dependant on the local flow. The first is shown in Figure 9.2. This method starts with an assumed thrust distribution which is used to provide an interim flow solution. The flow through the rotor is extracted from the interim solution and used to determine a thrust distribution which is consistent with the induced velocity. Thus the thrust is redefined and fed back into the solver. This method has been used by DERA (Defence Evaluation and Research Agency UK) [9.1]. It was found that after approximately four iterations the thrust distribution remained constant and hence pitch controls reached a converged value. At this point the final solution is reached.



DERA [9.1] used a combined rotor/fuselage model to model the thrust/induced velocity relationship. A more computationally efficient method is depicted in Figure 9.3. This method places the rotor thrust model within the code of the solver; as the CFD iterates towards a solution the thrust is varied according to the rotor's local flow velocities. This method represents a completely coupled aeroelastic solution, which, to the author's knowledge, does not exist. The key

advantage is that only one CFD solution is generated. The rotor flapping and pitch variations are solved simultaneously to the flow.

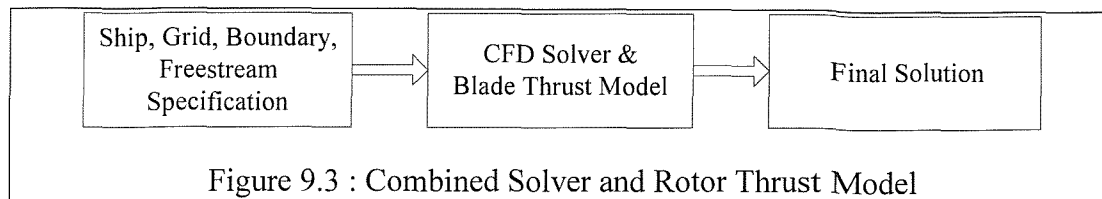


Figure 9.3 : Combined Solver and Rotor Thrust Model

This model is possible within CFX as the flow velocities are available throughout the domain at any iteration and the thrust distribution can be altered also at any iteration. Therefore only the relationship between thrust and local velocities must be determined and expressed in computer code. This statement may imply a simple relationship between the two quantities, but in reality the relationship is hard to determine and dependant on the complexity of the model. Ideally this model would include collective and cyclic pitch, blade flapping, blade lead/lag motion, and the introduction of tip vortices.

The fuselage and tail rotor were removed from the model in Chapter 4. Modelling the fuselage requires vast increase in the number of grid cells, complexity of the grid block structure and lengthy validation cases to ensure that the fuselage model was producing accurate drag and modifying the airflow appropriately. These factors put a fuselage model beyond the scope of this study. The tail rotor was not modelled purely because the grid resolution was not great enough in the relevant region. Both of these features can easily be added when computing resources become available.

All the solutions are presented time averages of the flow solution; the time variant component has been neglected. The reason for this simplification is again lack of computational resources. A grid containing the ship and helicopter model has approximately  $7 \cdot 10^3$  grid cells and requires around 2000 iterations to reach a solution, what presently takes about 48 hours of computing time<sup>1</sup>. A time dependant solution requires around 100 iterations for each time step and one time step is typically 0.01s. Therefore, if a solution is to be traced for 10 seconds,  $10^5$  iterations are required. Assuming that iterations take the same length of time, 100

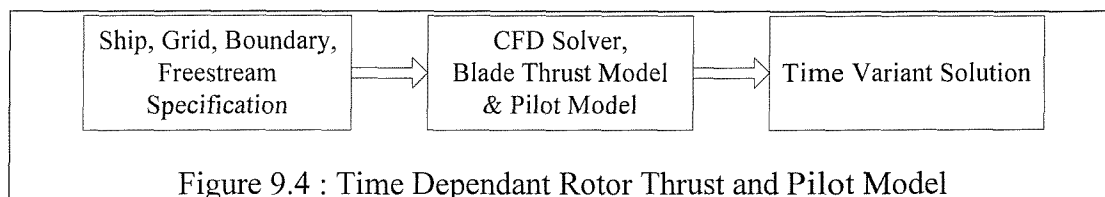
---

<sup>1</sup> One 195MHz processor of an eight processor Power Challenge.

days of computing time would be needed. Such a length of time puts this flow solution out of the reach of present computing capacity, however Moore's Law [9.2] does provide an insight into when this will be possible. Moore (founder of Intel) projects that the speed of computer processors doubles every eighteen months. Using this prediction, the time variant solution will take less than a week in six years time and less than a day in ten years time.

Once a 3D time dependant solution is introduced, there are many possible variants of the model introduced. The helicopter no longer needs to be modelled as stationary but can be moving along a predetermined flight. Also a pilot model can be introduced such that the pilot has an assigned flight path and may deviate from that course when encountering gusts or other disturbances. The pilot model will then endeavour to return the aircraft to that course.

To instigate these attributes, a pilot model and an advanced blade element model would need to be integrated into the solver such that blade controls could be modified at each time step, as shown in Figure 9.4. This is possible in the present version of CFD as the user can adjust forces applied to the fluid using a subroutine.



A time variant solution would yield information about the location of the aircraft and the input pitch controls.

There are other additions that can be made to the model, which require both time dependant solutions and moving grids. The ship and sea surfaces have both been modelled as stationary surfaces. The introduction of moving grids would allow these to be modelled as moving bodies. The sea would not necessarily remain flat and the ship could have displacements in six degrees of freedom. Both these features would add realism at the expense of computational speed.

The greatest assumption of the model is that a finite number of blades can be removed and replaced by an actuator disc which exerts a thrust whilst allowing the

flow of fluid through it. This assumption has been used as the basis of many theories to produce realistic flow solutions, for example, hover, climb, forward flight and rapid descent. Approximately 512 cells cover the actuator disc used in Chapter 8. Ultimately it will be possible to remove the actuator disc and replace it with moving blades. This not only requires moving grids but also significantly more cells. Shiu-Wu [9.3] states that a Navier-Stokes code requires 200 cells around the circumference of a blade section. Therefore the cells would have a length of  $10^{-3}$ m for a blade of chord 0.1m.  $2 \times 10^{11}$  cubic cells would be required to fill a cylinder with a circular cross sectional area of radius 6.4m and a height of 2m.

This vast increase in number of grid cells can be equated to increase in computational effort and storage requirements. However the model would represent a more accurate airflow. A pilot model would have to be present in the solution to ensure the blade pitch variations were kept consistent with thrust requirements. Naturally airflow over the blades would need extensive verification before being input into the model. This flow solution would also include discrete tip vortices. Using Moore's Law [9.2] this computation will not be possible for at least another 15 years.

## 10 References

- [2.1] Healey J.V., 'The prospects for simulating the helicopter/ship interface', Naval Engineers Journal, March 1987.
- [2.2] Ferrier B., Polvi H., Thibodeau F.A., 'Helicopter/Ship Analytic Dynamic Interface', NATO/RTO/AVT Symposium on Fluid Dynamics Problems of Vehicles Operating Near Or In The Air-Sea Interface, Amsterdam, Netherlands, 5<sup>th</sup>-8<sup>th</sup> October 1998.
- [2.3] Carico D., Reddy B., DiMarzio C., 'Ship airwake measurement and modelling options for Rotorcraft applications', AGARD, Aircraft Ship Operations, Nov. 01, 1991, 24 pages.
- [2.4] J. Val. Healey, 'Establishing a Database for Flight in the Wake of Structures, Journal of Aircraft, Vol. 29, No. 4, July-Aug., 1992.

- [2.5] Tate S.J., Padfield G.D., 'Simulating Flying Qualities at the helicopter/ship dynamic interface', American Helicopter Society 50th Annual Forum, Washington DC, May 11-13, 1994.
- [2.6] Tate S.J., Padfield G.D., 'Simulating Flying Qualities at the helicopter/ship dynamic interface', American Helicopter Society 50th Annual Forum, Washington DC, May 11-13, 1994.
- [2.7] Jewell W.F., Clement W.F., Johns J.B., 'Realtime piloted investigation of helicopter flying qualities during approach and landing on nonaviation ships', AIAA 86-0490, 24th AIAA Aerospace Science Conference, Reno, Nevada, January 1986.
- [2.8] Wilkinson C.H., Zan S.J., Gilbert N.E., Funk J.D., 'Modelling and simulation of ship air wakes for helicopter operations - a collaborative venture', NATO/RTO/AVT Symposium on Fluid Dynamics Problems of Vehicles Operating Near Or In The Air-Sea Interface, Amsterdam, Netherlands, 5th-8th October 1998.
- [2.9] Fang R, 'Determination of limitations for helicopter ship-borne operations', AGARD, Aircraft Ship Operations, Nov 1991.
- [2.10] Finlay B.A., 'United Kingdom Approach to Deriving Military Ship Helicopter Operating Limits', AGARD, Aircraft Ship Operations, Nov 1991.
- [2.11] Longobardi R., Vismara G., Paggi B., 'EH101 Ship Interface Trials', AHS Annual Forum 48th, Washington, June 3-5, 1992, Proceedings, Vol. 1, p663-669.
- [2.12] Wensheng S., Zheng G., Hong X., 'Investigation of Air Flow On Flight Deck and Shipboard Operation Envelope', Nanjing University Aeronautics and Astronautics, Transactions (ISSN 1005-1120), Vol. 12 No. 1, June 1995, p45-51.
- [2.13] Newman S.J., 'A theoretical model for predicting the blade sailing behaviour of a semi-rigid rotor helicopter', Vertica, Vol. 14, No. 4, 1990, pp 531-544.

- [2.14] Newman S.J., 'The application of a theoretical blade sailing model to predict the behaviour of articulated rotor helicopters', *Aeronautical Journal of the Royal Aeronautical Society*, Vol. 96, No. 956, pp 233-239.
- [2.15] Newman S.J., 'The problems of rotor engagement and disengagement of a shipborne helicopter', *Journal of Naval Science*, Vol. 20, No. 1, 1994, pp56-64.
- [2.16] Newman S.J., 'The verification of a theoretical helicopter rotor blade sailing method by means of wind tunnel testing', *Aeronautical Journal of the Royal Aeronautical Society*, Vol. 99, No. 982, 1995, pp 41-51.
- [2.17] Healey J.V., 'The aerodynamics of ship structures', AGARD, Aircraft Ship Operations, Nov. 01, 1991, 14 pages.
- [2.18] Crowley J.S., Geyer S.L., 'Helicopter rotor blade injury - a persistent safety hazard in the US army', *Aviation, Space and Environmental Medicine* (ISSN-0095-6562), Vol. 64, No. 9, Sept. 93, P854-858.
- [2.19] Smith E.C., Keller J.A., Kang H., 'Recent developments in the analytical investigation of shipboard rotorcraft engage and disengage operations', NATO/RTO/AVT Symposium on Fluid Dynamics Problems of Vehicles Operating Near Or In The Air-Sea Interface, Amsterdam, Netherlands, 5<sup>th</sup>-8<sup>th</sup> October 1998.
- [2.20] Healey J.V., 'The Airwake of a DD-963 Class Destroyer', *Naval Engineer Journal*, Vol. 101, No.2 1989, pp36-42.
- [2.21] Arney A.M., Blackwell J., Feik R.A., 'Modelling the Helicopter/Ship Dynamic Interface', *The Australian Aeronautical Conference 1989*, Melbourne, 9-11 October 1989, p23-26.
- [2.22] Arney A.M., Blackwell J., Erm L.P., Gilbert N.E., 'A review of Australian activity on modelling the helicopter/ship dynamic interface', AGARD, Aircraft Ship Operations, Nov. 01, 1991, 13 pages.
- [2.23] Blackwell J., Arney A.M., Gilbert N.E., Truong T.T., 'Modelling the Helicopter/Ship Dynamic Interface for the Seahawk/FFG-7', *National*

- Conference Publication - Institution of Engineers, Australia, 1993, vol. 2, No. 93, Pt. 6, p227-284.
- [2.24] Reddy W.D., 'Ship Airwake Measurement and Flow Visualisation', AIAA paper 92-4088, 1992, p118-131.
- [2.25] Fu-Shang Wei, Baitis E., Meyers W., 'Analytical Modelling of SH-2F Helicopter Shipboard Operation', Journal of Aircraft, Vol. 29, No. 5., Sept.-Oct. 1992.
- [2.26] Ferrier B., Langlois B., 'Simulation tools in the calculation of aircraft-ship interface operational limits', NATO/RTO/AVT Symposium on Fluid Dynamics Problems of Vehicles Operating Near Or In The Air-Sea Interface, Amsterdam, Netherlands, 5<sup>th</sup>-8<sup>th</sup> October 1998.
- [2.27] St. Denis and Pierson, 'On the motions of ships in confused Seas', Trans. of SNAME, Vol. 61. New York.
- [2.28] Rhoades M.M., Healey J. Val., 'Flight deck aerodynamics of a nonaviation ship', Journal of Aircraft, Vol. 29, No. 4, July-Aug. 1992.
- [2.29] Johns M.K., Healey J.Val., ' The airwake of a DD-963 Class Destroyer', Naval Engineers Journal, May 1989.
- [2.30] Rhoades M.M., 'A study of the airwake aerodynamics over the flight deck of an AOR model ship', Naval Postgraduate School, Monterey Ca., Sep. 1990.
- [2.31] Tai T.C., Carico D., 'Simulation of DD-963 ship airwake by Navier-Stokes method.', Journal of Aircraft, 1995, Vol. 32, No. 6, pp1399-1401.
- [2.32] Zan S.J., Syms G.F., Cheney B.T., 'Analysis of patrol frigate air wakes', NATO/RTO/AVT Symposium on Fluid Dynamics Problems of Vehicles Operating Near Or In The Air-Sea Interface, Amsterdam, Netherlands, 5th-8th October 1998.
- [2.33] Syms G., Zan S.J., ' Analysis of rotor forces in a ship airwake', AGARD, FDP Symposium on 'Aerodynamics and Aeroacoustics of Rotorcraft', Berlin, Germany, 10<sup>th</sup>-13<sup>th</sup> Oct. 1994.

- [2.34] Tai T.C., 'Simulation and Analysis of LHD Ship Airwake by Navier-Stokes Method', NATO/RTO/AVT Symposium on Fluid Dynamics Problems of Vehicles Operating Near Or In The Air-Sea Interface, Amsterdam, Netherlands, 5<sup>th</sup>-8<sup>th</sup> October 1998.
- [2.35] Murakami S., Kato S., 'Numerical prediction of flow around a building with various turbulence models: comparison of k- $\epsilon$  EVM, ASM, DSM, and LES with wind tunnel tests', 1996 ASHRAE Transactions. AT-1996-10-1, page 741.
- [2.36] Landsberg A.M., Boris J.P., Sandberg W., Young T.R., 'Analysis of the non-linear coupling effects of a helicopter downwash with an unsteady ship airwake', AIAA Aerospace Sciences Meetings and Exhibitions, 33rd Reno, NV, Jan 9-12, 1995, AIAA paper 95-0047, 15p, 11refs.
- [2.37] Davenport A.G., 1982, Engineering Meteorology. E.J. Plate, Editor. Elsevier Scientific Publishing Company, Amsterdam, Netherlands, Chapter 12, 527-569.
- [2.38] Zhang H., Prasad J.V.R., Sankar L.N., Mello O.A.F., Fank J.D., 'Ground Effect Simulation Model for Rotorcraft Interaction Study', American Institute of Aeronautics and Astronautics, Aug. 1995, p130-136, AIAA paper 95-3405.
- [2.39] Zhang H., Mello O.A.F., Prasad J.V.R., Sankar L.N., Funk J.D., 'A Simulation model of a ship ground effect for rotorcraft/ship interaction study', AHS 51st Annual Forum, Fort Worth, TX, May 9-11, 1995, p1094-1100.
- [2.40] Zhang H., Prasad J.V.R., Mavris D.N., 'Ship Airwake effects on the helicopter rotor aerodynamic loads', AIAA Atmospheric Flight Mechanics Conference, Scottsdale, AZ, Aug 1-3, 1994, Technical Papers (A94-30422 10-08). AIAA paper 94-3509.
- [2.41] Cheeseman I.C., Bennett W.E., 'The Effect of the Ground on a Helicopter Rotor in Forward Flight', ARC R&M No. 3021, Sept. 1995.

- [2.42] Plate E.J. (ed.), 'Engineering Meteorology', Elsevier, Amsterdam, The Netherlands, 1982, Ch. 13, pp. 527-569.
- [2.43] Long N.L., Liu J. and Modi A.V., 'Higher order accurate solutions of ship airwake flow fields using parallel computers', NATO/RTO/AVT Symposium on Fluid Dynamics Problems of Vehicles Operating Near Or In The Air-Sea Interface, Amsterdam, Netherlands, 5<sup>th</sup>-8<sup>th</sup> October 1998.
- [2.44] Wakefield N.H., Newman S.J., Wilson P.A., 'CFD predictions of external airflow on helicopter operations when operating from ship flight decks', NATO/RTO/AVT Symposium on Fluid Dynamics Problems of Vehicles Operating Near Or In The Air-Sea Interface, Amsterdam, Netherlands, 5<sup>th</sup>-8<sup>th</sup> October 1998.
- [2.45] Newman S.J., 'Foundations of Helicopter Flight', pub. Edward Arnold 1994. ISBN 0-340-587024.
- [2.46] Tattersall P., Albone C.M., Soliman M.M., Allen C.B., 'Prediction of ship airwakes over flight decks using CFD', NATO/RTO/AVT Symposium on Fluid Dynamics Problems of Vehicles Operating Near Or In The Air-Sea Interface, Amsterdam, Netherlands, 5<sup>th</sup>-8<sup>th</sup> October 1998.
- [2.47] Maslov L.A., Valuev N.O., Zharinov A.V., 'The experience of aerodynamic research behind aircraft-carrier ship with elements for safe operation of ship-based aircraft', NATO/RTO/AVT Symposium on Fluid Dynamics Problems of Vehicles Operating Near Or In The Air-Sea Interface, Amsterdam, Netherlands, 5th-8th October 1998.
- [2.48] Mahaffey W.A., Mukerjee T., Singhal A.K., Keck J., 'Turbulent ship airwake environment prediction methodology', CHAM of North America Inc., 1525-A Sparkman Drive, Huntsville, ALA. 35805, Report 4031, 1985.
- [3.1] Ilinica A, Camarero R., Trepanier J.Y., Reggio, 'Error estimator and adaptive moving grids for finite volume schemes', AIAA Journal, Vol. 33, No. 11, November 1995.
- [3.2] Oliger J., Zhu X., 'Stability and error estimation for component adaptive grid methods', Applied Numerical Mathematics 20 (1996), pp407-426.

- [3.3] CFX4.1 Flow Solver User Guide. 1995.
- [3.4] 'Computational Fluid Dynamics - The Basics with Applications', Anderson J.D., McGraw-Hill. ISBN 0-07-001685-2. 1995.
- [3.5] Versteeg H.K., Malalasekera W., 'An Introduction to Computational Fluid Dynamics, The Finite Volume Method', Longman, 1995.
- [3.6] Kumarasamy S., Barlow J.B., 'Unsteady flow over a bluff body adjacent to a plane wall', AIAA-96-2488-CP. 1996.
- [3.7] Newman S.J., 'Blade Sailing Contract 94/06, Department of Aeronautics and Astronautics, University of Southampton, August 1994.
- [4.1] Simon Newman, 'Foundations of Helicopter Flight', Edward Arnold. 1994.
- [4.2] 'CFX 4.1 Flow Solver User Guide', sections 12.3.2, 5.16.2, 8.2.3 and 8.4. 1995
- [5.1] 'Aerodynamic Performance Of A 27-Percent-Scale AH-64 Wind-Tunnel Model With Baseline/Advanced Rotor Blades', Kelley H.L., Wilson J.C., Presented at the 41st Annual Forum & Technology Display, May15-17,1985, Ft. Worth, Texas.
- [5.2] 'The Effect Of The Ground On A Helicopter Rotor In Forward Flight', Cheeseman I.C., Bennett W.E., ARC R&M 3021 (1957).
- [6.1] Wakefield N.H., Newman S.J., Wilson P.A., 'CFD predictions of external airflow on helicopter operations when operating from ship flight decks', NATO/RTO/AVT Symposium on Fluid Dynamics Problems of Vehicles Operating Near Or In The Air-Sea Interface, Amsterdam, Netherlands, 5th-8th October 1998.
- [6.2] Wakefield N.H., Newman S.J., Wilson P.A., 'CFD predictions of external airflow on helicopter operations when operating from ship flight decks', International Powered Lift Conference, 2-4 September 1998, Royal Aeronautical Society, London.

- [6.3] Plate E.J.(ed.), 'Engineering Meteorology', Elsevier, Amsterdam, The Netherlands, 1982, Ch.13.
- [6.4] Versteeg H.K., Malalasekera W., 'An Introduction to Computational Fluid Dynamics, The Finite Volume Method', Longman, 1995.
- [6.5] Newman S.J., 'A Theoretical and Experimental Investigation Into The Rotor Blade Aeroelastic Behaviour of a Shipborne Helicopter During Rotor Engagement and Braking', AGARD Conference Proceedings No. 552., 75th Fluid Dynamics Symposium, Berlin, Oct. 1994.
- [7.1] Castles W., and DeLeeuw J.H., 'The normal component of the induced velocity in the vicinity of a lifting rotor and some examples of its application', NACA TN 2912. 1953
- [7.2] Mangler K.W. and Squire H.B., 'The induced velocity field of a rotor,' R&M No. 2642 (1953).
- [7.3] Simon Newman, 'Foundations of Helicopter Flight', Edward Arnold, 1994.
- [7.4] Etter, D.M., 'Structured Fortran 77 for Engineers and Scientists', Third Edition, The Benjamin/Cummings Publishing Company Inc. 1983.
- [7.5] Payne P.R., 'Helicopter Dynamics and Aerodynamics', Sir Isaac Pitman & Sons Ltd., 1959.
- [7.6] Glauert H., 'A general theory of the autogiro,' R&M No.1111 (1926).
- [8.1] Cheney B.T., Zan S.J., 'CFD Code Validation Data and Flow Topology for The Technical Co-operation Program AER-TP2 Simple Frigate Shape', LTR-A-035 April 1999. National Research Council Canada.
- [8.2] Wilkinson C.H., Zan S.J., Gilbert N.E., Funk J.D., 'Modelling and simulation of ship air wakes foe helicopter operations - a collaborative venture', NATO/RTO/AVT Symposium on Fluid Dynamics Problems of Vehicles Operating Near Or In The Air-Sea Interface, Amsterdam, Netherlands, 5th-8th October 1998.

- [8.3] Syms G., Zan S.J., ' Analysis of rotor forces in a ship airwake', AGARD, FDP Symposium on 'Aerodynamics and Aeroacoustics of Rotorcraft', Berlin, Germany, 10th-13th Oct. 1994.
- [8.4] Tattersall P., Albone C.M., Soliman M.M., Allen C.B., 'Prediction of ship airwakes over flight decks using CFD', NATO/RTO/AVT Symposium on Fluid Dynamics Problems of Vehicles Operating Near Or In The Air-Sea Interface, Amsterdam, Netherlands, 5th-8th October 1998.
- [8.5] Wensheng S., Zheng G., Hong Z., 'Investigation of Air Flow On Flight Deck And Shipboard Operation Envelope,' Transactions of Nanjing University of Aeronautics and Astronautics, Vol.12 No. 1, June 1995
- [8.6] Fang R., 'Determination of Limitations for Helicopter Ship-Borne Operations', AGARD, Aircraft Ship Operations, Nov 1991.
- [9.1] Tattersall P., Albone C.M., Soliman M.M., Allen C.B., 'Prediction of ship airwakes over flight decks using CFD', NATO/RTO/AVT Symposium on Fluid Dynamics Problems of Vehicles Operating Near Or In The Air-Sea Interface, Amsterdam, Netherlands, 5<sup>th</sup>-8<sup>th</sup> October 1998.
- [9.2] Biedron R.T., Mehrotra P., Nelson M.L., Preston F.S., Rehder J.J., Rogers J.L., Rudy D.H., Sobieski J., Storaasli O.O., 'Compute as Fast as the Engineers can Think!' NASA/TM-1999-209715.
- [9.3] Shiu-Wu Chau, 'Numerical Investigation of Free-Stream Rudder Characteristics Using a Multi-Block Finite Volume Method', Institut Fur Schiffbau Der Universitat Hamburg, July 1997, Bericht Nr. 580.
- [9.4] Fang R., 'Determination of Limitations for Helicopter Ship-Borne Operations', AGARD, Aircraft Ship Operations, Nov 1991.